frontiers | Research Topics

Advances in cortical architectonic & functional imaging with MRI: Methodology and applications

Edited by
Chitresh Bhushan and Anand Joshi

Published in
Frontiers in Neuroscience

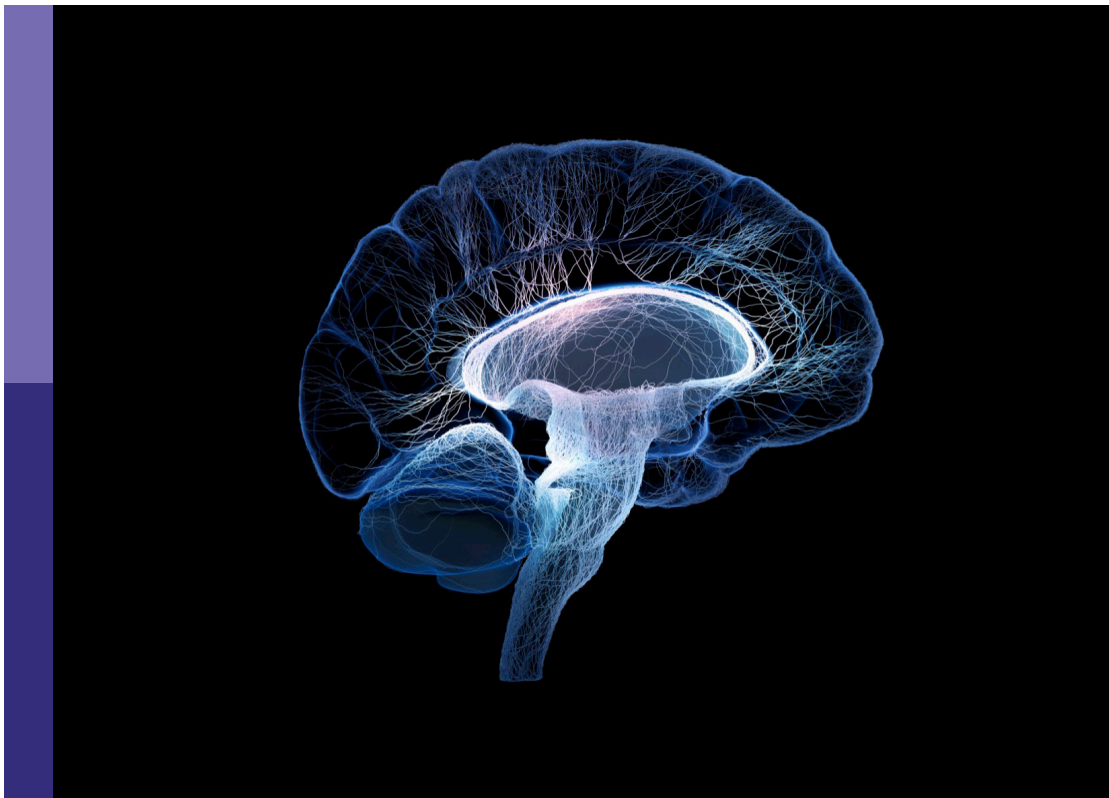

ISSN 1664-8714
ISBN 978-2-8325-2216-5
DOI 10.3389/978-2-8325-2216-5

About Frontiers

Frontiers is more than just an open access publisher of scholarly articles: it is a pioneering approach to the world of academia, radically improving the way scholarly research is managed. The grand vision of Frontiers is a world where all people have an equal opportunity to seek, share and generate knowledge. Frontiers provides immediate and permanent online open access to all its publications, but this alone is not enough to realize our grand goals.

Frontiers journal series

The Frontiers journal series is a multi-tier and interdisciplinary set of open-access, online journals, promising a paradigm shift from the current review, selection and dissemination processes in academic publishing. All Frontiers journals are driven by researchers for researchers; therefore, they constitute a service to the scholarly community. At the same time, the *Frontiers journal series* operates on a revolutionary invention, the tiered publishing system, initially addressing specific communities of scholars, and gradually climbing up to broader public understanding, thus serving the interests of the lay society, too.

Dedication to quality

Each Frontiers article is a landmark of the highest quality, thanks to genuinely collaborative interactions between authors and review editors, who include some of the world's best academicians. Research must be certified by peers before entering a stream of knowledge that may eventually reach the public - and shape society; therefore, Frontiers only applies the most rigorous and unbiased reviews. Frontiers revolutionizes research publishing by freely delivering the most outstanding research, evaluated with no bias from both the academic and social point of view. By applying the most advanced information technologies, Frontiers is catapulting scholarly publishing into a new generation.

What are Frontiers Research Topics?

Frontiers Research Topics are very popular trademarks of the *Frontiers journals series*: they are collections of at least ten articles, all centered on a particular subject. With their unique mix of varied contributions from Original Research to Review Articles, Frontiers Research Topics unify the most influential researchers, the latest key findings and historical advances in a hot research area.

Find out more on how to host your own Frontiers Research Topic or contribute to one as an author by contacting the Frontiers editorial office: frontiersin.org/about/contact

Advances in cortical architectonic & functional imaging with MRI: Methodology and applications

Topic editors

Chitresh Bhushan — GE Global Research, United States

Anand Joshi — University of Southern California, United States

Citation

Bhushan, C., Joshi, A., eds. (2023). *Advances in cortical architectonic & functional imaging with MRI: Methodology and applications*. Lausanne: Frontiers Media SA.

doi: 10.3389/978-2-8325-2216-5

Table of contents

frontiers | Frontiers in Neuroscience

ORIGINAL RESEARCH
published: 02 June 2022
doi: 10.3389/fnins.2022.879253

Altered Brain Activity in Strabismic Amblyopic Children as Determined by Regional Homogeneity: A Resting-State Functional Magnetic Resonance Imaging Study

Si-Wen Tan[1,2†], Guo-Qian Cai[3†], Qiu-Yu Li[1†], Yu Guo[3], Yi-Cong Pan[1], Li-Juan Zhang[1], Qian-Min Ge[1], Hui-Ye Shu[1], Xian-Jun Zeng[3] and Yi Shao[1]**

[1] Department of Ophthalmology, The First Affiliated Hospital of Nanchang University, Nanchang, China, [2] The First Clinical Medical College, Nanchang University, Nanchang, China, [3] Department of Radiology, The First Affiliated Hospital of Nanchang University, Nanchang, China

OPEN ACCESS

Edited by:
Chitresh Bhushan,
GE Global Research, United States

Reviewed by:
Zonglei Zhen,
Beijing Normal University, China
Gan Tan,
University of South China, China

***Correspondence:**
Xian-Jun Zeng
375135747@qq.com
Yi Shao
freebee99@163.com

† These authors have contributed equally to this work

Specialty section:
This article was submitted to Brain Imaging Methods, a section of the journal Frontiers in Neuroscience

Received: 19 February 2022
Accepted: 13 May 2022
Published: 02 June 2022

Citation:
Tan S-W, Cai G-Q, Li Q-Y, Guo Y, Pan Y-C, Zhang L-J, Ge Q-M, Shu H-Y, Zeng X-J and Shao Y (2022) Altered Brain Activity in Strabismic Amblyopic Children as Determined by Regional Homogeneity: A Resting-State Functional Magnetic Resonance Imaging Study. Front. Neurosci. 16:879253. doi: 10.3389/fnins.2022.879253

Objective: Earlier research has determined that amblyopia or strabismus may cause remarkable brain anatomical and functional variations. Nonetheless, thus far, the spontaneous changes in brain activity in children with strabismus amblyopia (SA) remain unclear. The purpose of this study was to determine the association between abnormal brain activity in children with SA and its behavioral manifestations.

Patients and Methods: A total of 24 children with SA (10 male and 14 female children) as well as 24 healthy controls (HCs), including 10 male and 14 female children were closely matched in sex and age, and examined using resting-state functional magnetic resonance imaging (fMRI). The regional homogeneity (ReHo) technique was applied to evaluate spontaneous cerebral activity variations in children with SA and HCs. Moreover, associations between altered ReHo values in distinct cerebral areas and the degree of strabismus were assessed using Pearson correlation analysis.

Results: Remarkably increased ReHo values were observed in the right lingual, right superior frontal medial, bilateral superior parietal, and right inferior parietal gyri of children with SA compared with HCs. In contrast, mean ReHo values in children with SA were lower in the right cerebellum, left superior frontal gyrus, and left putamen nucleus. Furthermore, esotropia showed a positive correlation with ReHo values of the left putamen.

Conclusion: The anomalous spontaneous activity changes in several brain areas that are caused by SA may indicate neuropathologic mechanisms of visual deficits and oculomotor disorders in children with SA.

Keywords: strabismus amblyopia, regional homogeneity, resting-state functional MRI, children, ReHo

INTRODUCTION

Strabismus and amblyopia are two common ocular diseases. Strabismus is an ophthalmic disease owing to the disorder of extraocular muscles, which is considered relevant to the dysplasia of cerebral visual pathways that regulate eye movements. Both the eyes of the strabismus patients cannot focus on the target at the same time, and the optical axes of both eyes are separated. In addition, amblyopia is a visual disorder caused by ocular maldevelopment, which can be detected by decreased visual acuity and sensitivity. Still, there were no organic lesions in the eye examination. Strabismus amblyopia (SA) is one form of amblyopia caused by strabismus. During the early phase of visual development, strabismus can cause the production of two separate images by the eyes that do not coincide, leading to abnormal vision, including double vision or visual confusion (**Figure 1**). In such cases, nerve impulses relayed by squinting would be suppressed by the brain. Over time, long-term suppression would lead to the development of amblyopia (Korah et al., 2014).

In pediatric populations, strabismus reportedly has a marked influence on the development of amblyopia. The combined condition, SA, leads to functional deficiency, including defective motor, visual, and sensory cognition as well as impaired stereoscopic depth perception (Levi et al., 2015). These inadequacies are evidenced by imprecision or incompetence in reading, grasping, or driving, which will affect the quality of the patient's daily life.

Functional magnetic resonance imaging (fMRI) is a common method that can precisely detect brain function. Its main advantage compared with traditional MRI is its ability to display subtle microscopic structural differences and satisfactory spatial resolution. When a person looks at an object, light passes through the retina, and nerve impulses are relayed along the visual pathway to the cerebral cortex, which produces the corresponding cortical activity to generate vision. This cortical activity can be observed and recorded by fMRI. Patients with SA differ from persons with normal vision in terms of the location, range, and degree of activation in cortical areas, which can also be detected by fMRI technology. Previously, fMRI techniques have been applied to detect cerebral activity alternations in either amblyopia or strabismus patients, separately (Lee et al., 2001; Chen and Tarczy-Hornoch, 2011).

The regional homogeneity (ReHo) is an extensively applied method that belongs to the resting-state fMRI (rs-fMRI), which is deemed dependable and accurate. Previous studies have shown that it has a high neurobiological relevance and test-retest reliability. A decline in ReHo values represents reduced synchrony and disordered activity. However, an increased ReHo value suggests increased synchrony of spontaneous neuronal activity. The ReHo technique has been successfully used in many researches on eye disorders (Cui et al., 2014; Song et al., 2014, 2017; Shao et al., 2015; Guo et al., 2016; Huang et al., 2016, 2017; Tang et al., 2018; Shi et al., 2019; Xu et al., 2019; Zhang et al., 2020; Tong et al., 2021; Yu et al., 2021; **Table 1**), along with many neurogenic diseases, like Parkinson's disease (Dai et al., 2012) and sleep disorders (Li et al., 2016).

Here, the ReHo technique was applied to analyze the alternations of spontaneous cerebral activity between children with SA and healthy controls (HCs) and to determine the relevance between the altered ReHo values and abnormal vision.

PATIENTS AND METHODS

Patients

Twenty-four children with SA, including 10 male patients and 14 female patients, from the Ophthalmology Department of the First Affiliated Hospital of Nanchang University, were recruited to participate in this study. The following are the inclusion criteria: (i) children under 12 years old; (ii) diagnosed with SA; (iii) with a best-corrected visual acuity (VA) $\geq$0.20 logMAR units, and central fixation of both eyes with greater than one line difference; and (iv) no other eye diseases (such as optic neuritis, cataract, or glaucoma, etc.). Patients meeting the following criteria were excluded: (i) had eye operation record (intraocular and extraocular were both included); (ii) had other disorders besides eye disease (such as ischemic disease, inflammation, or infection); (iii) had a mental disease or cerebral infarction; (iv) was either addicted to illicit drugs or was an alcoholic.

Twenty-four HCs matched to those basic clinical characteristics of the SA group, like sex and age were also incorporated in this research, including 10 boys as well as 14 girls. All HCs conformed to the following standards: (i) an absence of abnormal MRI in the brain; (ii) no ophthalmic surgery history and best-corrected VA not greater than 0 logMAR units; (iii) a state of sanity; (iv) no MRI examination contraindications (like a cardiac pacemaker or implanted metal devices). Our study has gained the approval of the Medical Ethics Committee of the First Affiliated Hospital of Nanchang University, and the protocol adhered to the principles of the Declaration of Helsinki. All participants (including the child and their parents) gave informed consent and details of the objectives of the research, and the latent danger to patients were explained in detail.

Magnetic Resonance Imaging Parameters

We used a 3-T magnetic resonance scanner (Trio, Siemens, Munich, Germany) to undergo the MRI scanning. During the entire scanning process, we asked all participants to breathe smoothly and remain their eyes closed, but keep awake. A three-dimensional spoiled gradient recalled echo sequence was applied to collect the data. Relevant details about the apparatus are as follows: 176 structural images (gap: 0.5 mm; repetition time (TR): 1,900 ms; echo time (TE): 2.26 ms; thickness: 1.0 mm; field of view: 250 $\times$ 250 mm; flip angle: 9°; acquisition matrix: 256 $\times$ 256). In addition, 240 functional images (TR: 2,000 ms; TE: 30 ms; thickness: 4.0 mm; gap: 1.2 mm; field of view: 220 $\times$ 220 mm; flip angle: 90°; acquisition matrix: 64 $\times$ 64; 29 axial) were likewise acquired. The duration time of the whole scanning process is 15 min.

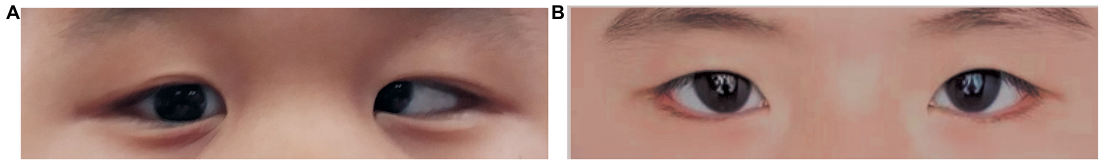

FIGURE 1 | Eyes of children with strabismus amblyopia **(A)** and healthy children **(B)**.

TABLE 1 | ReHo method applied in ophthalmological diseases (partially).

Author	Year	Disease	Brain areas	
			UDS > HCs	**UDS < HCs**
Song et al., 2014	2014	Glaucoma	RDACC, MFG, RCAL	Calcarine, PG, LIPL, LCPL
Cui et al., 2014	2014	Diabetic retinopathy	PLC, ACC, FL	OL, PG
Shao et al., 2015	2015	Optic neuritis	LFG, RIPL	LCPL, LMTG, RI, RSTG, LMFG, ACC, MFG, SFG, RPG
Huang et al., 2016	2016	Comitant strabismus	RITC/FG/CAL, RLG, CG	
Song et al., 2017	2017	Pituitary adenoma	LSOG, MOG	LIFG, RMTG
Huang et al., 2017	2017	Retinal detachment		ROL, RSTG, cuneus, LMFG
Tang et al., 2018	2018	Acute eye pain	LSFG, RIPL, LP	PG, LMFG
Shi et al., 2019	2019	Exotropia	V2	BA47
Xu et al., 2019	2019	Corneal ulcer	CPL, LITG, RLG, LMFG, LAG, LCG, RAG, SFG	RAC, LPG
Zhang et al., 2020	2020	Diabetic vitreous hemorrhage	CPL, RS/MOG, SFG	RI, MFG
Tong et al., 2021	2021	Iridocyclitis		RIOG, calcarine, RMTG, RPG, LSOG, LP
Guo et al., 2016	2021	Diabetic optic neuropathy	RMFG, LAC, SFG/LFSO	
Yu et al., 2021	2021	Dry eye	MFG, IFG, SFG	

HCs, healthy controls; RDACC, right dorsal anterior cingulated cortex; MFG, medial frontal gyrus; RCAL, right cerebellar anterior lobe; PG, precuneus gyrus; LIPL, left inferior parietal lobule; LCPL, left cerebellum posterior lobe; PLC, posterior lobe of cerebellum; ACC, anterior cingulate cortex; FL, frontal lobe; OL, occipital lobe; LFG, left fusiform gyrus; RIPL, right inferior parietal lobule; LMTG, left middle temporal gyrus; RI, right insula; RSTG, right superior temporal gyrus; LMFG, left middle frontal gyrus; SFG, superior frontal gyrus; RPG, right precuneus gyrus; RITC/FG/CAL, right inferior temporal cortex/fusiform gyrus/cerebellum anterior lobe; RLG, right lingual gyrus; CG, cingulate gyrus; LSOG, left superior occipital gyrus; MOG, middle occipital gyrus; LIFG, left inferior frontal gyrus; RMTG, right middle temporal gyrus; ROL, right occipital lobe; LSFG, left superior frontal gyrus; RIPL, right inferior parietal lobule; LP, left precuneus; V2, the right secondary visual cortex; BA47, Brodmann area 47; CPL, cerebellum posterior lobe; LITG, left inferior temporal gyrus; LAG, left angular gyrus; LCG, left cingulate gyrus; RAG, right angular gyrus; RAC, right anterior cingulate; LPG, left precentral gyrus; CPL, cerebellar posterior lobes; RS, right superior; RI, right insula; RIOG, right inferior occipital gyrus; LP, left precuneus; RMFG, right middle frontal gyrus; LAC, left anterior cingulate; LFSO, left frontal superior orbital gyrus; IFG, inferior frontal gyrus.

Functional Magnetic Resonance Imaging Data Processing

Firstly, the MRIcro software[1] was applied to analyze the collected data. Then, we used the Data Processing Assistant for rs-fMRI software (DPARSF)[2] and the Statistical Parametric Mapping 8 (SPM8) to preprocess the received information. We removed the data of the first 10 time points to eliminate interference which may be caused by an unsteady magnetic field. Furthermore, slice timing was carried out to correct time differences.

Owing to the differences in brain volume and structure between subjects, spatial standardization was used to process the available images. During this process, we unified the images according to the Montreal Neuroscience Institute standard (MNI152_T1_3mm. nii), and the voxels were immediately re-sampled with a resolution of 3 mm × 3 mm × 3 mm. To dislodge the linear chemotactic effect produced while the subject adapts to the scanning environment, the linear drift was eliminated. Eventually, to reduce high-frequency physiological noise, such as the heartbeat or respiration, only data between 0.01 and 0.08 Hz were collected.

[1]http://www.MRIcro.com

[2]http://rfMRI.org/

Statistical Analysis

We used the SPSS 20.0 software (IBM Corporation, Armonk, NY, United States) to compare the ReHo values of certain brain areas in the SA and HC groups, and used the two-sample *t*-test and the Representational state transfer (REST) software to analyze distinctions between this two groups. When the p-value < 0.05,

TABLE 2 | Participant characteristics.

Condition	SA	HCs	*t*	*P*-value*
Male/female	14/10	14/10	N/A	>0.999
Age (years)	8.21 ± 2.24	8.43 ± 1.97	0.256	0.902
Weight (kg)	20.76 ± 2.54	21.17 ± 3.64	0.365	0.891
Handedness	24R	24R	N/A	N/A
Duration of ON (years)	8.21 ± 2.24	N/A	N/A	N/A
BCVA-left eye	0.15 ± 0.05	0.95 ± 0.20	–3.654	0.003
BCVA-right eye	0.20 ± 0.05	1.10 ± 0.15	–3.217	0.004
IOP-L	15.54 ± 4.67	15.47 ± 4.19	0.586	0.932
IOP-R	15.85 ± 5.43	16.11 ± 5.12	0.612	0.901

*Independent t-tests comparing the two groups (*p < 0.05, represented statistically significant differences). Data shown as mean standard deviation or n.*
BCVA, best-corrected visual acuity; HCs, healthy controls; IOP, intraocular pressure; L, left; N/A, not applicable; R, right; SA, strabismus amblyopia.

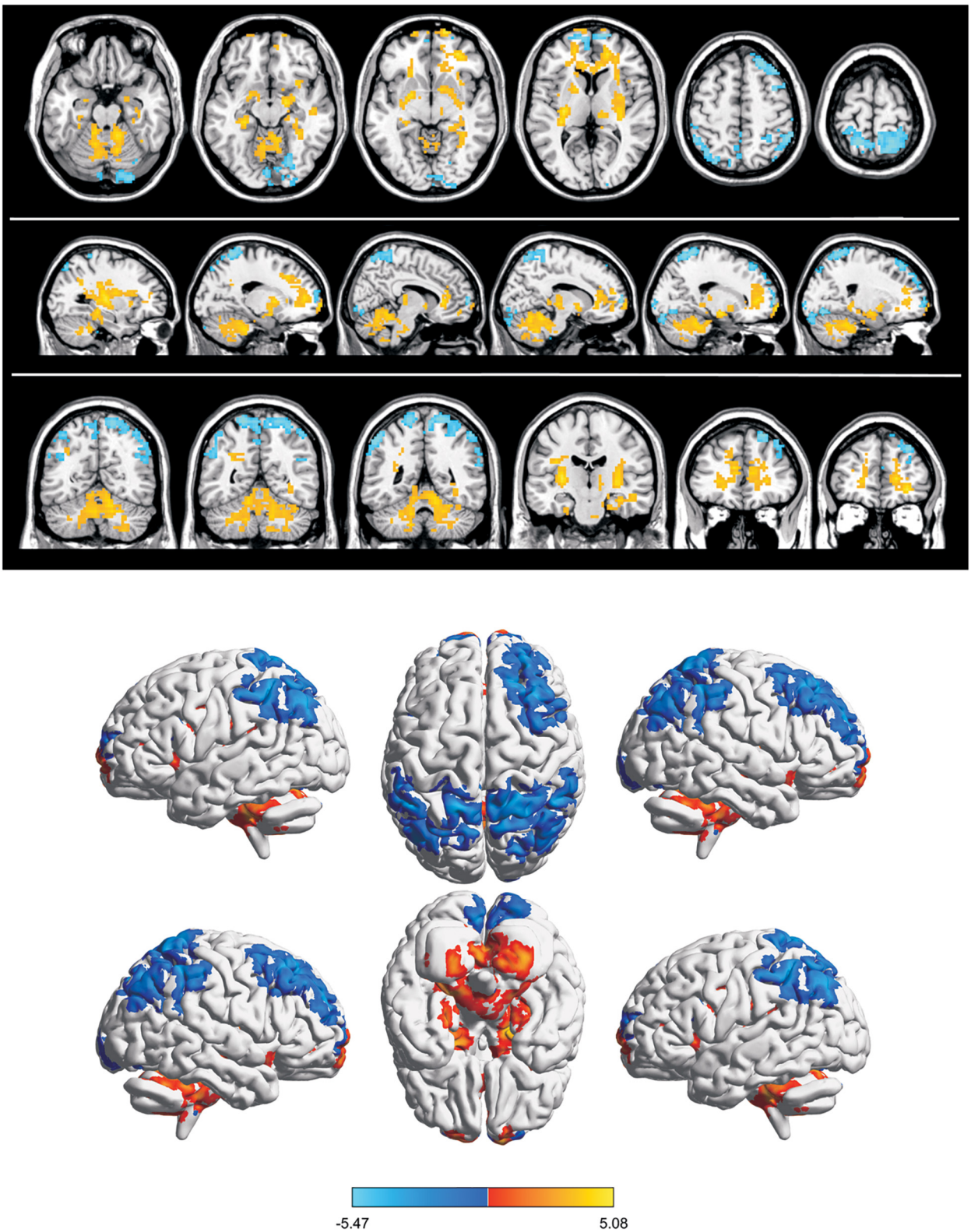

FIGURE 2 | Spontaneous brain activity in SA group. Blue regions (right cerebellum, left frontal superior gyrus, and left putamen nucleus) indicate lower reHo values, whereas red regions (right parietal superior gyrus, left parietal superior gyrus, right lingual gyrus, right frontal superior medial gyrus, and right parietal inferior) show higher ReHo values (AlphaSim-corrected, $P < 0.05$,cluster size > 40).

TABLE 3 | Brain areas with significantly different ReHo values between two groups.

Brain area	MNI coordinates			BA	Peak voxels*	*T*-value	*P*-values
	X	Y	Z				
SA > HC							
RLG	21	–75	–12	18	275	–4.16	0.004
RFSMG	12	66	9	8	749	–5.22	< 0.001
RPIG	54	–45	54	40	451	–4.66	0.003
LPSG	–18	–54	69	7	714	–5.47	< 0.001
RPSG	18	–48	72	7	388	–5.05	< 0.001
SA < HC							
RC	12	–45	–21		1600	4.5	0.003
LFSG	30	45	–6	13	1548	4.95	< 0.001
LPN	–30	–18	6	13	749	5.08	< 0.001

The statistical threshold was set at voxel with P < 0.05 for multiple comparisons using false discovery rate.
**Peak voxels: number of voxels in each cluster.*
SA, strabismus amblyopia; HC, healthy control; MNI, Montreal Neurological Institute; BA, Brodmann's area; RLG, right lingual gyrus; RFSMG, right frontal superior medial gyrus; RPIG, right parietal inferior gyrus; LPSG, left parietal superior gyrus; RPSG, right parietal superior gyrus; RC, right cerebellum; LFSG, left frontal superior gyrus; LPN, left putamen nucleus.

it was deemed as statistically significant. The collected data were compared and analyzed by AlphaSim. Corrected thresholds were set at $P < 0.01$, and the cluster size at > 40 voxels. Then, the REST software is used to identify brain regions with significantly changed ReHo values as regions of interest (ROI). The mean ReHo of all voxels in each brain area was taken as the ReHo value of this ROI. In addition, the Pearson correlation analysis was applied to distinguish between the ReHo value and the degree of strabismus in SA individuals.

RESULTS

Demographics and Visual Measurements

There are no significant differences were observed in gender ($p > 0.999$) and age ($p = 0.902$) between the two groups. However, significant differences appeared in the best-corrected VA of both eyes ($p = 0.003$ and $p = 0.004$, respectively) (**Table 2**).

Regional Homogeneity Differences

Compared with the HC group, the mean ReHo values of the following brain areas in the SA group were remarkably increased: right lingual (RL), right superior frontal medial (RSFM), bilateral superior parietal (SP), and right inferior parietal (RIP) [**Figure 2** (red areas), **Table 3**]. However, the ReHo values of the right cerebellum (RC), left putamen (LP), and left superior frontal (LSF) gyrus were remarkably decreased in the SA group [**Figure 2** (blue areas), **Table 3**]. The comparison of the ReHo values in two groups are presented in **Figure 3**. Through analysis, there was a positive correlation between esotropia degree and ReHo values of the left putamen ($r = 0.8975$, $p < 0.0001$) (**Figure 4**).

DISCUSSION

Children with SA showed increased ReHo values in the RL, RSFM, RIP, and SP areas compared with the HCs, while the mean ReHo values for the RC, LSF, and LP regions were significantly lower (**Figure 5**).

The lingual gyrus is located in the occipital lobe and has connections with the parahippocampal and the fusiform gyrus. It is a crucial part of the ventral visual stream, which processes visual details, like color, form, and size, processes complex visual stimuli by identifying essential characteristics. Therefore, this area is vital for visual attention and judgment. Earlier research reported an increased ReHo value of the lingual gyrus in patients with concomitant strabismus (CS) (Huang et al., 2016). In our study, an increased ReHo value of the RL was also detected in children with SA, which could be explained by visual compensation.

The frontal lobes are the largest cortical region in the human brain. It is also regarded as a very vital and the most complex area because it has extraordinary rich connections (including afferent and efferent connections) with almost all other parts of the central nervous system (Nauta, 1972). Especially, it is involved smooth pursuit eye movement (Heide et al., 1996). The early abnormal visual conditions experienced

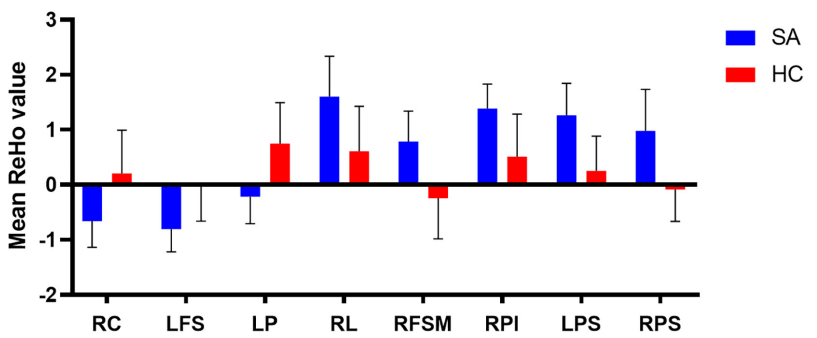

FIGURE 3 | The mean ReHo values in different brain regions in SA and HC groups. RC, right cerebellum; LFS, left frontal superior; LP, left putamen; RL, right lingual; RFSM, right frontal superior medial; RPI, right parietal inferior; LPS, left parietal superior; RPS, right parietal superior.

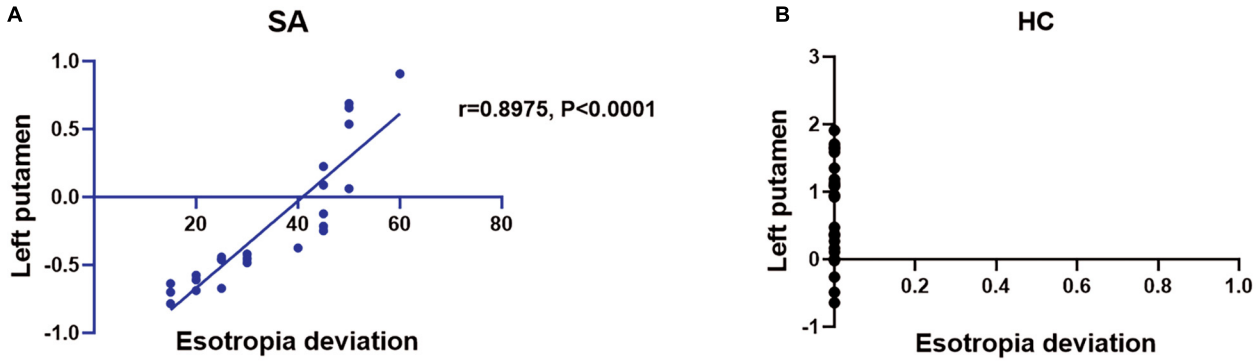

FIGURE 4 | The ReHo value of brain activity in SA group. **(A)** The esotropia deviation is in proportion to ReHo value in left putamen ($r = 0.8975$, $P < 0.0001$). **(B)** The esotropia deviation is disproportionate to left putamen. SA, strabismus amblyopia; HC, healthy control.

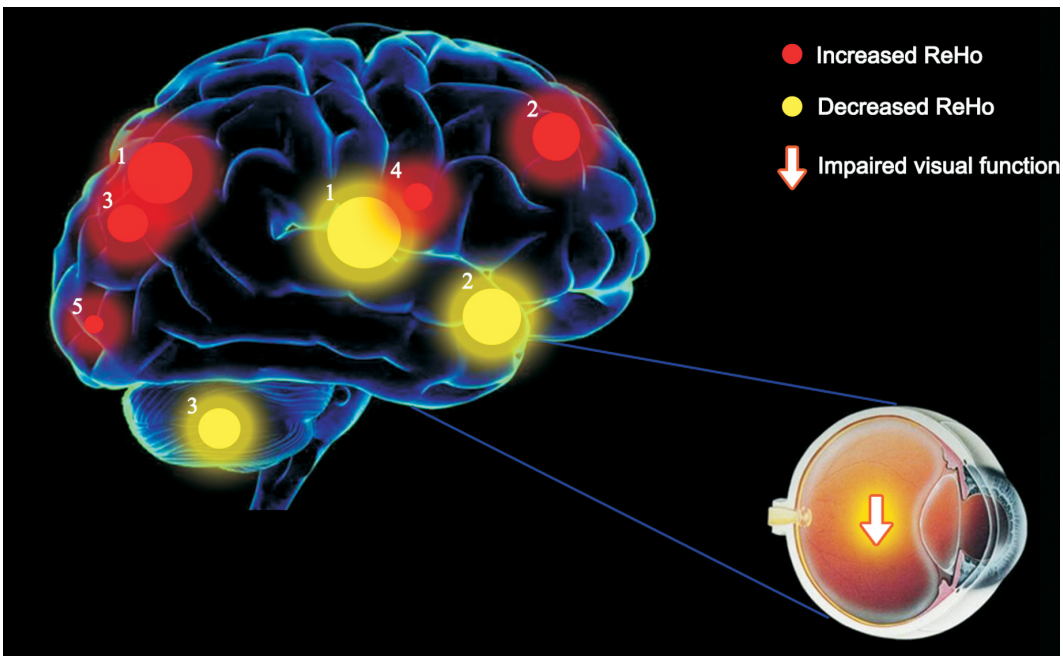

FIGURE 5 | The ReHo values of the altered brain regions. Variable degree of the ReHo values in SA group of the following regions were decreased: 1- Left putamen; ($t = 5.08$), 2- Left frontal sup (BA 13, $t = 4.95$), 3- Right cerebellum ($t = 4.5$). The ReHo values of the following brain regions were higher than HCs: 1- Left parietal sup (BA 7, $t = -5.47$), 2- Right frontal sup medial (BA 8, $t = -5.22$), 3- Right parietal sup (BA 7, $t = -5.05$), 4- Right parietal inf (BA 40, $t = -4.66$), 5- Right lingual (BA 18, $t = -4.16$). The degree of quantitative change was indicated by the size of spots. ReHo, regional homogeneity; HCs, healthy controls; BA, Brodmann's area.

by the SA children may disturb the neurodevelopmental processes as well as brain maturation, these changes may lead to a more terrible binocular vision and visual acuity. Therefore, the abnormal changes of ReHo values in frontal lobes may be one reason which causes declined visual function in children with SA.

Parietal lobules are somatosensory areas, which integrate information about feeling, touch, and vision, and facilitate the recognition and recall of size, shape, texture, and the weight of objects. A previous study has confirmed that the parietal lobe has a strong relationship with the visual cortex (Hishida et al., 2019). Ouyang et al. (2017) investigate the parietal lobes in patients with CS using voxel-based morphometry and recognized that compared with the HCs, the volume of the gray matter was reduced in the parietal occipital lobes. The increased ReHo value in this study may be the expression of compensatory brain development.

The cerebellum is involved in motor and balance control, including precise eye movements (Herzfeld et al., 2015). The V1 lobule of the cerebellum is related to spatial vision tasks and has extensive fiber crossing with other areas of the brain. Similarly, the cerebellum is considered as a vital area that controls the movement of the eyes and hands (Nitschke et al., 2005). In

TABLE 4 | Brain regions alternation and its potential impact.

Brain regions	Experimental result	Brain function	Anticipated results
Lingual gyrus	SAs > HCs	component of the ventral visual stream, process information	Visual hallucination
Frontal superior medial gyrus	SAs > HCs	Associated with ocular diseases	forced grasping reflex, groping reflex
Parietal inferior gyrus	SAs > HCs	production, expression and reception of language	Body schema disorder, Gerstmann syndrome
Parietal superior gyrus	SAs > HCs	Cortical sensation like stereognosis and two point discrimination	Cortical sensation deprivation
Cerebellum	SAs < HCs	balance and motor control, execution of accurate eye movements	Cerebellar ataxia
Frontal superior gyrus	SAs < HCs	Control autocinesis, language, affection	paralysis
Putamen nucleus	SAs < HCs	Regulate muscle tone, coordination of fine activities	Hyperexplexia, movement disorder

HCs, healthy controls; SA, strabismus amblyopia.

another study, a relationship between activation of the cerebellar vermis and visually guided saccades was reported (Hayakawa et al., 2002). A previous research demonstrated that the posterior interposed nucleus located in the cerebellum is an essential brain area in the process of conjugate eye movement in monkeys with strabismus (Joshi and Das, 2013). The observed declined ReHo value of this area may due to visual dysfunction caused by SA, which leads to significant functional brain activity alternations.

The putamen plays an integral role in the learning and memory system, as well as in the processing of visual information (Romero et al., 2008). Lee et al. (2006) used a visuomotor task to detect neuronal activity changes, they found significantly activated signals in the putamen with or without motor-related stimuli. In this study, dropped ReHo value was found in the left putamen in children with SA (**Table 4**), which could be the result of the visual defect in SA patients.

In addition, we also found some statistically significant voxels in MRI images in white matter. In previous MRI studies, activated signals are often found in the white matter of the brain. However, whether this signal has the significance for some potential neural activities has been controversial. White matter contains connecting fibers specialized in processing signals between different brain regions, accounting for about half of the brain (Harris and Attwell, 2012). Most of the reports on MRI activation of brain white matter involve the corpus callosum. The corpus callosum contains the largest white matter tract in the brain, which is involved in the transmission of information between the two cerebral hemispheres (Aboitiz et al., 1992), including cognitive, motor, auditory and visual information (Goldstein et al., 2022). Some studies reported that pathways related to visual-motor interhemispheric transfer tasks were observed in the knee of the corpus callosum (Tettamanti et al., 2002; Omura et al., 2004; Weber et al., 2005; Gawryluk et al., 2009). Fabri et al. (2011) found that the posterior part of the corpus callosum can be activated by visual stimulation by performing different tasks on healthy subjects, which is consistent with the previous results of the interhemispheric transfer task (Gawryluk et al., 2011a). In addition, fMRI activation has also been reported in the internal capsule. Studies have shown that activation can be detected in the inner capsule when performing motor tasks (Gawryluk et al., 2011b; Mazerolle et al., 2013). Moreover, the activation signal of fMRI can also be detected in the white matter of the healthy control group and Alzheimer's disease group during a memory task (Weis et al., 2011).

In this study, we speculate that the activated white matter signal may be a compensatory development of the brain of children with SA to compensate for the abnormal visual experience. In addition, it has been reported that in childhood and early adolescence, the development of the whole brain's white matter tract will increase, which contributed to improving cognitive ability (Barnea-Goraly et al., 2005). Therefore, the increased white matter signal found in this paper may also be the physiological result of brain development. Among the rapidly growing published MRI articles (Bandettini, 2012), the articles related to the activation of white matter MRI imaging are still relatively rare. We hope to have more research on the white matter function and its abnormalities.

CONCLUSION

In summary, the abnormal spontaneous brain activity in children with SA demonstrated in the present study could be attributed to both the development of SA and resultant visual compensation.

From the second trimester of pregnancy, the volume of gray matter brain cells increased rapidly and peaked before the age of six. Similarly, the volume of subcortical gray matter peaked at 14.5 years old. From the second trimester of pregnancy to early childhood, the volume of white matter also increased rapidly (Bethlehem et al., 2022). Therefore, in early childhood, the brain can continuously, quickly and completely compensate for some abnormalities (Benton and Tranel, 2000), resulting in compensatory structural abnormalities of the brain. In addition, if the dominant eye is wounded, or if the other eye is subsequently affected by a disease or disorder, permanent monocular visual impairment observed in amblyopia can become a risk factor for blindness (Harrad and Williams, 2002). Therefore, early treatment of this disease is vital (Fu et al., 2014). The findings of this study lay a foundation for further research into the discovery and diagnosis of SA. Furthermore, this study offers important information to gain a better understanding of SA and provides new insights for treatment.

DATA AVAILABILITY STATEMENT

The raw data supporting the conclusions of this article will be made available by the authors, without undue reservation.

ETHICS STATEMENT

The studies involving human participants were reviewed and approved by the Medical Ethics of The First Affiliated Hospital of Nanchang University (No: 2020038). Written informed consent to participate in this study was provided by the participants' legal guardian/next of kin. Written informed consent was obtained from the minor(s)' legal guardian/next of kin for the publication of any potentially identifiable images or data included in this article.

AUTHOR CONTRIBUTIONS

S-WT, G-QC, and Q-YL: conceptualization. S-WT, YG, and Y-CP: methodology. S-WT, L-JZ, and Q-MG: formal analysis and investigation. S-WT, H-YS, X-JZ, and YS: writing—original draft preparation. S-WT, G-QC, and YS: writing—review and editing. YG and YS: funding acquisition. S-WT, H-YS, and YS: resources. S-WT and Y-CP: supervision. All authors contributed to the article and approved the submitted version.

FUNDING

This work was supported by the Natural Science Foundation of China (Nos: 81660158, 81160118, 81400372, 81460092, and 81500742), the Natural Science research Foundation of Guangdong Province (Nos: 2017A030313614, 2017A020215187, and 2018A030313117), and the Medical Science Foundation of Guangdong Province (No: A2016184).

SUPPLEMENTARY MATERIAL

The Supplementary Material for this article can be found online at: https://www.frontiersin.org/articles/10.3389/fnins.2022.879253/full#supplementary-material

REFERENCES

Aboitiz, F., Scheibel, A. B., Fisher, R. S., and Zaidel, E. (1992). Fiber composition of the human corpus callosum. *Brain Res.* 598, 143–153.

Bandettini, P. A. (2012). Functional MRI: a confluence of fortunate circumstances. *NeuroImage* 61, A3–A11. doi: 10.1016/j.neuroimage.2012.01.130

Barnea-Goraly, N., Menon, V., Eckert, M., Tamm, L., Bammer, R., Karchemskiy, A., et al. (2005). White matter development during childhood and adolescence: a cross-sectional diffusion tensor imaging study. *Cereb. Cortex* 15, 1848–1854. doi: 10.1093/cercor/bhi062

Benton, A., and Tranel, D. (2000). *Historical Notes on Reorganization of Function and Neuroplasticity. Cerebral Reorganization of Function After Brain Damage.* New York, NY: Oxford University Press. 3–23.

Bethlehem, R. A. I., Seidlitz, J., White, S. R., Vogel, J. W., Anderson, K. M., Adamson, C., et al. (2022). Brain charts for the human lifespan. *Nature* 604, 525–533. doi: 10.1038/s41586-022-04554-y

Chen, V. J., and Tarczy-Hornoch, K. (2011). Functional magnetic resonance imaging of binocular interactions in visual cortex in strabismus. *J. Pediatr. Ophthalmol. Strabismus* 48, 366–374. doi: 10.3928/01913913-20101118-01

Cui, Y., Jiao, Y., Chen, Y. C., Wang, K., Gao, B., Wen, S., et al. (2014). Altered spontaneous brain activity in type 2 diabetes: a resting-state functional MRI study. *Diabetes* 63, 749–760. doi: 10.2337/db13-0519

Dai, X. J., Gong, H. H., Wang, Y. X., Zhou, F. Q., Min, Y. J., Zhao, F., et al. (2012). Gender differences in brain regional homogeneity of healthy subjects after normal sleep and after sleep deprivation: a resting-state fMRI study. *Sleep Med.* 13, 720–727. doi: 10.1016/j.sleep.2011.09.019

Fabri, M., Polonara, G., Mascioli, G., Salvolini, U., and Manzoni, T. (2011). Topographical organization of human corpus callosum: an fMRI mapping study. *Brain Res.* 1370, 99–111. doi: 10.1016/j.brainres.2010.11.039

Fu, J., Li, S. M., Liu, L. R., Li, J. L., Li, S. Y., Zhu, B. D., et al. (2014). Prevalence of amblyopia and strabismus in a population of 7th-grade junior high school students in Central China: the Anyang Childhood Eye Study (ACES). *Ophthalmic epidemiol.* 21, 197–203. doi: 10.3109/09286586.2014.904371

Gawryluk, J. R., Brewer, K. D., Beyea, S. D., and D'Arcy, R. C. (2009). Optimizing the detection of white matter fMRI using asymmetric spin echo spiral. *NeuroImage* 45, 83–88. doi: 10.1016/j.neuroimage.2008.11.005

Gawryluk, J. R., D'Arcy, R. C., Mazerolle, E. L., Brewer, K. D., and Beyea, S. D. (2011a). Functional mapping in the corpus callosum: a 4T fMRI study of white matter. *NeuroImage* 54, 10–15. doi: 10.1016/j.neuroimage.2010.07.028

Gawryluk, J. R., Mazerolle, E. L., Brewer, K. D., Beyea, S. D., and D'Arcy, R. C. (2011b). Investigation of fMRI activation in the internal capsule. *BMC Neurosci.* 12:56. doi: 10.1186/1471-2202-12-56

Goldstein, A., Covington, B. P., Mahabadi, N., and Mesfin, F. B. (2022). "Neuroanatomy, corpus callosum," in *StatPearls*, (Treasure Island (FL): StatPearls Publishing LLC).

Guo, C., Li, M., Qi, X., Lin, G., Cui, F., Li, F., et al. (2016). Intranasal delivery of nanomicelle curcumin promotes corneal epithelial wound healing in streptozotocin-induced diabetic mice. *Sci. Rep.* 6:29753. doi: 10.1038/srep29753

Harrad, R., and Williams, C. (2002). Risk, causes and outcomes of visual impairment after loss of vision in the non-amblyopic eye, a population-based study, by J. S. Rahi, S. Logan, C. Timms, I. Russel-Eggitt, and D. Taylor. *Lancet* 360, 597–602.

Harris, J. J., and Attwell, D. (2012). The energetics of CNS white matter. *J. Neurosci.* 32, 356–371. doi: 10.1523/JNEUROSCI.3430-11.2012

Hayakawa, Y., Nakajima, T., Takagi, M., Fukuhara, N., and Abe, H. (2002). Human cerebellar activation in relation to saccadic eye movements: a functional magnetic resonance imaging study. *Ophthalmologica* 216, 399–405. doi: 10.1159/000067551

Heide, W., Kurzidim, K., and Kömpf, D. (1996). Deficits of smooth pursuit eye movements after frontal and parietal lesions. *Brain* 119, 1951–1969. doi: 10.1093/brain/119.6.1951

Herzfeld, D. J., Kojima, Y., Soetedjo, R., and Shadmehr, R. (2015). Encoding of action by the Purkinje cells of the cerebellum. *Nature* 526, 439–442. doi: 10.1038/nature15693

Hishida, R., Horie, M., Tsukano, H., Tohmi, M., Yoshitake, K., Meguro, R., et al. (2019). Feedback inhibition derived from the posterior parietal cortex regulates the neural properties of the mouse visual cortex. *Eur. J. Neurosci.* 50, 2970–2987. doi: 10.1111/ejn.14424

Huang, X., Li, D., Li, H. J., Zhong, Y. L., Freeberg, S., Bao, J., et al. (2017). Abnormal regional spontaneous neural activity in visual pathway in retinal detachment patients: a resting-state functional MRI study. *Neuropsychiatr. Dis. Treat.* 13, 2849–2854. doi: 10.2147/NDT.S147645

Huang, X., Li, S. H., Zhou, F. Q., Zhang, Y., Zhong, Y. L., Cai, F. Q., et al. (2016). Altered intrinsic regional brain spontaneous activity in patients with comitant strabismus: a resting-state functional MRI study. *Neuropsychiatr. Dis. Treat.* 12, 1303–1308. doi: 10.2147/NDT.S105478

Joshi, A. C., and Das, V. E. (2013). Muscimol inactivation of caudal fastigial nucleus and posterior interposed nucleus in monkeys with strabismus. *J. Neurophysiol.* 110, 1882–1891. doi: 10.1152/jn.00233.2013

Korah, S., Philip, S., Jasper, S., Antonio-Santos, A., and Braganza, A. (2014). Strabismus surgery before versus after completion of amblyopia therapy in children. *Cochrane Database Syst. Rev.* 10:Cd009272. doi: 10.1002/14651858.CD009272.pub2

Lee, I. H., Seitz, A. R., and Assad, J. A. (2006). Activity of tonically active neurons in the monkey putamen during initiation and withholding of movement. *J. Neurophysiol.* 95, 2391–2403. doi: 10.1152/jn.01053.2005

Lee, K. M., Lee, S. H., Kim, N. Y., Kim, C. Y., Sohn, J. W., Choi, M. Y., et al. (2001). Binocularity and spatial frequency dependence of calcarine activation in two types of amblyopia. *Neurosci. Res.* 40, 147–153. doi: 10.1016/s0168-0102(01)00220-6

Levi, D. M., Knill, D. C., and Bavelier, D. (2015). Stereopsis and amblyopia: a mini-review. *Vis. Res.* 114, 17–30. doi: 10.1016/j.visres.2015.01.002

Li, Y., Liang, P., Jia, X., and Li, K. (2016). Abnormal regional homogeneity in Parkinson's disease: a resting state fMRI study. *Clin. Radiol.* 71, e28–e34. doi: 10.1016/j.crad.2015.10.006

Mazerolle, E. L., Gawryluk, J. R., Dillen, K. N., Patterson, S. A., Feindel, K. W., Beyea, S. D., et al. (2013). Sensitivity to white matter FMRI activation increases with field strength. *PLoS One* 8:e58130. doi: 10.1371/journal.pone.0058130

Nauta, W. J. (1972). Neural associations of the frontal cortex. *Acta Neurobiol. Exp.* 32, 125–140.

Nitschke, M. F., Arp, T., Stavrou, G., Erdmann, C., and Heide, W. (2005). The cerebellum in the cerebro-cerebellar network for the control of eye and hand movements–an fMRI study. *Prog. Brain Res.* 148, 151–164. doi: 10.1016/S0079-6123(04)48013-3

Omura, K., Tsukamoto, T., Kotani, Y., Ohgami, Y., Minami, M., and Inoue, Y. (2004). Different mechanisms involved in interhemispheric transfer of visuomotor information. *Neuroreport* 15, 2707–2711.

Ouyang, J., Yang, L., Huang, X., Zhong, Y. L., Hu, P. H., Zhang, Y., et al. (2017). The atrophy of white and gray matter volume in patients with comitant strabismus: evidence from a voxel-based morphometry study. *Mol. Med. Rep.* 16, 3276–3282. doi: 10.3892/mmr.2017.7006

Romero, M. C., Bermudez, M. A., Vicente, A. F., Perez, R., and Gonzalez, F. (2008). Activity of neurons in the caudate and putamen during a visuomotor task. *Neuroreport* 19, 1141–1145. doi: 10.1097/WNR.0b013e328307c3fc

Shao, Y., Cai, F. Q., Zhong, Y. L., Huang, X., Zhang, Y., Hu, P. H., et al. (2015). Altered intrinsic regional spontaneous brain activity in patients with optic neuritis: a resting-state functional magnetic resonance imaging study. *Neuropsychiatr. Dis. Treat.* 11, 3065–3073. doi: 10.2147/NDT.S92968

Shi, H., Wang, Y., Liu, X., Xia, L., Chen, Y., Lu, Q., et al. (2019). Cortical alterations by the abnormal visual experience beyond the critical period: a resting-state fMRI study on constant exotropia. *Curr. Eye Res.* 44, 1386–1392. doi: 10.1080/02713683.2019.1639767

Song, G., Qiu, J., Li, C., Li, J., Gui, S., Zhu, H., et al. (2017). Alterations of regional homogeneity and functional connectivity in pituitary adenoma patients with visual impairment. *Sci. Rep.* 7:13074. doi: 10.1038/s41598-017-13214-5

Song, Y., Mu, K., Wang, J., Lin, F., Chen, Z., Yan, X., et al. (2014). Altered spontaneous brain activity in primary open angle glaucoma: a resting-state functional magnetic resonance imaging study. *PLoS One* 9:e89493. doi: 10.1371/journal.pone.0089493

Tang, L. Y., Li, H. J., Huang, X., Bao, J., Sethi, Z., Ye, L., et al. (2018). Assessment of synchronous neural activities revealed by regional homogeneity in individuals with acute eye pain: a resting-state functional magnetic resonance imaging study. *J. Pain Res.* 11, 843–850. doi: 10.2147/JPR.S156634

Tettamanti, M., Paulesu, E., Scifo, P., Maravita, A., Fazio, F., Perani, D., et al. (2002). Interhemispheric transmission of visuomotor information in humans: fMRI evidence. *J. Neurophysiol.* 88, 1051–1058. doi: 10.1152/jn.2002.88.2.1051

Tong, Y., Huang, X., Qi, C. X., and Shen, Y. (2021). Disrupted neural activity in individuals with iridocyclitis using regional homogeneity: a resting-state functional magnetic resonance imaging study. *Front. Neurol.* 12:609929. doi: 10.3389/fneur.2021.609929

Weber, B., Treyer, V., Oberholzer, N., Jaermann, T., Boesiger, P., Brugger, P., et al. (2005). Attention and interhemispheric transfer: a behavioral and fMRI study. *J. Cogn. Neurosci.* 17, 113–123. doi: 10.1162/0898929052880002

Weis, S., Leube, D., Erb, M., Heun, R., Grodd, W., and Kircher, T. (2011). Functional neuroanatomy of sustained memory encoding performance in healthy aging and in Alzheimer's disease. *Int. J. Neurosci.* 121, 384–392. doi: 10.3109/00207454.2011.565892

Xu, M. W., Liu, H. M., Tan, G., Su, T., Xiang, C. Q., Wu, W., et al. (2019). Altered regional homogeneity in patients with corneal ulcer: a resting-state functional MRI study. *Front. Neurosci.* 13:743. doi: 10.3389/fnins.2019.00743

Yu, K., Guo, Y., Ge, Q. M., Su, T., Shi, W. Q., Zhang, L. J., et al. (2021). Altered spontaneous activity in the frontal gyrus in dry eye: a resting-state functional MRI study. *Sci. Rep.* 11:12943.

Zhang, Y. Q., Zhu, F. Y., Tang, L. Y., Li, B., Zhu, P. W., Shi, W. Q., et al. (2020). Altered regional homogeneity in patients with diabetic vitreous hemorrhage. *World J. Diabetes* 11, 501–513. doi: 10.4239/wjd.v11.i11.501

Conflict of Interest: The authors declare that the research was conducted in the absence of any commercial or financial relationships that could be construed as a potential conflict of interest.

Publisher's Note: All claims expressed in this article are solely those of the authors and do not necessarily represent those of their affiliated organizations, or those of the publisher, the editors and the reviewers. Any product that may be evaluated in this article, or claim that may be made by its manufacturer, is not guaranteed or endorsed by the publisher.

frontiers | Frontiers in Neuroscience

ORIGINAL RESEARCH
published: 02 June 2022
doi: 10.3389/fnins.2022.833837

Impaired Functional Homotopy and Topological Properties Within the Default Mode Network of Children With Generalized Tonic-Clonic Seizures: A Resting-State fMRI Study

Yongxin Li[1†], Bing Qin[2†], Qian Chen[3*] and Jiaxu Chen[1*]*

[1] Formula-Pattern Research Center, School of Traditional Chinese Medicine, Jinan University, Guangzhou, China,
[2] Department of Neurosurgery, Epilepsy Center, The First Affiliated Hospital, Jinan University, Guangzhou, China,
[3] Department of Pediatric Neurosurgery, Shenzhen Children's Hospital, Shenzhen, China

OPEN ACCESS

Edited by:
Chitresh Bhushan,
GE Global Research, United States

Reviewed by:
Ling-Li Zeng,
National University of Defense Technology, China
Jessica Wisnowski,
University of Southern California, United States

***Correspondence:**
Yongxin Li
yxin-li@163.com
Qian Chen
chenqian68@126.com
Jiaxu Chen
chenjiaxu@hotmail.com

[†] These authors have contributed equally to this work

Specialty section:
This article was submitted to Brain Imaging Methods, a section of the journal Frontiers in Neuroscience

Received: 12 December 2021
Accepted: 27 April 2022
Published: 02 June 2022

Citation:
Li Y, Qin B, Chen Q and Chen J (2022) Impaired Functional Homotopy and Topological Properties Within the Default Mode Network of Children With Generalized Tonic-Clonic Seizures: A Resting-State fMRI Study. Front. Neurosci. 16:833837. doi: 10.3389/fnins.2022.833837

Introduction: The aim of the present study was to examine interhemispheric functional connectivity (FC) and topological organization within the default-mode network (DMN) in children with generalized tonic-clonic seizures (GTCS).

Methods: Resting-state functional MRI was collected in 24 children with GTCS and 34 age-matched typically developing children (TDC). Between-group differences in interhemispheric FC were examined by an automated voxel-mirrored homotopic connectivity (VMHC) method. The topological properties within the DMN were also analyzed using graph theoretical approaches. Consistent results were detected and the VMHC values were extracted as features in machine learning for subject classification.

Results: Children with GTCS showed a significant decrease in VMHC in the DMN, including the hippocampal formation (HF), lateral temporal cortex (LTC), and angular and middle frontal gyrus. Although the patients exhibited efficient small-world properties of the DMN similar to the TDC, significant changes in regional topological organization were found in the patients, involving the areas of the bilateral temporal parietal junction, bilateral LTC, left temporal pole, and HF. Within the DMN, disrupted interhemispheric FC was found between the bilateral HF and LTC, which was consistent with the VMHC results. The VMHC values in bilateral HF and LTC were significantly correlated with clinical information in patients. Support vector machine analysis using average VMHC information in the bilateral HF and LTC as features achieved a correct classification rate of 89.34% for the classification.

Conclusion: These results indicate that decreased homotopic coordination in the DMN can be used as an effective biomarker to reflect seizure effects and to distinguish children with GTCSs from TDC.

Keywords: generalized tonic-clonic seizure children, default-mode network, voxel-mirrored homotopic connectivity, graph theory, support vector machine

INTRODUCTION

Epilepsy is one of the most common serious neurological brain disorders, affecting over 65 million people worldwide (Thurman et al., 2011). Patients with epilepsy are clinically characterized by seizure symptoms and impaired consciousness. Generalized tonic-clonic seizures (GTCS) encompass a group of seizure types that are characterized by generalized spike-wave discharges (2.5–5 Hz), involving the bilateral hemispheres during seizures (Ji et al., 2014). Using routine MRI, focal anatomical brain lesions usually cannot be detected in patients with GTCS. The clinical characteristics of patients with GTCS include muscle rigidity, violent muscle contraction of the entire body, and complete loss of consciousness (Zhang et al., 2011). Pieces of evidence have shown significant cognitive and psychosocial impacts in patients with GTCS, including impaired attention, memory, and executive function (Hommet et al., 2006; Paige and Cavanna, 2013). For people with GTCS, their quality of life is affected. As a result, this type of epilepsy is attracting much medical attention in clinical practice (Kenyon et al., 2014; Ryvlin and Beniczky, 2020). Although many effects have been observed in the past, the neural mechanisms underlying the GTCS remain unclear.

Previous studies on epilepsy mainly used information on clinical manifestations and EEG data (Myers et al., 2018; Trinka et al., 2019). The accepted view is that epileptic seizures are induced by an imbalance between excitatory and inhibitory activities (Fisher et al., 2017a). Normal neuronal processing was disrupted in patients with epilepsy. Recently, neuroimaging techniques have been applied to explore the neuromechanism of the human brain, and epilepsy is considered as a functional brain network disorder by this technique (Engel et al., 2013; Fitsiori et al., 2019; Jia et al., 2020; Goodman and Szaflarski, 2021). For GTCS, this type of epilepsy belongs to generalized seizures, which are widespread throughout the entire brain or bilaterally distributed networks (Fisher et al., 2017a). This bilateral epilepsy feature can lead us to think about the brain organization by the fMRI method. Growing evidence in the neuroimaging domain has found that patients with GTCS showed bilateral impairments of their functional network, which is thought to be associated with the abnormalization of multiple interconnected brain systems (Wang et al., 2011; Jia et al., 2020; Li et al., 2020a; Parsons et al., 2020). The alterations in brain activity and connections of the patients with GTCS were involved in some brain systems, including the default mode network (DMN), thalamocortical system, and visual and dorsal attention networks (Wang et al., 2011, 2019a; Liu et al., 2017). Regarding the DMN, previous studies have detected that this network directly contributes to internal mentation (Buckner et al., 2008). Patients with GTCS showed a significant decrease in functional connectivity (FC) and spontaneous activity in the DMN (Song et al., 2011; Parsons et al., 2020). The alterations in brain activity in the DMN were mainly located in the medial prefrontal cortex, posterior midbrain regions, and lateral parietal cortex for epileptic patients with GTCS (Hamandi et al., 2006; Blumenfeld et al., 2009). The findings from these previous studies indicated that abnormal connectivity and activity in the DMN may be the neural substrate of the impaired consciousness and cognitive impairments in patients with GTCS. Although these previous studies have found changes in the DMN in GTCS, the specific role of the DMN in measuring seizure induced network organization, and detecting neuroimaging biomarkers still needs further investigation. Therefore, the ability to identify and track the specific DMN abnormalities in GTCS may provide an objective biomarker for GTCS diagnosis and understanding the neural mechanism of GTCS.

Combining the previous neuroimaging findings and clinical characteristics of GTCS, we can see that interhemispheric synchronization would be affected in patients with GTCS. During seizures, generalized spike-wave discharges may induce changes in interhemispheric communication. Thus, alterations in the functional interaction between the bilateral hemispheres have recently attracted people's attention. One study used multimodal MRI data to characterize interhemispheric functional and anatomic connectivity in patients with GTCS (Ji et al., 2014). Compared with the healthy controls, patients with GTCS showed both increased and decreased interhemispheric functional connectivity. The length for the fiber bundles connecting the bilateral anterior cingulate cortex and the bilateral cuneus was short in patients. Meanwhile, a neuroimaging study based on the voxel-mirrored homotopic connectivity (VMHC) method was used to study the resting state functional connectivity between the two hemispheres (Yang et al., 2014). Patients with GTCS showed significant increases in VMHC in the anterior cingulate and medial prefrontal gyrus. No areas showed a significant decrease in VMHC in patients with GTCS. The VMHC in the bilateral thalamus, orbital frontal cortex, and cerebellum showed negative correlations with illness duration. We can see that some results of the above two studies are inconsistent. For example, the VMHC values in the inferior frontal gyrus of patients showed a significant decrease in one study, but not in the other. The possible reason for this inconsistency may be that one study only included adults, and the other study included both adults and children. However, in the above two studies, most regions showing significant changes were mainly located in the DMN, which may be critical to the pathophysiology of patients with GTCS. Considering the bilateral seizure feature of GTCS and the inconsistent results in these previous studies, researching the interhemispheric communication in the DMN of patients with GTCS would provide useful information to understand this disease. In the present study, we focused on the interhemispheric functional connectivity of the DMN to detect the specific role of this network in GTCS.

Additionally, the subjects of these previous studies were adult patients with GTCS. Only a few studies have focused on the brain organization and activity of children with GTCS. One recent neuroimaging study in patients with epilepsy with GTCS found that both children and adult patients showed increased functional diversity in frontocentral neocortical regions (Wang et al., 2019a). Another study from our group on children with GTCS also detected a significant reduction in gray matter volume and an increase in spontaneous activity in the temporal lobe, hippocampus, thalamus, and other deep nuclei in patients (Wang et al., 2018). The consistent results from these two studies were that significant changes of brain functional activity in the DMN

were detected of children with GTCS. The graph theory method was also applied in children with GTCS from our group. Children with GTCS still exhibited efficient small-world properties of their whole brain gray matter structural covariance network and functional network similar to the normal controls (Li et al., 2020a,b). Significant changes in nodal betweenness of the structural network were located in the thalamus, temporal pole, and some regions of the DMN (Li et al., 2020b). The functional connections within the DMN were decreased significantly, and the internetwork connections were increased significantly in children with GTCS (Li et al., 2020a). Both graph theory studies in children with GTCS demonstrated a disrupted topological organization in some regions of the brain's functional and structural network. Previous studies have consistently pointed out that connection abnormalities of the brain network still exist in children with GTCS. However, the functional organization and topological properties within the DMN are still unclear in children with GTCS. Considering the important role of the DMN in the human brain, researching the functional organization of the DMN in children with GTCS can enrich our knowledge to understand the pathophysiology of this type of epilepsy.

Thus, the aim of the present study was to explore the alteration of interhemispheric functional connectivity and topological properties within the DMN in children with GTCS. According to clinical and previous neuroimaging results, we hypothesized that children with GTCS would show abnormal functional connectivity between the left and right regions within the DMN. The specific change in interhemispheric connectivity can reflect the epilepsy's clinical manifestations. To test this hypothesis, we combined the VMHC method and graph the theory method on resting-state fMRI data in children with GTCS. Using the VMHC method, functional homotopy between hemispheres can be quantified for children with GTCS. Graph theory can be used to quantify network topology and brain connections of the DMN in children with GTCS. We used these two methods from different perspectives to study the interhemispheric connectivity changes in the DMN. The consistent results from these two methods were selected as regions of interest for the correlation analysis with the clinical characteristics. The interhemispheric connectivity values of the regions of interest were also extracted as features for further machine learning to detect whether these functional homotopies in the DMN can correctly distinguish the children with GTCS from the typically developing children.

MATERIALS AND METHODS

Subjects

Twenty-four children with GTCS (9 females; mean ages: 69.94 ± 46.36 months) were included in the study. All the patients were diagnosed with GTCS. The inclusion criteria for the patient group were as follows: (1) met the criteria of GTCS diagnosis according to the current International League Against Epilepsy seizure type classification (Fisher et al., 2017b), such as limb movement, loss of consciousness during seizures, and no partial seizures; (2) a specific pattern of electrophysiological activity on electroencephalogram (generalized spike-and-wave or poly-spike-wave discharges); and (3) no abnormality was detected for all the patients in routine MRI examinations. Each patient was treated with at least one antiepileptic drug (AED: topiramate, valproic acid, oxcarbazepine, and/or levetiracetam, 11 patients with 1 AED, 10 patients with 2 AEDs, and 3 patients with 3 AEDs) to control seizures before imaging data collection. All the patients were seizure free for at least 2 days prior to MRI examination. A group of typically developing children (TDC, 10 females, 24 males, mean age: 69.38 ± 28.82 months) were included for comparisons with patient cohorts. All TDC had no history of neurological disorders or psychiatric illnesses. During the MRI scanning, the participants under the age of four were sedated with 10% chloral hydrate to reduce their head movement (dosage: 50 mg/kg, the maximum dose is 1 g). Eighteen participants (9 children with GTCS and 9 TDC) of this study were under 4 years. Demographic and clinical information of both groups can be found in **Table 1**.

Before the image data were collected, the study purpose, procedures, possible risks, and discomforts were explained to the participants and their parents or the guardians. The parents or the guardians of all the participants gave written informed consent. This study was approved by the Ethical Committee of the Shenzhen Children's Hospital.

Data Acquisition

Data were acquired using a German Siemens Trio Tim 3.0T scanner (MAGNETOM, Germany, 8-channel head coil) at the Shenzhen Children's Hospital, Shenzhen, China. Foam cushions and earplugs were used for all the subjects to reduce head movements and machine noise, respectively. High-resolution three-dimensional (3D)T1-weighted MPRAGE images covering the entire brain were acquired for all the subjects: TR (repetition time, ms) = 2,300; TE (echo time, ms) = 2.26; FOV (field of view, mm) = 200 × 256; acquisition matrix = 200 × 256; 160 sagittal slices; slice thickness (mm) = 1; flip angle (degree) = 8. Resting-state fMRI data were collected axially by using an echo-planar imaging sequence with 130 volumes: TR (ms) = 2,000, TE (ms) = 30, FOV (mm) = 220 × 220, matrix size = 94 × 94, slice thickness (mm) = 3, flip angle (degree) = 90, 36 interleaved axial slices covered the entire brain. During the imaging scanning, the participants over the age of four were instructed to keep still with their eyes closed, remain awake, and instructed not to think about anything. All the participants were lying quietly, as motionless as possible. To avoid falling asleep of these participants, we observed throughout the whole scanning process, and asked their conditions after that. During the scanning, we observed throughout the whole scanning process. The T1 data were checked during the scanning process. During the scanning process, T1 images were scanned first and then scanned the resting-state image. If there are serious head-moving artifacts, we would tell the participant to keep still and rescan the T1 image. If the second scan still existed serious head-moving artifacts, we would stop the data collection of this participant and not include in the data analysis. During the whole data collection process, 12 subjects (5 TDCs and 7 patients) failed to obtain complete imaging connection by the above reason.

TABLE 1 | Demographic and clinical information data of the subjects.

Characteristics	Patient group		Control group		Comparisons
	(Mean ± *SD*)	(median + IQR)	(Mean ± *SD*)	(median + IQR)	
Gender (female/male)	9/15	\	10/24	\	$X^2 = 0.42$ ($P = 0.52$)
Age (month)	69.94 ± 46.36	55 + 65	69.38 ± 28.82	58 + 47	$t = 0.06$ ($P = 0.95$)
Seizure onset age (month)	37.35 ± 46.22	18 + 30	\	\	\
Duration (month)	32.58 ± 31.20	27 + 41	\	\	\

SD, standard deviation; IQR, inter-quartile range.

Data Preprocessing

The resting-state fMRI data were preprocessed using the data assistant software DPABI (Yan et al., 2016), which runs on MATLAB 8.2 (Mathworks, Natick, MA, United States). The first 10 time points were removed to ensure magnetization equilibrium. The remaining volumes were corrected by the acquisition time delay among different slices and realigned to the first volume to correct the head motions. All the participants had less than 3-mm maximum displacement in the *x*-, *y*-, or z-axis and 3° of angular motion during data acquisition. Subsequently, each subject's high-resolution anatomical image was co-registered to the mean functional images by rigid body transformation. The transformed structural images were then segmented in to gray matter, white matter, cerebrospinal fluid by using a unified segmentation algorithm, and normalized to the Montreal Neurological Institute (MNI) space by using a 12-parameter non-linear transformation. The transformation parameters were applied to the functional images and resampled the functional images to a 3-mm isotropic voxel. The functional images were spatially smoothed with a Gaussian kernel of 6-mm full width at half maximum. The smoothed images were masked by the default gray matter mask of the software. Then, the masked images were subjected to temporal bandpass filtering (0.01–0.08 Hz) and linear detrending to reduce the effect of low-frequency drifts and physiological high-frequency noise.

To minimize the potential effects of head motion on subsequent graph theory analyses, mean framewise displacement values were also calculated during the realignment steps and compared between the two groups. For each subject, the mean framewise displacement values were the across translational and rotational directions of scan-to-scan deviations between two images (Power et al., 2012). No participant was excluded, and the mean framewise displacement value exceeded 0.5 mm. The framewise displacement was not significantly different between the two groups (the TDC: mean = 0.12 ± 0.10 mm; the children with GTCS: mean = 0.13 ± 0.09 mm). Spurious covariates and their temporal derivatives, including Friston-24 head motion parameters, white matter signals, and cerebrospinal fluid signals, were removed from the data using linear regression.

Interhemispheric Correlation and Statistical Analysis

The VMHC was also calculated with the data-assistant DPABI. VMHC assumes symmetric morphology between hemispheres. To account for differences in the geometric configuration of the cerebral hemispheres, we firstly averaged the normalized T1 images of all the subjects to create a mean normalized T1 image. This mean T1 image was then averaged with its left-right mirrored version to generate a group-specific symmetrical T1 template. Then, the individual T1 images in MNI space were non-linearly registered to the symmetrical T1 template, and those transformations were applied to the above-processed functional data. For each subject, the homotopic connectivity was computed as the Pearson's correlation coefficient between the residual time series of each voxel and that of its symmetrical interhemispheric counterpart (Zuo et al., 2010). Correlation values were then Fisher *z*-transformed to improve the normality. The resultant values were referred to as the VMHC and were applied for the group comparisons.

To test for regional group differences in VMHC, individual-level VMHC maps were entered into a group-level voxel wise *t*-test. Significant differences of VMHC between the children with GTCS and the TDC were set at the threshold of voxel wise $p < 0.01$ (FDR corrected) and cluster size of 6.

Topological Analysis in Default-Mode Network and Statistical Analysis

Because the present study mainly focused on the functional abnormality in DMN, we also used graph theory to investigate the alterations of brain topology in DMN. The brain network topological characterizations were analyzed using GRETNA[1] (Wang et al., 2015). First, we defined 17 anatomic nodes to examine brain topology in DMN (**Supplementary Table 1**). Each node was defined as an 8-mm radius sphere centered on the MNI coordinates from a previous study (Andrews-Hanna et al., 2010). These nodes were grouped into two hubs, including posterior cingulate cortex (PCC) and anterior medial prefrontal cortex (aMPFC), respectively, and two subsystems, a "dorsal medial prefrontal cortex" (dMPFC) subsystem and a "medial temporal lobe" (MTL) subsystem. Second, the averaged time series from each node were extracted and then computed the temporal correlation among time series using Pearson correlation. Third, all resulting correlation coefficients were transformed into *z*-scores using Fisher's *z*-transformation to improve the normality of the correlation coefficients. The normalized correlation value of each pair was regarded as the network edges. Thereafter, a 17- × -17 correlation matrix was produced for each subject. A binary matrix was obtained according to a predefined threshold

[1]http://www.nitrc.org/projects/gretna/

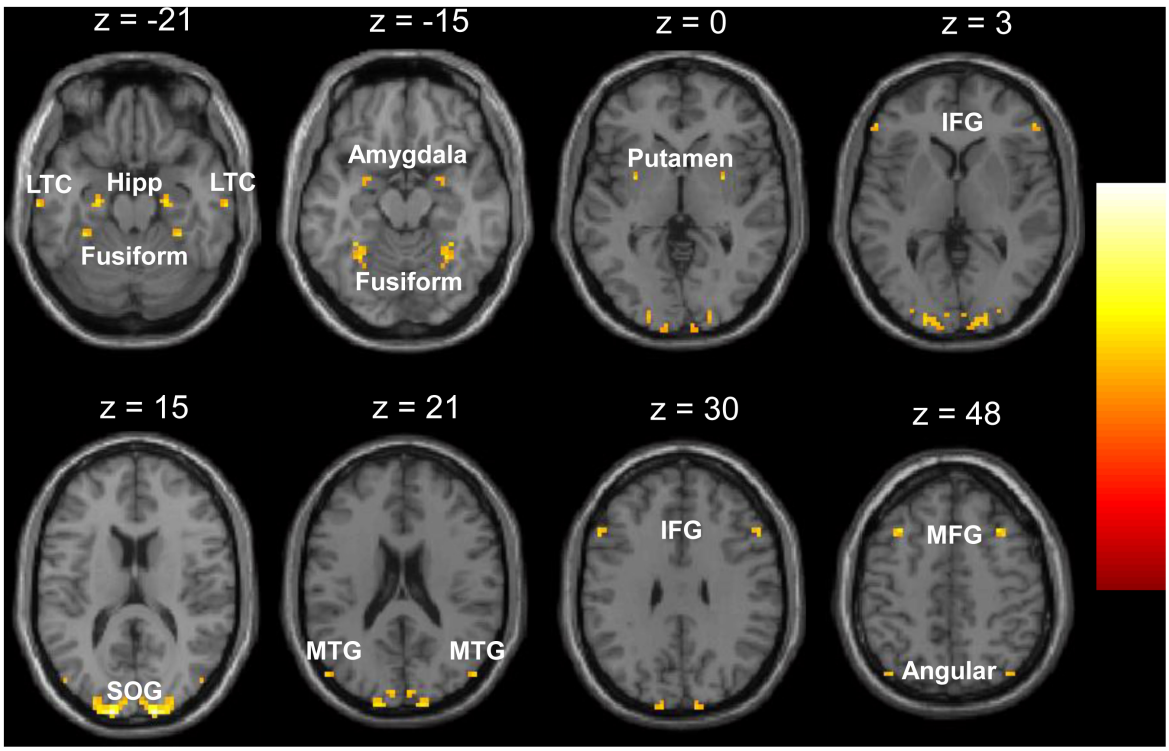

FIGURE 1 | Regions showing significant decrease of voxel-mirrored homotopic connectivity (VMHC) in the children with generalized tonic-clonic seizures (GTCS). The threshold of resulting statistical maps was a combination of $p < 0.01$ (FDR correction) and minimum cluster number of 6. Hipp, hippocampus; LTC, lateral temporal cortex; MTG, middle temporal gyrus; SOG, superior occipital gyrus; IFG, inferior frontal gyrus; MFG, middle frontal gyrus.

(see below for the "Threshold" selection), where edges with positive correlation values were set to 1 and, otherwise, set to 0. Finally, different levels of network topological properties were performed, including global network metrics and regional nodal properties. The global network architecture of the functional networks was characterized using small-world [small-worldness (σ), clustering coefficients (C_p), normalized clustering coefficient (γ), characteristic path length (L_p), normalized characteristic path length (λ)], and network efficiency [local efficiency (E_{loc}) and global efficiency (E_g)]. The regional characteristics, such as nodal efficiency, nodal local efficiency, nodal shortest path, nodal degree centrality, and betweenness centrality, were also assessed. The definitions of these network properties can be found in previous graph studies (Bassett and Bullmore, 2006; Sporns and Honey, 2006).

In the present study, a threshold of connection sparsity, S, was used for all functional matrices. Currently, there is no criterion for selecting a single threshold for constructing functional brain networks. Instead of selecting a single threshold, we investigated the topological properties of each matrix over a wide range of threshold levels (0.1–0.5 with an interval of 0.01). Using this approach, all resulting networks have the same number of edges. The range of sparsity values was chosen here to allow small-world network properties to be properly estimated. At the lower bound of the range, the networks of both groups were not fragmented. For densities above 0.45, the graphs became increasingly random ($\sigma < 1.5$) (Stam and Reijneveld, 2007). This reference found that the small-world model synchronized as rapidly as a fully random

TABLE 2 | Significant group differences in voxel-mirrored homotopic connectivity (VMHC).

Cluster location	Statistical values		Peak (MNI)		
	Cluster size	*t*-value	*x*-	*y*-	*z*-
Control > patient					
Superior occipital gyrus	149	8.11	±15	−99	15
Middle frontal gyrus	14	5.36	±33	21	48
Hippocampus	10	5.23	±24	−12	−21
Lateral temporal cortex	6	5.23	±66	−20	−21
Fusiform	20	5.22	±30	−54	−15
Putamen	7	4.95	±30	0	0
Inferior frontal gyrus	6	4.84	±54	21	30
Middle temporal gyrus	6	4.80	±51	−78	21
Angular	6	4.68	±39	−75	45
Amygdala	6	4.57	±27	0	−12
Patient > control	No				

The MNI coordinates and t-values for the local maxima of the centers of the voxel clusters. The threshold for significant clusters reported here was set at $p < 0.01$ (FDR corrected) and cluster size of 6.
VMHC, voxel-mirrored homotopic connectivity; MNI, Montreal Neurological Institute.

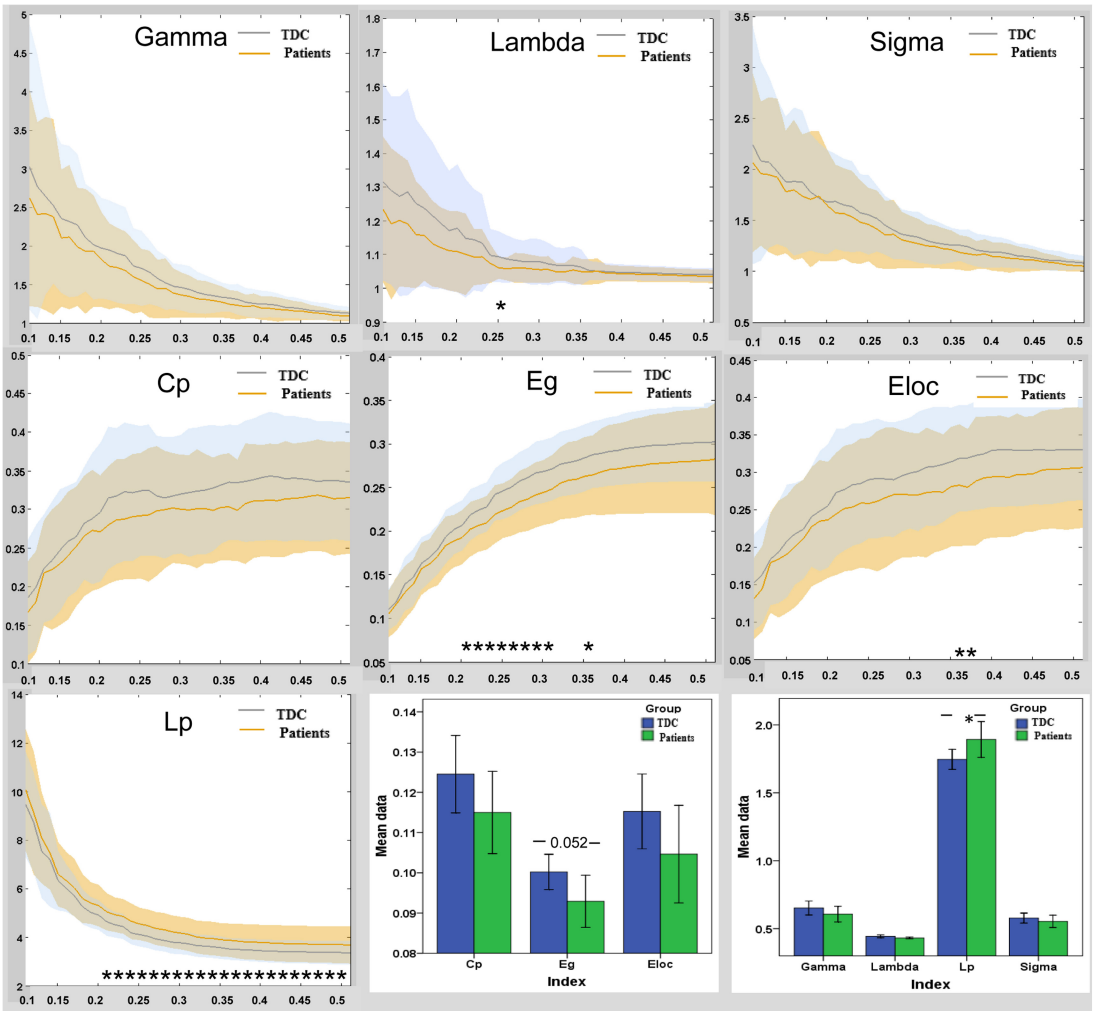

FIGURE 2 | Group differences in global functional properties of brain topology in DMN between the patient and TDC. In the range of sparsity (0.1 ∼ 0.5), the functional networks of DMN in both groups exhibited a small-world property. Bar plots of the global efficiency, local efficiency, clustering co-efficiency, gamma, lambda, L_p, and sigma for the children with GTCS and TDC. Asterisks (*) indicate a significant difference between the two groups. E_g, global efficiency; E_{loc}, local efficiency; C_p, clustering coefficient; L_p, characteristic path length; TDC, typically developing children.

TABLE 3 | Default-mode network (DMN) regions showing disrupted nodal topologic properties in children with GTCS compared with the controls.

Regions	Cluster coefficient (*t*/*p*)	Nodal efficiency (*t*/*p*)	Nodal local efficiency (*t*/*p*)	Degree centrality (*t*/*p*)	Betweenness centrality (*t*/*p*)
L TPJ		2.29/0.026		–	–
R TPJ	**2.08/0.042**	–	**2.08/0.042**	–	–
L LTC	1.89/0.065	**2.04/0.049**		2.0/0.051	–
R LTC	–	**2.39/0.02**	**2.11/0.039**	–	–
L TempP	–	–	–	–	**–2.49/0.016**
L HF	–	**2.40/0.02**	–	1.99/0.051	–

R, right hemisphere; L, left hemisphere; TPJ, temporal parietal junction; LTC, lateral temporal cortex; TempP, temporal pole; HF, hippocampal formation. Significant correlation results were marked in bold.

network for thresholds > 0.5. So, the maximum threshold was selected at 0.5 in the present study to ensure that the thresholded network displayed small-worldness.

We also calculated the area under the curve (AUC) for each network metric (global and local topological properties). The AUC is a summarized scalar, which can reflect the topological characterization of brain networks for each network metric. AUC was independent of single threshold selection and sensitive to topological alterations in brain disorders (Suo et al., 2015). Between-group differences in the AUCs were

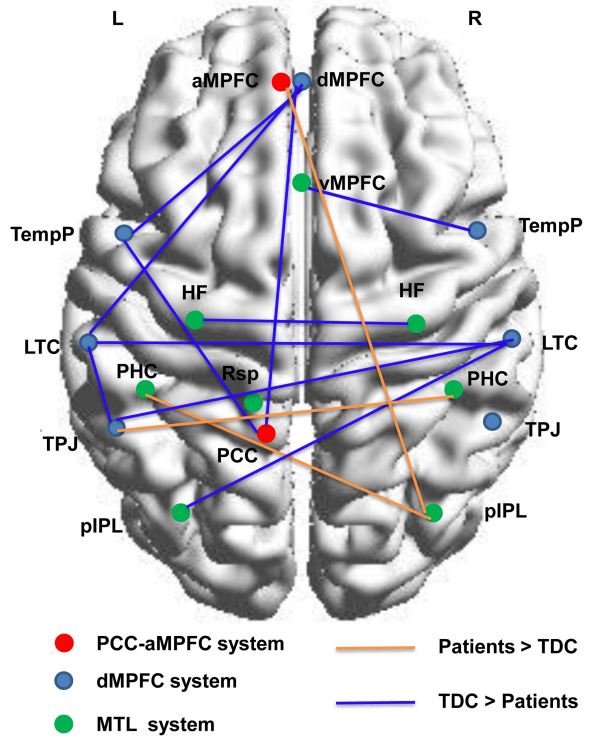

FIGURE 3 | Connected networks in the DMN that showed significant changes of functional connections in the children with GTCS. The orange lines indicate the FC values are increased in the patient group, and the blue lines indicate the FC values are decreased in the patient group. The threshold is set at $p < 0.05$. L, left hemisphere; R, right hemisphere; TDC, typically developing children.

analyzed using independent sample *t*-test with age and gender as covariates ($p < 0.05$). Between-group differences were identified in the nodal metrics.

We used a network-based statistic (NBS) approach for the functional connectivity networks to localize the specific connected components, which reflects the functional connections in DMN that differed between each pair of groups (Zalesky et al., 2010). A set of suprathreshold links among all connected components was defined using the NBS method. The non-parametric permutation method was used to estimate the significance for each component (1,000 permutations). The threshold ($p < 0.05$) was adopted to address the comparisons in functional connectivity. Using the above process, significant between-group differences in the network metrics in the DMN were identified.

Brain-Behavioral Relationships

We further calculated the brain-behavioral relationships in the patient group. The statistical analysis results of VMHC and functional connectivity in the DMN were combined. The consistent results in both analyses were selected as our region-of-interest (ROI). The mean VMHC values and the mean FC values were extracted in these ROIs, respectively. The correlations between these image indexes and the clinical characteristics (epilepsy duration and onset age of the first seizure) were calculated. And, also, the correlation between the mean VMHC values and the mean FC values in the ROIs was also calculated. The threshold ($p < 0.05$) was adopted to address the correlation results. During the comparison process, age and sex were controlled.

Support Vector Machine Analysis

The support vector machine (SVM) method was operated using PRoNTo (Pattern Recognition for Neuroimaging Toolbox) software version 2.0[2] in MATLAB (Abbasi and Goldenholz, 2019; Wissel et al., 2020). This method was applied to test the ability to differentiate children with GTCS from the TDC using the extracted VMHC values in abnormal brain regions. The regions showed significant difference between groups both in VMHC results, and FC results were selected and the signals of VMHC values in these regions were used as features of the SVM classifier. A "leave-one-out" method was used during the cross-validation step (Li et al., 2014). The statistical significance of the observed classification accuracy was estimated by permutation tests (Zeng et al., 2012). This involved repeating the classification procedure 1,000 times. The number of permutations achieving higher sensitivity and specificity than the true labels was used to derive a *p*-value. Statistical significance of classification accuracy was determined by this process.

RESULTS

Group Differences in Voxel-Mirrored Homotopic Connectivity

There were no significant differences in age or gender distribution between the two groups (see **Table 1**). Compared with the TDC, the children with GTCS showed a significant decrease in VMHC in some regions, such as the superior occipital gyrus, hippocampal formation (HF), fusiform, putamen, amygdala, angular, lateral temporal cortex (LTC), middle temporal gyrus, inferior and middle frontal gyrus (see **Figure 1**). No areas showed a significant increase in VMHC in the patient group. **Table 2** illustrates the details of group differences in VMHC.

Group Differences in Global Network Metrics in Default-Mode Network

Children with GTCS and TDC showed small-world organization ($\sigma > 1$) of the brain functional connectome in the DMN: high normalized C_p ($\gamma > 1$) and similar normalized Lp ($\lambda \approx 1$) (**Figure 2**). The result was unified using a metric called small-worldness ($\sigma > 1$). Compared to the TDC, the patients showed significantly increased L_p values ($t = 2.13$, $p = 0.038$) in the functional network of the DMN. No significant differences in other global network parameters were observed (**Figure 2**).

[2]http://www.mlnl.cs.ucl.ac.uk/pronto

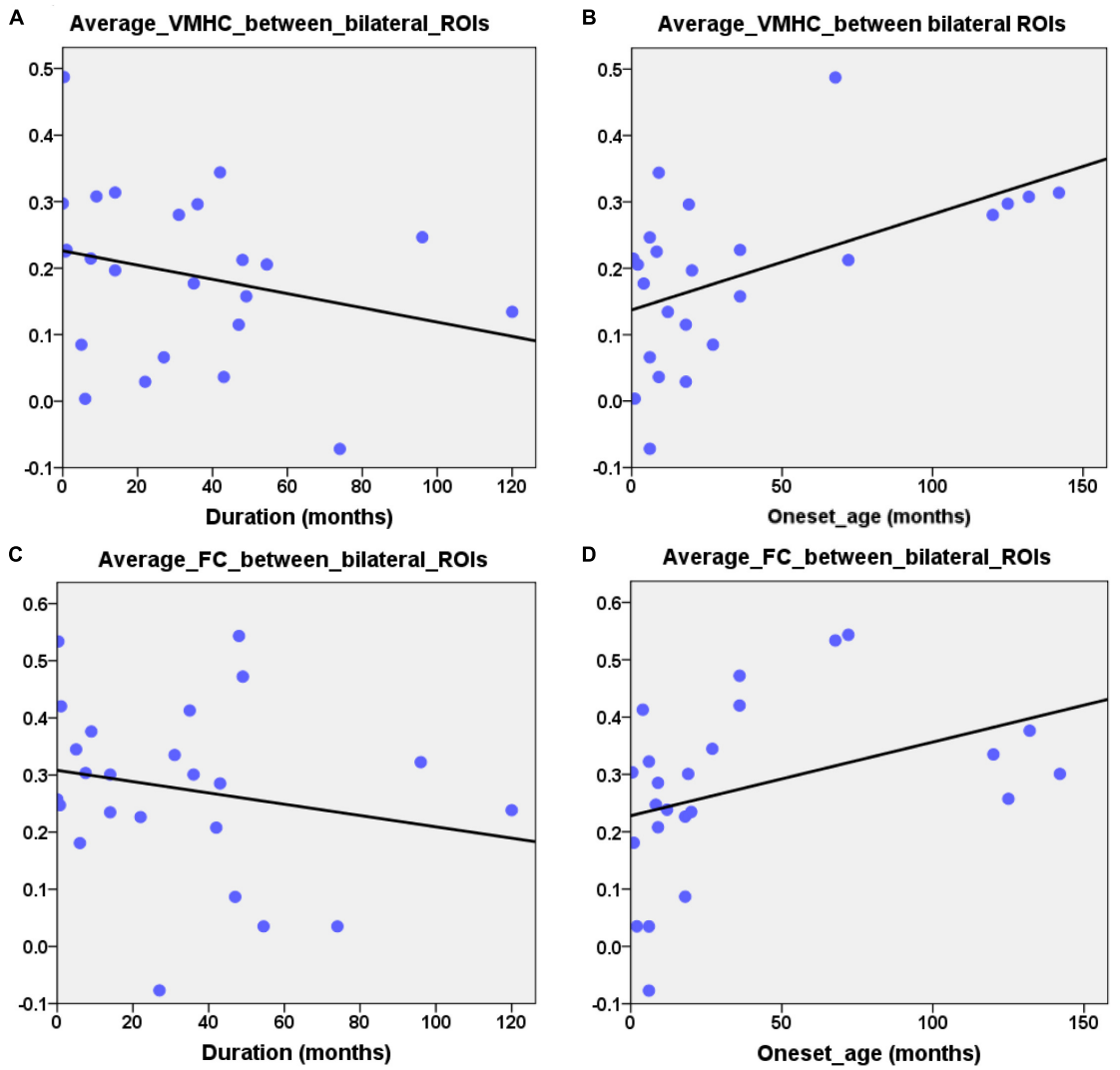

FIGURE 4 | Partial correlation between the neuroimage indexes and the clinical characteristic. **(A)** Significantly negative correlation between epilepsy duration and the average VMHC values of ROIs (bilateral HF and LTC, $r = –0.445$, $p = 0.038$). **(B)** Significantly positive correlation between the first seizure onset age and the average VMHC values of ROIs (bilateral HF and LTC, $r = 0.445$, $p = 0.038$). **(C,D)** Scatterplot showing correlation between the average FC of bilateral ROIs (HF and LTC) and clinical characteristic (epilepsy duration: $r = –0.281$, $p = 0.205$, the onset age of first seizure: $r = 0.281$, $p = 0.205$). Age and gender were controlled during the above correlation analyses.

Group Differences in Regional Topological Organization in Default-Mode Network

Brain regions in the DMN with significant intergroup differences were identified ($p < 0.05$, **Table 3**). The children with GTCS showed decreased Cp in the right temporal parietal junction (TPJ). Decreased nodal efficiency was found in the left TPJ, bilateral LTC, and left HF. For the patient group, significant decreases in nodal local efficiency were found in the right TPJ and LTC. Near significant decreases in nodal degree centrality were found in the left LTC and left HF. Significant increases in nodal betweenness centrality were found in the left temporal pole (TempP) of the children with GTCS.

Group Differences in Functional Connectivity

Based on NBS analysis, a decreased functional connectivity network in the DMN with 11 nodes and 10 connections was identified in the patient group, involving the bilateral LTC, bilateral HF, dMPFC, left TempP, left PCC, left TPJ, and left posterior inferior parietal lobule (pIPL). In particular, the functional connectivity between the bilateral HF and between the bilateral LTC showed a significant decrease in the patient group. An increased functional connectivity network with 5 nodes and 3 connections was identified in the patients, involving the bilateral parahippocampal cortex (PHC), left TPJ, right pIPL, and aMPFC. Node locations

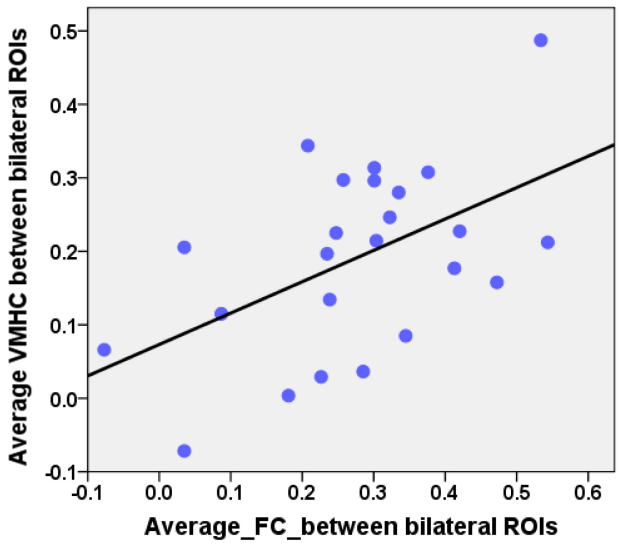

FIGURE 5 | Correlation between the average VMHC values and the average FC values in patients. The average VMHC values were extracted from the bilateral HF and bilateral LTC of the group comparison results of the whole brain VMHC analyses. The average FC values were extracted from the bilateral HF and bilateral LTC of the NBS results of the DMN. Scatterplot showing significantly positive correlation between the average VMHC values and the average FC values in patients ($r = 0.512$, $p = 0.015$). Age and gender were controlled during this correlation analysis.

and significant changes in their connections are visualized in **Figure 3**.

Relationship Between the Network Metrics and Epilepsy Duration

Combining the group comparison results of VMHC and NBS results of FC in the DMN, we found that the consistent results between the two methods mainly focused on the bilateral HF and bilateral LTC. Therefore, we selected these regions as our ROIs. The mean VMHC values and the FC values between the bilateral ROIs were extracted. Partial correlations between the epilepsy duration and the mean VMHC values of the bilateral ROIs (bilateral HF and bilateral LTC, $r = -0.445$, $p = 0.038$, **Figure 4A**) showed a significant correlation in the patient group. The mean VMHC values of the bilateral ROIs (bilateral HF and bilateral LTC) also showed significant correlations with the onset age of the first seizure (partial correlation: $r = 0.445$, $p = 0.038$, **Figure 4B**). The mean FC between the bilateral ROIs (bilateral HF and bilateral LTC) showed no significant correlation with the clinical characteristics (epilepsy duration, partial correlation: $r = -0.281$, $p = 0.205$ and onset age of the first seizure, partial correlation: $r = 0.281$, $p = 0.205$, **Figures 4C,D**). Additionally, after extracting the imaging index from the bilateral HF and bilateral LTC, the mean VMHC showed a significantly positive correlation with the mean FC (partial correlation: $r = 0.512$, $p = 0.015$, **Figure 5**). All correlation analyses were controlled for age and sex.

Support Vector Machine Classification

Based on the group comparison and the neuroimaging-clinical correlation results, we selected the bilateral HF and bilateral LTC as a mask. The VMHC in this mask was extracted as a feature in the model. **Figure 6** shows the result of the SVM classification between 24 children with GTCS and 34 TDC based on the feature of VMHC in the bilateral HF and bilateral LTC derived from resting-state fMRI. The analysis of SVM classification achieved an accuracy of 89.34%, which was statistically significant at $p < 0.001$. The overall classification accuracy of the algorithm measures its ability to correctly classify an individual as a patient with GTCS or TDC. The model obtained a sensitivity of 87.50% and specificity of 91.18%. The area under the receiver operating characteristic curve (AUC) value was 0.93.

DISCUSSION

In the present study, we combined VMHC and graph-based theoretical approaches to investigate the functional alterations in the DMN of children with GTCS. The children with GTCS showed a significant decrease in VMHC in some regions, most of which belong to the DMN, such as the HF, LTC, and angular and middle frontal gyrus. Although the patients exhibited efficient small-world properties of their functional default mode network that were similar to the TDC, the DMN of the patients also exhibited a significant increase in L_p. Group differences in regional topological organization were found in the areas of the bilateral TPJ, bilateral LTC, left TempP and left HF. In the DMN, the regions that exhibited a significant decrease in network connectivity were mainly within the dMPFC subsystem, and the regions that exhibited a significant increase in network connectivity were mainly between these subsystems in the children with GTCS. The FCs between the bilateral ROIs (left HF vs. right HF and left LTC vs. right LTC) were decreased significantly in patients, which was consistent with the VMHC results of the present study. The average VMHC values in bilateral HF and LTC were significantly correlated with the epilepsy duration and the onset age of first seizure in children with GTCS. The VMHC values in the bilateral HF and LTC also showed a significant correlation with the FC values among similar regions. Machine learning showed that the feature of VMHC values in the bilateral HF and bilateral LTC exhibited discriminative power in the classification of the children with GTCS from the TDC (accuracy of 89.34%). Together, our findings indicated that the brain functional homotopy, network architecture, and communities in the DMN of the children with GTCS were changed significantly. Our results provided preliminary evidence that the functional homotopy and topological organization of the DMN were disrupted in children with GTCS. The significant correlation results and the discriminative power in classification of the VMHC values in the HF and LTC may provide novel evidence to detect possible neuroimaging biomarkers in children with GTCS epilepsy syndrome.

Disrupted Interhemispheric Functional Connectivity of the Default-Mode Network in Children With Generalized Tonic-Clonic Seizures

As neuroimaging techniques improve, modeling brain connectivity has received much attention and interest. The focus is on the brain organization and how alterations in connectivity underlie neurological disorder. In the past few years, investigating the functional interactions between regions has become a powerful tool to explore the human brain. In a resting state fMRI study, the disruption of FC networks in GTCS has been reported (Wang et al., 2011, 2019b; Liu et al., 2017; Parsons et al., 2020). Connectivity changes in a number of brain regions involved the HP, thalamus, insula, temporal cortex, cerebellum, precuneus, and medial prefrontal cortex. It is worth noting that the disrupted functional network connectivity in patients with GTCS was mainly related to the DMN (Song et al., 2011). The DMN is the most important brain network that is engaged in the modulation of internal mentation and external cognitive processes (Raichle et al., 2001). Previous studies have shown the deactivation and FC disruption of the DMN in patients with generalized seizures. For example, a previous study in idiopathic generalized epilepsy found enhanced negative FC in the precuneus of the thalamocortical pathway (Gong et al., 2021). The interaction between the thalamocortical pathway and the DMN was disrupted in the generalized epilepsy. A study using individual component analysis found both decreased and increased FC in the DMN and dorsal attention network in patients with GTCS (Wang et al., 2011). Additionally, a previous study found that DMN connectivity is altered in both generalized and focal epilepsies (Yang et al., 2021). Functional abnormalities in the DMN area are common characteristic among epilepsy syndromes. Understanding the brain connectivity of the DMN in epilepsy is particularly important, given that seizures may disrupt the brain network. In the present study, we used the VMHC method to detect interhemispheric connectivity changes in children with GTCS. The children with GTCS showed a significant decrease in VMHC in the superior occipital gyrus, HP, fusiform, putamen, amygdala, angular, LTC, middle temporal gyrus, and inferior and middle frontal gyrus. Because most of these regions are part of the DMN, this reduced interhemispheric connectivity in the DMN may be related to the impaired cognitive abilities that characterize children with GTCS. One of our recent studies using whole brain connectivity has found that the functional connectivity between bilateral middle temporal gyrus showed a significant decrease in children with GTCS (Li et al., 2020a). In the present study, the aberrant interhemispheric functional connectivity results in the DMN of children with GTCS were consistent with these previous functional interaction studies in GTCS. This result indicates that functional reorganization within the DMN rise may give rise to GTCS in children with epilepsy. The brain connectivity results were also supported by previous neuroimaging studies on brain activity of GTCS. A simultaneous EEG-fMRI study found that the patients with GTCS showed negative activation in the posterior cingulate gyrus, precuneus, and lateral parietal cortex and incomplete synchronized activities in the medial frontal cortex when the generalized spike wave appeared (Hamandi et al., 2006). Interictal epilepsy activity may reduce functional integration in the DMN, as shown in the present study. Another study using the regional homogeneity method found that the patients with GTCS showed regional homogeneity changes bilaterally and symmetrically in the precuneus, posterior cingulate gyrus, anterior cingulate gyrus, inferior parietal lobe, inferior frontal gyrus, and putamen (Zhong et al., 2011). One of our recent studies has also found that children with GTCS showed a significant decrease in spontaneous brain activity in the bilateral angular and left inferior and middle temporal gyrus (Wang et al., 2018). Many of these affected brain regions are components of the DMN. The long-term injurious effects of epileptic action may induce decreased regional synchronization and spontaneous brain activity in the DMN of patients with GTCS. This explanation can also be used in the present study to explain the significant decrease in interhemispheric connectivity in the DMN of children with GTCS.

In the present study, the VMHC results were not in accord with the two previous studies in adults with a similar method. In these two previous studies, adults with GTCS showed significant enhancement of the VMHC in the angular cortex, cuneus, prefrontal cortex, and anterior cingulate cortex (Ji et al., 2014; Yang et al., 2014). A significant decrease in the VMHC was found in adults with GTCS in the olfactory, supramarginal, inferior frontal gyrus, and temporal lobe in one study but not in the other. There were multiple changes in VMHC in the DMN in these previous studies. In this study, we only detected a significant decrease in interhemispheric connectivity in children with GTCS, especially in the DMN. For patients with GTCS, the interhemispheric connectivity changes of the DMN in the present study were different from these two previous studies. One possible reason for the above inconsistency may be that the research subjects were different. While previous studies focused on adults with GTCS, this study focused on children with GTCS. Childhood is a specific period with fast development of the brain. Chronic epilepsy can cause functional reorganization. A previous study indicated that the default regions in human brain integrate into a cohesive, interconnected network over development (Fair et al., 2008). The functional integration of the DMN is weak at a child's age, and then is stronger over development. Chronic epilepsy may disturb the normal development of the DMN in children with GTCS. Thus, the FC between the bilateral regions of the DMN showed a decrease in the children with GTCS in this study. For adults with GTCS, the weak connectivity of the DMN gradually strengthened over development. Additionally, the seizure onset ages and the epilepsy durations were different among these studies. In the present study, the mean seizure onset age was approximately 3 years, and the mean epilepsy duration was approximately 2.5 years. In these two previous studies with VMHC methods, the mean seizure onset ages were approximately 13–17 years, and the mean epilepsy durations were approximately 3–7 years. A previous study showed that early and later ages of the seizure onset have differential impacts on brain resting-state organization (Doucet et al., 2015). The adult patients in the above previous studies had a longer epilepsy duration than

the patients in the present study, which may indicate that adult patients have a long period to restore the function of the DMN. In the present study, the ages of the seizure onset were small, and the epilepsy durations were relatively short in children with GTCS. The seizure onset ages and the epilepsy durations may be another factor that induced the significant decrease in VMHC in the DMN in the present study.

A previous study has shown that motion-associated differences in brain connectivity cannot fully be attributed to motion artifacts but, rather, also reflect individual variability in functional organization (Zeng et al., 2014). The correlate of head motion consists of reduced distant functional connectivity primarily in the default network areas in individuals with high head motion. In the present study, we did not find a significant difference in head motion FD values between the two groups. According to the common suggestions, we also used head motion parameters as covariates during the analysis. This step can eliminate the effect of head motion on brain connectivity as much as possible. As the sample size of the present study is relatively small, the motion-associated differences in brain connectivity between the two groups are not shown. Future studies should consider this question with larger sample sizes.

Altered Topological Organization of the Default-Mode Network in Children With Generalized Tonic-Clonic Seizures

In the present study, the graph theory method was used to map the topological properties of the DMN. Our results showed that both children with GTCS and TDC have a small-world topology in the functional DMN. Such a small-world topology in the whole brain network has been related to normal human cognitive functioning (He and Evans, 2010) and other pathological states (Fornito et al., 2015; Li et al., 2020a). Previous neuroimaging studies on epilepsy also found that patients with idiopathic generalized epilepsy or GTCS demonstrated a small-world property of the functional and structural networks (Zhang et al., 2011; Liao et al., 2013). Therefore, the graph results in this study indicated that the functional networks of the DMN in both groups showed high efficiency in information processing and transfer. Notably, we were only interested in the DMN but not the whole brain network in this study. Compared with the TDC, children with GTCS showed a reduction in Eg and an increase in Lp in the DMN. Group differences in regional topological organization were also found in the areas of the bilateral TPJ, bilateral LTC, left TempP, and left HF. The change trend of topological organization was consistent with a previous study that focused on the integration of the DMN in adults with GTCS (Song et al., 2011). This previous study showed that the degree and FC of brain areas within the DMN were significantly reduced in patients with GTCS. One study across the generalized types found that the DMN showed more significantly altered connectivity than other resting state networks in patients with idiopathic generalized epilepsies (Parsons et al., 2020). The disruption of functional network organization in the DMN is a common feature in generalized epilepsy. This evidence from previous neuroimaging studies, together with the present graph results, suggests that children with GTCS may have a less optimized network organization of the functional DMN than the TDC.

We also used the NBS approach for the functional connection of the DMN to localize the specific connected components. Importantly, the NBS graph connectivity analysis was consistent with the VMHC results in identifying that the interhemispheric connectivity between bilateral ROIs (left HF vs. right HF and left LTC vs. right LTC) was decreased significantly in patients. Our findings are in good agreement with previous reports that showed a significant decrease in interhemispheric FC in the DMN of adults with GTCS (Song et al., 2011; Ji et al., 2014; Li et al., 2016). In addition to the connectivity results from adults with GTCS supporting our results, recent graph theory results in children with GTCS have also supported the present graph connectivity results. One recent study using graph theory analysis on the GM structural covariance network has found that children with GTCS showed significant alterations in nodal betweenness in the right thalamus, bilateral temporal pole, and some regions of the DMN (Li et al., 2020b). Another recent graph theory study on the functional network has found a significant decrease in C_p and nodal local efficiency in the bilateral putamen, MTG, and temporal pole of the MTG of children with GTCS (Li et al., 2020a). Bilateral changes in nodal characteristics and the interhemispheric connectivity of the regions belonging to the DMN were the common results among these graph theory studies in children with GTCS. The interpretation for the disrupted interhemispheric connectivity in DMN may be that the capacity of brain communication between the bilateral regions of DMN was reduced. Taken together, our graph theory and connectivity findings in DMN tend to imply that GTCS in children is characterized by reduced interhemispheric connectivity within the DMN. The importance of the interhemispheric connection results is discussed in the following section by combining the correlation and machine learning results.

Here, we should notice that the present work is an extension of our previous research (Li et al., 2020a). The sample size was enlarged, and the research objectives were also different. The previous study is mainly focused on the whole-brain topological organization, while the present study is focused on the functional homotopy and topological properties within the DMN. And, also, the graph results of the present study can further enrich our understanding the disrupted interhemispheric connectivity in DMN.

Clinical Relevance of Functional Homotopy in the Default-Mode Network in Children With Generalized Tonic-Clonic Seizures

In the present study, it is worth noting that the average VMHC values in the bilateral HF and LTC were significantly correlated

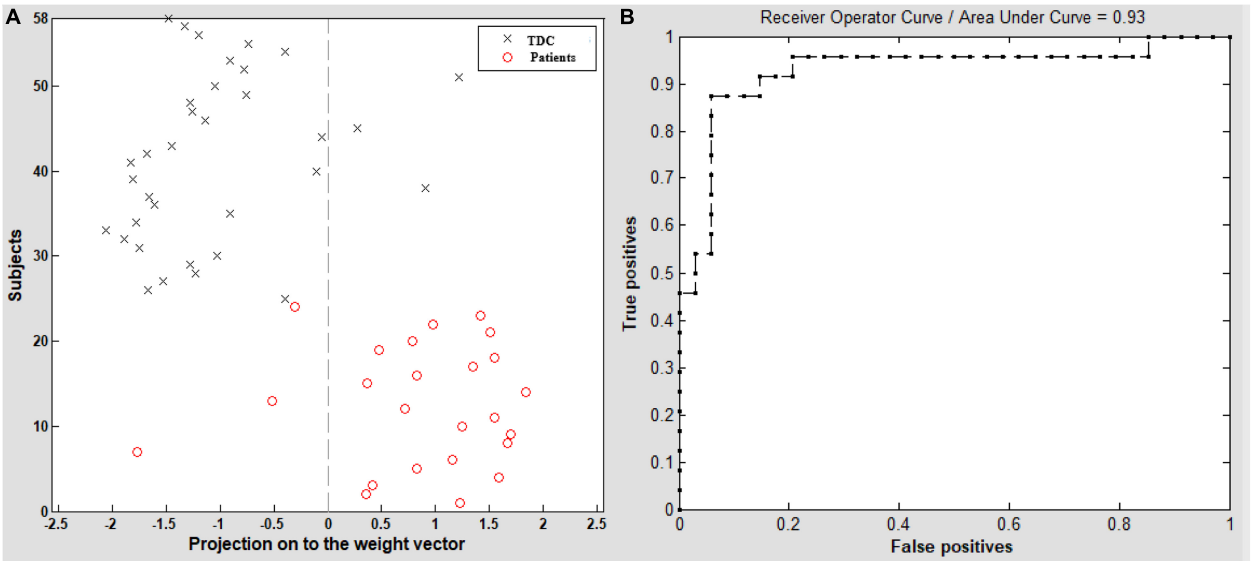

FIGURE 6 | A classification plot **(A)** and a receiver operating characteristic (ROC) curve **(B)** for the comparison between groups. VMHC maps of 24 children with GTCS and 34 TDC were used for classification, which yielded an accuracy of 89.34% (87.50% sensitivity, 91.18% specificity), statistically significant at $p < 0.001$. TDC, typically developing children.

with the epilepsy duration. Previous studies have confirmed that epilepsy duration is one of the main clinical factors affecting a patient's functional organization (Wang et al., 2011, 2018, 2019b; Liu et al., 2017). In these previous studies, the FC between the regions within the DMN or between the DMN and other subnetworks of the brain showed negative correlations with the epilepsy duration. In adults with GTCS, regional synchronization and functional rich-club connectivity in the regions of the DMN were also found to be negatively correlated with the epilepsy duration (Zhong et al., 2011; Li et al., 2016). The correlation result in the present study was consistent with these previous adult studies and indicated that the functional reorganization in the DMN can reflect the effect of epilepsy duration in both adults and children with GTCS. Children with longer illness durations showed lower VMHC between the bilateral HF and LTC. The VMHC-duration correlation results in the present study further support the proposal that the damaging effect of GTCS might disrupt the functional homotopy of the DMN in children (Li et al., 2020a,b). The significant negative correlation between the epilepsy duration and VMHC values in the bilateral HF and LTC further confirmed that reduced interhemispheric connectivity in DMN can reflect the seizure effect on the information communication in children with GTCS.

In addition to the epilepsy duration, the onset age of the first seizure is another factor that affects the resting-state connectivity of patients with epilepsy (Doucet et al., 2015). This previous study has shown that the age of the seizure onset can lead to different perturbations of network modularity and connectivity at the global and local levels in temporal lobe epilepsy, with different implications for regional plasticity and adaptive reorganization. A recent study has found that the FC between the insular and thalamic projections was significantly correlated with the onset of illness in patients with GTCS (Gong et al., 2021). The onset age of illness can affect the brain network organization in patients with GTCS. In the present study, we further found that the average VMHC values in bilateral HF and LTC were positively correlated with the onset age of first seizure in children with GTCS. In line with these previous correlation findings, these partial correlation results indicated that children with later onset ages would show less disruption of interhemispheric connections in the DMN. Additionally, the children with a later onset age would have less cognitive impairment. Thus, both correlation results in the present study imply that the dysfunction of the interhemispheric connectivity in the DMN would play an important role in the understanding of the neuromechanism of functional disorder in GTCS.

In the present study, VMHC values in bilateral HF and LTC also showed a positive correlation with the FC values between the bilateral HF and LTC. VMHC is a new validated neuroimaging index that can quantify functional homotopy by providing a voxel-wise measure of connectivity between hemispheres (Zuo et al., 2010). The brain's essential functional architecture can be measured by this index. Resting-state FC is measured with the correlations in MRI signals to examine the synchronizations between spontaneous neurophysiological events in spatially remote brain regions (Biswal et al., 1995). Thus, the positive correlation between the VMHC and FC of the bilateral HF and LTC can be easy to understand. However, significant partial neuroimaging-behavioral correlations were detected for the VMHC but not for the FC in the bilateral HF and LTC. This result can be explained by the different analysis processes of these neuroimaging indices. The VMHC quantifies

the resting-state FC between each voxel in one hemisphere and its mirrored counterpart in the other. A voxel-wise measure of the VMHC values was calculated and averaged to obtain the mean VMHC between the bilateral HF and LTC. For the average FC, the average MRI signals were extracted from the predefined ROIs of the HF and LTC. The FCs between the bilateral HF and bilateral LTC were calculated and averaged to acquire final average FC. The VMHC used a voxel-wise measure that can reflect the signal fluctuation between different voxels in the same region. This index is more sensitive than the FC index in reflecting the interhemispheric organization in children with GTCS. This opinion should be confirmed in further studies.

Clinical Relevance of Network Alterations in Children With Generalized Tonic-Clonic Seizures

To confirm the importance of the interhemispheric connection results, a machine learning method was used to detect whether the functional homotopy of bilateral HF and LTC can classify the children with GTCS from the TDC. Machine learning is an emerging trend in medicine that can be used to develop and/or optimize clinically useful algorithms for clinical medicine and basic research. In recent years, an increasing number of clinical and experimental applications of machine learning methods for epilepsy have become available in the diagnosis of epilepsy, surgical management of epilepsy, and medical management of epilepsy (Abbasi and Goldenholz, 2019; Sone and Beheshti, 2021). Machine learning techniques have enabled imaging analysis and epilepsy diagnosis from a wide range of clinical data. In addition to the clinical manifestations and EEG characteristics, the specificity of brain neuroimaging in epilepsy can also be used as a feature in epilepsy diagnosis. A common application of machine learning for brain imaging in epilepsy is the differentiation between brains with epilepsy and healthy brains (Bharath et al., 2019; Zhou et al., 2020). A previous study in our group using machine learning found that the GM volume and fALFF value in the right thalamus can be used as features to discriminate children with GTCS from the TDC (Wang et al., 2018). In the present study, the VMHC values in the bilateral HF and LTC were set as features of the machine model, and the SVM model was used to discriminate between the two groups. We classified the children with GTCS from the TDC by the linear SVM classifier, corresponding to an accuracy of 89.34% based on the VMHC values of bilateral HF and LTC. The machine learning results were consistent with these previous studies and demonstrated that specific changes in interhemispheric connectivity in the DMN allowed accurate discrimination between children with GTCS and the TDC at the level of an individual. Combining the significant correlation results, the VMHC values of bilateral HF and LTC can be considered as biomarkers to classify children with GTCS from TDC at the individual subject level. The disruption of interhemispheric connectivity in the DMN has potential value in the application of epilepsy diagnosis.

Limitations

Several limitations of this study should be noted. First, all children with GTCS were medicated in the present study. A previous study detected that using antiepileptic drugs can affect normal neuronal function and produce cognitive impairment in children (Ijff and Aldenkamp, 2013). The present results may also be affected by antiepileptic drugs. Future studies should be conducted to exclude the effect of antiepileptic drugs on interhemispheric connectivity in children with GTCS. Second, 18 children under the age of 4 were sedated with 10% chloral hydrate during image collection. Although this approach can improve the success rate of neuroimaging data collection in children, the use of sedatives in younger children may also affect brain connectivity. Future studies need to be conducted to clarify the effect of sedative drugs on brain connectivity. Third, the sample size of the patient group was relatively small compared with the size of the TDC. During the data connection, some patients were unwilling to cooperate with the MRI scan, and we could not obtain valid data from these subjects. Future studies should collect larger sample sizes to provide further insights into the issue. Finally, it should be noted that all analyses in the present study were performed on the same dataset. Although the functional homotopy of bilateral HF and LTC has the high ability to classify the children with GTCS from the TDC by the linear SVM classifier, the machine learning results were not validated by a new sample of testing data. Future studies should collect more samples as testing data to verify the stability of the present classification model.

CONCLUSION

In the present study, we combined the VMHC method and graph theory to investigate the interhemispheric organization of the DMN in children with GTCS. Although both the children with GTCS and the TDC exhibited small-world topology in the functional network of the DMN, the children with GTCS showed changes of the optical topological organization in the DMN. Both VMHC and graph connectivity analyses found that the children with GTCS showed a significant decrease in interhemispheric connectivity in the bilateral HF and LTC. The brain connectivity results indicate that the brain functional homotopy, network architecture, and communities in the DMN of the children with GTCS were changed significantly. Importantly, we found that the functional homotopy of bilateral HF and LTC was significantly correlated with the epilepsy duration and the age of the seizure onset. This neuroimaging-behavioral coupling may reflect seizure effects on brain organization in children with GTCS. VMHC values in the bilateral HF and bilateral LTC exhibited discriminative power in the classification of children with GTCS from the TDC. Machine learning results reflect that decreased VMHC in the DMN can be considered as a biomarker to classify children with GTCS from the TDC at the individual subject level. In conclusion, dysfunction of the interhemispheric connectivity in the DMN will play an important role in the

understanding of the neuromechanism of GTCS in children and has potential value in the diagnosis of epilepsy.

DATA AVAILABILITY STATEMENT

The original contributions presented in the study are included in the article/**Supplementary Material**, further inquiries can be directed to the corresponding authors.

ETHICS STATEMENT

The studies involving human participants were reviewed and approved by the Ethical Committee of the Shenzhen Children's Hospital. Written informed consent to participate in this study was provided by the participants' legal guardian/next of kin.

AUTHOR CONTRIBUTIONS

YL and QC conceived and designed the experiments. QC performed the experiments. YL analyzed image data, sorted the results, and wrote and reviewed the manuscript. QC, BQ, and JC were responsible for patient management and conceptualized the study. All authors contributed to the article and approved the submitted version.

FUNDING

This study was supported by the National Natural Science Foundation of China (No. 81601483) as well as by the Medical Science and Technology Research Foundation of Guangdong Province (No. A2021076). This work was also supported by the Key-Ares Research and Development Program of Guangdong Province (No. 2020B1111100001), the Administration of Traditional Chinese Medicine of Guangdong Province (No. 20221099), China Scholarship Council (No. 201906785005) and Huang Zhendong Research Fund for Traditional Chinese Medicine of Jinan University.

ACKNOWLEDGMENTS

We thank all the participants in the present study for their cooperation. We would also like to thank the radiographers at the Department of Pediatric Radiology of Shenzhen Children's Hospital for their support during the imaging data collection.

SUPPLEMENTARY MATERIAL

The Supplementary Material for this article can be found online at: https://www.frontiersin.org/articles/10.3389/fnins.2022.833837/full#supplementary-material

REFERENCES

Abbasi, B., and Goldenholz, D. M. (2019). Machine learning applications in epilepsy. *Epilepsia* 60, 2037–2047.

Andrews-Hanna, J. R., Reidler, J. S., Sepulcre, J., Poulin, R., and Buckner, R. L. (2010). Functional-Anatomic Fractionation of the Brain's Default Network. *Neuron* 65, 550–562. doi: 10.1016/j.neuron.2010.02.005

Bassett, D. S., and Bullmore, E. T. (2006). Small-world brain networks. *Neuroscientist* 12, 512–523.

Bharath, R. D., Panda, R., Raj, J., Bhardwaj, S., Sinha, S., Chaitanya, G., et al. (2019). Machine learning identifies "rsfMRI epilepsy networks" in temporal lobe epilepsy. *Eur. Radiol.* 29, 3496–3505. doi: 10.1007/s00330-019-5997-2

Biswal, B., Yetkin, F. Z., Haughton, V. M., and Hyde, J. S. (1995). Functional connectivity in the motor cortex of resting human brain using echo-planar MRI. *Magn. Reson. Med.* 34, 537–541. doi: 10.1002/mrm.1910340409

Blumenfeld, H., Varghese, G. I., Purcaro, M. J., Motelow, J. E., Enev, M., McNally, K. A., et al. (2009). Cortical and subcortical networks in human secondarily generalized tonic-clonic seizures. *Brain* 132, 999–1012. doi: 10.1093/brain/awp028

Buckner, R. L., Andrews-Hanna, J. R., and Schacter, D. L. (2008). The brain's default network: anatomy, function, and relevance to disease. *Ann. N.Y. Acad. Sci.* 1124, 1–38. doi: 10.1196/annals.1440.011

Doucet, G. E., Sharan, A., Pustina, D., Skidmore, C., Sperling, M. R., and Tracy, J. I. (2015). Early and late age of seizure onset have a differential impact on brain resting-state organization in temporal lobe epilepsy. *Brain Topogr.* 28, 113–126. doi: 10.1007/s10548-014-0366-6

Engel, J. Jr., Thompson, P. M., Stern, J. M., Staba, R. J., Bragin, A., and Mody, I. (2013). Connectomics and epilepsy. *Curr. Opin. Neurol.* 26:186.

Fair, D. A., Cohen, A. L., Dosenbach, N. U., Church, J. A., Miezin, F. M., Barch, D. M., et al. (2008). The maturing architecture of the brain's default network. *Proc. Natl. Acad. Sci. U.S.A.* 105, 4028–4032. doi: 10.1073/pnas.0800376105

Fisher, R. S., Cross, J. H., D'Souza, C., French, J. A., Haut, S. R., Higurashi, N., et al. (2017a). Instruction manual for the ILAE 2017 operational classification of seizure types. *Epilepsia* 58, 531–542. doi: 10.1111/epi.13671

Fisher, R. S., Cross, J. H., French, J. A., Higurashi, N., Hirsch, E., Jansen, F. E., et al. (2017b). Operational classification of seizure types by the International League Against Epilepsy: position Paper of the ILAE Commission for Classification and Terminology. *Epilepsia* 58, 522–530. doi: 10.1111/epi.13670

Fitsiori, A., Hiremath, S. B., Boto, J., Garibotto, V., and Vargas, M. I. (2019). Morphological and Advanced Imaging of Epilepsy: beyond the Basics. *Children* 6:6030043. doi: 10.3390/children6030043

Fornito, A., Zalesky, A., and Breakspear, M. (2015). The connectomics of brain disorders. *Nat. Rev. Neurosci.* 16, 159–172.

Gong, J., Jiang, S., Li, Z., Pei, H., Li, Q., Yao, D., et al. (2021). Distinct effects of the basal ganglia and cerebellum on the thalamocortical pathway in idiopathic generalized epilepsy. *Hum. Brain Mapp.* 42, 3440–3449. doi: 10.1002/hbm.25444

Goodman, A. M., and Szaflarski, J. P. (2021). Recent Advances in Neuroimaging of Epilepsy. *Neurotherapeutics* 18, 811–826.

Hamandi, K., Salek-Haddadi, A., Laufs, H., Liston, A., Friston, K. J., Fish, D. R., et al. (2006). EEG-fMRI of idiopathic and secondarily generalized epilepsies. *Neuroimage* 31, 1700–1710. doi: 10.1016/j.neuroimage.2006.02.016

He, Y., and Evans, A. (2010). Graph theoretical modeling of brain connectivity. *Curr. Opin. Neurol.* 23, 341–350. doi: 10.1097/WCO.0b013e32833aa567

Hommet, C., Sauerwein, H. C., De Toffol, B., and Lassonde, M. (2006). Idiopathic epileptic syndromes and cognition. *Neurosci. Biobehav. R* 30, 85–96. doi: 10.1016/j.neubiorev.2005.06.004

Ijff, D. M., and Aldenkamp, A. P. (2013). Cognitive side-effects of antiepileptic drugs in children. *Handb. Clin. Neurol.* 111, 707–718.

Ji, G.-J., Zhang, Z., Xu, Q., Zang, Y.-F., Liao, W., and Lu, G. (2014). Generalized Tonic-Clonic Seizures: aberrant Interhemispheric Functional and Anatomical Connectivity. *Radiology* 271, 839–847. doi: 10.1148/radiol.13131638

Jia, X., Xie, Y., Dong, D., Pei, H., Jiang, S., Ma, S., et al. (2020). Reconfiguration of dynamic large-scale brain network functional connectivity in generalized tonic-clonic seizures. *Hum. Brain Mapp.* 41, 67–79. doi: 10.1002/hbm.24787

Kenyon, K., Mintzer, S., and Nei, M. (2014). Carbamazepine treatment of generalized tonic–clonic seizures in idiopathic generalized epilepsy. *Seizure* 23, 234–236. doi: 10.1016/j.seizure.2013.11.016

Li, F., Huang, X., Tang, W., Yang, Y., Li, B., Kemp, G. J., et al. (2014). Multivariate pattern analysis of DTI reveals differential white matter in individuals with obsessive-compulsive disorder. *Hum. Brain Mapp.* 35, 2643–2651. doi: 10.1002/hbm.22357

Li, R., Liao, W., Li, Y., Yu, Y., Zhang, Z., Lu, G., et al. (2016). Disrupted structural and functional rich club organization of the brain connectome in patients with generalized tonic-clonic seizure. *Hum. Brain Mapp.* 37, 4487–4499. doi: 10.1002/hbm.23323

Li, Y., Chen, Q., and Huang, W. (2020a). Disrupted topological properties of functional networks in epileptic children with generalized tonic-clonic seizures. *Brain Behav.* 10:e01890. doi: 10.1002/brb3.1890

Li, Y., Wang, Y., Wang, Y., Wang, H., Li, D., Chen, Q., et al. (2020b). Impaired Topological Properties of Gray Matter Structural Covariance Network in Epilepsy Children With Generalized Tonic–Clonic Seizures: A Graph Theoretical Analysis. *Front. Neurol.* 11:253. doi: 10.3389/fneur.2020.00253

Liao, W., Zhang, Z., Mantini, D., Xu, Q., Wang, Z., Chen, G., et al. (2013). Relationship between large-scale functional and structural covariance networks in idiopathic generalized epilepsy. *Brain Connect.* 3, 240–254. doi: 10.1089/brain.2012.0132

Liu, F., Wang, Y., Li, M., Wang, W., Li, R., Zhang, Z., et al. (2017). Dynamic functional network connectivity in idiopathic generalized epilepsy with generalized tonic–clonic seizure. *Hum. Brain Mapp.* 38, 957–973. doi: 10.1002/hbm.23430

Myers, K. A., Sivathamboo, S., and Perucca, P. (2018). Heart rate variability measurement in epilepsy: how can we move from research to clinical practice? *Epilepsia* 59, 2169–2178. doi: 10.1111/epi.14587

Paige, A. L., and Cavanna, A. E. (2013). *Generalized Tonic–Clonic Seizures*. Berlin: Springer.

Parsons, N., Bowden, S. C., Vogrin, S., and D'Souza, W. J. (2020). Default mode network dysfunction in idiopathic generalised epilepsy. *Epilepsy Res.* 159:106254. doi: 10.1016/j.eplepsyres.2019.106254

Power, J. D., Barnes, K. A., Snyder, A. Z., Schlaggar, B. L., and Petersen, S. E. (2012). Spurious but systematic correlations in functional connectivity MRI networks arise from subject motion. *Neuroimage* 59, 2142–2154. doi: 10.1016/j.neuroimage.2011.10.018

Raichle, M. E., MacLeod, A. M., Snyder, A. Z., Powers, W. J., Gusnard, D. A., and Shulman, G. L. (2001). A default mode of brain function. *Proc. Natl. Acad. Sci. U.S.A.* 98, 676–682.

Ryvlin, P., and Beniczky, S. (2020). Seizure detection and mobile health devices in epilepsy: recent developments and future perspectives. *Epilepsia* 61, S1–S2. doi: 10.1111/epi.16702

Sone, D., and Beheshti, I. (2021). Clinical Application of Machine Learning Models for Brain Imaging in Epilepsy: A Review. *Front. Neurosci.* 15:684825. doi: 10.3389/fnins.2021.684825

Song, M., Du, H., Wu, N., Hou, B., Wu, G., Wang, J., et al. (2011). Impaired resting-state functional integrations within default mode network of generalized tonic-clonic seizures epilepsy. *PLoS One* 6:e17294. doi: 10.1371/journal.pone.0017294

Sporns, O., and Honey, C. J. (2006). Small worlds inside big brains. *Proc. Natl. Acad. Sci. U.S.A.* 103, 19219–19220. doi: 10.1073/pnas.0609523103

Stam, C. J., and Reijneveld, J. C. (2007). Graph theoretical analysis of complex networks in the brain. *Nonlin. Biomed. Phys.* 1:3.

Suo, X., Lei, D., Li, K., Chen, F., Li, F., Li, L., et al. (2015). Disrupted brain network topology in pediatric posttraumatic stress disorder: A resting-state fMRI study. *Hum. Brain Mapp.* 36, 3677–3686. doi: 10.1002/hbm.22871

Thurman, D. J., Beghi, E., Begley, C. E., Berg, A. T., Buchhalter, J. R., Ding, D., et al. (2011). Standards for epidemiologic studies and surveillance of epilepsy. *Epilepsia* 52, 2–26. doi: 10.1111/j.1528-1167.2011.03121.x

Trinka, E., Kwan, P., Lee, B., and Dash, A. (2019). Epilepsy in Asia: disease burden, management barriers, and challenges. *Epilepsia* 1, 7–21. doi: 10.1111/epi.14458

Wang, J., Li, Y., Wang, Y., and Huang, W. (2018). Multimodal Data and Machine Learning for Detecting Specific Biomarkers in Pediatric Epilepsy Patients With Generalized Tonic-Clonic Seizures. *Front. Neurol.* 9:1038. doi: 10.3389/fneur.2018.01038

Wang, J., Wang, X., Xia, M., Liao, X., Evans, A., and He, Y. (2015). GRETNA: a graph theoretical network analysis toolbox for imaging connectomics. *Front. Hum. Neurosci.* 9:386. doi: 10.3389/fnhum.2015.00386

Wang, Z., Larivière, S., Xu, Q., Vos de Wael, R., Hong, S.-J., Wang, Z., et al. (2019a). Community-informed connectomics of the thalamocortical system in generalized epilepsy. *Neurology* 93, 1112–1122. doi: 10.1212/WNL.0000000000008096

Wang, Z., Wang, X., Rong, R., Xu, Y., Zhang, B., and Wang, Z. (2019b). Impaired hippocampal functional connectivity in patients with drug resistant, generalized tonic-clonic seizures. *Neuroreport* 30, 700–706. doi: 10.1097/WNR.0000000000001262

Wang, Z., Lu, G., Zhang, Z., Zhong, Y., Jiao, Q., Zhang, Z., et al. (2011). Altered resting state networks in epileptic patients with generalized tonic–clonic seizures. *Brain Res.* 1374, 134–141. doi: 10.1016/j.brainres.2010.12.034

Wissel, B. D., Greiner, H. M., Glauser, T. A., Holland-Bouley, K. D., Mangano, F. T., Santel, D., et al. (2020). Prospective validation of a machine learning model that uses provider notes to identify candidates for resective epilepsy surgery. *Epilepsia* 61, 39–48. doi: 10.1111/epi.16398

Yan, C. G., Wang, X. D., Zuo, X. N., and Zang, Y. F. (2016). DPABI: data Processing & Analysis for (Resting-State) Brain Imaging. *Neuroinformatics* 14, 339–351.

Yang, S., Zhang, Z., Chen, H., Meng, Y., Li, J., Li, Z., et al. (2021). Temporal variability profiling of the default mode across epilepsy subtypes. *Epilepsia* 62, 61–73. doi: 10.1111/epi.16759

Yang, T., Ren, J., Li, Q., Li, L., Lei, D., Gong, Q., et al. (2014). Increased interhemispheric resting-state in idiopathic generalized epilepsy with generalized tonic–clonic seizures: A resting-state fMRI study. *Epilepsy Res.* 108, 1299–1305. doi: 10.1016/j.eplepsyres.2014.06.010

Zalesky, A., Fornito, A., and Bullmore, E. T. (2010). Network-based statistic: identifying differences in brain networks. *Neuroimage* 53, 1197–1207. doi: 10.1016/j.neuroimage.2010.06.041

Zeng, L.-L., Shen, H., Liu, L., Wang, L., Li, B., Fang, P., et al. (2012). Identifying major depression using whole-brain functional connectivity: a multivariate pattern analysis. *Brain* 135, 1498–1507. doi: 10.1093/brain/aws059

Zeng, L.-L., Wang, D., Fox, M. D., Sabuncu, M., Hu, D., Ge, M., et al. (2014). Neurobiological basis of head motion in brain imaging. *Proc. Natl. Acad. Sci. U.S.A.* 111, 6058–6062. doi: 10.1073/pnas.1317424111

Zhang, Z., Liao, W., Chen, H., Mantini, D., Ding, J.-R., Xu, Q., et al. (2011). Altered functional–structural coupling of large-scale brain networks in idiopathic generalized epilepsy. *Brain* 134, 2912–2928. doi: 10.1093/brain/awr223

Zhong, Y., Lu, G., Zhang, Z., Jiao, Q., Li, K., and Liu, Y. (2011). Altered regional synchronization in epileptic patients with generalized tonic–clonic seizures. *Epilepsy Res.* 97, 83–91. doi: 10.1016/j.eplepsyres.2011.07.007

Zhou, B., An, D., Xiao, F., Niu, R., Li, W., Li, W., et al. (2020). Machine learning for detecting mesial temporal lobe epilepsy by structural and functional neuroimaging. *Front. Med.* 14:630–641. doi: 10.1007/s11684-019-0718-4

Zuo, X. N., Kelly, C., Di Martino, A., Mennes, M., Margulies, D. S., Bangaru, S., et al. (2010). Growing Together and Growing Apart: regional and Sex Differences in the Lifespan Developmental Trajectories of Functional Homotopy. *J. Neurosci.* 30, 15034–15043. doi: 10.1523/JNEUROSCI.2612-10.2010

Conflict of Interest: The authors declare that the research was conducted in the absence of any commercial or financial relationships that could be construed as a potential conflict of interest.

frontiers | Frontiers in Neuroscience

ORIGINAL RESEARCH
published: 28 June 2022
doi: 10.3389/fnins.2022.899473

The Enhanced Interhemispheric Functional Connectivity in the Striatum Is Related to the Cognitive Impairment in Individuals With White Matter Hyperintensities

Huahong Zhu[1,2,3,4,5,6], *Ruomeng Qin*[2,3,4,5,6], *Yue Cheng*[2,3,4,5,6], *Lili Huang*[2,3,4,5,6], *Pengfei Shao*[2,3,4,5,6], *Hengheng Xu*[2,3,4,5,6], *Yun Xu*[1,2,3,4,5,6]* *and Qing Ye*[2,3,4,5,6]*

[1] Department of Neurology, Nanjing Drum Tower Hospital, Clinical College of Nanjing Medical University, Nanjing, China, [2] State Key Laboratory of Pharmaceutical Biotechnology, Department of Neurology, Nanjing Drum Tower Hospital, Nanjing University Medical School, Nanjing, China, [3] Institute for Brain Sciences, Nanjing University, Nanjing, China, [4] Jiangsu Key Laboratory for Molecular Medicine, Nanjing University Medical School, Nanjing, China, [5] Jiangsu Province Stroke Center for Diagnosis and Therapy, Nanjing, China, [6] Nanjing Neurology Clinic Medical Center, Nanjing, China

OPEN ACCESS

Edited by:
Chitresh Bhushan,
GE Global Research, United States

Reviewed by:
Alaka Acharya,
Harbin Institute of Technology, China
Christian O'Reilly,
McGill University, Canada

***Correspondence:**
Yun Xu
xuyun20042001@aliyun.com
Qing Ye
yeqingyouxiang@126.com

Specialty section:
This article was submitted to Brain Imaging Methods, a section of the journal Frontiers in Neuroscience

Received: 18 March 2022
Accepted: 09 June 2022
Published: 28 June 2022

Citation:
Zhu H, Qin R, Cheng Y, Huang L, Shao P, Xu H, Xu Y and Ye Q (2022) The Enhanced Interhemispheric Functional Connectivity in the Striatum Is Related to the Cognitive Impairment in Individuals With White Matter Hyperintensities. Front. Neurosci. 16:899473. doi: 10.3389/fnins.2022.899473

Objective: The cognitive performance of individuals with white matter hyperintensities (WMH) tends to vary considerably. This study aimed to explore the relationship of the synchronous spontaneous activities in homotopic areas across hemispheres, named as voxel-mirrored homotopic connectivity (VMHC), with the cognitive performance of individuals with WMH.

Materials and Methods: Eighty-two WMH subjects without cognitive impairment (CI), 56 WMH subjects with CI, and 92 healthy subjects (HS) underwent neuropsychological tests and multimodal magnetic resonance imaging scans. VMHC maps were analyzed among the three groups. Correlative analyses were performed between VMHC values and cognitive function.

Results: No significant difference in WMH volume, brain volume, or gray matter atrophy rate was shown between WMH subjects with and without CI. In contrast, those with CI displayed lower VMHC in the bilateral cuneus and calcarine and higher VMHC in the lentiform nucleus and caudate nucleus (LNCN) than those without CI. Furthermore, the VMHC in the LNCN was negatively associated with the global function and the memory function in WMH subjects.

Conclusion: The enhanced VMHC in the LNCN was associated with the development of CI in individuals with WMH. This finding may contribute to the exploration of surrogate markers for the CI caused by WMH.

Keywords: white matter hyperintensities, voxel-mirrored homotopic connectivity, cognitive impairment, cognitive heterogeneity, functional magnetic resonance imaging

INTRODUCTION

White matter hyperintensities (WMH) is commonly detected on magnetic resonance imaging (MRI) scans of the brain in the elderly. As the population ages, as much as 72–96% of the elderly would show WMH (Zhuang et al., 2018; Lampe et al., 2019). WMH in the elderly usually reflects axonal loss and demyelination resulting from chronic ischemia related to cerebral small vessel disease (Gouw et al., 2011). Many evidences have shown that the burden of WMH is negatively associated with cognitive function (Prins and Scheltens, 2015; Alber et al., 2019; Wu et al., 2019), and the increase of WMH burden is significantly paralleled by cognitive decline (LADIS Study Group, 2011; Schmidt et al., 2012). On the other hand, the cognitive performance of individuals with WMH tends to vary considerably, and a portion of these individuals even maintain normal cognitive function (Stern, 2002; Jokinen et al., 2016). The mechanisms underlying the high heterogeneity remain relatively unknown. Exploring the mechanisms is of value to the identification of surrogate markers related to the cognitive impairment (CI) in these individuals, thus directing the prevention of CI.

Functional magnetic resonance imaging (fMRI) technique detects alterations in synchronous activities of functionally related areas, also named as functional connectivity (FC), associated with aging or pathology. Voxel-mirrored homotopic connectivity (VMHC) refers to the voxel-based intrinsic FC between homotopic areas across hemispheres. VMHC reliably and reproducibly measures interhemispheric communication underlying the coherent cognitive function and behavior. A study on healthy individuals found that the VMHC in frontal, parietal, and temporal regions decreased with aging, and correlated with cognitive decline (Zhao et al., 2020). Other studies showed that the abnormal VMHC in frontal, parietal, or temporal regions was significantly associated with CI in individuals with stroke, Alzheimer's Disease (AD), or type 2 diabetes mellitus (Li et al., 2018; Yao et al., 2020; Zhang et al., 2021). On the other hand, less evidence on the relationship between VMHC and cognitive function has been shown in individuals with WMH, despite that WMH may disrupt white matter tracts that connect hemispheres. Exploring the pattern of VMHC and its relationship with cognitive function in individuals with WMH may contribute to the identification of surrogate markers for CI.

The present study enrolled WMH subjects without CI, WMH subjects with CI, and healthy subjects (HS), and all subjects underwent multimodal MRI scanning and neuropsychological testing. We aimed to (1) identify the difference in the VMHC patterns among the three groups; (2) determine the relationship between the VMHC and cognitive function.

MATERIALS AND METHODS

Subjects

The present study enrolled 138 subjects with WMH and 92 HS subjects. All the subjects were recruited from the Department of Neurology in The Affiliated Drum Tower Hospital of Nanjing University from January 2017 to December 2020. All the subjects have provided informed consent. The study had been approved by the Ethics Committee of The Affiliated Drum Tower Hospital of Nanjing University Medical School. All subjects underwent neuropsychological tests and multimodal MRI scans. As described previously (Chen et al., 2019), the inclusion criteria for subjects with WMH were: (1) age >50 years; and (2) presence of WMH on brain MRI (Fazekas grade 1∼3), no cerebral microbleeds or recent subcortical infarction. A HS group included those cognitively normal [measured by Montreal Cognitive Assessment (MoCA)] participants showing no clinical symptoms of cerebral small vessel disease, no presence of visible WMH on MRI (Fazekas grade 0), and no other MRI presentative characteristics of cerebral small vessel disease. The exclusion criteria were: (1) history of ischemic stroke with cerebral infarction diameter >15 mm, or cardiogenic cerebral infarction; (2) other cognitive disorders such as AD, Parkinson's disease, Lewy body dementia, etc.; (3) intracranial hemorrhage, brain trauma, brain tumor and mental system disease, and severe somatic diseases, such as thyroid disease, anemia, malignant tumor, etc.; and (4) diseases such as multiple sclerosis, radiation brain injury, and other white matter diseases caused by poisoning, immunity, metabolism, infection and other factors.

Neuropsychological Assessments

All the participants completed a series of neuropsychological tests. Neuropsychological assessments included global cognitive function, memory function, executive function, visuospatial ability and information processing speed. Global cognitive function was measured using the Mini-Mental State Examination (MMSE) and MoCA. An Auditory-verbal Learning Test-delayed recall (AVLT-DR) and a Rey-Osterrieth complex Figure Test (CFT) with its 20-min delayed recall (CFT-DR) were used to measured memory function. A Stroop Color and Word Test C (Stroop C) and Trail Making Tests (TMT)-B were used to measure executive function. An immediate recall of CFT was used to measure visuospatial performance. A Stroop Color and Word Test A (Stroop A) and TMT-A were used to measure information processing speed. Raw data of each neuropsychological test (except the MoCA and MMSE) were Z-transformed according to the following equation:

$$Z_i = \frac{(r_i - m)}{S}$$

Z_i represents the Z scores for the ith subject, r_i represents the raw score for the ith subject, m represents the average score for each test for all subjects, and S represents the standard deviation of the test scores for all subjects. We performed Z-transformation across all subjects in all groups, and then the Z-transformed values of the relevant neuropsychological tests were averaged to obtain each cognitive domain. The purpose of the Z-transform is to facilitate the unification of different neuropsychological

test data into a unified cognitive domain data. Due to the high sensitivity of the MoCA test for CI (Nasreddine et al., 2005), WMH subjects were diagnosed with CI when MoCA scores was ≤19 (education years: 1–6) or ≤24 (education years ≥7). According to the scores of neuropsychological tests, all subjects with WMH were divided into a WMH without CI group (n = 82) and a WMH with CI group (n = 56).

Magnetic Resonance Imaging Procedures

As described previously (Ye et al., 2019), all subjects were scanned using a 3-Tesla magnetic resonance scanner (Ingenia 3.0T, Philips Medical Systems, Eindhoven, Netherlands) with a 32-channel head coil at the Drum Tower Hospital. All subjects were instructed to relax, close their eyes, and stay awake during scanning. Resting-state functional images, including 230 volumes, were acquired by a gradient-echo-planar imaging sequence: repetition time = 2,000 ms, echo time = 30 ms, flip angle = 90°, matrix = 64 × 64, voxel size = 3 mm× 3 mm× 3 mm, field of view = 192 mm× 192 mm, thickness = 4.0 mm, gap = 0 mm, and number of slices = 35. 3D T1-weighted turbo fast echo sagittal images with high resolution were acquired with the following parameters: repetition time = 9.8 ms, echo time = 4.6 ms, flip angle = 8°, matrix = 256 × 256, field of view = 256 mm× 256 mm, thickness = 1.0 mm, gap = 0 mm, and number of slices = 192. 3D fluid-attenuated inversion recovery (FLAIR) sagittal images were obtained with the following imaging parameters: repetition time = 4,500 ms, echo time = 344 ms, flip angle = 90°, matrix = 272 × 272, thickness = 1.0 mm, gap = 0 mm, and number of slices = 200.

Magnetic Resonance Imaging Data Preprocessing and Static Voxel-Mirrored Homotopic Connectivity Analysis

The fMRI data were preprocessed using a toolbox for Data Processing Assistant for Resting-State fMRI (DPARSF) v2.3[1] on Statistical Parametric Mapping software (SPM12)[2]. The preprocessing procedures included (1) removal of the first 10 time points to allow for T1 equilibration effects; (2) time correction for acquisition time delay among slices; (3) realignment to correct motion effects (subjects with head motion artifacts exceeding 2° in rotation or 2 mm in translation were excluded); (4) spatial normalization of the resulting images into the standard Montreal Neurological Institute (MNI) space and re-sample into a voxel size of 3 mm × 3 mm × 3 mm; (5) spatial smoothing with a Gaussian kernel of 6 mm× 6 mm× 6 mm; (6) nuisance covariates regression [white matter, cerebrospinal fluid, global signal, 6-head motion parameters, 6-head motion parameters at one time point earlier, and the 12 corresponding squared items (Friston 24-parameter model) as covariates]; and (7) linear detrending and temporal bandpass filter (0.01–0.1 Hz).

After preprocessing, the Pearson's correlation coefficient between the residual time series of each voxel and its mirrored counterpart in the opposite hemisphere was calculated to obtain VMHC maps. Details of the VMHC calculations have been described in a previous study (Zuo et al., 2010). Detailed procedures are shown in **Supplementary Material**.

White Matter Hyperintensities Segmentation and Quantification

The volume of WMH lesions was evaluated on T1 and T2-FLAIR images using the Lesion Segmentation Tool (LST) toolbox version 2.0.15[3] for SPM12. Detailed procedures are shown in **Supplementary Material**. Notably, although the HS group included subjects with Fazekas grade 0 of WMH, the LST toolbox may detect tiny WMH lesions invisible on MRI. Thus, the HS group may have a small amount of WMH burden.

Volume Assessment of Brain

As illustrated in a previous study (Ye et al., 2017), brain volume was estimated utilizing the Voxel-Based Morphometry 8 (VBM8) toolbox for SPM12. Detailed procedures are shown in **Supplementary Material**.

Statistical Analysis

In the analysis for demographic characteristics, cognitive function, and volume data, normally distributed data were presented as mean ± standard deviation (SD) and analyzed using a one-way analysis of variance (ANOVA). Non-normally distributed data were presented as medians (quartiles) and analyzed using a Kruskal–Wallis test. The Chi-square test was applied in the analysis of gender. To improve the normal distribution of WMH volume data, the raw data were converted into $\log_{10}$ values.

In the analysis for VMHC data, an analysis of covariance (ANCOVA) was performed to identify the differences of VMHC maps among groups, controlling for age, gender, and education. The Resting State fMRI Data Analysis Toolkit (REST) 1.8 software[4] was used in this procedure. The threshold was set at a corrected $P < 0.01$, determined by Monte Carlo simulation for multiple comparisons (voxel-wise $P < 0.01$). The full-width at half-maximum (FWHM) was estimated on VMHC maps and was used to calculate the threshold of the cluster size with the program AlphaSim in the REST software. Then, the average VMHC value of each region with significant group differences was derived in each subject. A post hoc test was conducted to reveal the detailed difference in the VMHC among the three groups.

We performed partial correlation analyses to test the relationship between the cognitive function and the VMHC values in each brain region with significant group differences, controlling for age, gender, and education. The Statistical Package

[1] http://resting-fmri.sourceforge.net
[2] http://www.fil.ion.ucl.ac.uk/spm
[3] www.statistical-modelling.de/lst.html
[4] http://restfmri.net/forum/index.php

TABLE 1 | Demographic, neuropsychological, and brain volume data.

Items	HS group (*n* = 92)	WMH without CI group (*n* = 82)	WMH with CI group (*n* = 56)	*F* or χ^2	*P*-value
Age (year)	60.32 ± 7.42	64.63 ± 7.6	64.77 ± 8.3	8.891	**<0.001**[a,b]
Male (%)	51 (55.43)	40 (48.78)	24 (42.86)	1.136	0.323
Education (year)	12 (9–16)	12 (9–15)	9 (9–12)	–	**0.026**[b]
MMSE	29 (28–30)	29 (28–30)	28 (26–29)	–	**<0.001**[b,c]
MoCA	27 (25–28)	26 (25–27)	22 (19–23)	–	**<0.001**[b,c]
Memory	0.38 ± 0.76	0.18 ± 0.65	−0.19 ± 0.70	11.261	**<0.001**[b,c]
Executive function	0.34 (−0.20–1.00)	0.25 (−0.28–0.73)	−0.26 (−0.65–0.07)	–	**<0.001**[b,c]
Visuospatial ability	0.56 (0.01–1.11)	0.29 (−0.26–0.77)	−0.26 (−0.53–0.29)	–	**<0.001**[b,c]
Processing speed	0.42 ± 0.77	0.34 ± 0.76	−0.25 ± 0.7	15.001	**<0.001**[b,c]
Gray matter atrophy (%)	41.35 ± 1.91	41.79 ± 2.16	41.02 ± 2.14	2.441	0.089
Brain volume (ml)	1350.4 ± 123.57	1344.88 ± 104.1	1340.15 ± 126.83	0.137	0.872
LogWMH	−0.03 ± 0.50	0.49 ± 0.31	0.54 ± 0.34	50.393	**<0.001**[a,b]

Education, MMSE, MoCA, executive function, and visuospatial ability data are presented as medians (quartiles) and were analyzed using a Kruskal–Wallis test. Chi-square test was applied in the comparisons of gender. Other data are presented as mean ± stand deviation (SD) and were analyzed using a one-way ANOVA. A log_{10} transformation was performed on the WMH volume data to improve the normal distribution of the data. Significance is highlighted in bold ($P < 0.05$).

[a]*$P < 0.05$, differs between WMH without CI group and HS group.*

[b]*$P < 0.05$, differs between WMH with CI group and HS group.*

[c]*$P < 0.05$, differs between WMH without CI group and WMH with CI group.*

CI, cognitive impairment; HS, healthy subjects; MMSE, Mini-Mental State Examination; MoCA, Montreal cognitive assessment; WMH, white matter hyperintensity.

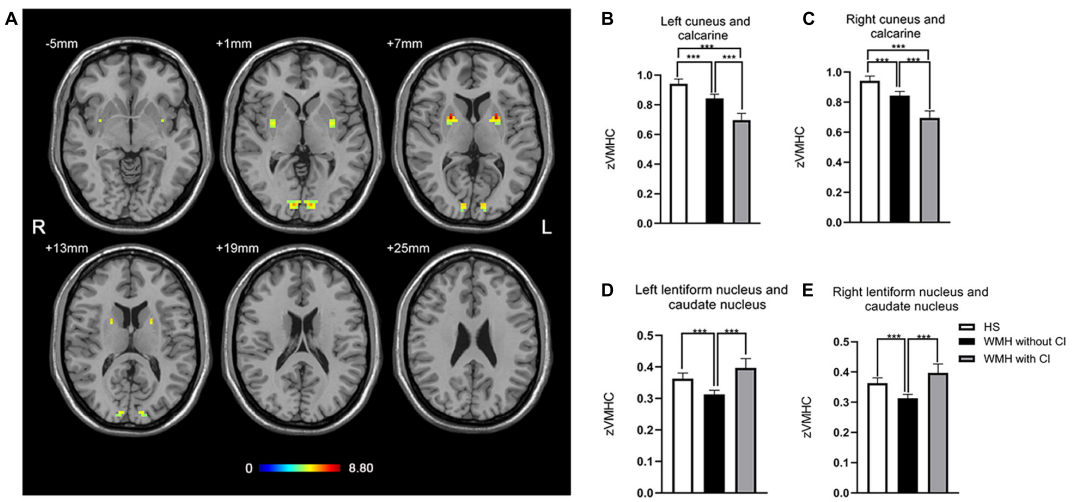

FIGURE 1 | The differences in VMHC among groups. **(A)** Statistical maps showed VMHC differences in the bilateral cuneus and calcarine and the bilateral LNCN among the WMH without CI group, the WMH with CI group, and the HS group. The threshold was set at a corrected $P < 0.01$, determined by Monte Carlo simulation for multiple comparisons (voxel wise $P < 0.01$, cluster size >1,161 mm^3). The color bar indicates the *F*-value. **(B,C)** In the bilateral cuneus and calcarine, both the WMH without CI group and the WMH with CI group had lower VMHC than the HS group, and the WMH with CI group had even lower VMHC than the WMH without CI group. **(D,E)** In the bilateral LNCN, the WMH without CI group displayed lower VMHC than the HS group, and the WMH with CI group had comparable VMHC to the HS group and higher VMHC than the WMH without CI group. Histogram indicated mean value and standard error of VMHC. ***$P < 0.001$. CI, cognitive impairment; HS, healthy subjects; LNCN, lentiform nucleus and caudate nucleus; VMHC, voxel-mirrored homotopic connectivity; WMH, white matter hyperintensity.

TABLE 2 | Brain regions with significant differences in VMHC between groups.

Brain regions	Peak MNI coordinates *x*, *y*, *z* (mm)	Peak *F*-value	BA	Cluster size (mm^3)
Left cuneus and calcarine	−9, −90, 3	8.0726	17, 18	1161
Right cuneus and calcarine	9, −90, 3	8.0726	17, 18	1161
Left lentiform nucleus and caudate nucleus	−24, 3, 6	8.7673	–	891
Right lentiform nucleus and caudate nucleus	24, 3, 6	8.7673	–	891

The thresholds were set at a corrected $P < 0.01$ determined by Monte Carlo simulation for multiple comparisons (voxel-wise $P < 0.01$). BA, Brodmann area; MNI, Montreal neurological institute.

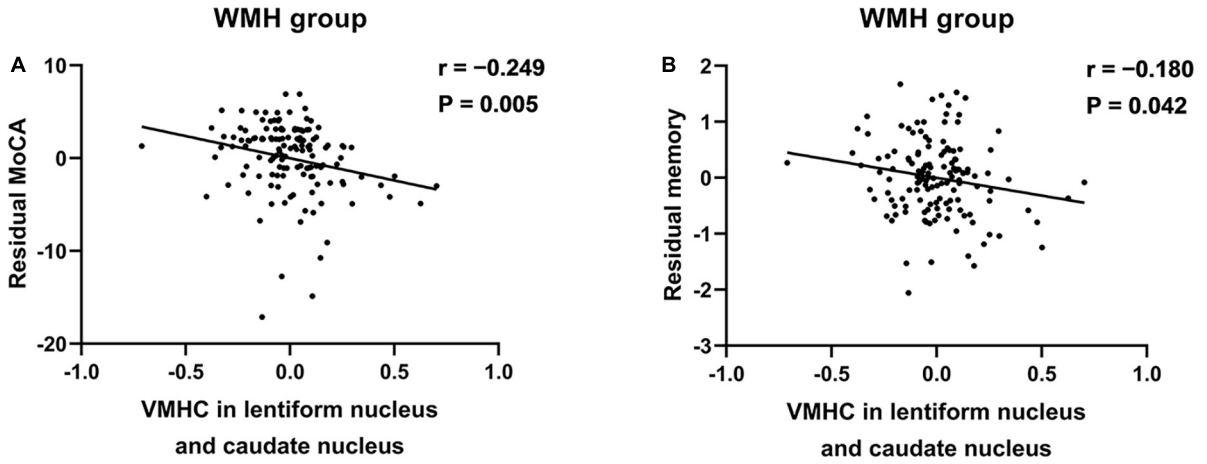

FIGURE 2 | The association between the VMHC in the LNCN and cognitive function in WMH subjects. **(A)** The VMHC was negatively associated with the MoCA scores. **(B)** The VMHC was negatively associated with the memory function. The significance level for correlation analyses was set at $P < 0.05$. Partial correlation analyses were conducted between the residuals of variables after regression on the nuisance variables. LNCN, lentiform nucleus and caudate nucleus; MoCA, Montreal cognitive assessment; VMHC, voxel-mirrored homotopic connectivity; WMH, white matter hyperintensity.

for Social Sciences (SPSS) 19.0 software was used, and the significance was set at a $P < 0.05$.

RESULTS

Demographic Characteristics

As described in **Table 1**, both the WMH without CI group and the WMH with CI group were significantly older than the HS group. No significant difference in gender was shown among the three groups. Although the WMH with CI group displayed significantly poorer performance in all cognitive domains than the WMH without CI group, there was no significant difference in gray matter atrophy rate, brain volume, or WMH volume between the two groups.

Difference in Voxel-Mirrored Homotopic Connectivity Among Groups

As shown in **Figure 1A**, the group difference of VMHC was shown in the bilateral cuneus and calcarine and the bilateral lentiform nucleus and caudate nucleus (LNCN) ($P < 0.01$, FWHM = 5.6 mm, cluster size >1,161 mm^3, Monte Carlo corrected at the cluster-level). Specifically, in the bilateral cuneus and calcarine, both the WMH without CI group and the WMH with CI group had lower VMHC than the HS group, and the WMH with CI group had even lower VMHC than the WMH without CI group (**Figures 1B,C**). In the bilateral LNCN, however, only the WMH without CI group displayed lower VMHC than the HS group, and the WMH with CI group had comparable VMHC to the HS group and higher VMHC than the WMH without CI group (**Figures 1D,E**). Detailed coordinate information on the regions described above is available in **Table 2**.

The Association of Voxel-Mirrored Homotopic Connectivity With Cognitive Function

In WMH subjects, the VMHC in the bilateral LNCN was significantly negatively correlated with both MOCA scores ($r = -0.249$, $P = 0.005$) and memory function ($r = -0.180$, $P = 0.042$) (**Figures 2A,B**).

DISCUSSION

The main findings of this study were as follows: (1) compared with WMH subjects without CI, those with CI displayed decreased VMHC in the cuneus and calcarine but increased VMHC in the LNCN; (2) the VMHC in the LNCN was associated with global function and memory function in WMH subjects. These findings contribute to the understanding of the relationship between interhemispheric connectivity and the cognitive heterogeneity in subjects with WMH.

Voxel-mirrored homotopic connectivity reflects the major role of interhemispheric communication in the integration of brain function underlying coherent behavior and cognition (Kelly et al., 2011). Interhemispheric coordination is of great importance for cognitive processes and handling complicated tasks (Belger and Banich, 1992; Wang et al., 2013). Ding et al. (2015) found that patients with subcortical vascular cognitive impairment displayed decreased VMHC in bilateral lingual gyrus, putamen, and precentral gyrus than patients with subcortical cerebrovascular disease and normal cognitive function. The decreased VMHC in the occipital regions was also shown in the present study, but we did not find altered VMHC in the putamen and precentral gyrus. This divergence may be due to the different grouping method and inclusion criteria for subjects. The striatum, including the caudate nucleus and the lentiform nucleus, is involved in

motivation (Wolfram et al., 1997), implicit learning (Packard and Knowlton, 2002; Graybiel, 2008), inhibitory control, working memory, and set-shifting/flexibility (Grahn et al., 2008; McNab and Klingberg, 2008). The striatum is involved in integrating information from multiple cortical regions, thereby constituting a network that underlies decision making (Nagano-Saito et al., 2014). As shown in previous studies, the dysfunction of the striatum was associated with CI in multiple conditions or disorders (Asensio et al., 2010; Bailey and Goldman, 2017). Lewis et al. (2003) revealed that selective impairments in working memory and executive dysfunction were associated with reduced activity in the striatum in patients with Parkinson's disease. Our findings support the role of the striatum in the development of CI in subjects with WMH.

In this study, the WMH without CI group displayed lower VMHC in the LNCN than both the HS group and the WMH with CI group, and no significant difference was shown between the latter two groups. This may suggest a U-shape curve of the VMHC in the LNCN related to the CI in subjects with WMH; that is, the VMHC may decrease significantly in WMH subjects with normal cognitive function, but then increase with the onset of CI. The decreased VMHC in WMH subjects with normal cognitive function may reflect the impaired inter-hemispheric connectivity related to disrupted white matter tracts. Then, with the onset of CI, compensatory enhancement in interhemispheric connectivity may be induced by the functional deterioration. The U-shaped curve of FC was also shown in previous studies. Meng et al. (2018) founded that compared with healthy control subjects, the baseline FC in the nucleus basalis of Meynert decreased in patients with mild cognitive impairment but increased in patients with AD and treated with cholinesterase inhibitor. Taya et al. (2018) explored global and local characteristic (clustering coefficient, normalized clustering coefficient, characteristic path length, normalized characteristic path length, and small-worldness) of an electroencephalogram-based network during performing a piloting task. They showed that the characteristic path length of the network firstly decreased and then increased during the training on a piloting task (Taya et al., 2018). A possible explanation for the U-shaped curve is that the connectivity between brain regions is disrupted by brain pathology or unfamiliar tasks, followed by enhanced connectivity to maintain cognitive performance after adapting to the pathology or tasks.

In WMH subjects, the VMHC in the LNCN was negatively correlated with both global function and memory function. The characteristic changes of the VMHC in the LNCN may be involved in the development of CI in subjects with WMH. On the other hand, comparable WMH volume, brain volume, and gray matter atrophy rate were shown between the two groups and could not be used to explain the difference in cognitive function. Thus, the altered VMHC may be more relevant to the CI and might contribute to the exploration for potential imaging biomarkers for the CI in individuals with WMH.

Both the WMH with CI group and the WMH without CI group showed decreased VMHC in the bilateral occipital lobes relative to the HS group, and the VMHC in the WMH with CI group was even lower than the WMH without CI group. The occipital cortex is mainly involved in visual information processing (Thiebaut de Schotten et al., 2014) and is also related to multiple functions such as memory (Cansino et al., 2017) and motor perception (Hidaka et al., 2017). The dysfunction of the occipital lobe affects not only the processing of visual information but also the performance of various cognitive tasks (Tohid et al., 2015). Zhang et al. (2021) found significantly decreased VMHC in the occipital lobe in patients with type 2 diabetes mellitus. And the decreased VMHC was associated with poor global function. Wang et al. (2015) showed that AD patients had significantly weaker VMHC in the occipital lobe than mild cognitive impairment subjects, and the VMHC in the occipital gyrus was positively correlated with the cognitive performance. Although we did not find significant association of the VMHC in the occipital lobe with cognitive function in subjects with WMH, the group difference in the VMHC between the two WMH groups might suggest a role of the VMHC in the development of CI.

Our study has several limitations. First, periventricular WMH burden and deep WMH burden were not analyzed in the present study, despite that periventricular WMH and deep WMH reflect different etiological and functional features (Kim et al., 2008). Although no significant difference in the total WMH burden was shown between the two WMH groups, there might be difference in periventricular WMH burden or/and deep WMH burden underlying the cognitive differences between groups. Second, in the present cross-sectional study, only the association relationships rather than the causal relationships were obtained between the VMHC alterations and cognitive function. Longitudinal studies would be helpful for exploring the causal relationships. Finally, the diagnosis of CI was based on clinical criteria, and we did not assess pathological markers to exclude other cognitive disorders. The CI might not be caused by the WMH burden in some cases but by other pathologies, e.g., AD pathology.

CONCLUSION

The increased VMHC in the striatum was related to the presence of CI in subjects with WMH. The abnormal interhemispheric connectivity may be associated with the cognitive heterogeneity in individuals with WMH and may contribute to the exploration of surrogate markers for CI in these individuals.

DATA AVAILABILITY STATEMENT

The original contributions presented in this study are included in the article/**Supplementary Material**, further inquiries can be directed to the corresponding author/s.

ETHICS STATEMENT

The studies involving human participants were reviewed and approved by the Ethics Committee of The Affiliated Drum Tower Hospital of Nanjing University Medical School. The patients/participants provided their written informed consent to participate in this study.

AUTHOR CONTRIBUTIONS

QY and YX contributed to the conceptualization, project administration, and writing and review. HZ contributed to the research project conception, data analysis, and writing – original draft. RQ contributed to the acquisition of the neuropsychological test. YC contributed to the acquisition of the data and statistical analysis. LH contributed to the acquisition of the data. PS and HX contributed to the acquisition of the image data. All authors approved the final version of the manuscript.

FUNDING

This research was supported by the National Natural Science Foundation of China (81801060, 81630028, and 81920108017), Key Research and Development Program of Jiangsu Province of China (BE2020620), National Key Research and Development Program of China (2016YFC1300500-504), and Jiangsu Province Key Medical Discipline (ZDXKA2016020).

ACKNOWLEDGMENTS

We sincerely thank all the subjects in this study.

SUPPLEMENTARY MATERIAL

The Supplementary Material for this article can be found online at: https://www.frontiersin.org/articles/10.3389/fnins.2022.899473/full#supplementary-material

REFERENCES

Alber, J., Alladi, S., Bae, H.-J., Barton, D. A., Beckett, L. A., Bell, J. M., et al. (2019). White matter hyperintensities in vascular contributions to cognitive impairment and dementia (VCID): knowledge gaps and opportunities. *Alzheimers Dement (N Y)* 5, 107–117. doi: 10.1016/j.trci.2019.02.001

Asensio, S., Romero, M. J., Romero, F. J., Wong, C., Alia-Klein, N., Tomasi, D., et al. (2010). Striatal dopamine D2 receptor availability predicts the thalamic and medial prefrontal responses to reward in cocaine abusers three years later. *Synapse* 64, 397–402. doi: 10.1002/syn.20741

Bailey, M., and Goldman, J. G. (2017). Characterizing cognitive impairment in Parkinson's disease. *Semin. Neurol.* 37, 167–175. doi: 10.1055/s-0037-1601894

Belger, A., and Banich, M. T. (1992). Interhemispheric interaction affected by computational complexity. *Neuropsychologia* 30, 923–929. doi: 10.1016/0028-3932(92)90036-l

Cansino, S., Trejo-Morales, P., Estrada-Manilla, C., Pasaye-Alcaraz, E. H., Aguilar-Castañeda, E., Salgado-Lujambio, P., et al. (2017). Effective connectivity during successful and unsuccessful recollection in young and old adults. *Neuropsychologia* 103, 168–182. doi: 10.1016/j.neuropsychologia.2017.07.016

Chen, X., Huang, L., Ye, Q., Yang, D., Qin, R., Luo, C., et al. (2019). Disrupted functional and structural connectivity within default mode network contribute to WMH-related cognitive impairment. *NeuroImage Clin.* 24:102088. doi: 10.1016/j.nicl.2019.102088

Ding, W., Cao, W., Wang, Y., Sun, Y., Chen, X., Zhou, Y., et al. (2015). Altered functional connectivity in patients with subcortical vascular cognitive impairment-a resting-state functional magnetic resonance imaging study. *PLoS One* 10:e0138180. doi: 10.1371/journal.pone.0138180

Gouw, A. A., Seewann, A., van der Flier, W. M., Barkhof, F., Rozemuller, A. M., Scheltens, P., et al. (2011). Heterogeneity of small vessel disease: a systematic review of MRI and histopathology correlations. *J. Neurol. Neurosurg. Psychiatry* 82, 126–135. doi: 10.1136/jnnp.2009.204685

Grahn, J. A., Parkinson, J. A., and Owen, A. M. (2008). The cognitive functions of the caudate nucleus. *Progr. Neurobiol.* 86, 141–155. doi: 10.1016/j.pneurobio.2008.09.004

Graybiel, A. M. (2008). Habits, rituals, and the evaluative brain. *Annu. Rev. Neurosci.* 31, 359–387. doi: 10.1146/annurev.neuro.29.051605.112851

Hidaka, S., Higuchi, S., Teramoto, W., and Sugita, Y. (2017). Neural mechanisms underlying sound-induced visual motion perception: an fMRI study. *Acta Psychol.* 178, 66–72. doi: 10.1016/j.actpsy.2017.05.013

Jokinen, H., Melkas, S., Madureira, S., Verdelho, A., Ferro, J. M., Fazekas, F., et al. (2016). Cognitive reserve moderates long-term cognitive and functional outcome in cerebral small vessel disease. *J. Neurol. Neurosurg. Psychiatry* 87, 1296–1302. doi: 10.1136/jnnp-2016-313914

Kelly, C., Zuo, X.-N., Gotimer, K., Cox, C. L., Lynch, L., Brock, D., et al. (2011). Reduced interhemispheric resting state functional connectivity in cocaine addiction. *Biol. Psychiatry* 69, 684–692. doi: 10.1016/j.biopsych.2010.11.022

Kim, K. W., MacFall, J. R., and Payne, M. E. (2008). Classification of white matter lesions on magnetic resonance imaging in elderly persons. *Biol. Psychiatry* 64, 273–280. doi: 10.1016/j.biopsych.2008.03.024

LADIS Study Group (2011). 2001–2011: a decade of the LADIS (Leukoaraiosis And DISability) Study: what have we learned about white matter changes and small-vessel disease? *Cerebrovasc. Dis.* 32, 577–588. doi: 10.1159/000334498

Lampe, L., Kharabian-Masouleh, S., Kynast, J., Arelin, K., Steele, C. J., Löffler, M., et al. (2019). Lesion location matters: the relationships between white matter hyperintensities on cognition in the healthy elderly. *J. Cereb. Blood Flow Metab.* 39, 36–43. doi: 10.1177/0271678X17740501

Lewis, S. J. G., Dove, A., Robbins, T. W., Barker, R. A., and Owen, A. M. (2003). Cognitive impairments in early Parkinson's disease are accompanied by reductions in activity in frontostriatal neural circuitry. *J. Neurosci.* 23, 6351–6356. doi: 10.1523/JNEUROSCI.23-15-06351.2003

Li, K.-C., Luo, X., Zeng, Q.-Z., Xu, X.-J., Huang, P.-Y., Shen, Z.-J., et al. (2018). Distinct patterns of interhemispheric connectivity in patients with early- and late-onset Alzheimer's disease. *Front. Aging Neurosci.* 10:261. doi: 10.3389/fnagi.2018.00261

McNab, F., and Klingberg, T. (2008). Prefrontal cortex and basal ganglia control access to working memory. *Nat. Neurosci.* 11, 103–107. doi: 10.1038/nn2024

Meng, D., Li, X., Bauer, M., Taylor, J.-P., and Auer, D. P. (2018). Altered nucleus basalis connectivity predicts treatment response in mild cognitive impairment. *Radiology* 289, 775–785. doi: 10.1148/radiol.2018180092

Nagano-Saito, A., Martinu, K., and Monchi, O. (2014). Function of basal ganglia in bridging cognitive and motor modules to perform an action. *Front. Neurosci.* 8:187. doi: 10.3389/fnins.2014.00187

Nasreddine, Z. S., Phillips, N. A., Bédirian, V., Charbonneau, S., Whitehead, V., Collin, I., et al. (2005). The montreal cognitive assessment, MoCA: a brief screening tool for mild cognitive impairment. *J. Am. Geriatr. Soc.* 53, 695–699. doi: 10.1111/j.1532-5415.2005.53221.x

Packard, M. G., and Knowlton, B. J. (2002). Learning and memory functions of the Basal Ganglia. *Annu. Rev. Neurosci.* 25, 563–593. doi: 10.1146/annurev.neuro.25.112701.142937

Prins, N. D., and Scheltens, P. (2015). White matter hyperintensities, cognitive impairment and dementia: an update. *Nat. Rev. Neurol.* 11, 157–165. doi: 10.1038/nrneurol.2015.10

Schmidt, R., Berghold, A., Jokinen, H., Gouw, A. A., van der Flier, W. M., Barkhof, F., et al. (2012). White matter lesion progression in LADIS. *Stroke* 43, 2643–2647. doi: 10.1161/STROKEAHA.112.662593

Stern, Y. (2002). What is cognitive reserve? Theory and research application of the reserve concept. *J. Int. Neuropsychol. Soc.* 8, 448–460. doi: 10.1017/S1355617702813248

Taya, F., Sun, Y., Babiloni, F., Thakor, N. V., and Bezerianos, A. (2018). Topological changes in the brain network induced by the training on a piloting task: an EEG-based functional connectome approach. *IEEE Trans. Neural Syst. Rehabil. Eng.* 26, 263–271. doi: 10.1109/TNSRE.2016.2581809

Thiebaut de Schotten, M., Urbanski, M., Valabregue, R., Bayle, D. J., and Volle, E. (2014). Subdivision of the occipital lobes: an anatomical and functional MRI connectivity study. *Cortex* 56, 121–137. doi: 10.1016/j.cortex.2012.12.007

Tohid, H., Faizan, M., and Faizan, U. (2015). Alterations of the occipital lobe in schizophrenia. *Neurosciences (Riyadh)* 20, 213–224. doi: 10.17712/nsj.2015.3.20140757

Wang, L., Li, K., Zhang, Q.-E., Zeng, Y.-W., Jin, Z., Dai, W.-J., et al. (2013). Interhemispheric functional connectivity and its relationships with clinical characteristics in major depressive disorder: a resting state fMRI study. *PLoS One* 8:e60191. doi: 10.1371/journal.pone.0060191

Wang, Z., Wang, J., Zhang, H., Mchugh, R., Sun, X., Li, K., et al. (2015). Interhemispheric functional and structural disconnection in Alzheimer's disease: a combined resting-state fMRI and DTI study. *PLoS One* 10:e0126310. doi: 10.1371/journal.pone.0126310

Wolfram, S., Peter, D., and Read, M. P. (1997). A neural substrate of prediction and reward. *Science (1979)* 275, 1593–1599. doi: 10.1126/science.275.5306.1593

Wu, X., Ge, X., Du, J., Wang, Y., Sun, Y., Han, X., et al. (2019). Characterizing the penumbras of white matter hyperintensities and their associations with cognitive function in patients with subcortical vascular mild cognitive impairment. *Front. Neurol.* 10:348. doi: 10.3389/fneur.2019.00348

Yao, G., Li, J., Liu, S., Wang, J., Cao, X., Li, X., et al. (2020). Alterations of functional connectivity in stroke patients with basal ganglia damage and cognitive impairment. *Front. Neurol.* 11:980. doi: 10.3389/fneur.2020.00980

Ye, Q., Chen, X., Qin, R., Huang, L., Yang, D., Liu, R., et al. (2019). Enhanced regional homogeneity and functional connectivity in subjects with white matter hyperintensities and cognitive impairment. *Front. Neurosci.* 13:695. doi: 10.3389/fnins.2019.00695

Ye, Q., Su, F., Gong, L., Shu, H., Liao, W., Xie, C., et al. (2017). Divergent roles of vascular burden and neurodegeneration in the cognitive decline of geriatric depression patients and mild cognitive impairment patients. *Front. Aging Neurosci.* 9:288. doi: 10.3389/fnagi.2017.00288

Zhang, Y., Wang, J., Wei, P., Zhang, J., Zhang, G., Pan, C., et al. (2021). Interhemispheric resting-state functional connectivity abnormalities in type 2 diabetes patients. *Ann. Palliative Med.* 10, 8123–8133. doi: 10.21037/apm-21-1655

Zhao, J., Manza, P., Wiers, C., Song, H., Zhuang, P., Gu, J., et al. (2020). Age-related decreases in interhemispheric resting-state functional connectivity and their relationship with executive function. *Front. Aging Neurosci.* 12:20. doi: 10.3389/fnagi.2020.00020

Zhuang, F.-J., Chen, Y., He, W.-B., and Cai, Z.-Y. (2018). Prevalence of white matter hyperintensities increases with age. *Neural Regen. Res.* 13, 2141–2146. doi: 10.4103/1673-5374.241465

Zuo, X.-N., Kelly, C., Di Martino, A., Mennes, M., Margulies, D. S., Bangaru, S., et al. (2010). Growing together and growing apart: regional and sex differences in the lifespan developmental trajectories of functional homotopy. *J. Neurosci.* 30, 15034–15043. doi: 10.1523/JNEUROSCI.2612-10.2010

Conflict of Interest: The authors declare that the research was conducted in the absence of any commercial or financial relationships that could be construed as a potential conflict of interest.

Publisher's Note: All claims expressed in this article are solely those of the authors and do not necessarily represent those of their affiliated organizations, or those of the publisher, the editors and the reviewers. Any product that may be evaluated in this article, or claim that may be made by its manufacturer, is not guaranteed or endorsed by the publisher.

frontiers | Frontiers in Neuroscience

ORIGINAL RESEARCH
published: 04 July 2022
doi: 10.3389/fnins.2022.915164

Structure–Function Decoupling: A Novel Perspective for Understanding the Radiation-Induced Brain Injury in Patients With Nasopharyngeal Carcinoma

Ya-fei Kang[1†], Rui-ting Chen[2†], Hao Ding[3,4†], Li Li[5], Jian-ming Gao[6], Li-zhi Liu[5] and You-ming Zhang[2,7]*

[1] Shaanxi Provincial Key Research Center of Child Mental and Behavioral Health, School of Psychology, Shaanxi Normal University, Xi'an, China, [2] Department of Radiology, Xiangya Hospital, Central South University, Changsha, China, [3] Department of Radiology, Affiliated Hospital of Guilin Medical University, Guilin, China, [4] Department of Radiology, The First Affiliated Hospital of Guangxi Medical University, Nanning, China, [5] State Key Laboratory of Oncology in South China, Collaborative Innovation Center for Cancer Medicine, Sun Yat-sen University Cancer Center, Guangzhou, China, [6] State Key Laboratory of Oncology in South China, Department of Radiation Oncology, Collaborative Innovation Center for Cancer Medicine, Sun Yat-sen University Cancer Center, Guangzhou, China, [7] National Clinical Research Center for Geriatric Diseases, Xiangya Hospital, Central South University, Changsha, China

OPEN ACCESS

Edited by:
Chitresh Bhushan, GE Global Research, United States

Reviewed by:
Russell W. Chan, New York University, United States
Hongjian He, Zhejiang University, China

***Correspondence:**
You-ming Zhang
zhangym0820@csu.edu.cn

† These authors have contributed equally to this work

Specialty section:
This article was submitted to Brain Imaging Methods, a section of the journal Frontiers in Neuroscience

Received: *07 April 2022*
Accepted: *09 June 2022*
Published: *04 July 2022*

Citation:
Kang Y-f, Chen R-t, Ding H, Li L, Gao J-m, Liu L-z and Zhang Y-m (2022) Structure–Function Decoupling: A Novel Perspective for Understanding the Radiation-Induced Brain Injury in Patients With Nasopharyngeal Carcinoma. Front. Neurosci. 16:915164. doi: 10.3389/fnins.2022.915164

Radiation-induced functional and structural brain alterations are well documented in patients with nasopharyngeal carcinoma (NPC), followed by radiotherapy (RT); however, alterations in structure–function coupling remain largely unknown. Herein, we aimed to assess radiation-induced structure–function decoupling and its importance in predicting radiation encephalopathy (RE). We included 62 patients with NPC (22 patients in the pre-RT cohort, 18 patients in the post-RT-RE$_{+ve}$ cohort, and 22 patients in the post-RT-RE$_{-ve}$ cohort). A metric of regional homogeneity (ReHo)/voxel-based morphometry (VBM) was used to detect radiation-induced structure–function decoupling, which was then used as a feature to construct a predictive model for RE. Compared with the pre-RT group, patients in the post-RT group (which included post-RT-RE$_{+ve}$ and post-RT-RE$_{-ve}$) showed higher ReHo/VBM coupling values in the substantia nigra (SN), the putamen, and the bilateral thalamus and lower values in the brain stem, the cerebellum, the bilateral medial temporal lobes (MTLs), the bilateral insula, the right precentral and postcentral gyri, the medial prefrontal cortex (MPFC), and the left inferior parietal lobule (IPL). In the post-RT group, negative correlations were observed between maximum dosage of RT (MDRT) to the ipsilateral temporal lobe and ReHo/VBM values in the ipsilateral middle temporal gyrus (MTG). Moreover, structure–function decoupling in the bilateral superior temporal gyrus (STG), the bilateral precentral and postcentral gyri, the paracentral lobules, the right precuneus and IPL, and the right MPFC exhibited excellent predictive performance (accuracy = 88.0%) in identifying patients likely to develop RE. These findings show that ReHo/VBM may be a novel effective imaging metric that reflects the neural mechanism underlying RE in patients with NPC.

Keywords: nasopharyngeal carcinoma, structure–function coupling, radiation encephalopathy, ReHo/VBM, individual prediction

INTRODUCTION

Radiotherapy (RT) is the mainstay of treatment for non-metastatic nasopharyngeal carcinoma (NPC) because of its high sensitivity to ionizing radiation. However, high-dose radiation inevitably causes acute or delayed toxicity. As a delayed radiation-related complication, radiation-induced brain injury (RBI) has recently attracted attention for its serious neuropsychiatric symptoms, unclear pathogenesis, and insufficient investigations on individual prediction (Tang et al., 2012). Therefore, an in-depth understanding of RBI pathogenesis and the ability to perform individual predictions are of great clinical significance.

Recently, several studies have used non-invasive functional magnetic resonance imaging (fMRI) techniques to examine radiation-induced structural and functional alterations in gray matter (GM; Lin et al., 2017; Ding et al., 2018; Zhang et al., 2018, 2021). Several studies of voxel-based morphometry (VBM) and surface-based morphometry have reported radiation-induced cortical volume, cortical thickness, and surface area abnormalities in multiple brain regions, such as the bilateral temporal lobes, the precentral gyrus, and the inferior parietal lobule (IPL; Lv et al., 2014; Lin et al., 2017; Zhang et al., 2021). Similarly, more recent fMRI studies have also documented altered regional neuronal activity and functional connectivity (FC) in the intratemporal and extratemporal lobes (Ma et al., 2017; Qiu et al., 2018; Zhang et al., 2020a, 2021; Zhao et al., 2021). However, on close inspection of the distribution of the affected brain regions in previous structural and functional studies, we observed an interesting phenomenon; the affected brain regions with radiation-induced structural abnormalities were not well matched with those revealed by studies in the functional domain. This phenomenon indicates that an investigation into the relationship between structural and functional profiles, followed by RT, may be a new direction to elucidate the neural mechanism of RBI.

The nature of the relationship between functional co-activation and brain anatomy is one of the fundamental issues in neuroscience (Gu et al., 2021). Some investigators believe that cerebral functions are shaped and constrained by the underlying neuroanatomical structure (Honey et al., 2009; Shen et al., 2012; Hermundstad et al., 2013; Wang et al., 2017). Specific molecular traits and cellular organization may be responsible for particular cerebral functions. For example, the selective increase in the expression of gene zif268 and the N-methyl-D-aspartate receptor in CA1 neurons of the hippocampus are tightly associated with fear memory retrieval and long-term memory consolidation (Hall et al., 2001; Wittenberg and Tsien, 2002). Moreover, specific cell differentiation of excitatory neuronal populations in layers 2 and 3 pyramidal neurons and layer 5 pyramidal tract neurons of the primary motor cortex is anatomical substrates for the global assessment of motor performance and reinforcement-based motor learning of skilled behaviors (Anderson et al., 2010; Levy et al., 2020). The advent of the fMRI technique has enabled *in vivo* investigations of the cerebral structure–function relationship in human populations and diseases. One such study showed that improved alignment between the functional signals and the architecture of the underlying white matter network is associated with increased cognitive flexibility (Medaglia et al., 2018). However, to the best of our knowledge, radiation-induced changes in the structure–function coupling have not been investigated in patients with NPC.

The machine learning approach can help to screen out classification-related information from the altered structure–function coupling throughout the whole brain after RT, thus enabling the prediction of temporal lobe necrosis [also named radiation encephalopathy (RE)] in the early stage. Predictive MRI biomarkers of RE could enable the stratification of patients with NPC for customized treatment and thus, help to improve disease control and survival. Therefore, we aimed to construct the structure–function coupling-based predictive model to predict RE in patients with NPC after RT and, thereby, enable clinicians to take preventive strategies (e.g., neuroprotective agents) (Yang et al., 2021) to stop or slow down the deterioration of RBI (Zhang et al., 2020c). Considering that the median interval from RT to RE was approximately 38–45 months (Zhou et al., 2013; Feng et al., 2018), to ensure the clinical significance of individualized prediction, the proposed predictive model for RE should be developed and validated based on MRI data within the latency of RE.

In this study, we first computed VBM and ReHo mapping for each patient with NPC. The ReHo/VBM metric was then established to measure the radiation-induced effect on the structure–function relationship. Subsequently, we applied a machine learning strategy to evaluate the prediction ability of the ReHo/VBM metric for RE. Given our previously reported divergent patterns of radiation-induced structural and functional alterations in the GM of patients with NPC (Zhang et al., 2018, 2020c, 2021), we hypothesized that the ReHo/VBM metric will be an effective imaging metric that reflects the radiation-induced altered structure–function relationship in patients with NPC. Our objectives for performing this study were as follows: (1) to investigate the ReHo/VBM alterations in the normal-appearing GM in patients with NPC, followed by RT; and (2) to build a predictive model for identifying the patients with NPC who are likely to develop RE.

Abbreviations: NPC, nasopharyngeal carcinoma; RT, radiotherapy; ReHo, regional homogeneity; VBM, voxel-based morphometry; MDRT, maximum dosage of RT; RBI, radiation-induced brain injury; fMRI, functional magnetic resonance imaging; GM, gray matter; FC, functional connectivity; RE, radiation encephalopathy; UICC/AJCC, International Union against Cancer/American Joint Committee on Cancer; TNM, tumor, nodes, and metastasis tumor staging system; IMRT, intensity-modulated radiation therapy; 2D-CRT, two-dimensional conventional radiotherapy; BOLD, blood oxygen level-dependent; 3D MPRAGE, three-dimensional T1-weighted magnetization prepared rapid acquisition gradient echo; TR, repetition time; TE, echo time; FOV, field of view; DPABI, Data Processing and Analysis for Brain Imaging; MNI, Montreal Neurological Institute; CSF, cerebrospinal fluid; SVM, support vector machine; CV, cross-validation; LASSO, the least absolute shrinkage and selection operator; ROC, receiver operator characteristic curve; FDR, false-discovery rate; SN, substantia nigra; MTL, medial temporal lobes; MPFC, medial prefrontal cortex; MTG, middle temporal gyri; STG, superior temporal gyrus; IPL, inferior parietal lobule; DMN, default mode network; PAG, periaqueductal gray matter; SST, SN-striatum-thalamus.

MATERIALS AND METHODS

Participants

We enrolled a total of 62 patients with NPC in this study, 22 of whom were in the pre-RT group, and the remaining 40 were in the post-RT group. According to the follow-up results of RE occurrence, the post-RT patients were further divided into two subgroups, namely, post-RT-RE$_{+ve}$ (n = 18) and post-RT-RE$_{-ve}$ (n = 22). The time intervals between RT and fMRI examinations were 10.77 ± 9.74 months in enrolled post-RT-RE$_{-ve}$ patients with NPC and 17.00 ± 17.61 months in post-RT-RE$_{+ve}$. The procedures for participant selection and grouping and the main analytical process are illustrated in **Figure 1**.

The clinical staging of patients with NPC was based on the seventh edition of the International Union against Cancer/American Joint Committee on Cancer (UICC/AJCC) TNM (T = Tumor, N = Nodes, and M = Metastasis) (2009). The post-RT patients were treated with intensity-modulated radiation therapy (IMRT) or two-dimensional conventional RT (2D-CRT); details are described in our previous work (Zhang et al., 2018). Concurrent chemoradiotherapy with/without neoadjuvant and/or adjuvant chemotherapy was recommended for patients at stages IIb to IVa–b (Zhang et al., 2021), alongside one or more chemotherapeutics, such as cisplatin, paclitaxel, nedaplatin, and fluorouracil. To minimize the confounding effect of chemotherapy on ReHo/VBM changes, efforts were made to balance the clinical stages of the enrolled patients with NPC between groups (**Table 1**) and standardize between-group chemotherapy regimens (Zhang et al., 2018, 2021). The inclusion criteria were as follows: (1) pathological evidence of NPC; (2) normal-appearing brain parenchyma on MRI; (3) aged <65 years; (4) right-handedness; and (5) Karnofsky Performance Scale score of >80; the subjects would be excluded if they presented with (1) brain tumor or atrophy, (2) brain invasion, (3) MRI contraindications, (4) a history of neuropsychological disorders and intracranial surgery, and (5) other substantial intracranial diseases (Zhang et al., 2018, 2021).

Magnetic Resonance Imaging Acquisition

Imaging data were acquired on a Magnetom Tim Trio 3T scanner (Siemens, Munich, Germany) using blood oxygen level-dependent (BOLD) and three-dimensional T1-weighted magnetization prepared rapid acquisition gradient echo (MPRAGE) sequences. Scanning parameters for BOLD and three-dimensional (3D) T1 MPRAGE sequences are documented in our previous studies (Zhang et al., 2018, 2020a, 2021). Briefly, for the BOLD sequence, the parameters were as follows: repetition time (TR) = 2,400 ms, echo time (TE) = 30 ms, field of view (FOV) = 230 mm × 230 mm, matrix size = 64 × 64, time points = 240, flip angle = 90°, and 40 axial slices. Patients were instructed to remain calm and awake with eyes closed during the resting-state fMRI scanning. For the 3D T1 MPRAGE sequence, the parameters were as follows: voxel size = 1.0 mm × 1.0 mm × 1.0 mm, FOV = 256 mm × 256 mm, matrix size = 256 × 256, thickness/gap = 1.0/0 mm, TR = 2,300 ms, TE = 2.98 ms, flip angle = 9°, and 176 sagittal slices.

Functional Magnetic Resonance Imaging and Structural Magnetic Resonance Imaging Data Preprocessing

The fMRI and structural MRI data were preprocessed using Data Processing Assistant for Resting-State fMRI Advanced Edition[1], the VBM8[2] modules in the toolbox for Data Processing and Analysis for Brain Imaging (DPABI)[3], and the SPM12[4] software implemented in MATLAB 2016b.

The main preprocessing steps for BOLD fMRI data and 3D T1 data were described in **Supplementary Appendix**.

Regional Homogeneity Mapping Acquisition and Regional Homogeneity/Voxel-Based Morphometry Calculation

The preprocessed BOLD data were used to calculate ReHo by measuring the similarity between the time series in a given voxel and those in the 26 neighboring voxels (Zang et al., 2004). Individual ReHo maps were obtained for each participant for subsequent analyses (Zhang et al., 2020a).

As both the ReHo maps and the modulated GM maps were normalized to the MNI coordinate system, we performed voxel-wise ReHo/VBM analysis by calculating the ratio of the ReHo value to GM volume of the voxel at the same coordinate. Fisher's z-transformation was used to improve the normality of the obtained ReHo/VBM measurements. The z-transformed ReHo/VBM maps were smoothed using a 6-mm full-width-at-half-maximum isotropic Gaussian kernel and used for subsequent intergroup statistical and classification analyses.

Support Vector Machine Analysis

The easylearn software (Pedregosa et al., 2011)[5] was used to perform the machine learning analysis. A linear kernel support vector machine (SVM) classifier was used for the classification of RE. Detailed information on this process is described below.

Cross-Validation

We conducted a nested stratified K-fold (K = 10) cross-validation (CV) setup. The inner CV (first CV) served to optimize regularization parameters, while the outer CV (second CV) estimated predictive performance when using optimal parameters obtained in the inner CV. In each fold, the algorithm splits the sample into 10 equal parts, of which one part is used as a test set to estimate the performance of a model (outer CV) that is trained by the training set (the remaining nine parts), which used inner CV for hyperparameter tuning. The procedure was repeated until every part was used as the test set.

[1]http://rfmri.org/DPARSF_V2.3

[2]http://www.neuro.uni-jena.de/vbm/download/

[3]http://rfmri.org/dpabi

[4]https://www.fil.ion.ucl.ac.uk/spm/software/spm12/

[5]https://github.com/lichao312214129/easylearn

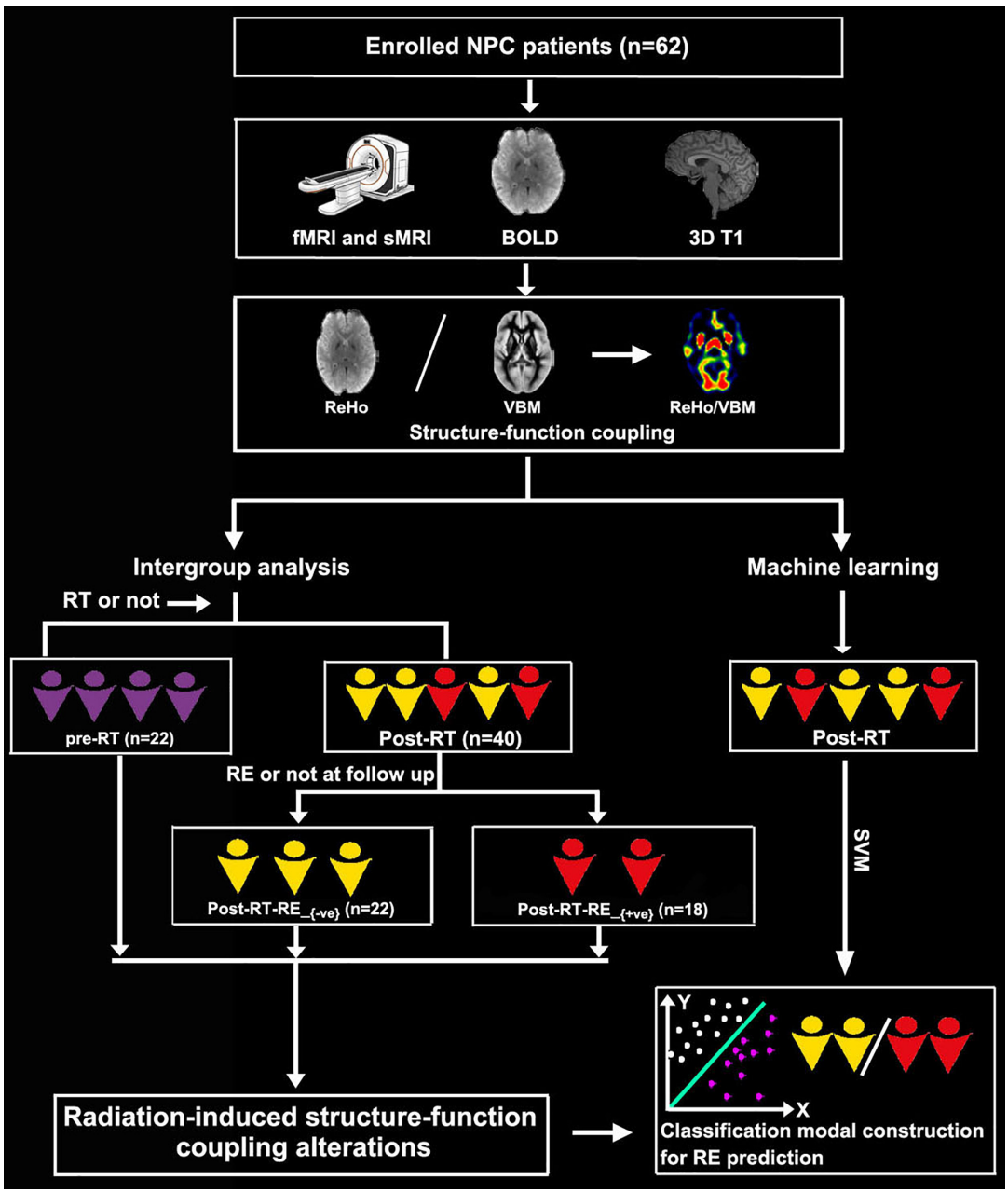

FIGURE 1 | Flowchart for grouping and analysis of the enrolled patients with NPC. NPC, nasopharyngeal carcinoma; fMRI, functional MRI; sMRI, structural MRI; BOLD, blood oxygenation-level dependent; RT, radiotherapy; RE, radiation encephalopathy; ReHo, regional homogeneity; VBM, voxel-based morphometry.

Feature Selection and Model Construction

Feature selection was strictly limited to the training set. During each fold of inner CV, two-sample *t*-tests between the Post-RT RE_{+ve} and Post-RT-RE_{-ve} groups were performed with a value of $p < 0.05$ to obtain a mask for the subsequent feature dimension reduction analysis. The least absolute shrinkage and selection operator (LASSO) was then used to select important features for improving classification efficiency. The selected features were then trained to build a classification model. The optimal classification model selected by the inner CV was tested on the test set. Classification accuracy, sensitivity, specificity, and area under the ROC curve (AUC) were calculated for performance evaluation. The classifier performance was accessed using a permutation test (repeated 1,000 times).

Statistical Analysis

Clinical Data Analysis

Several statistics were used to describe different data types. Frequencies were used to describe qualitative data. Means and standard deviations were used to describe quantitative clinical

TABLE 1 | Clinical parameters.

Clinical features	Pre-RT group (n = 22)	Post-RT-RE$_{-ve}$ group (n = 22)	Post-RT-RE$_{+ve}$ group (n = 18)	P value
Sex, n				
Female	4	6	4	0.927
Male	18	16	14	
Age (years), mean ± SD	43.82 ± 8.40	43.91 ± 10.27	45.28 ± 9.63	0.867
Clinical staging				
I/II, n	8	5	6	0.592
III/IV, n	14	17	12	
RT technology				
IMRT, n	NA	19	12	0.138
2D-CRT, n	NA	3	6	
Time intervals between RT and fMRI examinations (month)		10.77 ± 9.74	17.00 ± 17.61	0.192
Maximum dosage of RT for temporal lobes (Gy)				
Right	NA	66.14 ± 8.31#	66.54 ± 9.06*	0.911
Left	NA	69.49 ± 5.87#	64.41 ± 7.71*	0.073
The location of RE				
Right, n	NA	NA	3 (16.7)	NA
Left, n	NA	NA	6 (33.3)	
Bilateral, n	NA	NA	9 (50.0)	

*NA denotes not available. #Denotes radiation dose of three patients were not available. *Denotes radiation dose of 10 patients were not available.*

data with a Gaussian distribution, and medians and interquartile ranges were used to describe non-normally distributed data. A chi-square test was used to examine intergroup differences in clinical stage, sex, and RT technique, and a one-way analysis of variance was used to detect intergroup differences in age. For the post-RT subgroups, a two-sample t-test was used to examine intergroup differences in maximum temporal lobe RT dosage and the time interval between RT and fMRI examination. For all analyses, $p < 0.05$ was considered significant.

Regional Homogeneity/Voxel-Based Morphometry Analysis

To evaluate intergroup differences in the structure–function coupling, all voxel-wise contrasts of the smoothed ReHo/VBM maps were performed using the statistical analysis module in the DPABI toolbox (see text footnote 3). Specifically, a two-sample t-test was applied to examine intergroup differences in ReHo/VBM using pairwise comparisons, with sex and age considered nuisance covariates. We used a two-tailed false-discovery rate (FDR) correction ($p < 0.01$) for multiple intergroup comparisons. In order to uncover the possible inter-group differences between the two subgroups (post-RT-RE$_{+ve}$ and post-RT-RE$_{-ve}$) and reveal the candidate neural mechanism of structure–function decoupling in RBI, alphasim correction with a threshold of $p < 0.001$ at the voxel level and $p < 0.01$ at the cluster level was used if the intergroup comparison results could not be corrected using the FDR method. To examine the relationship between ReHo/VBM alterations and radiation dose to the ipsilateral temporal lobe, we performed a voxel-wise Pearson's correlation between the ReHo/VBM value and the maximum radiation dose administration confined to the bilateral temporal lobes ($p < 0.05$, FDR corrected).

RESULTS

Clinical Data

A total of 62 patients with NPC were included, comprising 48 male and 14 female patients. Age ranged from 14 to 63 years, with a mean age of 44.27 years. The tumor stage ranged from T1N0M0 to T4N2M0. No significant differences in age ($p = 0.867$), sex ($p = 0.927$), or clinical stage ($p = 0.592$) were observed among the pre-RT, post-RT-RE$_{-ve}$, and post-RT-RE$_{+ve}$ groups. In the post-RT group, we found no significant differences between the post-RT-RE$_{-ve}$ and post-RT-RE$_{+ve}$ subgroups in the time interval between RT and fMRI examination ($p = 0.192$), RT technique ($p = 0.138$), or maximum dosage of RT (MDRT) to the right ($p = 0.911$) and left ($p = 0.073$) temporal lobes. In the post-RT-RE$_{+ve}$ group, brain necrotic lesions in the left, right, and bilateral temporal lobes were detected in six, three, and nine patients, respectively (**Table 1**).

Regional Homogeneity/Voxel-Based Morphometry Coupling Analysis

Compared with the pre-RT group, patients in the post-RT-RE$_{-ve}$ group showed higher ReHo/VBM coupling values in the substantia nigra (SN) and lower values in the brain stem (e.g., midbrain tegmentum and pons), the anterior lobe and vermis of the cerebellum, the bilateral medial temporal lobes (MTLs; hippocampus/parahippocampal gyrus), the bilateral insula, and the right precentral and postcentral gyri ($p < 0.05$, FDR corrected; **Figure 2**). Compared with the pre-RT group, patients in the post-RT-RE$_{+ve}$ group displayed lower ReHo/VBM coupling values in the anterior lobe and vermis of the cerebellum, the bilateral MTL, midbrain tegmentum, the medial prefrontal cortex (MPFC), the bilateral insula, the left IPL, and the right precentral and postcentral gyri ($p < 0.01$, FDR corrected;

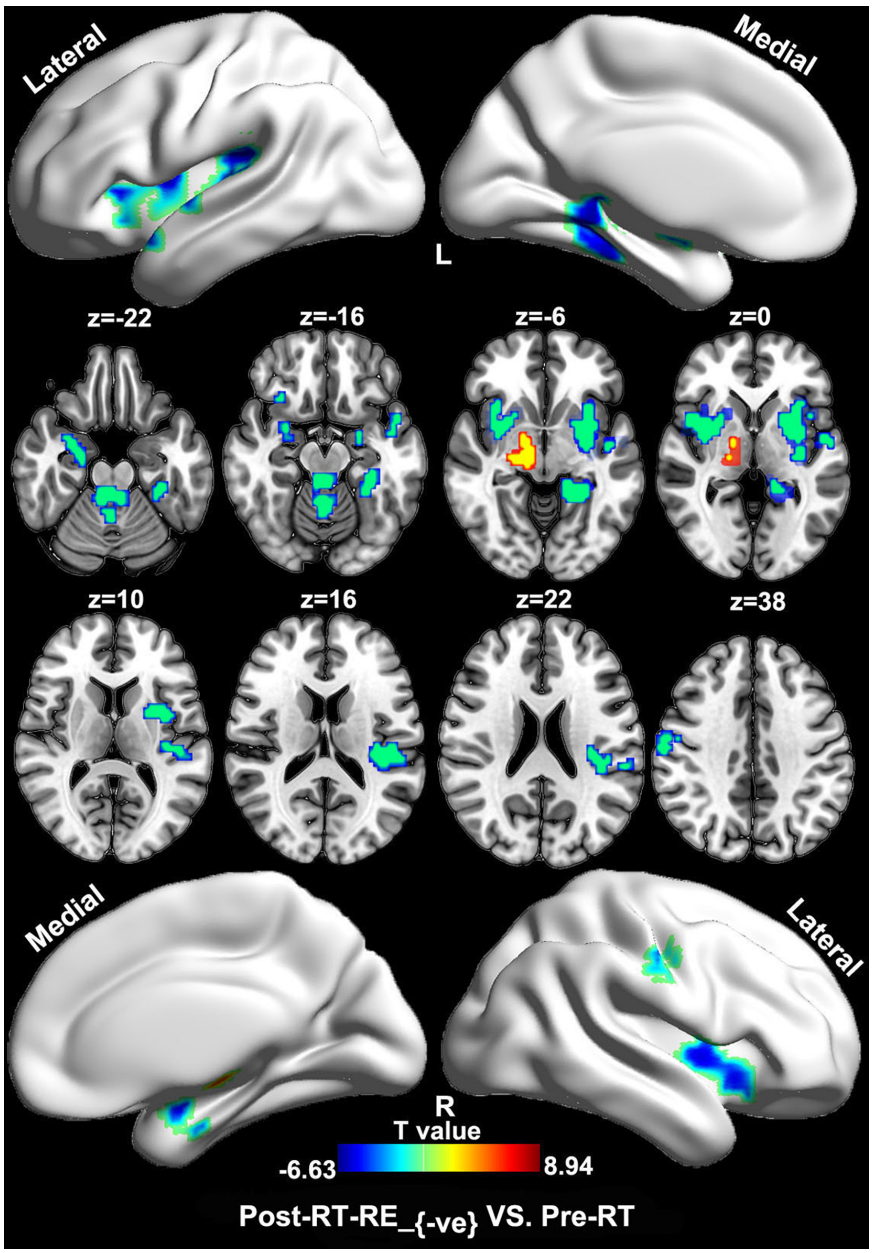

FIGURE 2 | Between-group differences in ReHo/VBM (pre-RT vs. post-RT-RE$_{-ve}$). Compared with the pre-RT group, patients in the post-RT-RE$_{-ve}$ group showed increased ReHo/VBM coupling values in SN and decreased values in brainstem, the cerebellum anterior lobe and vermis, the bilateral hippocampus/parahippocampal gyrus, the bilateral insula, and the right precentral as well as the postcentral gyrus ($p < 0.05$, FDR corrected).

Figure 3) and higher ReHo/VBM coupling values in the right SN and the bilateral thalamus and putamen ($p < 0.01$, FDR corrected; **Figure 3**). Compared with the post-RT-RE$_{-ve}$ group, patients in the post-RT-RE$_{+ve}$ group showed significantly higher ReHo/VBM coupling values in the right superior temporal gyrus (STG; $p < 0.001$, alphasim corrected; **Supplementary Figure 1**).

Correlation Analysis

In the post-RT group (which includes the post-RT-RE$_{-ve}$ and post-RT-RE$_{+ve}$ subgroups), significant negative correlations were observed between MDRT to the ipsilateral temporal lobe and ReHo/VBM coupling values in the ipsilateral middle temporal gyri (MTGs; **Supplementary Figure 2**).

Support Vector Machine Analysis

In the classification model construction, we observed that ReHo/VBM coupling values in several cortical brain regions (e.g., the bilateral STG, the bilateral precentral and postcentral gyri, the paracentral lobules, the right precuneus and IPL, the right MPFC, and the left SN) differentiated patients with and without RE, with

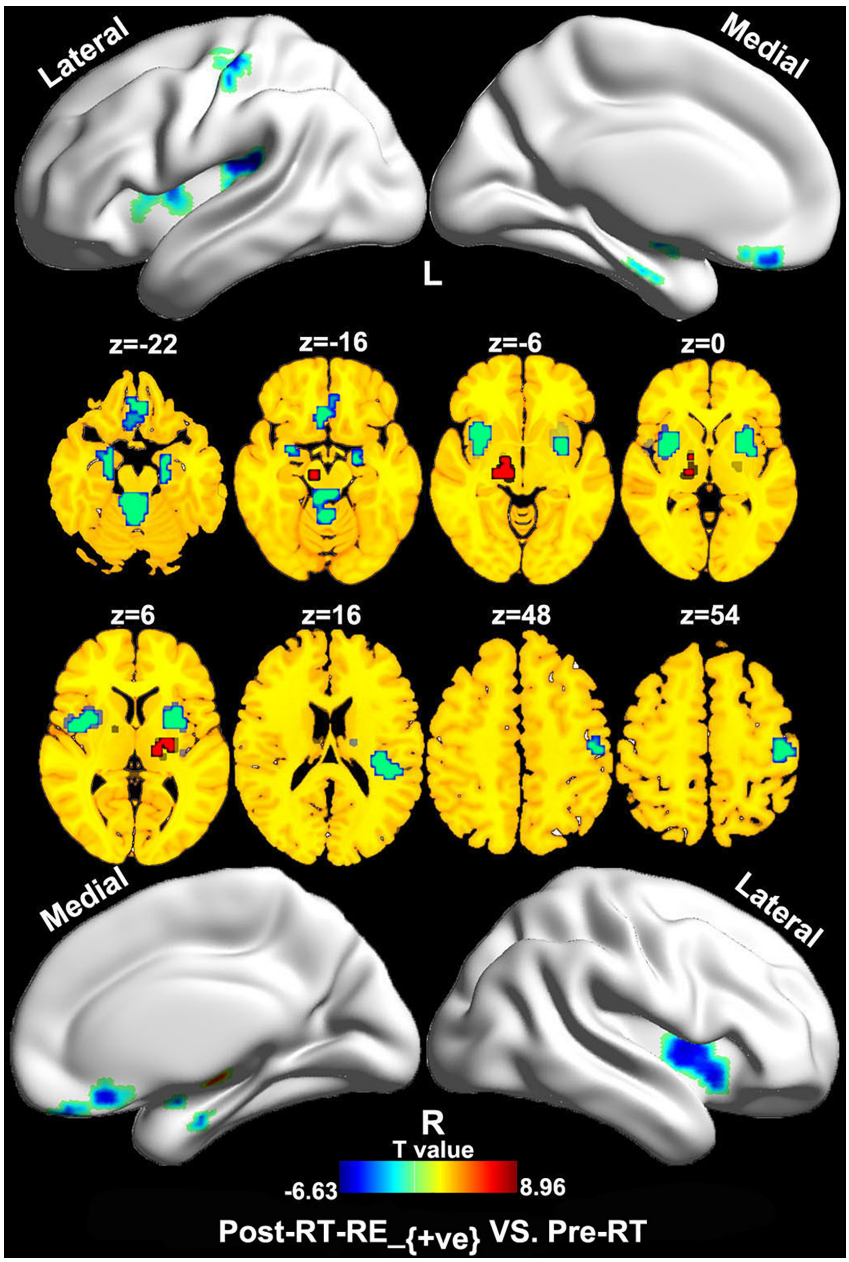

FIGURE 3 | Between-group differences in ReHo/VBM (pre-RT vs. post-RT-RE$_{+ve}$). Compared with the pre-RT group, patients in the post-RT-RE$_{+ve}$ group displayed decreased ReHo/VBM coupling values in the cerebellum anterior lobe and vermis, the bilateral MTL, the midbrain tegmentum, the MPFC, the bilateral insula, the left inferior parietal lobule, and the right precentral and postcentral gyrus ($p < 0.05$, FDR corrected). Meanwhile, these patients also showed increased ReHo/VBM coupling values in the right SN, the bilateral thalamus, and the putamen ($p < 0.05$, FDR corrected).

an AUC, accuracy, sensitivity, and specificity of 0.92, 85.1, 85.8, and 85.7% in the training set; and 0.94, 88.0, 85.0, and 90.0% in the test set, respectively (**Figure 4**).

DISCUSSION

This is the first study using ReHo/VBM to detect the effects of RT on structure–function coupling in normal-appearing GM of patients with NPC. Several brain regions with structure–function decoupling were observed within and outside the radiation field, which suggested that RBI is a multisystem disease that involves the dysfunction of regional structure and functional coordination in both near-end (nearby or in the path of irradiation) and far-end brain regions. Our finding of a negative correlation between MDRT to the ipsilateral temporal lobe and ReHo/VBM value in the ipsilateral MTG indicated that the alteration in brain structure–function coupling was primarily induced by

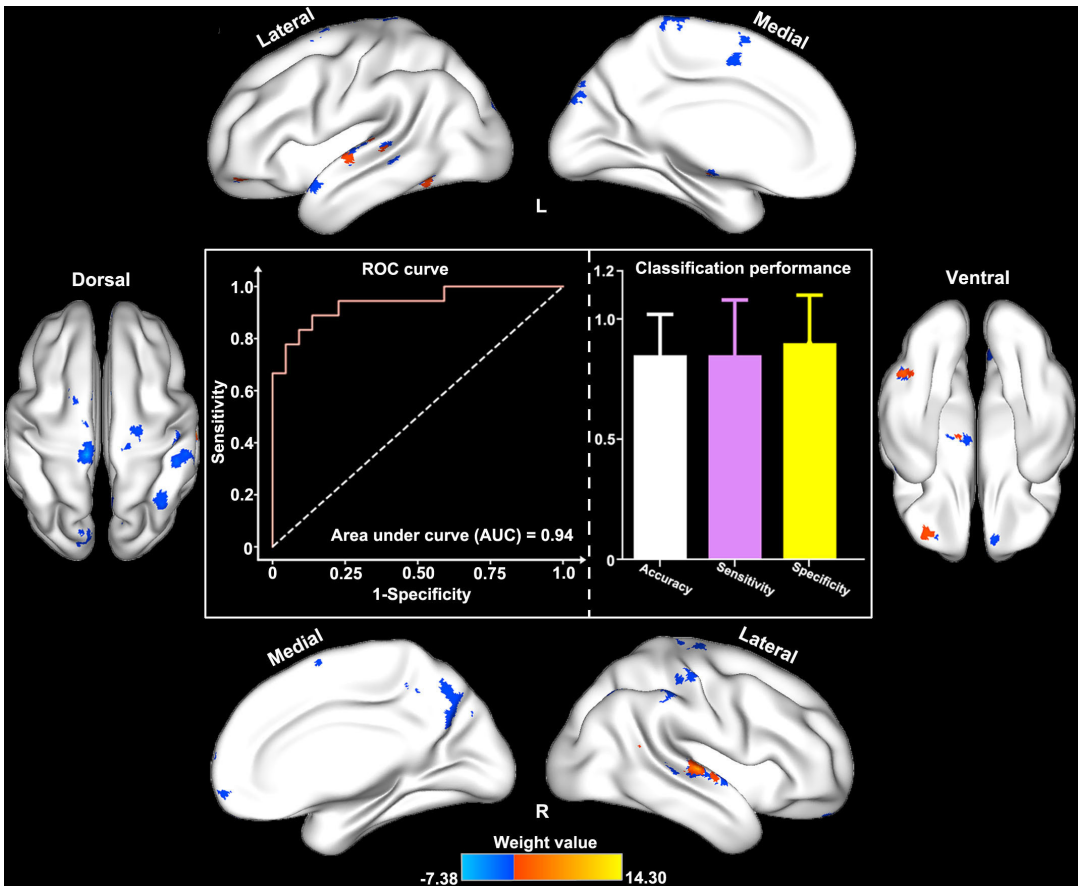

FIGURE 4 | Classification performance of structure–function decoupling in the prediction of RE. ReHo/VBM coupling values in a series of cortical brain regions (e.g., the bilateral STG and MTG, the bilateral pre/postcentral gyri, the paracentral lobules, the right precuneus and inferior parietal lobule, the right MPFC, and the left SN) differentiated patients with and without RE with the area under the curve, accuracy, sensitivity, and specificity of 0.94, 88.0, 85.0, and 90.0%, respectively.

RT. Notably, we found the structure–function decoupling in brain regions constituting the sensorimotor system, and the default mode network (DMN) exhibited impressive classification performance in the proposed model, which indicated that structure–function decoupling in these functional systems plays a crucial role in the identification of RE.

In this study, a ReHo/VBM ratio was adopted to characterize the coupling between the functional response and GM volume in the brain. For an individual, the voxel-wise ReHo/VBM ratio measures the amount of regional functional demand per unit of regional GM morphological changes, which could reflect the structure–function coupling for a specific voxel or region (Zhu et al., 2017). Therefore, the voxel-wise ReHo/VBM ratio could be used to identify alterations in the structure–function coupling in patients with NPC, followed by RT, which cannot be obtained by the separate ReHo or VBM analysis.

Compared with the pre-RT group, patients in the post-RT group (e.g., post-RT-RE$_{-ve}$ and post-RT-RE$_{+ve}$ subgroups) showed lower ReHo/VBM values in the bilateral MTL, the midbrain tegmentum, and the bilateral insula. The MTLs are responsible for learning and memory consolidation (Wittenberg and Tsien, 2002; Squire et al., 2004). Thus, structure–function decoupling in this area would likely lead to cognitive impairment, which is supported by a recent report of radiation-induced poor short-term memory in patients with NPC (Hsiao et al., 2010). The midbrain tegmentum plays an important role in visceral (e.g., cardiovascular control) and movement functions, sleeping rhythm, and pain modulation (Caminero and Cascella, 2021). Indeed, radiation-induced cardiovascular autonomic impairment (as evidenced by lower cardiovascular autonomic parameters and scores) and sleep disturbances were well-documented in patients with NPC during RT in previous studies (Huang et al., 2013; Qin et al., 2015). It is tempting to speculate that our findings of disrupted structure–function coupling in the midbrain may be central adaptive alterations secondary to the impaired visceral function and sleeping rhythm. Our findings of structure–function decoupling in the bilateral insula and midbrain tegmentum [covering the periaqueductal gray matter (PAG)] may be related to the abnormal encoding of pain intensity, impaired inhibition of nociceptive inputs, and augmented pain perception (Ossipov et al., 2014; Watson, 2016; Zhang et al., 2020b). In fact, chronic headache and oral and neuropathic pain are common clinical symptoms in patients with RT-induced injury (Gu et al., 2014; Hu et al., 2018), and we speculate that our findings of altered

ReHo/VBM in the insula and PAG may be a central response to RT-induced peripheral nociceptive stimuli. Unfortunately, the detailed data related to cognition, autonomic nervous system (ANS) function, sleep quality, as well as pain rating were not available for the patients with NPC in this study. The relationship between altered ReHo/VBM and the evaluation of data in cognition, ANS, sleep, and pain in patients with NPC after RT should be explored in future studies.

Compared with the pre-RT group, patients in the post-RT group showed significantly lower ReHo/VBM values in the precentral and postcentral gyri, the cerebellum, and the brainstem and significantly higher ReHo/VBM values in the SN, the putamen, and the thalamus. The observed structure–function decoupling in the precentral and postcentral gyri, the cerebellum, and the brainstem is consistent with previous neuroimaging studies that showed increased ReHo in the postcentral gyrus, decreased ReHo and cortical thickness in the precentral and postcentral gyri and the brainstem, and impaired functional connections between the cerebellum and the sensorimotor network (Ma et al., 2016; Lin et al., 2017; Zhang et al., 2020a), which indicates the impairment of sensorimotor function. Anatomically, the precentral and postcentral gyri are the highest regulation centers of the descending motor system and ascending somatosensory pathway, with extensive cortical–brainstem–cerebellum connections *via* ascending and descending projections (Lin et al., 2017; Zhang et al., 2021). During RT of NPC, the cerebellum and the brainstem are included in the radiation field and are exposed to a high dose of radiation. We speculate that the structure–function decoupling in the sensorimotor system may be secondary to radiation-related brainstem and cerebellum injury. In contrast to the decreased changing pattern of ReHo/VBM values in the pre-/post-central gyri and the cerebellum, our finding of increased ReHo/VBM values, followed by RT, in the SN, the putamen, and the thalamus is of particular interest. Considering that the SN-striatum-thalamus (SST) pathway and the descending motor system function together physiologically to perform a voluntary movement (Davis et al., 2015; Zhang et al., 2020b), it is tempting to speculate that the enhanced structure–function coupling in the SST pathway compensates for the impaired motor function caused by the aforementioned structure–function decoupling in the primary motor cortex. The SN, the putamen, and the thalamus are interconnected through the facilitation or inhibition of dopaminergic neurotransmitter release to perform a multitude of functions, such as motor planning and rewarding processing (Davis et al., 2015; Selemon and Begovic, 2020). Recent animal studies have reported that dopaminergic neurons are easily damaged by RT *via* direct particle strikes, oxidative stress, and microglial activation (Joseph et al., 2000; Rabin et al., 2004; Koike et al., 2005; Davis et al., 2015). As such, to maintain motor function as much as possible in patients with NPC, the increasing functional need of the SST pathway for voluntary movement and the RT-induced decrease in dopaminergic neurons may be two important factors that contribute to enhanced structure–function coupling in the SST pathway. However, further investigations on the sensorimotor system and the SST pathway with neuroimaging data, detailed neuro-electrophysiological data, and behavior tests are required to confirm this notion.

During the process of SVM model construction, ReHo/VBM values in several brain regions, such as the precentral and postcentral gyri, the precuneus, the IPL, and the MPFC, showed an excellent classification performance, which indicated that structure–function coupling alterations in sensorimotor system and DMN-related brain regions play an important role in identifying patients who are likely to develop RE. These findings are consistent with recent functional MRI study findings (Zhang et al., 2021; Zhao et al., 2021), which indicated that the biological classification information obtained from the sensorimotor system, and DMN was stable and robust. Moreover, ReHo/VBM values in regions that receive dense radiation dose exposure (e.g., the MTL) contributed less to the prediction of RE. These findings suggest that RT-induced structure–function coupling alterations in the inferior part of the temporal lobes are relatively small and can be suppressed by more powerful alterations in the abovementioned two brain networks. However, the exact cause of such an unexpected finding is unclear. Off-target effects of RT on near-end brain regions (e.g., the MTL and the brainstem) that alter brain activity in far-end regions (e.g., the precentral and postcentral gyri) may be one explanation (Beera et al., 2018; Zhang et al., 2021). Our finding of impressive classification performance of structure–function coupling in the precentral and postcentral gyri, the IPL, and the MPFC suggests that more attention should be paid in future studies to the functional and/or structural alterations in far-end brain regions rather than those within the radiation fields.

Several limitations of this study should be addressed. First, although potential confounding factors, such as age, RT technique, TNM stage, chemotherapy regimen, and the main side of the nasopharyngeal tumor, were balanced across groups, our findings should be interpreted with caution because of the cross-sectional study design. These confounding factors should be controlled in future longitudinal studies. Second, the lack of histopathological confirmation of RE is another limitation of this study; however, brain biopsies of RE are currently not possible in clinical practice because of ethical reasons and non-negligible medical risks, such as cerebral hemorrhage. Third, detailed information regarding RT-induced alterations in psychological state, cognitive, auditory, and sensorimotor functions, pain rating, ANS function, sleep quality, and quality of life were not acquired, which weakens the interpretability of our findings. Fourth, some brain regions observed in this study were discussed together at the brain network level, such as the sensorimotor system, DMN, and SST pathway; however, these speculations should be validated by further brain network-based research and specific neural pathway studies. Fifth, as the time interval between RT and fMRI examinations varied, further studies with a series of RT time points are warranted to obtain the dynamic profile of radiation-induced structure–function coupling alterations in patients with NPC. Sixth, the lack of genetic and high-field (e.g., 7.0 T) MRI data limits the precision and depth of our study, and future imaging genetic studies with high-resolution MRI data and detailed genetic information were needed to uncover the genetic basis and candidate neural

mechanism underlying the radiation-induced laminar functional and structural alterations. In addition, the small sample size in this study may have lowered the statistical power, which may have resulted in overfitting, although we minimized this issue by using multiple comparison corrections and building an SVM model.

An independent dataset would provide a better/reliable metric of classifier performance, as compared to the nested stratified cross validation approach. This could be part of future studies etc.

CONCLUSION

Radiation-induced alterations in ReHo/VBM were observed in multiple brain regions that involved the bilateral MTL, the midbrain tegmentum, the bilateral insula, the sensorimotor network, and the SST pathway. Structure–function coupling alterations in the precentral and postcentral gyri and the DMN-related regions exhibited excellent performance in identifying patients who were likely to develop RE. These findings suggest that ReHo/VBM may be a novel and effective imaging metric that reflects the neural mechanism underlying RBI in patients with NPC.

DATA AVAILABILITY STATEMENT

The original contributions presented in this study are included in the article/**Supplementary Material**, further inquiries can be directed to the corresponding author.

ETHICS STATEMENT

The studies involving human participants were reviewed and approved by the Medical Research Ethics Committee of Xiangya Hospital, Central South University. The patients/participants provided their written informed consent to participate in this study.

AUTHOR CONTRIBUTIONS

Y-mZ, LL, Y-fK, and J-mG conceived and designed the experiments. Y-fK, Y-mZ, and HD analyzed the data. Y-mZ, LL, J-mG, Y-fK, L-zL, and R-tC contributed to materials and analysis tools. Y-mZ, Y-fK, R-tC, and HD wrote the manuscript. All authors read and approved the final manuscript.

FUNDING

This study was supported in part by the National Natural Science Foundation of China (Grant/Award No. 82001784), Youth Science Foundation of Xiangya Hospital (Grant/Award No. 2019Q16), Natural Science Foundation (Youth Science Foundation Project) of Hunan Province (Grant/Award No. 2021JJ41054), and China Postdoctoral Science Foundation (Grant No. 2021M692007).

ACKNOWLEDGMENTS

We thank all the study participants for their efforts and enthusiasm to our clinical research. We also thank Sarina Iwabuchi, Ph.D., from Liwen Bianji (Edanz) (www.liwenbianji.cn) for editing a draft of this manuscript.

SUPPLEMENTARY MATERIAL

The Supplementary Material for this article can be found online at: https://www.frontiersin.org/articles/10.3389/fnins.2022.915164/full#supplementary-material

REFERENCES

Anderson, C. T., Sheets, P. L., Kiritani, T., and Shepherd, G. M. (2010). Sublayer-specific microcircuits of corticospinal and corticostriatal neurons in motor cortex. *Nat. Neurosci.* 13, 739–744. doi: 10.1038/nn.2538

Beera, K. G., Li, Y. Q., Dazai, J., Stewart, J., Egan, S., Ahmed, M., et al. (2018). Altered brain morphology after focal radiation reveals impact of off-target effects: implications for white matter development and neurogenesis. *Neuro Oncol.* 20, 788–798. doi: 10.1093/neuonc/nox211

Caminero, F., and Cascella, M. (2021). "Neuroanatomy, mesencephalon midbrain," in *StatPearls*, ed. B. Abai (Treasure Island, FL: StatPearls Publishing).

Davis, C. M., DeCicco-Skinner, K. L., and Hienz, R. D. (2015). Deficits in Sustained Attention and Changes in Dopaminergic Protein Levels following Exposure to Proton Radiation Are Related to Basal Dopaminergic Function. *PLoS One* 10:e0144556. doi: 10.1371/journal.pone.0144556

Ding, Z., Zhang, H., Lv, X. F., Xie, F., Liu, L., Qiu, S., et al. (2018). Radiation-induced brain structural and functional abnormalities in presymptomatic phase and outcome prediction. *Hum. Brain Mapp.* 39, 407–427. doi: 10.1002/hbm.23852

Feng, M., Huang, Y., Fan, X., Xu, P., Lang, J., and Wang, D. (2018). Prognostic variables for temporal lobe injury after intensity modulated-radiotherapy of nasopharyngeal carcinoma. *Cancer Med.* 7, 557–564. doi: 10.1002/cam4.1291

Gu, B., Yang, Z., Huang, S., Xiao, S., Zhang, B., Yang, L., et al. (2014). Radiation-induced brachial plexus injury after radiotherapy for nasopharyngeal carcinoma. *JPN J. Clin. Oncol.* 44, 736–742. doi: 10.1093/jjco/hyu062

Gu, Z., Jamison, K. W., Sabuncu, M. R., and Kuceyeski, A. (2021). Heritability and interindividual variability of regional structure-function coupling. *Nat. Commun.* 12:4894. doi: 10.1038/s41467-021-25184-4

Hall, J., Thomas, K. L., and Everitt, B. J. (2001). Cellular imaging of zif268 expression in the hippocampus and amygdala during contextual and cued fear memory retrieval: selective activation of hippocampal CA1 neurons during the recall of contextual memories. *J. Neurosci.* 21, 2186–2193. doi: 10.1523/JNEUROSCI.21-06-02186.2001

Hermundstad, A. M., Bassett, D. S., Brown, K. S., Aminoff, E. M., Clewett, D., Freeman, S., et al. (2013). Structural foundations of resting-state and task-based functional connectivity in the human brain. *Proc. Natl. Acad. Sci. U. S. A.* 110, 6169–6174. doi: 10.1073/pnas.1219562110

Honey, C. J., Sporns, O., Cammoun, L., Gigandet, X., Thiran, J. P., Meuli, R., et al. (2009). Predicting human resting-state functional connectivity from structural connectivity. *Proc. Natl. Acad. Sci. U. S. A.* 106, 2035–2040. doi: 10.1073/pnas.0811168106

Hsiao, K. Y., Yeh, S. A., Chang, C. C., Tsai, P. C., Wu, J. M., and Gau, J. S. (2010). Cognitive function before and after intensity-modulated radiation therapy in patients with nasopharyngeal carcinoma: a prospective study.

Int. J. Radiat. Oncol. Biol. Phys. 77, 722–726. doi: 10.1016/j.ijrobp.2009.06.080

Hu, W., Chen, L., Wang, C., Guo, L., Hua, X., Cai, Y., et al. (2018). Standardized nursing and therapeutic effect of oxycontin on oral mucosal pain in nasopharyngeal carcinoma patients. *J. Cancer Res. Ther.* 14, 1594–1599. doi: 10.4103/jcrt.JCRT_551_18

Huang, C. C., Huang, T. L., Hsu, H. C., Chen, H. C., Lin, H. C., Chien, C. Y., et al. (2013). Long-term effects of neck irradiation on cardiovascular autonomic function: a study in nasopharyngeal carcinoma patients after radiotherapy. *Muscle Nerve* 47, 344–350. doi: 10.1002/mus.23530

Joseph, J. A., Shukitt-Hale, B., McEwen, J., and Rabin, B. M. (2000). CNS-induced deficits of heavy particle irradiation in space: the aging connection. *Adv. Space Res.* 25, 2057–2064. doi: 10.1016/s0273-1177(99)01013-3

Koike, Y., Frey, M. A., Sahiar, F., Dodge, R., and Mohler, S. (2005). Effects of HZE particle on the nigrostriatal dopaminergic system in a future Mars mission. *Acta Astronaut.* 56, 367–378. doi: 10.1016/j.actaastro.2004.05.068

Levy, S., Lavzin, M., Benisty, H., Ghanayim, A., Dubin, U., Achvat, S., et al. (2020). Cell-Type-Specific Outcome Representation in the Primary Motor Cortex. *Neuron* 107:e959. doi: 10.1016/j.neuron.2020.06.006

Lin, J., Lv, X., Niu, M., Liu, L., Chen, J., Xie, F., et al. (2017). Radiation-induced abnormal cortical thickness in patients with nasopharyngeal carcinoma after radiotherapy. *Neuroimage Clin.* 14, 610–621. doi: 10.1016/j.nicl.2017.02.025

Lv, X. F., Zheng, X. L., Zhang, W. D., Liu, L. Z., Zhang, Y. M., Chen, M. Y., et al. (2014). Radiation-induced changes in normal-appearing gray matter in patients with nasopharyngeal carcinoma: a magnetic resonance imaging voxel-based morphometry study. *Neuroradiology* 56, 423–430. doi: 10.1007/s00234-014-1338-y

Ma, Q., Wu, D., Zeng, L. L., Shen, H., Hu, D., and Qiu, S. (2016). Radiation-induced functional connectivity alterations in nasopharyngeal carcinoma patients with radiotherapy. *Medicine* 95:e4275. doi: 10.1097/MD.0000000000004275

Ma, Q., Zeng, L. L., Qin, J., Luo, Z., Su, J., Wu, D., et al. (2017). Radiation-induced cerebellar-cerebral functional connectivity alterations in nasopharyngeal carcinoma patients. *Neuroreport* 28, 705–711. doi: 10.1097/WNR.0000000000000813

Medaglia, J. D., Huang, W., Karuza, E. A., Kelkar, A., Thompson-Schill, S. L., Ribeiro, A., et al. (2018). Functional Alignment with Anatomical Networks is Associated with Cognitive Flexibility. *Nat. Hum. Behav.* 2, 156–164. doi: 10.1038/s41562-017-0260-9

Ossipov, M. H., Morimura, K., and Porreca, F. (2014). Descending pain modulation and chronification of pain. *Curr. Opin. Support Palliat. Care* 8, 143–151. doi: 10.1097/SPC.0000000000000055

Pedregosa, F., Varoquaux, G., Gramfort, A., Michel, V., Thirion, B., Grisel, O., et al. (2011). Scikit-learn: machine learning in Python. *J. Mach. Learn. Res.* 12, 2825–2830.

Qin, L., Mo, Y. L., Li, L., Wei, Z. J., Zhu, X. D., Yin, X., et al. (2015). Sleep characteristics and psychological symptoms in patients with locally advanced nasopharyngeal carcinoma before and after intensity-modulated radiotherapy and concurrent chemotherapy. *Psychol. Health Med.* 20, 662–669. doi: 10.1080/13548506.2014.967703

Qiu, Y., Guo, Z., Han, L., Yang, Y., Li, J., Liu, S., et al. (2018). Network-level dysconnectivity in patients with nasopharyngeal carcinoma (NPC) early post-radiotherapy: longitudinal resting state fMRI study. *Brain Imaging Behav.* 12, 1279–1289. doi: 10.1007/s11682-017-9801-0

Rabin, B. M., Joseph, J. A., and Shukitt-Hale, B. (2004). Heavy particle irradiation, neurochemistry and behavior: thresholds, dose-response curves and recovery of function. *Adv. Space Res.* 33, 1330–1333. doi: 10.1016/j.asr.2003.09.051

Selemon, L. D., and Begovic, A. (2020). Reduced Midbrain Dopamine Neuron Number in the Adult Non-human Primate Brain after Fetal Radiation Exposure. *Neuroscience* 442, 193–201. doi: 10.1016/j.neuroscience.2020.07.005

Shen, K., Bezgin, G., Hutchison, R. M., Gati, J. S., Menon, R. S., Everling, S., et al. (2012). Information processing architecture of functionally defined clusters in the macaque cortex. *J. Neurosci.* 32, 17465–17476. doi: 10.1523/JNEUROSCI.2709-12.2012

Squire, L. R., Stark, C. E., and Clark, R. E. (2004). The medial temporal lobe. *Annu. Rev. Neurosci.* 27, 279–306. doi: 10.1146/annurev.neuro.27.070203.144130

Tang, Y., Luo, D., Rong, X., Shi, X., and Peng, Y. (2012). Psychological disorders, cognitive dysfunction and quality of life in nasopharyngeal carcinoma patients with radiation-induced brain injury. *PLoS One* 7:e36529. doi: 10.1371/journal.pone.0036529

Wang, Y., Cao, D. Y., Remeniuk, B., Krimmel, S., Seminowicz, D. A., and Zhang, M. (2017). Altered brain structure and function associated with sensory and affective components of classic trigeminal neuralgia. *Pain* 158, 1561–1570. doi: 10.1097/j.pain.0000000000000951

Watson, C. J. (2016). Insular balance of glutamatergic and GABAergic signaling modulates pain processing. *Pain* 157, 2194–2207. doi: 10.1097/j.pain.0000000000000615

Wittenberg, G. M., and Tsien, J. Z. (2002). An emerging molecular and cellular framework for memory processing by the hippocampus. *Trends Neurosci.* 25, 501–505. doi: 10.1016/s0166-2236(02)02231-2

Yang, X., Ren, H., and Fu, J. (2021). Treatment of Radiation-Induced Brain Necrosis. *Oxid. Med. Cell Longev.* 2021:4793517. doi: 10.1155/2021/4793517

Zang, Y., Jiang, T., Lu, Y., He, Y., and Tian, L. (2004). Regional homogeneity approach to fMRI data analysis. *Neuroimage* 22, 394–400. doi: 10.1016/j.neuroimage.2003.12.030

Zhang, B., Lian, Z., Zhong, L., Zhang, X., Dong, Y., Chen, Q., et al. (2020c). Machine-learning based MRI radiomics models for early detection of radiation-induced brain injury in nasopharyngeal carcinoma. *BMC Cancer* 20:502. doi: 10.1186/s12885-020-06957-4

Zhang, Y. M., Chen, M. N., Yi, X. P., Li, L., Gao, J. M., Zhang, J. L., et al. (2018). Cortical Surface Area Rather Than Cortical Thickness Potentially Differentiates Radiation Encephalopathy at Early Stage in Patients With Nasopharyngeal Carcinoma. *Front. Neurosci.* 12:599. doi: 10.3389/fnins.2018.00599

Zhang, Y. M., Gao, J. M., Zhou, H., Li, L., Liu, L. Z., Han, Z. D., et al. (2020a). Pre-symptomatic local brain activity and functional connectivity alterations in nasopharyngeal carcinoma patients who developed radiation encephalopathy following radiotherapy. *Brain Imaging Behav.* 14, 1964–1978. doi: 10.1007/s11682-019-00145-0

Zhang, Y. M., Kang, Y. F., Zeng, J. J., Li, L., Gao, J. M., Liu, L. Z., et al. (2021). Surface-Based Falff: a Potential Novel Biomarker for Prediction of Radiation Encephalopathy in Patients With Nasopharyngeal Carcinoma. *Front. Neurosci.* 15:692575. doi: 10.3389/fnins.2021.692575

Zhang, Y., Qu, M., Yi, X., Zhuo, P., Tang, J., Chen, X., et al. (2020b). Sensorimotor and pain-related alterations of the gray matter and white matter in Type 2 diabetic patients with peripheral neuropathy. *Hum. Brain Mapp.* 41, 710–725. doi: 10.1002/hbm.24834

Zhao, L. M., Kang, Y. F., Gao, J. M., Li, L., Chen, R. T., Zeng, J. J., et al. (2021). Functional Connectivity Density for Radiation Encephalopathy Prediction in Nasopharyngeal Carcinoma. *Front. Oncol.* 11:687127. doi: 10.3389/fonc.2021.687127

Zhou, G. Q., Yu, X. L., Chen, M., Guo, R., Lei, Y., Sun, Y., et al. (2013). Radiation-induced temporal lobe injury for nasopharyngeal carcinoma: a comparison of intensity-modulated radiotherapy and conventional two-dimensional radiotherapy. *PLoS One* 8:e67488. doi: 10.1371/journal.pone.0067488

Zhu, J., Zhuo, C., Xu, L., Liu, F., Qin, W., and Yu, C. (2017). Altered Coupling Between Resting-State Cerebral Blood Flow and Functional Connectivity in Schizophrenia. *Schizophr. Bull.* 43, 1363–1374. doi: 10.1093/schbul/sbx051

Conflict of Interest: The authors declare that the research was conducted in the absence of any commercial or financial relationships that could be construed as a potential conflict of interest.

Publisher's Note: All claims expressed in this article are solely those of the authors and do not necessarily represent those of their affiliated organizations, or those of the publisher, the editors and the reviewers. Any product that may be evaluated in this article, or claim that may be made by its manufacturer, is not guaranteed or endorsed by the publisher.

frontiers | Frontiers in Neuroscience

TYPE Original Research
PUBLISHED 19 July 2022
DOI 10.3389/fnins.2022.925698

OPEN ACCESS

EDITED BY
Chitresh Bhushan,
GE Global Research, United States

REVIEWED BY
Min Cai,
Fourth Military Medical University, China
Jiliang Fang,
China Academy of Chinese Medical Sciences, China
Xin Zhu,
The University of Aizu, Japan

*CORRESPONDENCE
Songhua Zhan
zhansonghua@sina.com
Wenli Tan
tanying2245@163.com

SPECIALTY SECTION
This article was submitted to Brain Imaging Methods, a section of the journal Frontiers in Neuroscience

RECEIVED 21 April 2022
ACCEPTED 27 June 2022
PUBLISHED 19 July 2022

CITATION
Chen Y, Kang Y, Luo S, Liu S, Wang B, Gong Z, Huang Y, Wang H, Zhan S and Tan W (2022) The cumulative therapeutic effect of acupuncture in patients with migraine without aura: Evidence from dynamic alterations of intrinsic brain activity and effective connectivity.
Front. Neurosci. 16:925698.
doi: 10.3389/fnins.2022.925698

The cumulative therapeutic effect of acupuncture in patients with migraine without aura: Evidence from dynamic alterations of intrinsic brain activity and effective connectivity

Yilei Chen[1], Yingjie Kang[1], Shilei Luo[1], Shanshan Liu[2], Bo Wang[2], Zhigang Gong[1], Yanwen Huang[1], Hui Wang[1], Songhua Zhan[1]* and Wenli Tan[1]*

[1]Department of Radiology, Shuguang Hospital Affiliated to Shanghai University of Traditional Chinese Medicine, Shanghai, China, [2]Department of Acupuncture and Moxibustion, Shuguang Hospital Affiliated to Shanghai University of Traditional Chinese Medicine, Shanghai, China

We explored the dynamic alterations of intrinsic brain activity and effective connectivity after acupuncture treatment to investigate the underlying neurological mechanism of acupuncture treatment in patients with migraine without aura (MwoA). The Functional Magnetic Resonance Imaging (fMRI) scans were separately obtained at baseline, after the first and 12th acupuncture sessions in 40 patients with MwoA. Compared with the healthy controls (HCs), patients with MwoA mostly showed a decreased dynamic amplitude of low-frequency fluctuation (dALFF) variability in the rostral ventromedial medulla (RVM), superior lobe of left cerebellum (Cerebellum_Crus1_L), right precuneus (PCUN.R), and so on. The decreased dALFF variability of RVM, Cerebellum_Crus1_L, and PCUN.R progressively recovered after the first and 12th acupuncture treatment sessions as compared to the baseline. There was gradually increased dynamic effective connectivity (DEC) variability in RVM outflow to the right middle frontal gyrus, left insula, right precentral gyrus, and right supramarginal gyrus, and gradually enhanced DEC variability from the right fusiform gyrus inflow to RVM. Furthermore, the gradually increased DEC variability was found from Cerebellum_Crus1_L outflow to the left middle occipital gyrus and the left precentral gyrus, from PCUN.R outflow to the right thalamus. These dALFF variabilities were positively correlated with the frequency of migraine attacks and negatively correlated with disease duration at baseline. The dynamic Granger causality analysis (GCA) coefficients of this DEC variability were positively correlated with Migraine-Specific Quality of Life Questionnaire scores and negatively correlated with the frequency of migraine attacks and visual analog scale (VAS) scores after 12th acupuncture sessions. Our results were analyzed by a longitudinal fMRI in the absence of a sham acupuncture

control group and provided insight into the dynamic alterations of brain activity and effective connectivity in patients with MwoA after acupuncture intervention. Acupuncture might relieve MwoA by increasing the effective connectivity of RVM, Cerebellum_Crus1_L, and PCUN.R to make up for the decreased dALFF variability in these brain areas.

KEYWORDS

migraine, Granger causality analysis, amplitude of low-frequency fluctuations, dynamic analysis, acupuncture

Introduction

Migraine is a prevalent primary headache disorder characterized by recurrent headache attacks, nausea or vomiting, and being sensitive to sound or light (Olesen et al., 2018). Migraine is a disabling and common neurological disorder with a 1-year prevalence of 12% in the general population (Schwedt et al., 2015), and prevalence in China is 9.3%, with a female to male ratio of about 2:1 (Yu et al., 2012). Migraine without aura (MwoA) is the most common type of migraine. Patients with migraine usually have frequent, severe, and disabling headache attacks, which cause an enormous individual and social burden (Leonardi et al., 2005). Migraine is typically treated by various pharmacological or non-pharmacological therapies to relieve pain or reduce migraine attacks. However, these methods may have limited efficacy and special patient populations. And some of them have shown adverse effects, such as weight gain, fatigue, sleep disturbance, gastrointestinal reaction, or medication overuse (Diener et al., 2015). Acupuncture, as one of the treatment modalities of Traditional Chinese Medicine (TCM), is widely used as a complementary and alternative treatment to prevent migraine attacks and relieve pain during a migraine in China. Acupuncture was recognized to migraine for its long-term prophylactic effect (Zhao et al., 2017; Xu et al., 2020). However, the mechanism of the cumulative impact of acupuncture treatment is currently unclear.

Recently, neuroimaging has provided new insight into understanding the central mechanism of acupuncture on migraine (Chang et al., 2021; Liu L. et al., 2021). Several Functional Magnetic Resonance Imaging (fMRI) studies have indicated that verum and sham acupuncture have different modulation effects on the amplitude of low-frequency fluctuation (ALFF) of the rostral ventromedial medulla (RVM)/trigeminocervical complex (TCC) in patients with migraine (Li et al., 2017b). Verum acupuncture elicited a more widespread and remarkable cerebral response, including the pain matrix, lateral and medial pain system, default mode network, and cognitive components of the pain processing system, compared to sham acupuncture (Zhao et al., 2014). Verum acupuncture could also normalize the abnormal network connectivity in the visual, default mode (DMN), sensorimotor, and frontal-parietal networks (Tu et al., 2020). Furthermore, it was demonstrated that acupuncture treatment could increase the functional connectivity (FC) of the right frontoparietal network (Li et al., 2017a). The connectivity of DMN was normalized after acupuncture intervention (Zou et al., 2019). Our previous studies demonstrated that acupuncture could improve the dysfunction of the cerebellum and activate the brain regions involved in the modulation of pain and emotion in patients with MwoA by the regional homogeneity (ReHo) analysis method (Liu S. et al., 2021). However, most of these studies above have focused on the static characterizations or traditional unidirectional FC of the brain. They have not explored the continuous effects of different periods of acupuncture. Brain activity is inherently dynamic (Bassett and Sporns, 2017). Recently, a number of studies have proposed that brain activity was dynamically changed over time, so dynamic ALFF was an effective tool to explore dynamic brain activity in healthy people (Liao et al., 2019). The dynamic ALFF method measured the variance of ALFF over time combining it with "sliding-window" approaches (Cui et al., 2020; Zhao et al., 2021). A tapered window, created by convolving a rectangle with a Gaussian, was used for segmenting extract time courses (Fu et al., 2021). The time-varying brain activity characterized by dynamic ALFF may underline the disruption of brain activity in various mental disorders (Fu et al., 2018), such as schizophrenia (Yang et al., 2019). Meanwhile, Granger causality analysis (GCA) is an fMRI-based directed connectivity analysis

Abbreviations: MwoA, migraine without aura; dALFF, dynamic amplitude of low-frequency fluctuation; GCA, dynamic Granger causality analysis; DEC, dynamic effective connectivity; ReHo, regional homogeneity; RVM, rostral ventromedial medulla; Cerebellum_Crus1_L, superior lobe of left cerebellum; IFGtriang.R, right inferior frontal gyrus, triangular part; DCG.R, right median cingulate and paracingulate gyri; PCUN.R, right precuneus; IPL.L, left inferior parietal, supramarginal and angular gyri; IOG.L, left inferior occipital gyrus; MFG.R, right middle frontal gyrus; INS.L, left insula; PreCG.R, right precentral gyrus; SMG.R, right supramarginal gyrus; FFG.R, right fusiform gyrus; MOG.L, left middle occipital gyrus; PreCG.L, left precentral gyrus; THA.R, right thalamus; MSQ, Migraine-Specific Quality of Life Questionnaire; VAS, visual analog scale; SDS, Self-Rating Depression Scale; TCM, Traditional Chinese Medicine; FC, functional connectivity; fMRI, Functional Magnetic Resonance Imaging; ROIs, region of interests; SD, standard deviation; healthy controls (HCs); GRF, Gaussian random field.

method to assess the causality between different brain regions, which can provide more information on connectivity analysis than unidirectional FC (Wei et al., 2020; Huang et al., 2021). To date, the dynamic characteristics of ALFF and GCA have rarely been investigated to monitor the effect of acupuncture in patients with migraine.

To prove the cumulative therapeutic effect of acupuncture and explore the central mechanism of continuous acupuncture treatment in patients with MWoA, we designed this prospective study. After obtaining the brain areas showing different dynamic ALFF between patients with MwoA and HCs, we observed the changes in dynamic ALFF in these brain areas during the different acupuncture intervention periods. Then, the seed-based dynamic GCA analysis was used to understand the causality among these brain areas, which would help ensure the critical brain areas when the new alternative therapy was developed.

Materials and methods

Participants

Forty patients with MwoA were enrolled from outpatient in the Department of Neurology or Acupuncture at Shuguang Hospital affiliated to the Shanghai University of Traditional Chinese Medicine. Thirty-six healthy controls (HCs), who were aged, education level matched with the patients, and right-handed, were recruited. These volunteers had never been diagnosed with head trauma, alcohol/drug abuse, and neurological or psychiatric disorders. All participants signed written informed consent. This trial was approved by the Ethics Committee of the Shuguang Hospital affiliated to Shanghai University of Traditional Chinese Medicine and was registered on www.chictr.org.cn (ChiCTR1900023105). The diagnosis of MWoA was established according to the International Classification of Headache Disorders, 3rd Edition ICHD-III criteria (Olesen et al., 2018). Inclusion criteria included that all patients: (1) were 18–65 years old and right-handed; (2) had two to eight times of migraine attacks during the past month; (3) had at least 6 months of migraine history; and (4) had no physical therapy and prophylactic headache medications during the past month, and had no psychoactive or vasoactive agents during the last 3 months. The exclusion criteria included the following: (1) suffered from other types of primary or secondary headache; (2) had a history of a brain tumor or head trauma; (3) had any other neurological or psychiatric disorder; (4) were pregnant or breast-feeding; (5) had the contraindications for MRI or acupuncture.

Study design

The total observation period for patients with MwoA in this study was 10 weeks. Weeks 1–4 were served as a baseline phase, and all patients recorded headache diaries during this phase. Weeks 5–10 were served as the intervention phase. During this phase, patients with MwoA were performed standard acupuncture treatment. All the patients kept recording their headache diaries. FMRI scans were administered before the first

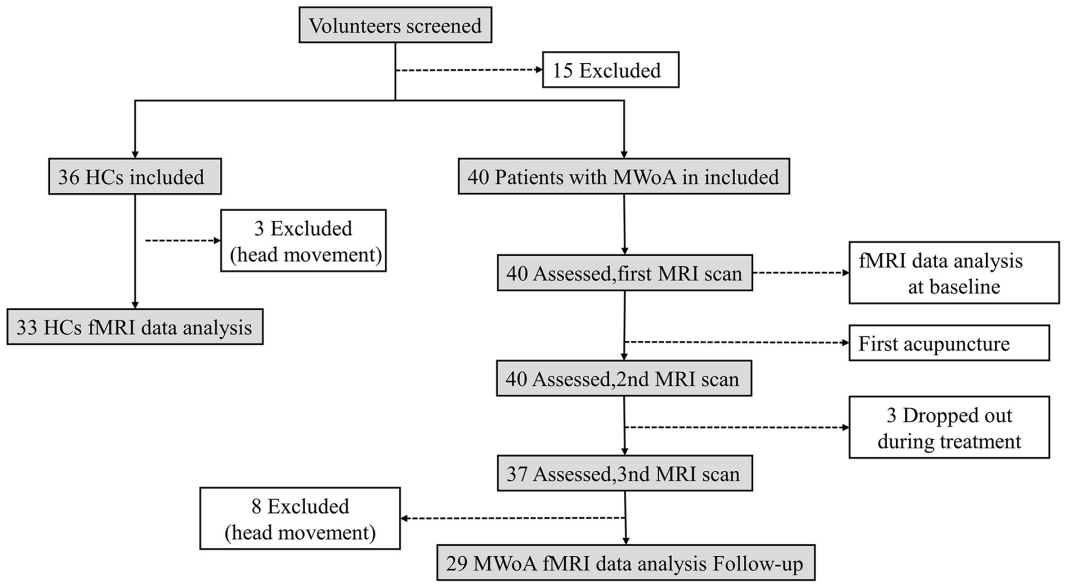

FIGURE 1
Flowchart displaying the screening, enrollment, and treatment. All abbreviations are defined in the Abbreviations section.

acupuncture session and immediately after the first and 12th acupuncture sessions for patients with MwoA (all fMRI scans were performed within 1 h before or after acupuncture). All patients with MwoA had been migraine-free for at least 72 h at the fMRI scans. The HCs group only received an fMRI scan at the baseline (**Figure 1**).

Acupuncture treatment

In our study, patients with MwoA were performed 12 sessions of acupuncture (twice a week, finished in 6 weeks), and every session lasted for 20 min. Acupoints were selected according to the standardized acupuncture protocol: Baihui (DU20), Taiyang (EX-HN5), bilateral Fengchi (GB20), Shuaigu (GB8), Xuanlu (GB5), Toulinqi (GB15), Hegu (LI4), and Taichong (LR3) (Chen et al., 2013; Zhao et al., 2017) (**Figure 2**). Two licensed acupuncturists (Wang B and Liu S, with 20 and 5 years of acupuncture experience, respectively) were responsible for all the acupuncture interventions. Sterile disposable acupuncture needles of 25–40 mm in length and 0.25 mm in diameter were inserted to achieve the sensation of deqi. Electrical stimulation was applied bilaterally at GB20 and GB8 at a frequency of 2 Hz and intensity ranging from 0.1 to 1.0 mA until the patient felt bearable. All participants agreed not to take any conventional medication for migraine during the study period. In case of severe pain, ibuprofen (as 300 mg extended-release capsules) was allowed as a rescue medication.

Clinical assessments

During the 6 weeks from the first fMRI scan to finishing all the acupuncture sessions, the frequency of migraine attacks (days/month), visual analog scale (VAS) (0–10 scale, 10 being the most intense imaginable pain), the Self-Rating Anxiety Scale (SAS), the Self-Rating Depression Scale (SDS), and the Migraine-Specific Quality of Life Questionnaire scores (MSQ) were assessed. Adverse events associated with acupuncture, including bleeding, subcutaneous bleeding, severe pain, fainting, and local infection, were recorded at each treatment.

Data acquisition

The MR scans were acquired on a 3T MRI scanner (uMR780 Platform, United Imaging Medical Systems, Shanghai, China) with a 12-channel flexible head coil at the MRI Center of Shuguang Hospital. The rest fMRI was obtained axially by a multislice gradient-echo echo-planar imaging (EPI) sequence, and the parameters were as follows: repetition time (TR) = 2,000 ms, echo time (TE) = 30 ms, flip angle = 90°, field of view = 240 mm × 240 mm, matrix = 64 × 64, 33 contiguous slices with 3.5 mm slice thickness, 240 time points. Structural images were acquired by a three-dimensional turbo fast echo (3D-TFE) sequence with a voxel size of 1 mm^3, and the parameters were as follows: TR = 7.2 ms, TE = 3.1 ms, slice thickness = 1.0 mm, flip angle = 10°, field of view = 256 mm × 256 mm, matrix = 256 × 256, 176 slices without an interslice gap. A cushion was placed into the coil to fix the head and reduce motion. The participants were instructed to keep still with eyes closed, relax but not fall asleep, and try not to think about anything.

Data preprocessing

The FMRI data preprocessing was performed by the DPABI software[1] in MATLAB. The preprocessing course consisted of the following steps: (1) the images of the first 10 time points were discarded, and the images of the remained 230 time points were used for data analysis; (2) slice timing correction; (3) head motion correction (the translation or rotation motion in any given data did not exceed 2.0 mm or 2.0°); (4) the co-registered functional images were spatially normalized to the Montreal Neurological Institute (MNI) space and resampled to 3-mm cubic voxels; (5) linear trend removal was performed to reduce the effect of low-frequency drifts; (6) nuisance covariates regression (the white matter signal, the cerebrospinal fluid signal, and 24 head motion parameters); (7) lintemporal band-pass filtering at a frequency band of 0.01–0.08 Hz. After the head motion control, 11 subjects (three HCs and eight patients with MwoA) were excluded.

Dynamic amplitude of low-frequency fluctuation analysis

The dynamic ALFF for each participant was performed by the DynamicBC (v2.2[2]) toolbox. Specifically, a temporal rectangular window was first chosen. Then, the ALFF values in each window were calculated. Window length was an essential parameter in resting-state dynamics computation. The "rule of thumb" in sliding-window length was that the minimum window length should be no less than 1/fmin (fmin = 0.01 Hz). Here, a window length of 50 TRs was considered as the optimal parameter to maintain the balance between capturing a rapidly shifting dynamic relationship and obtaining reliable estimates of the correlations between regions (Li et al., 2019; Cui et al., 2020). The sliding window was systematically shifted with a step size of five TRs (10 s) to calculate the dynamic amplitude

1 http://www.rfmri.org/

2 www.restfmri.net/forum/DynamicBC

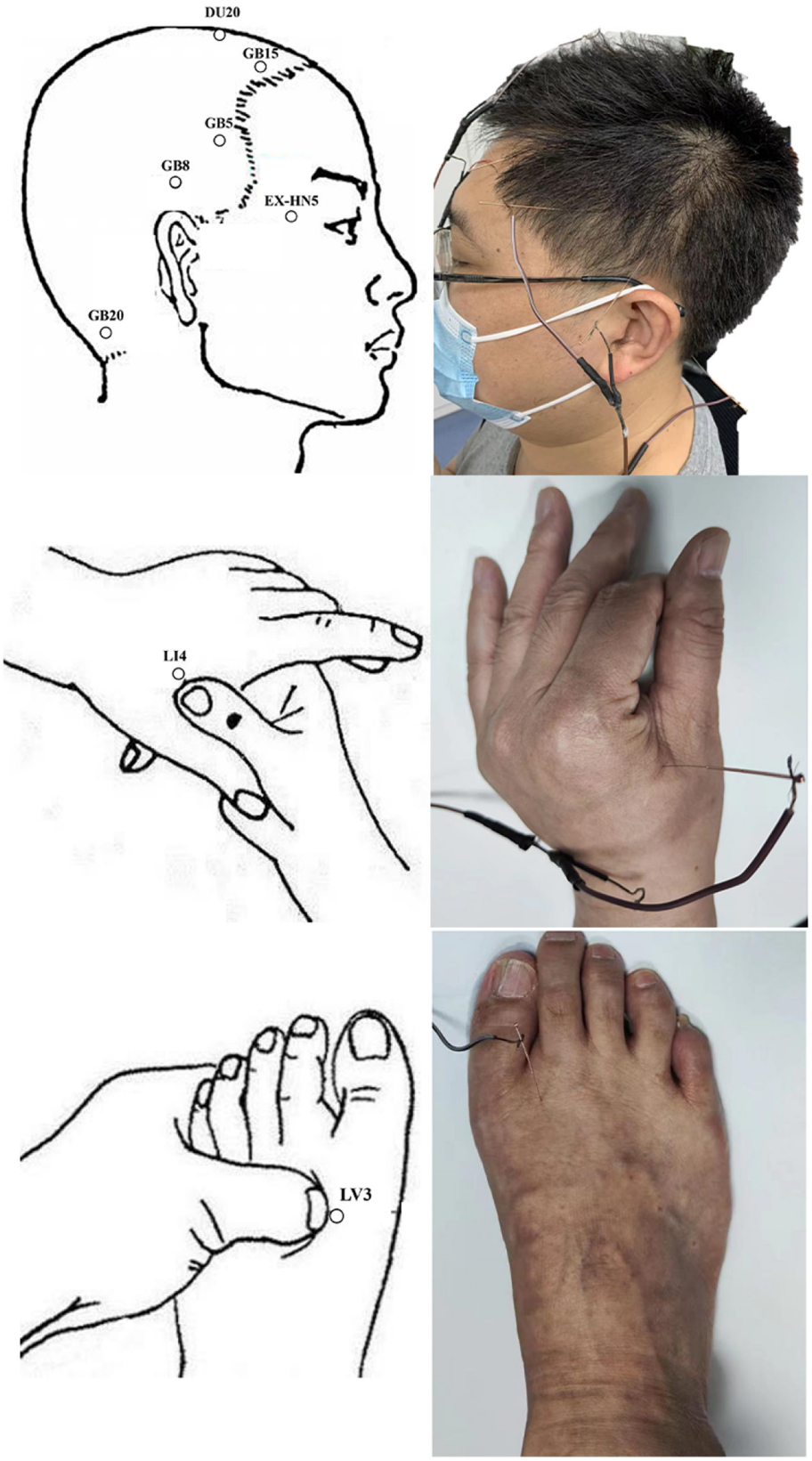

FIGURE 2
Diagram of electro-acupuncture treatment.

of low-frequency fluctuation (dALFF) of each participant. The preprocessed data of each individual were segmented into 37 windows, and the ALFF map was obtained for each sliding window. Subsequently, we measured the variance of these maps by the standard deviation (SD) and evaluated the temporal variability of dALFF across 37 windows. The dALFF variability of each voxel was further transformed into a *z*-score by subtracting the mean and being divided by the SD of global values. Finally, the mean normalized dALFF maps were spatially smoothed using an isotropic Gaussian kernel of 8 mm full-width at half-maximum.

Dynamic effective connectivity analysis

In this study, we performed seed-based dynamic Granger causality analysis (GCA) by the DynamicBC toolbox to detect the dynamic effective connectivity (DEC). The time series of each : region of interest (ROI) based on dALFF results was defined as the seed time series X, and the time course of voxels within the whole brain was defined as Y. A bivariate coefficient GCA to investigate the Granger causal influence between the per ROI and every voxel of the whole brain. A positive coefficient indicates that the activity in region X exerts a positive influence on the activity in region Y, whereas a negative coefficient indicated that the activity of region X exerted a negative effect on the activity of region Y. The dynamic GCA was estimated using the sliding window approach mentioned above, and the time series of each participant were also divided into 37 windows. Thus, for each participant, the averaged time course of the GCA coefficient of each ROI was extracted across 37 windows and concatenated to form a $2 \times W \times N$ matrix (where W denotes the number of windows and N denotes the number of ROIs). The DEC variability for each ROI was assessed with the SD of the averaged time course of the GCA coefficient across 37 windows. Finally, the dynamic GCA coefficient maps for all subjects were then converted to *z*-scores by Fisher *z*-transformation.

Statistical analyses

Demographic characteristics were evaluated between patients with MwoA and HCs. The differences between the two groups in age and education level were analyzed with a two-sample *t*-test; χ^2 test was used to analyze the difference in gender between the two groups. Two-sample *t*-tests or Mann–Whitney *U* test was used to compare the differences in the clinical variables between the two time points. $P < 0.05$ existed statistical difference.

Two-sample *t*-tests were performed to compare the difference in the dALFF variability between patients with MwoA at baseline and HCs within a gray matter mask with age, gender, education level, and head motion as covariates. The resultant T-maps were corrected for multiple comparisons correction by the Gaussian random field (GRF) theory (voxel $p < 0.001$, cluster $p < 0.05$, two-tailed).

To find the different effects of acupuncture during the different periods of treatment, we first performed repeated-measures one-way ANOVA to investigate the dALFF variability among the different periods. The SD value of each brain region with a significant difference between groups was extracted for statistical analysis in the SPSS version 25.0 (SPSS, Inc., Chicago, IL, United States), and *post hoc t*-tests were performed to detect the differences in dALFF variability between two periods (corrected by false discovery rate, $P < 0.05$).

For group-level analyses on DEC of the ROIs, the SD values of Zx → y and Zy → x dynamic GCA coefficient maps were calculated for each group. These maps were entered into repeated-measures one-way ANOVA to determine the difference among the different periods with age, sex, and education level included as covariates. Multiple comparison correction was performed based on Gaussian random field theory (GRF, voxel wise $p < 0.001$, cluster-wise $p < 0.05$, two-tailed). *Post hoc t*-tests were performed to detect the differences in DEC variability between two periods (false discovery rate corrected, $P < 0.05$).

Finally, the SD value of the dALFF and DEC variability in regions with significant differences in each individual with MwoA was extracted. Based on these regions, the Pearson/Spearman correlation analysis was used to probe the correlation of alterations in dALFF and DEC variability to the clinical data of patients with MwoA. The significance was set at a threshold of $p < 0.05$.

Validation analyses

To validate the main findings of dALFF variability and DEC variability obtained from the sliding-window length of 50 TRs, we carried out auxiliary analyses with different sliding window lengths (30 and 80 TRs).

Results

Demographic and clinical characteristics at baseline

The demographic information and clinical characteristics of all the participants were presented in **Table 1**. There was no statistical difference in age ($p = 0.408$), education level ($p = 0.313$), and gender ($p = 0.490$) between patients with MwoA and HCs. The disease duration of the MwoA patients group was 16.21 ± 12.56 years, the frequency of migraine attacks was 5.14 ± 1.53 days, and the VAS score was 7.81 ± 1.39 (**Table 1**).

TABLE 1 Demographic and clinical characteristics of patients with migraine without aura and healthy controls at baseline.

Characteristics	Migraine patients at baseline ($n = 40$)	HCs ($n = 33$)	*P*-value
Age (years)	38.02 ± 9.79	33.26 ± 5.76	0.408
Gender (male/female)	6/34	7/26	0.490
Education (years)	15.02 ± 3.19	15.76 ± 1.76	0.313
Height (cm)	163.03 ± 6.05	165.12 ± 8.11	0.494
Weight (kg)	51.23 ± 6.23	53.89 ± 7.79	0.362
Disease duration (years)	16.21 ± 12.56	–	–
Frequency of migraine attack (days)	5.14 ± 1.53	–	–
VAS score	7.81 ± 1.39	–	–

Differences in dynamic amplitude of low-frequency fluctuation analysis between patients with migraine without aura at baseline and healthy controls

The brain areas with a statistical difference in dynamic ALFF variability are shown in Table 2. Compared with HCs, patients with MwoA at baseline showed decreased dALFF variability in the RVM, superior lobe of left cerebellum (Cerebellum_Crus1_L), right inferior frontal gyrus, triangular part (IFGtriang. R), right median cingulate, paracingulate gyri (DCG.R), right precuneus (PCUN.R), left Inferior parietal, supramarginal, and angular gyri (IPL.L). Conversely, patients with MwoA showed increased dALFF variability only in the left Inferior occipital gyrus (IOG.L) compared with HCs.

Clinical outcomes

After 12 sessions of acupuncture treatment, the frequency of migraine attacks and the VAS score were significantly lower than those at baseline ($p < 0.001$). The SAS scores, SDS scores, and MSQ scores (restrictive, preventive, and emotional functional subscales) were significantly improved ($p < 0.001$) (Table 3). There was no adverse event associated with acupuncture.

Dynamic amplitude of low-frequency fluctuation analysis during the different periods of treatment in patients with migraine without aura

The seven brain regions with a significant statistical difference in dynamic ALFF analysis above were extracted as the ROIs. According to the repeated-measures one-way ANOVA test, we found that the dALFF variability was significantly different in RVM, Cerebellum_Crus1_L, and PCUN.R. *Post hoc* tests revealed that the dALFF variability of patients with MwoA was significantly increased in the RVM after the first acupuncture session compared with that at the baseline, after all sessions of acupuncture compared with that at the baseline, and that after the first acupuncture session. The dALFF variability of the Cerebellum_Crus1_L and PCUN.R after all acupuncture sessions was significantly increased compared with that after the first acupuncture session. There were no statistical differences in the dALFF variability within the other ROIs (Figure 3).

Seed-based dynamic Granger causality analysis analysis during the different periods of treatment in patients with migraine without aura

The bivariate RVM-to-whole-brain dynamic GCA showed that the DEC variability from RVM outflow to the right middle frontal gyrus (MFG.R), the left insula (INS.L), the right precentral gyrus (PreCG.R), and the right supramarginal gyrus (SMG.R) were significantly enhanced in repeated-measures one-way ANOVA tests (Table 4). *Post hoc* tests revealed that the DEC variability from RVM outflow to INS.L and PreCG.R after the first acupuncture session were enhanced compared with that at baseline. The DEC variability from RVM outflow to MFG.R, INS.L, PreCG.R, and SMG.R was significantly

TABLE 2 Brain regions with increased and decreased dALFF variability in migraine compared with healthy controls at the baseline.

Contrast	Brain regions	Peak MNI (*x*-, *y*-, *z*-)			Voxels	*T* score
MwoA < HCs	RVM	0	−28	−46	45	−3.77
	Cerebellum_ Crus1_L	−30	−69	−30	32	−3.39
	IFGtriang.R	42	21	15	39	−4.67
	DCG.R	6	12	36	21	−5.16
	PCUN.R	9	−57	54	26	−4.80
	IPL.L	−36	−63	54	37	−4.45
MwoA > HCs	IOG.L	−51	−78	−6	46	3.29

Gaussian Random Field theory correction, voxel *P*-value < 0.001, cluster *P*-value < 0.05. All abbreviations are defined in the Abbreviations section.

TABLE 3 Clinical outcomes in patients with migraine without aura during the study period (n = 29).

Assessment points (weeks)	Frequency of migraine attack (days)	VAS score	SAS score	SDS score	MSQ score (restrictive subscale)	MSQ score (preventive subscale)	MSQ score (emotional subscale)	*P*-value
At baseline	5.14 ± 1.53	7.81 ± 1.39	46.04 ± 7.03	49.68 ± 8.29	58.24 ± 15.65	60.89 ± 21.27	63.46 ± 23.05	$P < 0.001$
At Treatment	1.85 ± 1.32	3.67 ± 1.20	38.41 ± 8.03	39.38 ± 9.87	80.33 ± 10.36	85.39 ± 13.22	87.67 ± 16.37	

All abbreviations are defined in the Abbreviations section.

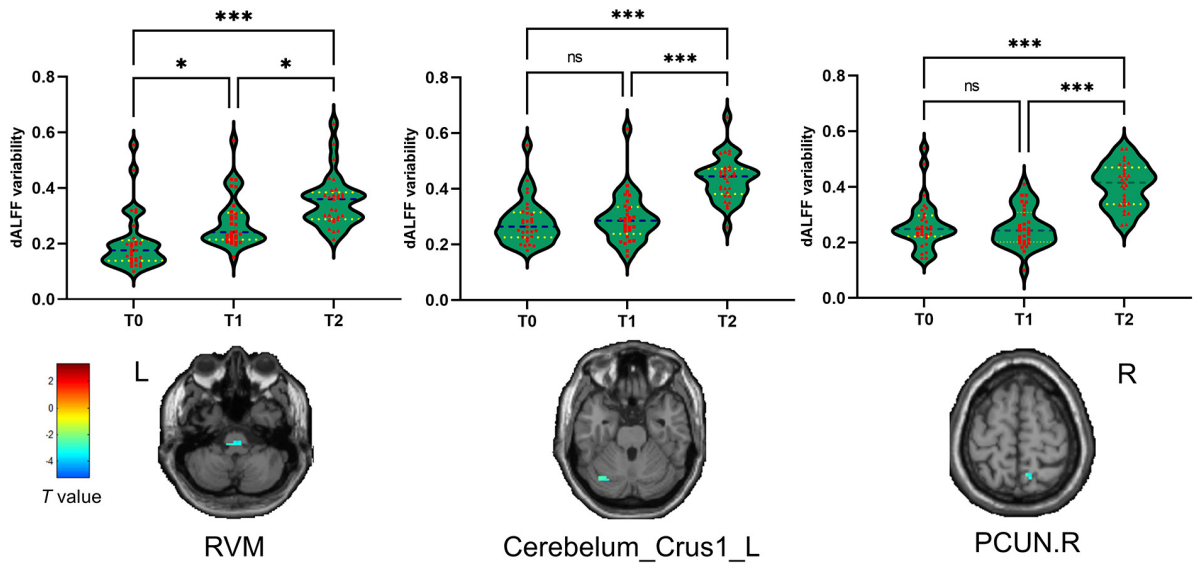

FIGURE 3
The dALFF variability significantly during the different periods of treatment. *$p < 0.05$, ***$p < 0.001$. The cool color represents decreased dALFF variability values. T0, the time point at baseline; T1, the time point after the first acupuncture session; T2, the time point after the 12th acupuncture sessions. All abbreviations are defined in the Abbreviations section.

TABLE 4 The DEC variability significantly during the different periods of treatment.

Contrast	Brain region	Peak MNI (x-, y-, z-)			Voxels	*F* score
Causal outflow from RVM to the rest of the brain (X to Y)	INS.L	−36	12	3	16	6.67
	MFG.R	36	42	12	15	7.43
	SMG.R	57	−18	18	19	6.39
	PreCG.R	57	3	21	21	8.75
Causal inflow to RVM from the rest of the brain (Y to X)	FFG.R	24	−45	−18	23	6.54
Causal outflow from Cerebellum_Crus1_L to the rest of the brain (X to Y)	MOG.L	−33	−66	30	16	6.89
	PreCG.L	−39	6	39	18	8.44
Causal outflow from Precuneus_R to the rest of the brain (X to Y)	THA.R	3	−18	0	19	8.91

Gaussian Random Field theory correction, voxel P-value < 0.001, cluster P-value < 0.05.

enhanced after all acupuncture sessions compared with that at baseline and after the first acupuncture session. Next, whole-brain-to-RVM dynamic GCA showed that the DEC variability from the right Fusiform gyrus (FFG.R) inflow to RVM was significantly enhanced. *Post hoc* tests revealed that the DEC variability from FFG.R to RVM after all acupuncture sessions was significantly increased compared with that after the first acupuncture session (Figure 4). Furthermore, the bivariate Cerebellum_Crus1_L-to-whole-brain dynamic GCA showed that the DEC variability from Cerebellum_Crus1_L outflow to the left middle occipital gyrus (MOG.L) and the left Precentral gyrus (PreCG.L) (Table 4) was significantly enhanced. *Post hoc* tests indicated that the DEC variability after all acupuncture sessions significantly enhanced compared with that at the baseline and after the first acupuncture session, while there was no significant difference in the DEC variability after the

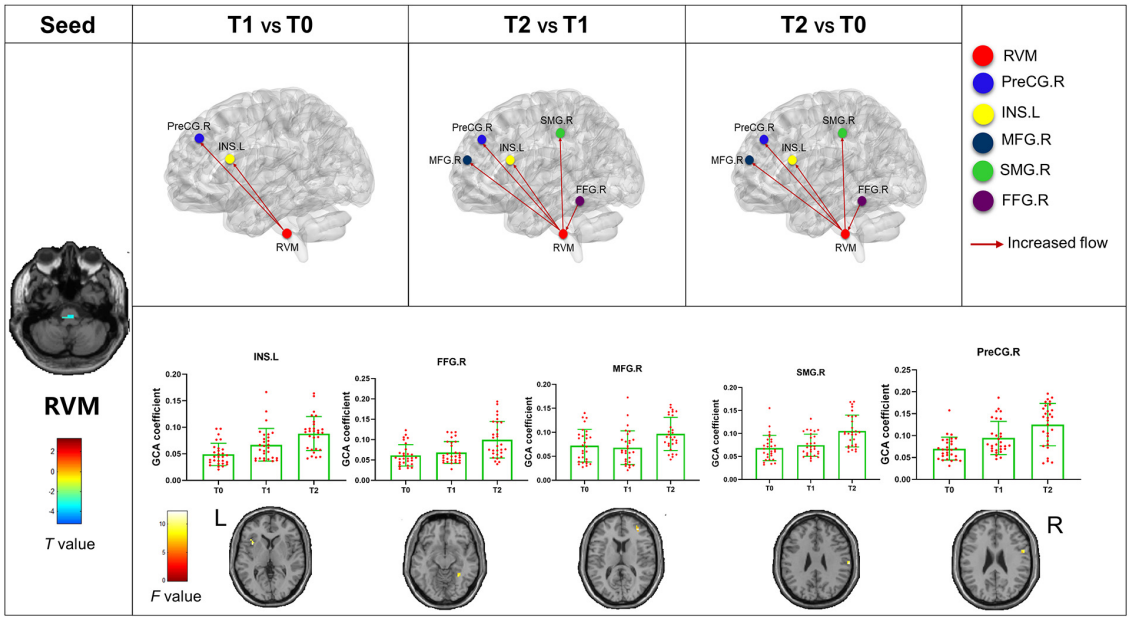

FIGURE 4
Abnormal effective connectivity pathways associated with the RVM. Each bar chart reflects the values of the dynamic GCA coefficient in the corresponding group. Fuchsia arrows indicate significantly enhanced DEC variability. T0, the time point at baseline; T1, the time point after the first acupuncture session; T2, the time point after the 12th acupuncture sessions. All abbreviations are defined in the Abbreviations section.

first acupuncture session compared with that at the baseline (Figure 5). In addition, we also observed that the bivariate PCUN.R-to-whole-brain dynamic GCA displayed significantly enhanced DEC variability from PCUN.R outflow to the right thalamus (THA.R) (Table 4), and *post hoc* tests indicated that the DEC variability after the first acupuncture session was enhanced compared with that at the baseline, after all sessions of acupuncture compared with that at the baseline, and after the first acupuncture session (Figure 6). There was no statistical difference in DEC variability in the remained ROIs.

Correlation between dynamic amplitude of low-frequency fluctuation variability, dynamic effective connectivity variability, and clinical variables at baseline and after all acupuncture sessions

The SD values of the dALFF variability in RVM in patients with MwoA at the baseline were significantly positively correlated with the frequency of migraine attacks and negatively correlated with the disease duration at baseline ($p < 0.001$, $r = 0.597$; $p = 0.033$, $r = -0.338$, respectively). The frequency of migraine attacks was also significantly positive correlated with the SD value of the dALFF variability in Cerebellum_Crus1_L at baseline ($p = 0.049$, $r = 0.314$) (Supplementary Figure 1).

The SD value of the dynamic GCA coefficient between MFG.R, INS.L, PreCG.R, SMG.R, and FFG.R with RVM was significantly positively correlated with the MSQ score and negatively correlated with the frequency of migraine attacks and VAS scores (Supplementary Figure 2 and Table 5) after all the acupuncture sessions. In addition, there were significant negative correlations between the SD value of the dynamic GCA coefficient from Cerebellum_Crus1_L to MOG.L and PreCG.L with the VAS scores ($p = 0.006$, $r = -0.360$; $p = 0.009$, $r = -0.340$, respectively), and there were significantly negative correlations between the SD value of the dynamic GCA coefficient from Cerebellum_Crus1_L to PreCG.L and frequency of migraine attack ($p = 0.002$, $r = -0.397$) (Supplementary Figure 3). Moreover, the VAS score and frequency of migraine attack were shown significantly negative correlations with the SD value of the dynamic GCA coefficient from PCUN.R to THA.R ($p < 0.001$, $r = -0.544$; $p < 0.001$, $r = -0.691$, respectively), and they were significantly positive correlated with MSQ score ($p < 0.001$, $r = -0.568$; $p < 0.001$, $r = -0.675$; $p < 0.001$, $r = -0.566$, respectively) (Supplementary Figure 4). No other significant linear correlation was observed.

Validation results

To verify the stability of our main results, other window sizes were included, such as 30 TRs and 80 TRs. The dynamic ALFF analysis and DEC analysis using

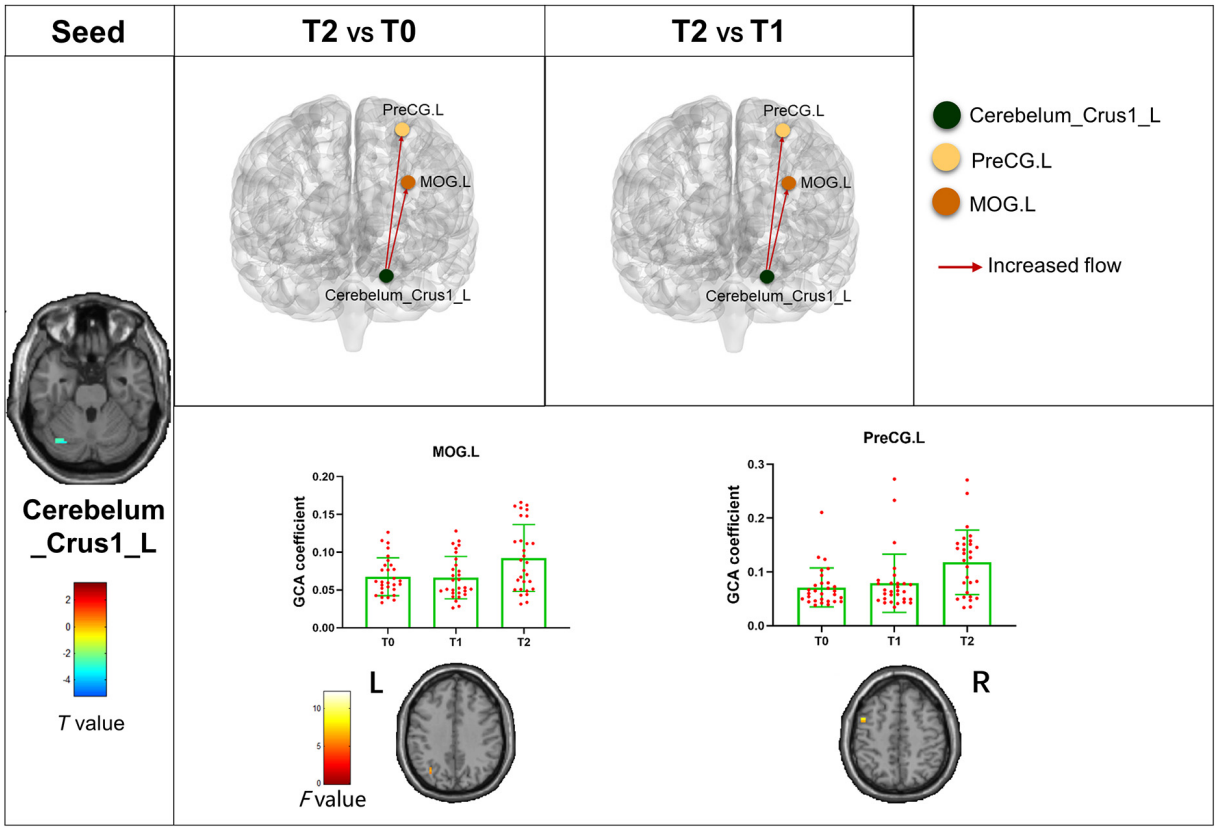

FIGURE 5
Abnormal effective connectivity pathways associated with the Cerebellum_Crus1_L. Each bar chart reflects the values of the dynamic GCA coefficient in the corresponding group. Fuchsia arrows indicate significantly enhanced DEC variability. T0, the time point at baseline; T1, the time point after the first acupuncture session; T2, the time point after the 12th acupuncture sessions. All abbreviations are defined in the Abbreviations section.

different sliding-window lengths supported our main results (**Supplementary Figures 5–8**).

Discussion

In this study, we applied the dALFF analysis to assess the abnormal changes of variability in patients with MwoA. The changes in dALFF and GCA variability after acupuncture were found. These alterations were associated with the clinical variables. The results could be summarized as follows: (1) the dALFF variability of patients with MwoA mainly were decreased compared with HCs at baseline, including RVM, Cerebellum_Crus1_L, PCUN.R, etc. (2) The decreased dALFF variability of RVM, Cerebellum_Crus1_L, and PCUN.R was progressively recovered, and the DEC variability was gradually increased after acupuncture treatment. (3) The dALFF variability of these brain areas was positively correlated with the frequency of migraine attacks and negatively correlated with the disease duration at baseline; the dynamic GCA coefficients were positively correlated with MSQ scores and negatively correlated with the frequency of migraine attacks and VAS scores after acupuncture treatment. Overall, our findings proved that the cumulative therapeutic effects of acupuncture treatment in patients with MwoA mostly focused on the changes in the brain dynamic activity and effective connectivity in RVM, Cerebellum_Crus1_L, and PCUN.R.

At first, we found the decreased dALFF variability of RVM in patients with MwoA. The ALFF has been proven to be an effective and reliable parameter for evaluating local intrinsic brain activity (Zang et al., 2007). As an extensive index of ALFF, the dynamic ALFF analysis subdivided the whole time series into multiple slices and then calculated ALFF in each slice. RVM was a part of the brainstem and a critical region of the descending pain modulatory system (Kong et al., 2010). ON and OFF cells within the RVM were activated by the onset and offset of noxious stimulation (Fields, 2004). But in migraine, its role was controversial. It was reported that patients with MwoA showed increased ALFF in posterior insula and putamen/caudate and reduced ALFF in RVM/trigeminocervical complex (TCC) (Li et al., 2017b). In another study, migraineurs had a significantly increasing fractional amplitude of low-frequency fluctuation

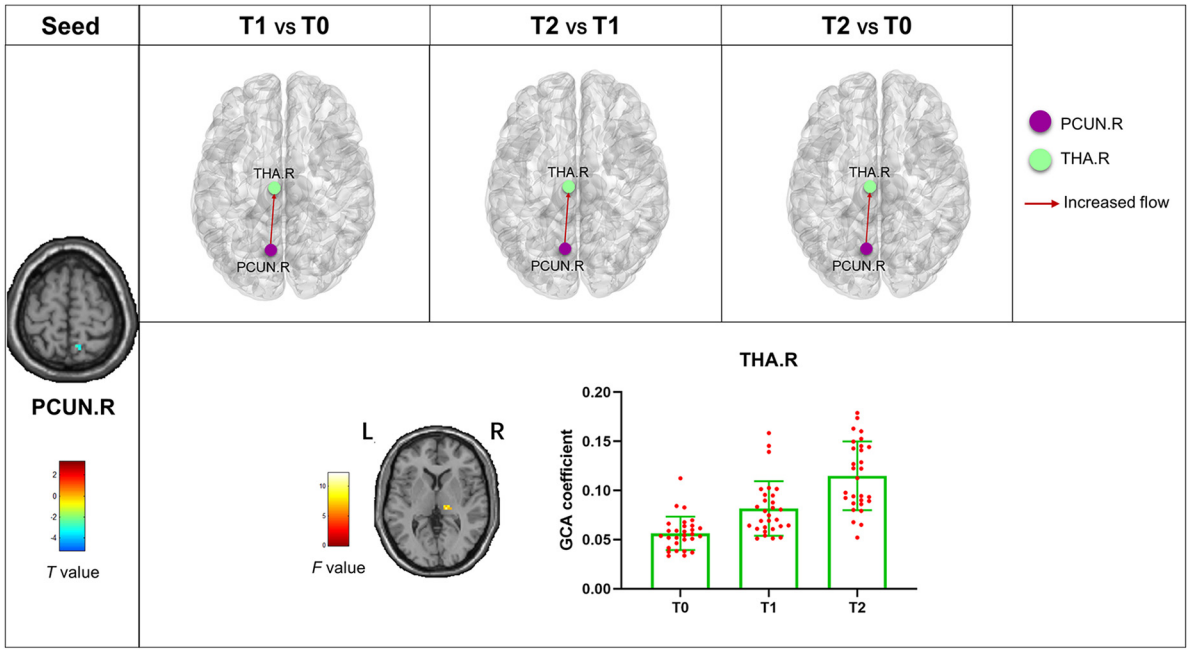

FIGURE 6
Abnormal effective connectivity pathways associated with the PCUN.R. Each bar chart reflects the values of the dynamic GCA coefficient in the corresponding group. Fuchsia arrows indicate significantly enhanced DEC variability. T0, the time point at baseline; T1, the time point after the first acupuncture session; T2, the time point after the 12th acupuncture sessions. All abbreviations are defined in the Abbreviations section.

TABLE 5 Correlation between the values of the dynamic GCA coefficient between MFG.R, INS.L, PreCG.R, SMG.R, and FFG.R with RVM and clinical variables after all acupuncture sessions.

ROIs	Frequency of migraine attack (days) (*r*, *p*-value)	VAS score (*r*, *p*-value)	MSQ score (restrictive subscale) (*r*, *p*-value)	MSQ score (preventive subscale) (*r*, *p*-value)	MSQ score (emotional subscale) (*r*, *p*-value)
INS.L	−0.515, <0.001	−0.508, <0.001	0.424, <0.001	0.412, 0.001	0.453, <0.001
MFG.R	−0.387, 0.004	−0.398, 0.002	0.408, 0.002	0.394, 0.005	0.422, <0.001
PreCG.R	−0.406, 0.002	−0.544, <0.001	0.468, <0.001	0.530, <0.001	0.508, <0.001
SMG.R	−0.534, <0.001	−0.323, 0.013	0.455, <0.001	0.527, <0.001	0.359, 0.006
FFG.R	−0.470, <0.001	−0.384, 0.003	0.429, <0.001	0.405, 0.002	0.340, 0.009

All abbreviations are defined in the Abbreviations section.

(fALFF) in bilateral ventral posteromedial (VPM) thalamus and brainstem encompassing RVM and TCC (Kim et al., 2021). The inconsistent results for RVM might be due to the different subtypes of migraine, different sample sizes, and methodological variability. In our study, the decreased dALFF variability of the RVM was progressively recovered, and this finding was concordant with many studies reporting that acupuncture treatment could normalize the impaired descending pain modulatory system in migraine (Li et al., 2016, 2017b). The DEC variability from RVM outflow to INS.L and PreCG.R after the first acupuncture session were enhanced compared with that at baseline, and the outflow to MFG.R, INS.L, PreCG.R, and SMG.R and inflow to RVM from FFG.R were enhanced after all acupuncture sessions compared with the first acupuncture session. According to these results, the treatment effect of acupuncture was gradually increased following the increase in intervention times. The insula was associated with the different aspects of sensorimotor and cognitive control of speech production (Schwedt et al., 2015; Battistella et al., 2018). The precentral gyrus was the traditional movement-related higher cortex and included the primary motor area, the somatomotor cortex, and the lateral premotor area (Meier et al., 2008; Arca et al., 2021). The prefrontal cortex was the central brain region for executive functions (Ueda et al., 2018; Ashina et al., 2021). The fusiform gyrus was responsible for processing color information, face and body recognition, and the emotional expression of facial stimuli (Parvizi et al., 2012; Bassez et al., 2020). So, the cumulative therapeutic effect of acupuncture was

embodied in affecting the cognitive, sensorimotor, speech, and executive functions of patients with MwoA through the RVM. This study also showed that the dALFF variability in RVM was correlated with the frequency of migraine attack and disease duration at the baseline, and these DEC variabilities of the RVM-to-whole-brain were correlated with the frequency of migraine attack and MSQ scores after acupuncture, which suggested that these brain regions might be the therapeutic targets in MwoA.

Our results also showed decreased dALFF variability in the Cerebellum_Crus1_L, IFGtriang.R, DCG.R, PCUN.R, and IPL.L. These regions were parts of the default, executive control, and cerebellar networks (Kim et al., 2017; Tu et al., 2019). A recent study revealed the abnormal dynamic low-frequency oscillation in the default mode network, salience network, and executive control network in patients with migraine (Chen et al., 2021). Another study showed the decreased ALFF value in the bilateral cerebellum posterior lobe, left cerebellum anterior lobe, bilateral orbital cortex, right middle frontal gyrus, bilateral occipital lobe, right fusiform gyrus, and bilateral postcentral gyrus in patients with migraine (Wang et al., 2016). These studies were generally consistent with the results of this study.

In addition, the dALFF variability of the Cerebellum_Crus1_L and PCUN.R was also slowly enhanced after acupuncture. Many studies have demonstrated the preventive effect of acupuncture on migraine might be through modulating the visual network, default mode network, sensorimotor network, frontal lobe network, and descending pain modulation system (Zou et al., 2019; Tu et al., 2020; Tian et al., 2021a,b). These are similar to the results of this study. The dALFF variability in Cerebellum_Crus1_L was correlated with the frequency of migraine attacks, which supported this perspective. Furthermore, acupuncture was a long-term and cumulative process (Zhao et al., 2017). Most of the studies of fMRI focused on the immediate effect of acupuncture on migraine. The changes in the whole process of acupuncture treatment were unknown. Thus, in our current study, the changes in dALFF variability at three time points during acupuncture treatment in patients with MwoA were observed to clarify the cumulative therapeutic effect of acupuncture. Moreover, the study additionally showed the enhanced DEC variability outflow from Cerebellum_Crus1_L to the left middle occipital gyrus and the left precentral gyrus and outflow from PCUN.R to the right thalamus enhanced gradually after the process of acupuncture treatment. The middle occipital gyrus was a vital component of the visual network and was responsible for the afferent input, integration, and perception of visual information (Zhu et al., 2018). Previous studies demonstrated a transient pathologic state with atypical thalamo-cortical connectivity in migraineurs (Coppola et al., 2021). These results might be able to intuitively explain the cumulative therapeutic effect of acupuncture. It was also shown that the cumulative therapeutic effects of acupuncture in migraine could be regarded as the consequence of interactions between pain modulation and cortical networks, which might provide an objective imaging marker to monitor the treatment in migraine. Moreover, these DEC variabilities of Cerebellum_Crus1_L and PCUN.R to-whole-brain were correlated with the frequency of migraine attack and MSQ scores after acupuncture treatment, which suggested that these brain regions might be the target areas for acupuncture improving MwoA.

Migraine attacks are often accompanied by psychiatric symptoms, such as anxiety, depression, agitation, panic, bipolar disorder, and sleep disturbances, such as difficulty falling asleep, excessive dreaming, and difficulty maintaining sleep (Tfelt-Hansen and Koehler, 2011). Therefore, when studying the psychosomatic symptoms associated with migraine, the comprehensive assessment of anxiety, depression, and sleep quality should be taken as a whole (McDermott and Ebmeier, 2009). This is a more comprehensive picture of the co-morbidity of migraine-related psychiatric disorders. In this study, the SAS and SDS scores of patients with MwoA improved significantly after acupuncture treatment, indicating that acupuncture can improve patients' anxiety and depression. However, in subsequent correlational analyses, improvement in these symptoms was not associated with dynamic alterations of intrinsic brain activity and effective connectivity. This may be due to the lack of comprehensiveness of the fMRI study indicators selected for this study.

Our study has several potential limitations. First, no sham acupuncture group was set up during the longitudinal follow-up of acupuncture treatment, making it impossible to evaluate the interaction between the groups and time and the placebo effect. However, all patients with MwoA performed a series of fMRI scans, which enabled us to get longitudinal evidence of the cumulative therapeutic effect of acupuncture. Second, the optimal sliding window length to obtain dynamic changes in brain activity remains unclear. We selected 50 TRs as the window length based on previous studies, validated our results by using different sliding window lengths, and demonstrated that our findings were stable and not influenced by this factor. Third, the small sample size might weaken the liability of our results, and they should be further proved by the study with a big sample size in the future. Fourth, multimodal brain imaging (i.e., diffusion tensor imaging) was helpful for observing the changes in anatomical connectivity in patients with MwoA after acupuncture treatment, and it could be employed in the future.

Conclusion

This prospective longitudinal study showed that the cumulative therapeutic effect of acupuncture in patients with MwoA. It manifested as the abnormal brain activity in RVM, Cerebellum_Crus1_L and PCUN.R were progressively recovered, and the effective connectivity of these brain areas with cognitive, sensorimotor, speech, executive, and cerebellar

networks was gradually enhanced to make up for these abnormal brain activity.

Data availability statement

The original contributions presented in this study are included in the article/**Supplementary Material**, further inquiries can be directed to the corresponding authors.

Ethics statement

The studies involving human participants were reviewed and approved by the Ethics Committee of the Shuguang Hospital Affiliated to Shanghai University of Traditional Chinese Medicine and was registered on www.chictr.org.cn (ChiCTR1900023105). The patients/participants provided their written informed consent to participate in this study.

Author contributions

WT and SZ designed the study. YC, YK, SLL, SSL, BW, ZG, YH, and HW performed the experiments. YC analyzed the data and was a major contributor in writing the manuscript. All authors read and approved the final manuscript.

Funding

This work was supported by funding from the Shanghai Science and Technology Committee (Nos. 18401970900 and 18401970300) and the Shanghai Health Care Commission Project (No. 202040194).

Acknowledgments

We would like to thank all the patients with migraine without aura and healthy controls who participated in our research.

Conflict of interest

The authors declare that the research was conducted in the absence of any commercial or financial relationships that could be construed as a potential conflict of interest.

Publisher's note

Supplementary material

The Supplementary Material for this article can be found online at: https://www.frontiersin.org/articles/10.3389/fnins.2022.925698/full#supplementary-material

References

Arca, K. N., VanderPluym, J. H., and Halker Singh, R. B. (2021). Narrative review of neuroimaging in migraine with aura. *Headache* 61, 1324–1333. doi: 10.1111/head.14191

Ashina, S., Bentivegna, E., Martelletti, P., and Eikermann-Haerter, K. (2021). Structural and functional brain changes in migraine. *Pain Ther.* 10, 211–223. doi: 10.1007/s40122-021-00240-5

Bassett, D. S., and Sporns, O. (2017). Network neuroscience. *Nat. Neurosci.* 20, 353–364. doi: 10.1038/nn.4502

Bassez, I., Van de Steen, F., Ricci, K., Vecchio, E., Gentile, E., Marinazzo, D., et al. (2020). Dynamic causal modelling of the reduced habituation to painful stimuli in migraine: an EEG study. *Brain Sci.* 10:712. doi: 10.3390/brainsci10100712

Battistella, G., Kumar, V., and Simonyan, K. (2018). Connectivity profiles of the insular network for speech control in healthy individuals and patients with spasmodic dysphonia. *Brain Struct. Funct.* 223, 2489–2498. doi: 10.1007/s00429-018-1644-y

Chang, C. M., Yang, C. P., Yang, C. C., Shih, P. H., and Wang, S. J. (2021). Evidence of potential mechanisms of acupuncture from functional MRI data for migraine prophylaxis. *Curr. Pain Headache Rep.* 25:49. doi: 10.1007/s11916-021-00961-4

Chen, H., Qi, G., Zhang, Y., Huang, Y., Zhang, S., Yang, D., et al. (2021). Altered dynamic amplitude of low-frequency fluctuations in patients with migraine without aura. *Front. Hum. Neurosci.* 15:636472. doi: 10.3389/fnhum.2021.636472

Chen, J., Zhao, L., Zheng, H., Li, Y., Yang, M., Chang, X., et al. (2013). Evaluating the prophylaxis and long-term effectiveness of acupuncture for migraine without aura: study protocol for a randomized controlled trial. *Trials* 10:361. doi: 10.1186/1745-6215-14-361

Coppola, G., Di Renzo, A., Tinelli, E., Petolicchio, B., Parisi, V., Serrao, M., et al. (2021). Thalamo-cortical networks in subtypes of migraine with aura patients. *J. Headache Pain* 22:58. doi: 10.1186/s10194-021-01272-0

Cui, Q., Sheng, W., Chen, Y., Pang, Y., Lu, F., Tang, Q., et al. (2020). Dynamic changes of amplitude of low-frequency fluctuations in patients with generalized anxiety disorder. *Hum. Brain Mapp.* 41, 1667–1676. doi: 10.1002/hbm.24902

Diener, H.-C., Charles, A., Goadsby, P. J., and Holle, D. (2015). New therapeutic approaches for the prevention and treatment of migraine. *Lancet Neurol.* 14, 1010–1022. doi: 10.1016/s1474-4422(15)00198-2

Fields, H. (2004). State-dependent opioid control of pain. *Nat. Rev. Neurosci.* 5, 565–575. doi: 10.1038/nrn1431

Fu, Z., Iraji, A., Turner, J. A., Sui, J., Miller, R., Pearlson, G. D., et al. (2021). Dynamic state with covarying brain activity-connectivity: on the pathophysiology of schizophrenia. *Neuroimage* 224:117385. doi: 10.1016/j.neuroimage.2020.117385

Fu, Z., Tu, Y., Di, X., Du, Y., Pearlson, G. D., Turner, J. A., et al. (2018). Characterizing dynamic amplitude of low-frequency fluctuation and its relationship with dynamic functional connectivity: an application to schizophrenia. *Neuroimage* 180(Pt B), 619–631. doi: 10.1016/j.neuroimage.2017.09.035

Huang, X., Zhang, D., Wang, P., Mao, C., Miao, Z., Liu, C., et al. (2021). Altered amygdala effective connectivity in migraine without aura: evidence from resting-state fMRI with Granger causality analysis. *J. Headache Pain* 22:25. doi: 10.1186/s10194-021-01240-8

Kim, J., Criaud, M., Cho, S. S., Diez-Cirarda, M., Mihaescu, A., Coakeley, S., et al. (2017). Abnormal intrinsic brain functional network dynamics in Parkinson's disease. *Brain* 140, 2955–2967. doi: 10.1093/brain/awx233

Kim, Y. E., Kim, M. K., Suh, S. I., and Kim, J. H. (2021). Altered trigeminothalamic spontaneous low-frequency oscillations in migraine without aura: a resting-state fMRI study. *BMC Neurol.* 21:342. doi: 10.1186/s12883-021-02374-7

Kong, J., Tu, P. C., Zyloney, C., and Su, T. P. (2010). Intrinsic functional connectivity of the periaqueductal gray, a resting fMRI study. *Behav. Brain Res.* 211, 215–219. doi: 10.1016/j.bbr.2010.03.042

Leonardi, M., Steiner, T. J., Scher, A. T., and Lipton, R. B. (2005). The global burden of migraine: measuring disability in headache disorders with WHO's classification of functioning, disability and health (ICF). *J. Headache Pain* 6, 429–440. doi: 10.1007/s10194-005-0252-4

Li, J., Duan, X., Cui, Q., Chen, H., and Liao, W. (2019). More than just statics: temporal dynamics of intrinsic brain activity predicts the suicidal ideation in depressed patients. *Psychol. Med.* 49, 852–860. doi: 10.1017/S0033291718001502

Li, Z., Liu, M., Lan, L., Zeng, F., Makris, N., Liang, Y., et al. (2016). Altered periaqueductal gray resting state functional connectivity in migraine and the modulation effect of treatment. *Sci. Rep.* 6:20298. doi: 10.1038/srep20298

Li, Z., Zeng, F., Yin, T., Lan, L., Makris, N., Jorgenson, K., et al. (2017b). Acupuncture modulates the abnormal brainstem activity in migraine without aura patients. *Neuroimage Clin.* 15, 367–375. doi: 10.1016/j.nicl.2017.05.013

Li, Z., Lan, L., Zeng, F., Makris, N., Hwang, J., Guo, T., et al. (2017a). The altered right frontoparietal network functional connectivity in migraine and the modulation effect of treatment. *Cephalalgia* 37, 161–176. doi: 10.1177/0333102416641665

Liao, W., Li, J., Ji, G. J., Wu, G. R., Long, Z., Xu, Q., et al. (2019). Endless fluctuations: temporal dynamics of the amplitude of low frequency fluctuations. *IEEE Trans. Med. Imaging* 38, 2523–2532. doi: 10.1109/TMI.2019.2904555

Liu, L., Tian, T., Li, X., Wang, Y., Xu, T., Ni, X., et al. (2021). Revealing the neural mechanism underlying the effects of acupuncture on migraine: a systematic review. *Front. Neurosci.* 15:674852. doi: 10.3389/fnins.2021.674852

Liu, S., Luo, S., Yan, T., Ma, W., Wei, X., Chen, Y., et al. (2021). Differential modulating effect of acupuncture in patients with migraine without aura: a resting functional magnetic resonance study. *Front. Neurol.* 12:680896. doi: 10.3389/fneur.2021.680896

McDermott, L. M., and Ebmeier, K. P. (2009). A meta-analysis of depression severity and cognitive function. *J. Affect. Disord.* 119, 1–8. doi: 10.1016/j.jad.2009.04.022

Meier, J. D., Aflalo, T. N., Kastner, S., and Graziano, M. S. (2008). Complex organization of human primary motor cortex: a high-resolution fMRI study. *J. Neurophysiol.* 100, 1800–1812. doi: 10.1152/jn.90531.2008

Olesen, J., Dodick, D., and Ducros, A. (2018). Headache Classification Committee of the International Headache Society (IHS) the international classification of headache disorders, 3rd edition. *Cephalalgia* 38, 1–211. doi: 10.1177/0333102417738202

Parvizi, J., Jacques, C., Foster, B. L., Witthoft, N., Rangarajan, V., Weiner, K. S., et al. (2012). Electrical stimulation of human fusiform face-selective regions distorts face perception. *J. Neurosci.* 32, 14915–14920. doi: 10.1523/JNEUROSCI.2609-12.2012

Schwedt, T. J., Chiang, C.-C., Chong, C. D., and Dodick, D. W. (2015). Functional MRI of migraine. *Lancet Neurol.* 14, 81–91. doi: 10.1016/s1474-4422(14)70193-0

Tfelt-Hansen, P. C., and Koehler, P. J. (2011). One hundred years of migraine research: major clinical and scientific observations from 1910 to 2010. *Headache* 51, 752–778. doi: 10.1111/j.1526-4610.2011.01892.x

Tian, Z., Guo, Y., Yin, T., Xiao, Q., Ha, G., Chen, J., et al. (2021a). Acupuncture modulation effect on pain processing patterns in patients with migraine without aura. *Front. Neurosci.* 15:729218. doi: 10.3389/fnins.2021.729218

Tian, Z., Yin, T., Xiao, Q., Dong, X., Yang, Y., Wang, M., et al. (2021b). The altered functional connectivity with pain features integration and interaction in migraine without aura. *Front. Neurosci.* 15:646538. doi: 10.3389/fnins.2021.646538

Tu, Y., Fu, Z., Zeng, F., Maleki, N., Lan, L., Li, Z., et al. (2019). Abnormal thalamocortical network dynamics in migraine. *Neurology* 92, e2706–e2716. doi: 10.1212/wnl.0000000000007607

Tu, Y., Zeng, F., Lan, L., Li, Z., Maleki, N., Liu, B., et al. (2020). An fMRI-based neural marker for migraine without aura. *Neurology* 94, e741–e751. doi: 10.1212/WNL.0000000000008962

Ueda, R., Yanagisawa, K., Ashida, H., and Abe, N. (2018). Executive control and faithfulness: only long-term romantic relationships require prefrontal control. *Exp. Brain Res.* 236, 821–828. doi: 10.1007/s00221-018-5181-y

Wang, J. J., Chen, X., Sah, S. K., Zeng, C., Li, Y. M., Li, N., et al. (2016). Amplitude of low-frequency fluctuation (ALFF) and fractional ALFF in migraine patients: a resting-state functional MRI study. *Clin. Radiol.* 71, 558–564. doi: 10.1016/j.crad.2016.03.004

Wei, H. L., Chen, J., Chen, Y. C., Yu, Y. S., Guo, X., Zhou, G. P., et al. (2020). Impaired effective functional connectivity of the sensorimotor network in interictal episodic migraineurs without aura. *J. Headache Pain* 21:111. doi: 10.1186/s10194-020-01176-5

Xu, S., Yu, L., Luo, X., Wang, M., Chen, G., Zhang, Q., et al. (2020). Manual acupuncture versus sham acupuncture and usual care for prophylaxis of episodic migraine without aura: multicentre, randomised clinical trial. *BMJ* 368:m697. doi: 10.1136/bmj.m697

Yang, S., Meng, Y., Li, J., Fan, Y. S., Du, L., Chen, H., et al. (2019). Temporal dynamic changes of intrinsic brain activity in schizophrenia with cigarette smoking. *Schizophr. Res.* 210, 66–72. doi: 10.1016/j.schres.2019.06.012

Yu, S., Liu, R., Zhao, G., Yang, X., Qiao, X., Feng, J., et al. (2012). The prevalence and burden of primary headaches in China: a population-based door-to-door survey. *Headache* 52, 582–591. doi: 10.1111/j.1526-4610.2011.02061.x

Zang, Y. F., He, Y., Zhu, C. Z., Cao, Q. J., Sui, M. Q., Liang, M., et al. (2007). Altered baseline brain activity in children with ADHD revealed by resting-state functional MRI. *Brain Dev.* 29, 83–91. doi: 10.1016/j.braindev.2006.07.002

Zhao, L., Chen, J., Li, Y., Sun, X., Chang, X., Zheng, H., et al. (2017). The long-term effect of acupuncture for migraine prophylaxis: a randomized clinical trial. *JAMA Intern. Med.* 177, 508–515. doi: 10.1001/jamainternmed.2016.9378

Zhao, L., Liu, J., Zhang, F., Dong, X., Peng, Y., Qin, W., et al. (2014). Effects of long-term acupuncture treatment on resting-state brain activity in migraine patients: a randomized controlled trial on active acupoints and inactive acupoints. *PLoS One* 9:e99538. doi: 10.1371/journal.pone.0099538

Zhao, L., Wang, D., Xue, S. W., Tan, Z., Wang, Y., and Lian, Z. (2021). Aberrant state-related dynamic amplitude of low-frequency fluctuations of the emotion network in major depressive disorder. *J. Psychiatr. Res.* 133, 23–31. doi: 10.1016/j.jpsychires.2020.12.003

Zhu, F., Liu, F., Guo, W., Chen, J., Su, Q., Zhang, Z., et al. (2018). Disrupted asymmetry of inter- and intra-hemispheric functional connectivity in patients with drug-naive, first-episode schizophrenia and their unaffected siblings. *EBioMedicine* 36, 429–435. doi: 10.1016/j.ebiom.2018.09.012

Zou, Y., Tang, W., Li, X., Xu, M., and Li, J. (2019). Acupuncture reversible effects on altered default mode network of chronic migraine accompanied with clinical symptom relief. *Neural Plast.* 2019:5047463. doi: 10.1155/2019/5047463

frontiers | Frontiers in Neuroscience

TYPE Brief Research Report
PUBLISHED 21 September 2022
DOI 10.3389/fnins.2022.961686

OPEN ACCESS

EDITED BY
Chitresh Bhushan,
GE Global Research, United States

REVIEWED BY
Haiqing Huang,
University of Pittsburgh, United States
Afis Ajala,
GE Global Research, United States

*CORRESPONDENCE
Yoko Ikoma
ikoma.yoko@qst.go.jp

SPECIALTY SECTION
This article was submitted to Brain Imaging Methods, a section of the journal Frontiers in Neuroscience

RECEIVED 05 June 2022
ACCEPTED 10 August 2022
PUBLISHED 21 September 2022

CITATION
Tachibana A, Ikoma Y, Hirano Y, Kershaw J and Obata T (2022) Separating neuronal activity and systemic low-frequency oscillation related BOLD responses at nodes of the default mode network during resting-state fMRI with multiband excitation echo-planar imaging. *Front. Neurosci.* 16:961686. doi: 10.3389/fnins.2022.961686

Separating neuronal activity and systemic low-frequency oscillation related BOLD responses at nodes of the default mode network during resting-state fMRI with multiband excitation echo-planar imaging

Atsushi Tachibana[1], Yoko Ikoma[1]*, Yoshiyuki Hirano[1,2,3], Jeff Kershaw[1] and Takayuki Obata[1,2]

[1]Department of Molecular Imaging and Theranostics, Institute for Quantum Medical Science, National Institutes for Quantum Science and Technology, Chiba, Japan, [2]Research Center for Child Mental Development, Chiba University, Chiba, Japan, [3]United Graduate School of Child Development, Osaka University, Kanazawa University, Hamamatsu University School of Medicine, Chiba University, and University of Fukui, Suita, Japan

Functional magnetic resonance imaging (fMRI) evaluates brain activity using blood oxygenation level-dependent (BOLD) contrast. Resting-state fMRI (rsfMRI) examines spontaneous brain function using BOLD in the absence of a task, and the default mode network (DMN) has been identified from that. The DMN is a set of nodes within the brain that appear to be active and in communication when the subject is in an awake resting state. In addition to signal changes related to neural activity, it is thought that the BOLD signal may be affected by systemic low-frequency oscillations (SysLFOs) that are non-neuronal in source and likely propagate throughout the brain to arrive at different regions at different times. However, it may be difficult to distinguish between the response due to neuronal activity and the arrival of a SysLFO in specific regions. Conventional single-shot EPI (Conv) acquisition requires a longish repetition time, but faster image acquisition has recently become possible with multiband excitation EPI (MB). In this study, we evaluated the time-lag between nodes of the DMN using both Conv and MB protocols to determine whether it is possible to distinguish between neuronal activity and SysLFO related responses during rsfMRI. While the Conv protocol data suggested that SysLFOs substantially influence the apparent time-lag of neuronal activity, the MB protocol data implied that the effects of SysLFOs

and neuronal activity on the BOLD response may be separated. Using a higher time-resolution acquisition for rsfMRI might help to distinguish neuronal activity induced changes to the BOLD response from those induced by non-neuronal sources.

KEYWORDS

resting-state fMRI, default mode network, low-frequency oscillation, multiband EPI, BOLD signal

Introduction

Brain functional magnetic resonance imaging (fMRI) utilizes blood oxygen level-dependent (BOLD) signal contrast to evaluate the neuronal activity in active areas of the brain (Ogawa et al., 1990). Neuronal activity leads to increased blood flow in specific regions, and the subsequent decrease in deoxy-hemoglobin concentration in the activated region is reflected by an increase in the BOLD signal intensity (Obata et al., 2004; Hirano et al., 2011, 2018). Therefore, the BOLD signal is not a direct measurement of brain activity, but rather a measure of secondary hemodynamic changes triggered by neuronal activation (Buxton et al., 2004; Liu, 2013). In addition to signal changes related to neural activity, the BOLD signal may be affected by global changes in arteriovenous blood flow velocity, cardiac pulsation, and respiration (Chang and Glover, 2009; Chang et al., 2009). Since the effect of those changes on the BOLD response is relatively slow in comparison to neuronal activity-related changes, they are called low-frequency oscillations (LFOs) (Murphy et al., 2013).

Tong et al. (2013) have explored low-frequency contributions to the BOLD signal that they identified as systemic low-frequency oscillations (SysLFOs). SysLFOs are considered to be non-neuronal in source and can be widely observed in the brain using fMRI. Although it is thought that SysLFO signal may derive from Mayer waves, CO2 concentration fluctuations and vasomotions, the detailed source of the signal is still unclear (Nilsson and Aalkjaer, 2003; Wise et al., 2004; Julien, 2006; Rivadulla et al., 2011; Sassaroli et al., 2012; Golestani et al., 2015). Tong et al. (2013) suggested that SysLFOs are endogenous to the cerebral blood flow and, due to the time they take to propagate, arrive at different regions at different times. Furthermore, if SysLFOs travel throughout the body with the blood flow, it is likely that related signals will be detectable at peripheral sites (Tong and Frederick, 2014). An example of this was provided by a study where near infrared spectroscopy (NIRS) and resting-state fMRI (rsfMRI) were simultaneously performed (Erdoğan et al., 2016). After bandpass filtering the data to the range 0.01–0.1 Hz, it was found that changes in oxygenation measured at the fingertip are significantly correlated with the global BOLD signal (GS), which was obtained by averaging over the whole brain excluding white matter (WM) and cerebrospinal fluid (CSF). The same group also proposed a method for estimating the arrival time of a SysLFO in a particular region of the brain. The method estimates the delay between the GS and the BOLD signal at each pixel, and then a SysLFO-MAP of the whole brain is created. SysLFO-MAPs were found to have a significant correlation with the cerebral blood flow measured with dynamic susceptibility contrast (DSC) MRI (Erdoğan et al., 2016; Tong et al., 2017).

Resting-state fMRI is performed while the subject is awake and at rest, so the data reflects the idle state of the brain (Biswal, 2012). It is thought that rsfMRI signals demonstrate the mechanical coupling and connectivity between various regions of the brain. One of the most important networks is the default mode network (DMN), which consists of nodes in the posterior cingulate cortex (PCC), left and right lower parietal lobes (L- and R-IPL), and medial prefrontal cortex (mPFC) (Greicius et al., 2003). The connectivity of neuronal activity is considered to be high if the BOLD signal changes at each of these nodes are highly correlated. Various studies have reported an association between brain diseases, such as dementia and schizophrenia, and DMN connectivity (Greicius et al., 2004; Liang et al., 2006; Barkhof et al., 2014).

Assuming there is some delay in the propagation of neuronal activity throughout the brain, it is likely that there is a time-lag between the different nodes of the DMN. However, it may be difficult to distinguish between the time-lag in the response due to neuronal activity and the arrival of a SysLFO in specific regions. The conventional single-shot EPI (Conv) acquisition protocol widely used for rsfMRI takes about 2,000 ms to image the whole brain. In contrast, multiband EPI (MB) acquisition enables imaging of the entire brain in a much shorter time (TR 500 ms), which means that BOLD signals can be measured with improved time-resolution (Feinberg et al., 2010). MB protocol data therefore contains four times more information about separate neuronal and possible SysLFO-related signals than data acquired with a Conv protocol. Using a higher time-resolution acquisition method might help to distinguish neuronal activity related time-lags from SysLFO delays.

In this study, we evaluated the time-lag between nodes of the DMN using both the Conv and MB protocols to determine

whether it is possible to distinguish between neuronal activity and SysLFO related responses during rsfMRI.

Materials and methods

Eighteen healthy female volunteers (age 26.6 ± 7.1 years) participated in this study. All subjects provided informed consent, and the institutional review board of the National Institutes for Quantum Science and Technology approved the research protocol (# 16-031).

Data acquisition

All MRI scans were conducted with a clinical 3T MRI system (MAGNETOM Verio 3T; Siemens Healthcare K.K., Erlangen, Germany) equipped with a 32-channel phased-array head matrix coil. A high-resolution T1-weighted sagittal three-dimensional anatomical image was acquired using magnetization prepared rapid-gradient echo (MPRAGE) with the following parameters: TR = 2,300 ms, TE = 1.95 ms, TI = 900 ms, flip angle = 9 degrees, matrix = 512 × 512, FOV = 250 mm × 250 mm, slice thickness = 1 mm, total acquisition time = 4 min 33 s. For rsfMRI scanning, Conv protocol data was acquired with the following parameters: TR = 2,000 ms, TE = 25 ms, flip angle = 90 degrees, matrix = 64 × 64, FOV = 240 mm × 240 mm, slice thickness = 3.8 mm, slice gap = 0.5 mm, repetitions = 204, total acquisition time = 6 min 52 s. The high time-resolution MB protocol rsfMRI data was acquired with a multiband EPI sequence (University of Minnesota sequence CMRR MB EPI VD13A R016a) using the following parameters: TR = 500 ms, TE = 30 ms, flip angle = 44 degrees, matrix = 64 × 64, FOV = 240 mm × 240 mm, slice thickness = 3.8 mm, slice gap = 0.456 mm, multiband factor = 6, repetitions = 600, total acquisition time = 5 min 7 s. All subjects were instructed to lie still and remain awake with their eyes open while watching a red dot on a screen positioned above them. The datasets generated during the current study are available from the corresponding author on reasonable request.

Preprocessing

Resting-state fMRI data was preprocessed using DPARSF (Version 4.3[1]) and SPM12.[2] The first 10 images for each subject were discarded to allow the longitudinal magnetization to reach

1 http://restfmri.net/forum/DPARSF
2 https://www.fil.ion.ucl.ac.uk/spm/

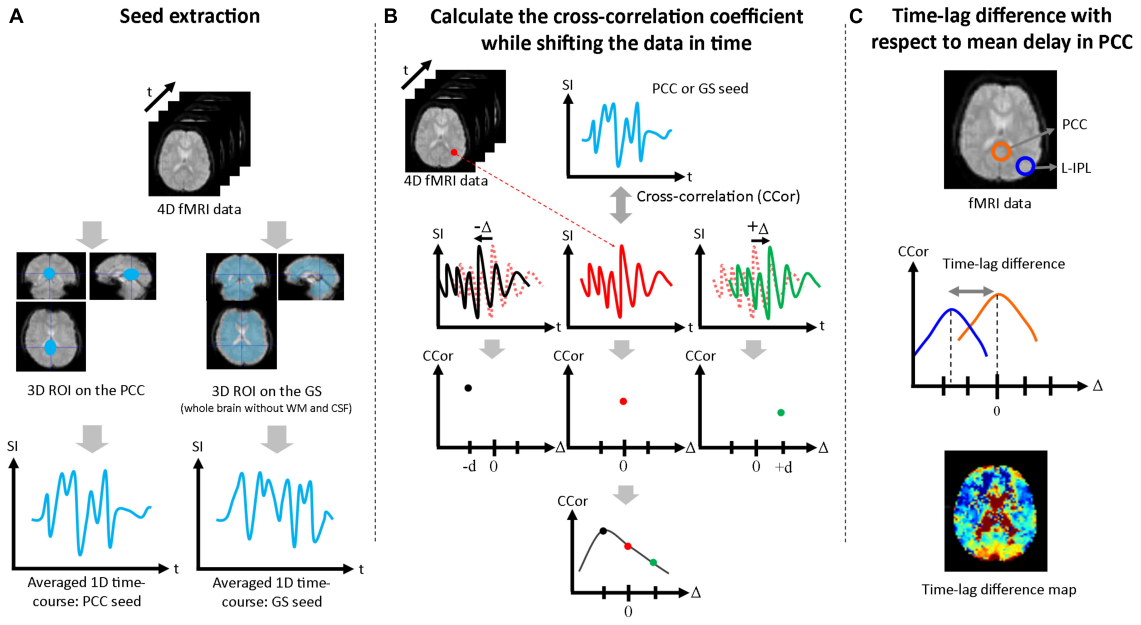

FIGURE 1
Procedure used to assess time-lags between nodes of the DMN. **(A)** The PCC ROI and GS ROI (whole brain excluding WM and CSF) were extracted and averaged over to generate the 1D seed data. **(B)** The correlation coefficient between the 1D seed and the time-course at each pixel was calculated. Each single-pixel time-course was shifted in time (Δ) and the correlation coefficient was calculated for each value of Δ [i.e., CCor(Δ)]. After cubic spline interpolation with respect to Δ, the maximum value of the correlation coefficient was taken as the time-lag for that pixel. **(C)** Time-lag differences were calculated with respect to the mean time-lag in the PCC ROI and maps were produced to visually evaluate the time-lag across the brain. Mean time-lag differences were also calculated for the mPFC, L-IPL and R-IPL for further analysis.

a steady-state. Slice-timing correction and motion correction were both applied. The data was registered and normalized to the Montreal Neurological Institute (MNI) space using the T1 image re-sampled to 3-mm isotropic voxels. Smoothing was performed with a 4 mm FWHM Gaussian kernel. Time courses were filtered for linear trends and then band-pass filtering (0.01–0.1 Hz) was applied. Confounding terms such as head motion, white matter signal and cerebrospinal fluid signal, were regressed out.

Time-lag analysis

Seed-based correlation analysis was performed to estimate the time-lags due to functional connectivity of the mPFC, L-IPL, and R-IPL with respect to seed data taken from the PCC and GS. First, a three-dimensional volume seed regions of interest (ROI) was drawn for both the PCC and GS (whole brain without WM and CSF) using the Automated Anatomical Labeling (AAL) brain template, and a one-dimensional seed time-course was produced by averaging over each ROI (Figure 1A). Second, the correlation coefficient was calculated between the one-dimensional seed time-courses and the time-course for each pixel in the brain. The single-pixel time-courses were also shifted in time (Δ), and the correlation coefficient between the seed time-course and the shifted single-pixel time-course at each Δ [i.e., CCor(Δ)] was calculated. The full range of Δ was $\pm$ 20 s in 2 s steps for the Conv protocol and $\pm$ 5 s in 0.5 s steps for the MB protocol. Cubic spline interpolation was then applied to CCor(Δ) as a function of Δ for each pixel, and the Δ corresponding to the highest value of CCor(Δ) was defined to be the time-lag for that pixel (Figure 1B). To facilitate comparison between the PCC and GS seed results, the mean time-lag in the PCC ROI was calculated and then subtracted from the time-lag of each pixel. Time-lag difference maps were then produced to visually evaluate the time-lag across the brain (Figure 1C),

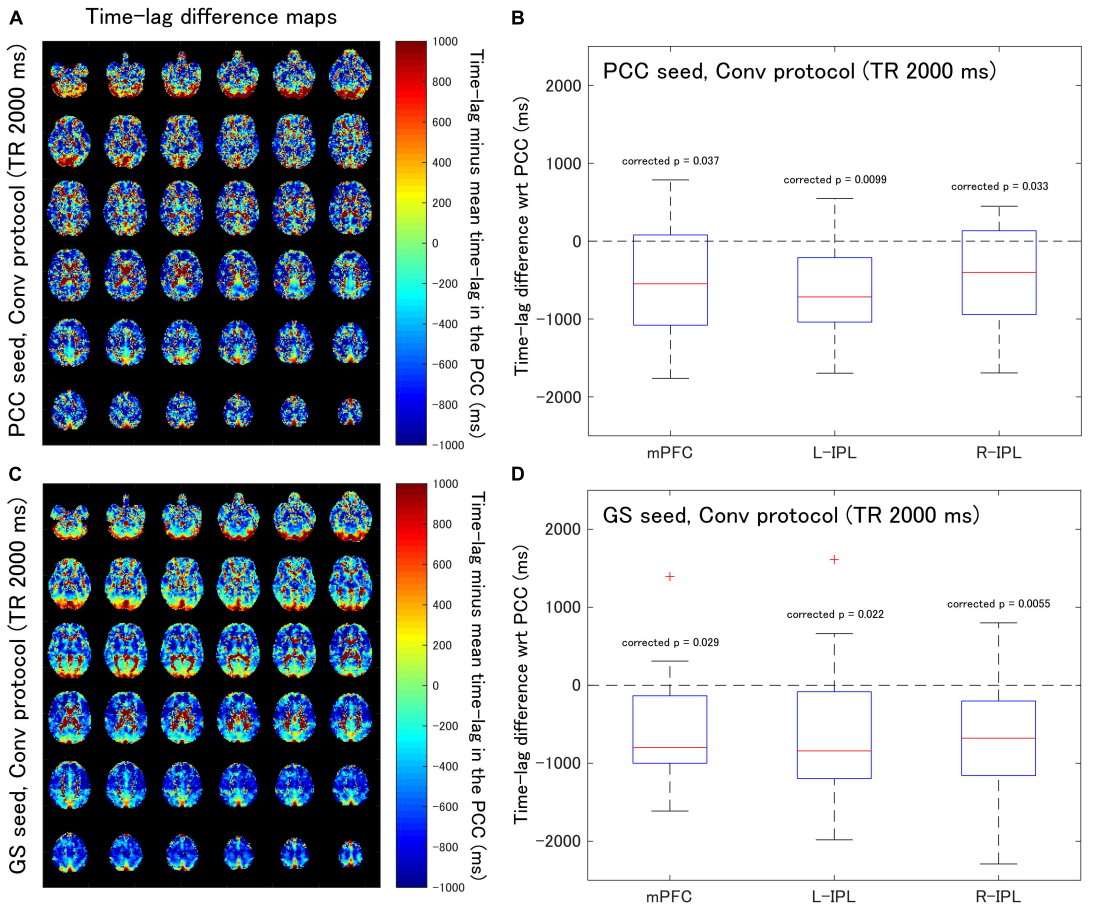

FIGURE 2
Assessment of the difference in time-lag between the PCC and each of the DMN nodes for data acquired with the Conv protocol (TR = 2,000 ms). Eighteen healthy female volunteers participated in this study. **(A)** Time-lag difference maps calculated using the PCC seed. **(B)** Box-whisker plots of the time-lag difference estimated using the PCC seed for each of the mPFC, L-IPL, and R-IPL ROIs. **(C)** Time-lag difference maps calculated with the GS seed. **(D)** Box-whisker plots of the time-lag difference estimated using the GS seed for each of the mPFC, L-IPL and R-IPL ROIs.

and the mean values in the mPFC, L-IPL, and R-IPL were calculated using ROIs drawn with reference to the AAL brain template. The Wilcoxon signed-rank test was then performed to determine whether the time-lags of each of the DMN nodes with respect to the PCC were significantly different from zero. Bonferroni correction for multiple comparisons was performed by multiplying each *p*-value by 3 for the three different nodes of the DMN.

Correlation analysis

Spearman's correlation analysis was performed for the mPFC, L-IPL, and R-IPL to evaluate the relationship between the time-lag of neuronal activity, as represented by the PCC seed analysis, and the time-lag of SysLFOs, as represented by the GS seed analysis. As comparisons were performed for the three different nodes of the DMN, Bonferroni correction for multiple comparisons was applied by multiplying each *p*-value by 3.

Results

Time-lag analysis

Supplementary Figure 1 contains the cross-correlation curves and maps at each Δ for one of the subjects (No. 7). Subsequently, time-lag difference maps were generated (**Figures 2A,C**, **3A,C**), and time-lag analysis was performed on the Conv and MB protocol data for both the PCC and GS seeds.

For the Conv protocol data (**Figure 2**), the median time-lags estimated with the PCC seed for the mPFC, L-IPL, and R-IPL ROIs differed from the time-lag of the PCC ROI by −547.7, −716.4, and −401.8 ms, respectively (**Figure 2B**). These differences in time-lag all differed significantly from zero (mPFC, corrected $p = 0.037$; L-IPL, corrected $p = 0.0099$; R-IPL, corrected $p = 0.033$), indicating that the responses were advanced in time compared to that of the PCC. Additionally, the median time-lags estimated using the GS seed differed from that of the PCC ROI by −799.1, −841.6, and −678.7 ms for the

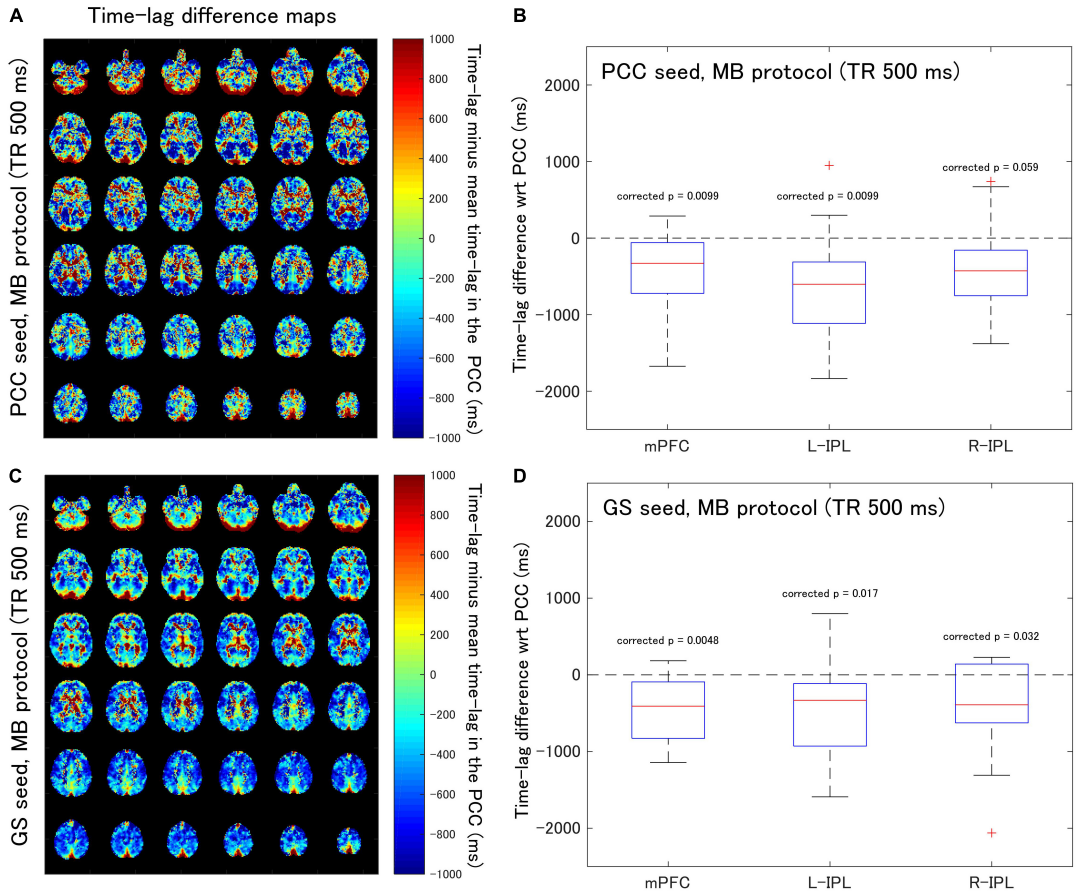

FIGURE 3
Assessment of the difference in time-lag between the PCC and each of the DMN nodes for data acquired with the MB protocol (TR = 500 ms). Eighteen healthy female volunteers participated in this study. **(A)** Time-lag difference maps calculated using the PCC seed. **(B)** Box-whisker plots of the time-lag difference estimated using the PCC seed for each of the mPFC, L-IPL and R-IPL ROIs. **(C)** Time-lag difference maps calculated with the GS seed. **(D)** Box-whisker plots of the time-lag difference estimated using the GS seed for each of the mPFC, L-IPL and R-IPL ROIs.

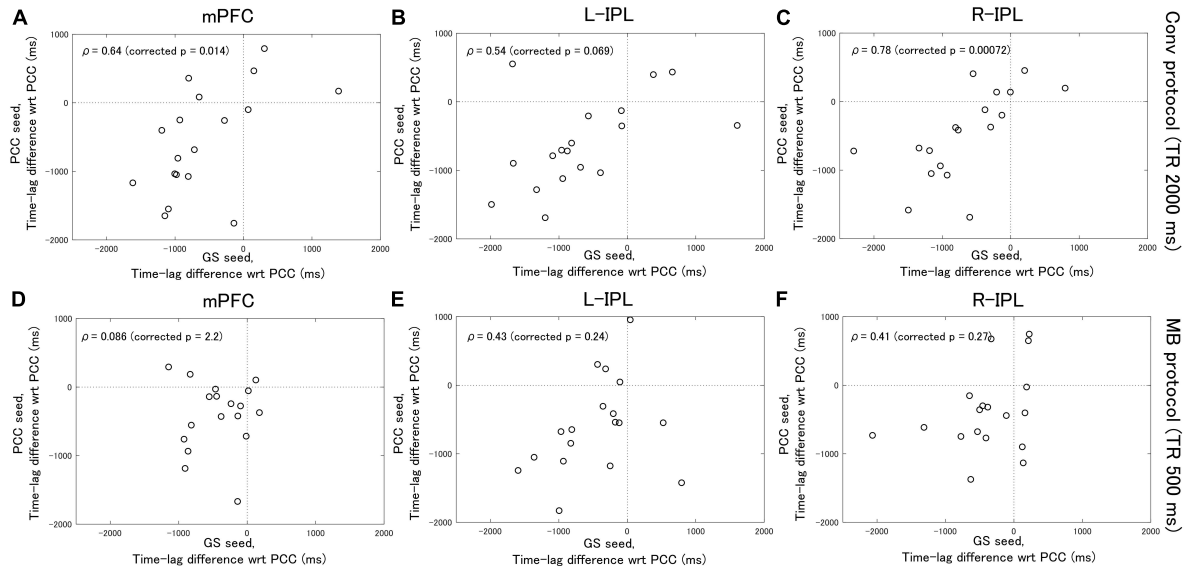

FIGURE 4
Spearman's correlation analysis between the time-lag differences calculated with the PCC seed and those calculated with the GS seed. Eighteen healthy female volunteers participated in this study. **(A–C)** Results calculated from the Conv protocol data. **(D–F)** Results calculated from the MB protocol data. The correlations obtained for the MB protocol data were considerably weaker than for the Conv protocol data.

mPFC, L-IPL, and R-IPL ROIs, respectively (Figure 2D). The response in each ROI was advanced in time with respect to the PCC because the differences were all significantly different from zero (mPFC, corrected p = 0.029; L-IPL, corrected p = 0.022; R-IPL, corrected p = 0.0055).

When time-lag analysis was performed on the MB protocol data (Figure 3), the median time-lags estimated with the PCC seed differed from the time-lag of the PCC ROI by −329.3, −602.4, and −427.8 ms for the mPFC, L-IPL, and R-IPL ROIs, respectively (Figure 3B). The differences for the mPFC (corrected p = 0.0099) and L-IPL (corrected p = 0.0099) were significantly different from zero, implying a faster response in comparison to the PCC for those ROIs. However, the response in the R-IPL did not significantly differ from that of the PCC (corrected p = 0.059). After analysing the data using the GS seed, it was found that the median time-lags of the mPFC, L-IPL, and R-IPL ROIs differed from the time-lag of the PCC ROI by −408.5, −331.2, and −390.6 ms, respectively (Figure 3D). These results were all significantly different from zero (mPFC, corrected p = 0.0048; L-IPL, corrected p = 0.017; R-IPL, corrected p = 0.032), so the responses were advanced in time compared to the PCC.

Correlation analysis

Analysis of the Conv protocol data found substantial correlations between the time-lag differences calculated with the PCC seed (see Figure 2B) and those calculated with the GS seed (see Figure 2D). Spearman's correlation coefficient for the mPFC, L-IPL, and R-IPL was 0.64 (corrected p = 0.014, Figure 4A), 0.54 (corrected p = 0.069, Figure 4B), and 0.78 (corrected p = 0.00072, Figure 4C), respectively. In contrast, applying a similar analysis to the MB protocol data found that the correlation between the time-lag differences calculated with the PCC (see Figure 3B) and GS (see Figure 3D) seeds was much weaker. Spearman's correlation coefficient for the mPFC, L-IPL, and R-IPL was 0.086 (corrected p = 2.2, Figure 4D), 0.43 (corrected p = 0.24, Figure 4E), and 0.41 (corrected p = 0.27, Figure 4F), respectively.

Discussion

The time-lag analysis results indicate that, even though the acquisition sampling rate of the Conv protocol is four times less than that of the MB protocol, a time-lag between nodes of the DMN was detectable with both protocols. In addition, the presence of significant time-lags between nodes indicates that the response in different nodes is highly correlated, but not simultaneous.

Based on the results of previous studies (Biswal, 2012; Erdoğan et al., 2016), in this manuscript the PCC and GS seeds are taken to represent the response due to neuronal activity and SysLFOs, respectively. The time-lag analysis with the PCC seed therefore provides an estimate of the delay in neuronal activity between the PCC and the other nodes of the DMN. Similarly, the time-lag analysis with the GS seed provides an estimate

of the delay between the response in different regions of the brain due to SysLFOs. Correlation analysis was then performed to compare the delays estimated with each seed. The fact that significant correlations between the delays are found for the Conv protocol data indicates that the arrival of the response due to neuronal activity cannot be distinguished from the arrival of the response due to SysLFOs. That is, functional connectivity evaluated from Conv protocol data may be heavily influenced by SysLFO signals that are of non-neuronal origin.

On the other hand, the correlation coefficients calculated from the MB protocol data suggest that the arrival of the response due to neuronal activity can be distinguished from the arrival of the response due to SysLFOs in the frequency domain 0.01–0.1 Hz. That is, the higher sampling rate of the MB protocol may allow the SysLFO contribution to the signal to be isolated. Therefore, with suitable adjustments to the analysis procedures, multiband EPI acquisition of rsfMRI data may permit resting-state neuronal activity to be studied without the obfuscating non-neuronal effects of SysLFOs.

There a number of limitations that could have affected the results of this study. First, a relatively high multiband factor of six was employed when acquiring the MB protocol data. With such a high factor it is possible that there was signal leakage from one slice into another simultaneously excited slice (Todd et al., 2016), and this may have influenced the results of the time-lag and correlation analysis. Experiments trialing multiple multiband factors and TR protocols would be required to determine whether the leakage has a significant effect on the results. Second, even though standard motion correction, registration and normalization were applied to the data, it is impossible to guarantee that imperfect correction has not affected the results to some degree. In a similar way, although the data was bandpass filtered, it is not possible to rule out some aliasing of high frequency BOLD signal into the filtered data as noise that influences the results.

Conclusion

In conclusion, a time-lag between nodes of the DMN was detectable with both the Conv and MB acquisition protocols, with the responses in the mPFC, L-IPL, and R-IPL being temporally advanced with respect to that in the PCC. Correlation analysis of the Conv protocol data suggested that SysLFOs substantially influence the apparent time-lag of neuronal activity. However, correlation analysis of the MB protocol data implied that the effects of SysLFOs and neuronal activity on the BOLD response may be separated. Therefore, using a higher time-resolution acquisition method for rsfMRI might help to distinguish neuronal activity induced changes to the BOLD response from those induced by SysLFOs.

Data availability statement

The raw data supporting the conclusions of this article will be made available by the authors, without undue reservation.

Ethics statement

The studies involving human participants were reviewed and approved by the Institutional Review Board of the National Institutes for Quantum Science and Technology (research protocol # 16-031). The patients/participants provided their written informed consent to participate in this study.

Author contributions

All authors contributed to the conception, design, analysis, and interpretation of the data as well as to drafting the manuscript and revising it critically and read and approved the final version of the manuscript.

Funding

This research was supported by a AMED Brain/MINDS Beyond program Grant Nos. JP22dm0307002 and JP22dm0307104.

Conflict of interest

The authors declare that the research was conducted in the absence of any commercial or financial relationships that could be construed as a potential conflict of interest.

Publisher's note

Supplementary material

The Supplementary Material for this article can be found online at: https://www.frontiersin.org/articles/10.3389/fnins.2022.961686/full#supplementary-material

References

Barkhof, F., Haller, S., and Rombouts, S. A. R. B. (2014). Resting-state functional MR imaging: a new window to the brain. *Radiology* 272, 29–49. doi: 10.1148/radiol.14132388

Biswal, B. B. (2012). Resting state fMRI: a personal history. *NeuroImage* 62, 938–944. doi: 10.1016/j.neuroimage.2012.01.090

Buxton, R. B., Uludağ, K., Dubowitz, D. J., and Liu, T. T. (2004). Modeling the hemodynamic response to brain activation. *NeuroImage* 23(Suppl. 1), S220–S233. doi: 10.1016/j.neuroimage.2004.07.013

Chang, C., Cunningham, J. P., and Glover, G. H. (2009). Influence of heart rate on the BOLD signal: the cardiac response function. *NeuroImage* 44, 857–869. doi: 10.1016/j.neuroimage.2008.09.029

Chang, C., and Glover, G. H. (2009). Relationship between respiration, end-tidal CO2, and BOLD signals in resting-state fMRI. *NeuroImage* 47, 1381–1393. doi: 10.1016/j.neuroimage.2009.04.048

Erdoğan, S. B., Tong, Y., Hocke, L. M., Lindsey, K. P., and deB Frederick, B. (2016). Correcting for blood arrival time in global mean regression enhances functional connectivity analysis of resting state fMRI-BOLD signals. *Front. Hum. Neurosci.* 10:311. doi: 10.3389/fnhum.2016.00311

Feinberg, D. A., Moeller, S., Smith, S. M., Auerbach, E., Ramanna, S., Gunther, M., et al. (2010). Multiplexed echo planar imaging for sub-second whole brain fmri and fast diffusion imaging. *PLoS One* 5:e0015710. doi: 10.1371/journal.pone.0015710

Golestani, A. M., Chang, C., Kwinta, J. B., Khatamian, Y. B., and Jean Chen, J. (2015). Mapping the end-tidal CO2 response function in the resting-state BOLD fMRI signal: spatial specificity, test-retest reliability and effect of fMRI sampling rate. *NeuroImage* 104, 266–277. doi: 10.1016/j.neuroimage.2014.10.031

Greicius, M. D., Krasnow, B., Reiss, A. L., and Menon, V. (2003). Functional connectivity in the resting brain: a network analysis of the default mode hypothesis. *Proc. Natl. Acad. Sci. U.S.A.* 100, 253–258. doi: 10.1073/pnas.0135058100

Greicius, M. D., Srivastava, G., Reiss, A. L., and Menon, V. (2004). Default-mode network activity distinguishes Alzheimer's disease from healthy aging: evidence from functional MRI. *Proc. Natl. Acad. Sci. U.S.A.* 101, 4637–4642. doi: 10.1073/pnas.0308627101

Hirano, Y., Stefanovic, B., and Silva, A. C. (2011). Spatiotemporal evolution of the functional magnetic resonance imaging response to ultrashort stimuli. *J. Neurosci.* 31, 1440–1447. doi: 10.1523/JNEUROSCI.3986-10.2011

Hirano, Y., Yen, C. C., Liu, J. V., Mackel, J. B., Merkle, H., Nascimento, G. C., et al. (2018). Investigation of the BOLD and CBV fMRI responses to somatosensory stimulation in awake marmosets (*Callithrix jacchus*). *NMR Biomed.* 31:3864. doi: 10.1002/nbm.3864

Julien, C. (2006). The enigma of Mayer waves: facts and models. *Cardiovasc. Res.* 70, 12–21. doi: 10.1016/j.cardiores.2005.11.008

Liang, M., Zhou, Y., Jiang, T., Liu, Z., Tian, L., Liu, H., et al. (2006). Widespread functional disconnectivity in schizophrenia with resting-state functional magnetic resonance imaging. *NeuroReport* 17, 209–213. doi: 10.1097/01.wnr.0000198434.06518.b8

Liu, T. T. (2013). Neurovascular factors in resting-state functional MRI. *NeuroImage* 80, 339–348. doi: 10.1016/j.neuroimage.2013.04.071

Murphy, K., Birn, R. M., and Bandettini, P. A. (2013). Resting-state fMRI confounds and cleanup. *NeuroImage* 80, 349–359. doi: 10.1016/j.neuroimage.2013.04.001

Nilsson, H., and Aalkjaer, C. (2003). Vasomotion: mechanisms and physiological importance. *Mol. Intervent.* 3, 79–89. doi: 10.1124/mi.3.2.79

Obata, T., Liu, T. T., Miller, K. L., Luh, W. M., Wong, E. C., Frank, L. R., et al. (2004). Discrepancies between BOLD and flow dynamics in primary and supplementary motor areas: application of the balloon model to the interpretation of BOLD transients. *NeuroImage* 21, 144–153. doi: 10.1016/j.neuroimage.2003.08.040

Ogawa, S., Lee, T. M., Kay, A. R., and Tank, D. W. (1990). Brain magnetic resonance imaging with contrast dependent on blood oxygenation (cerebral blood flow/brain metabolism/oxygenation). *Proc. Natl. Acad. Sci. U.S.A.* 87, 9868–9872.

Rivadulla, C., de Labra, C., Grieve, K. L., and Cudeiro, J. (2011). Vasomotion and neurovascular coupling in the visual thalamus in vivo. *PLoS One* 6:e0028746. doi: 10.1371/journal.pone.0028746

Sassaroli, A., Pierro, M., Bergethon, P. R., and Fantini, S. (2012). Low-frequency spontaneous oscillations of cerebral hemodynamics investigated with near-infrared spectroscopy: a review. *IEEE J. Select. Top. Quant. Electron.* 18, 1478–1492. doi: 10.1109/JSTQE.2012.2183581

Todd, N., Moeller, S., Auerbach, E. J., Yacoub, E., Flandin, G., and Weiskopf, N. (2016). Evaluation of 2D multiband EPI imaging for high-resolution, whole-brain, task-based fMRI studies at 3T: sensitivity and slice leakage artifacts. *NeuroImage* 124, 32–42. doi: 10.1016/j.neuroimage.2015.08.056

Tong, Y., Frederick, B. (2014). Tracking cerebral blood flow in BOLD fMRI using recursively generated regressors. *Hum. Brain Mapp.* 35, 5471–5485. doi: 10.1002/hbm.22564

Tong, Y., Hocke, L. M., Nickerson, L. D., Licata, S. C., Lindsey, K. P., and Frederick, B. D. (2013). Evaluating the effects of systemic low frequency oscillations measured in the periphery on the independent component analysis results of resting state networks. *NeuroImage* 76, 202–215. doi: 10.1016/j.neuroimage.2013.03.019

Tong, Y., Lindsey, K. P., Hocke, L. M., Vitaliano, G., Mintzopoulos, D., and Frederick, B. D. (2017). Perfusion information extracted from resting state functional magnetic resonance imaging. *J. Cerebr. Blood Flow Metab.* 37, 564–576. doi: 10.1177/0271678X16631755

Wise, R. G., Ide, K., Poulin, M. J., and Tracey, I. (2004). Resting fluctuations in arterial carbon dioxide induce significant low frequency variations in BOLD signal. *NeuroImage* 21, 1652–1664. doi: 10.1016/j.neuroimage.2003.11.025

frontiers | Frontiers in Neuroscience

TYPE Original Research
PUBLISHED 30 September 2022
DOI 10.3389/fnins.2022.952940

OPEN ACCESS

EDITED BY
Chitresh Bhushan,
GE Global Research, United States

REVIEWED BY
Debo Dong,
Southwest University, China
Linling Li,
Shenzhen University, China

*CORRESPONDENCE
Yongxin Li
yxin-li@163.com
Wenhua Huang
13822232749@139.com

SPECIALTY SECTION
This article was submitted to Brain Imaging Methods, a section of the journal Frontiers in Neuroscience

RECEIVED 25 May 2022
ACCEPTED 14 September 2022
PUBLISHED 30 September 2022

CITATION
Wang Y, Li Y, Yang L and Huang W (2022) Altered topological organization of resting-state functional networks in children with infantile spasms. *Front. Neurosci.* 16:952940. doi: 10.3389/fnins.2022.952940

Altered topological organization of resting-state functional networks in children with infantile spasms

Ya Wang[1], Yongxin Li[2]*, Lin Yang[3] and Wenhua Huang[1]*

[1]School of Basic Medical Sciences, Engineering Research Center for Translation of Medical 3D Printing Application, Guangdong Provincial Key Laboratory of Digital Medicine and Biomechanics, National Key Discipline of Human Anatomy, Southern Medical University, Guangzhou, China, [2]Formula-Pattern Research Center, School of Traditional Chinese Medicine, Jinan University, Guangzhou, China, [3]Department of Anesthesiology, The Fifth Affiliated Hospital of Southern Medical University, Guangzhou, China

Covering neuroimaging evidence has demonstrated that epileptic symptoms are associated with the disrupted topological architecture of the brain network. Infantile spasms (IS) as an age-specific epileptic encephalopathy also showed abnormal structural or functional connectivity in specific brain regions or specific networks. However, little is known about the topological alterations of whole-brain functional networks in patients with IS. To fill this gap, we used the graph theoretical analysis to investigate the topological properties (whole-brain small-world property and modular interaction) in 17 patients with IS and 34 age- and gender-matched healthy controls. The functional networks in both groups showed efficient small-world architecture over the sparsity range from 0.05 to 0.4. While patients with IS showed abnormal global properties characterized by significantly decreased normalized clustering coefficient, normalized path length, small-worldness, local efficiency, and significantly increased global efficiency, implying a shift toward a randomized network. Modular analysis revealed decreased intra-modular connectivity within the default mode network (DMN) and fronto-parietal network but increased inter-modular connectivity between the cingulo-opercular network and occipital network. Moreover, the decreased intra-modular connectivity in DMN was significantly negatively correlated with seizure frequency. The inter-modular connectivity between the cingulo-opercular and occipital network also showed a significant correlation with epilepsy frequency. Together, the current study revealed the disrupted topological organization of the whole-brain functional network, which greatly advances our understanding of neuronal architecture in IS and may contribute to predict the prognosis of IS as disease biomarkers.

KEYWORDS

infantile spasm, graph theory, small-world, modularity, functional brain network

Introduction

Multiple studies have found that epilepsy is a systemic disorder with disrupted brain networks, rather than a single source of pathophysiology in the human brain (Bernhardt et al., 2013; Vaessen et al., 2013). Infantile spasms (IS), one kind of epileptic encephalopathy, are characterized by clinical spasms and hypsarrhythmia on electroencephalogram (EEG), as well as delayed brain development or regression (Pavone et al., 2014; D'Alonzo et al., 2018). Although, currently, IS may cease by applying antiepileptic drugs, or spontaneously, a majority of IS children are left with other seizure types and motor delay, and often neurocognitive troubles. Considerable efforts have been made in the past decade, but the neural mechanism of IS remains largely unclear.

With the development of neuroimaging methods, understanding the mechanisms of IS has become a research priority currently. Functional magnetic resonance imaging (fMRI) provides an efficient and non-invasive way to explore the functional properties of the human brain (Bullmore, 2012; Goodman and Szaflarski, 2021). Our previous studies had shown that the seizure of IS was related to the impairment of the single functional network called default mode network (DMN) through regional homogeneity and functional connectivity analysis (Tan et al., 2016; Wang et al., 2017). Altered structural remodeling in the temporal lobe was also confirmed in patients with IS with voxel-based morphometry and tract-based spatial statistics (Fosi et al., 2015). Another study also evaluated initial MRI abnormalities with T2-weighted images in cerebral structure in IS children (Harini et al., 2018). Taken together, this neuroimage evidence highlights the abnormal functional interconnections and structural alternations of the brain in IS. The broadly distributed brain changes can be understood by the view of the brain network. The whole brain can be considered as a complex network to integrate various information inputs across multiple-distributed systems (He and Evans, 2010; Barch, 2013). In epilepsy, the seizure spreads across the cortical surface based on the network pathways. Broadly, changes in brain activation and structure would be detected. Thus, the network approach is an important way to explore the neural mechanism of epilepsy. The frequently used network approach is a seed-based functional connectivity. Although this approach can provide information about how regions are related to each other, it cannot reveal whole-brain connectivity patterns and topological organization. Complex network analysis is a powerful tool to map and characterize the connectivity patterns of the brain. A complex network analysis of IS can provide a complete view of how the disease affects children's brains. Currently, few published articles have focused on the topological organization of the whole-brain functional networks in patients with IS.

Many complex networks, such as social network, own efficient and economical topology to support both segregated and integrated information transmission. The characteristics and methods in graph theory that describe network topological properties employed in the analysis of brain networks came from neuroimaging techniques (e.g., MR images, EEG, and magnetoencephalography) (Bassett and Bullmore, 2006). The human brain networks are confirmed to exist with optimized topological properties, such as the small-world principle, high transmission efficiency, and modularity structure using these methods (Bullmore and Sporns, 2009; Bullmore and Sporns, 2012). In addition, the alterations of these properties have been detected in various clinical disorders, such as attention deficit hyperactivity disorder (Chen et al., 2019), depressive disorder (Sheng et al., 2022), Alzheimer's disease (Kim et al., 2015), stroke (Li Y. et al., 2021), epilepsy (Li R. et al., 2021), and schizophrenia (Hadley et al., 2016). Recently, our group also used the graph theory method in children with generalized tonic-clonic seizures and demonstrated disrupted topological organizations of their functional and structural networks in epileptic children (Li et al., 2020a,b). They all together suggest that graph theory-based network analysis could reveal the underlying system-level changes of different processes, which promote our understanding of the physiological mechanism in some respects. Paldino et al. (2017) predicted focal epilepsy duration based on global features of resting-state fMRI by machine learning algorithm and confirmed that the global brain network metrics, including the modularity, path length, and global efficiency, were independently related to the epilepsy duration. Meanwhile, a previous study also found abnormal small-world metrics and network efficiency. For example, the functional brain network in focal epilepsy displayed decreased path length and small-worldness (Park et al., 2018) and the temporal lobe epilepsy also exhibits abnormal small-world properties (Liao et al., 2010). In addition, the modular organization based on the fMRI brain network also shows topological changes in different epilepsies (Liao et al., 2010; Vaessen et al., 2013, 2014; Xu et al., 2013). For example, the brain network in mesial temporal lobe epilepsy demonstrated decreased connectivity within the parietal and frontal lobes (Liao et al., 2010), while the brain network in frontal lobe epilepsy showed different connected patterns with increased inner-modular and decreased inter-modular connectivity (Vaessen et al., 2014). These above global network metrics with inconsistent changes could help define epilepsy-related markers. Therefore, in this study, we employed small-world topology and modularity to explore the topological changes of seizure to the functional brain's intrinsic activity in patients with IS.

Here, we hypothesized that patients with IS may undergo disruptions in the small-world properties and intra- and inter-modular connectivity. To test our hypothesis, we leveraged resting-state functional MR images, which were often used to measure intrinsic or spontaneous brain neuronal activity to construct the whole-brain functional connectome (Fox and Raichle, 2007). Then, by calculating the topological metrics

with graph theoretical approaches, we attempt to find whether the seizure disrupts the whole-brain topological architecture of functional networks in patients with IS. If so, whether the altered topological properties are associated with clinical characteristics?

Materials and methods

Subjects

A total of 51 right-handed subjects were recruited from the Shenzhen Children's Hospital, including 17 patients with IS (5 girls; mean 2.5 years) and 34 age- and sex-matched healthy control participants (13 girls; mean 2.5 years). The data of one patient had been removed because of excessive head motion. All patients underwent comprehensive clinical assessments, including detailed seizure history and video-EEG telemetry (23 channels), and met the following inclusion criteria: (1) typical clinical symptoms of IS, such as spasms, hypsarrhythmia, and impaired consciousness; (2) evident EEG findings and at least one seizure and consistent with the diagnosis of IS; and (3) without accompanying neurological or psychiatric disorders other than epilepsy. All the subjects accepted resting-state functional MRI scanning at the time of recruitment. Written informed consents were obtained from the parents/legal guardians of all enrolled children. This study was approved by the Ethics Committee of Shenzhen Children's Hospital, and the method was carried out in accordance with the approved guidelines.

Image acquisition

All functional MR images were performed on a 3T scanner (MAGNETOM Trio Tim, Siemens, Germany) with an eight-channel head coil at the Shenzhen Children's Hospital, Guangdong, China. We obtained the data using an echo planar imaging sequence with parameters: TR/TE = 2,000/30 ms, matrix = 94 × 94, flip angle = 90°, FOV = 220 mm × 220 mm, slice thickness = 3 mm, 36 interleaved axial slices, and 130 volumes. During the entire scanning procedure, all the subjects under 4 years were sedated with 10% choral hydrate (dosage: 50 mg/kg/time, the maximum dose was 1 g). In the IS group, four subjects (24%) were not sedated compared with seven subjects (21%) who were not sedated in the control group. Others were instructed to keep their eyes closed and relax their minds without falling asleep. To avoid these influences, we performed a relatively short scan, observed the whole process, and asked about their conditions after scanning. A foam cushion and headphones were used to minimize head motion and scanner noise.

Data processing

The resting-state functional MR image preprocessing was performed by the GRETNA toolbox[1], which is based on the Statistical Parametric Mapping (SPM8[2]) (Wang et al., 2015). First, to ensure magnetization equilibrium, we removed the first 10 volumes. Then, we performed slice timing correction and realignment aiming at the remaining volumes. One patient was excluded from further calculations based on the criterion of head motion >2 mm and/or rotations >2°. The corrected data were then normalized to the Montreal Neurological Institute (MNI) space by estimating their transformation to the echo-planar imaging (EPI) template (Ashburner and Friston, 1999) and resampled into a voxel size of 3 mm × 3 mm × 3 mm thereafter. The resulting images were spatial smoothing by convolution with an isotropic Gaussian kernel (FWHM = 6 mm), then temporally band-pass filtered (0.01–0.08 Hz) to minimize the effects of low-frequency drift and high-frequency physiological noise, such as respiratory and cardiac noise. Linear trends were also removed. The 24 head motion parameters (Yan et al., 2013), global signal (Birn, 2012; Power et al., 2014; Murphy and Fox, 2017; Khatri and Kwon, 2022), mean white matter (WM) signal, and cerebrospinal fluid (CSF) signal were also regressed out from each voxel's time course. Finally, image volumes with Framewise Displacement (FD) >0.5 were scrubbed by replacing the frames of poor quality with linear interpolation to reduce the effects of head motion (Power et al., 2012).

Functional connectivity matrix construction

In this section, we constructed individual inter-regional functional connectivity matrices, of which the network nodes stand for brain regions of interest (ROIs) and edges between nodes stand for functional associations among different regions of the brain. The whole brain was parcellated into 160 ROIs functionally to define the network nodes, and then the mean time series for each region was extracted. We chose Dosenbach's 160-ROIs parcelation as our scheme since it broadly covers both the cerebral cortex and cerebellum, and also these functionally defining ROIs were obtained through meta-analysis based on large fMRI activation data, which thus could provide the additional foundation for interpreting developmental changes (Dosenbach et al., 2010). The pairwise functional association was estimated among the time series by computing Pearson correlation coefficients. We also performed Fisher's r-to-z transformation to improve the normality of the correlations. For

1 http://www.nitrc.org/projects/gretna/

2 http://www.fil.ion.ucl.ac.uk/spm/

network topology, we chose positive correlations to minimize effects on test–retest reliability. To exclude the confounding effects of spurious relationships in functional matrices, we applied a sparsity threshold to ensure the same number of edges for each matrix by applying a subject-specific connectivity strength threshold, and therefore, permitting an examination for relative network organization (He et al., 2009a). We set the sparsity threshold at multiple densities ranging from 0.05 to 0.4 at an interval of 0.02 based on previous experience to obtain a more efficient binary network than a random network.

Network metrics

In the study, we computed the properties of the functional networks with routines from the GRETNA toolbox to reflect the topological alterations in patients with IS. The network topological properties at the global level were collected, including clustering coefficient (C_p), characteristic path length (L_p), local efficiency (E_{loc}), global efficiency (E_{glob}), and modularity.

Small-world as an attractive architecture for the description of complex brain networks could reflect both specialized and integrated information processing and maximize the efficiency in information transmission at a low-wiring cost (Watts and Strogatz, 1998; Bassett and Bullmore, 2006; Li et al., 2014). The small-world topology is characterized through C_p and L_p, which quantifies the extent of local interconnectivity or cliquishness and the extent of overall communication efficiency of a network separately and could imply the segregation and integration of the network, respectively (Watts and Strogatz, 1998; Sporns and Zwi, 2004; Rubinov and Sporns, 2010). We benchmarked these above metrics against the random graph to evaluate the topological metrics of the brain networks (Maslov and Sneppen, 2002). Thus, in this study, the normalized clustering coefficient (γ), normalized path length (λ), and the small-worldness ($\sigma = \gamma/\lambda$) were leveraged to evaluate the small-world measures of the functional networks. Of note, the network that meets the criteria ($\gamma > 1$ and $\lambda \approx 1$ or $\sigma = \gamma/\lambda > 1$) was recognized as existing small-world properties, which thus ensures efficiently transmits information at both the local and global levels within this network.

Efficiency stands for the ability to exchange parallel information with low consumption and could be described at global and local levels (Latora and Marchiori, 2001). Meanwhile, the human brain functional network exist with economical small-world properties and could support the high-efficient transfer of parallel information (Achard and Bullmore, 2007). Therefore, we leverage the E_{loc} and E_{glob} to measure the ability to transmit information at the global and local levels separately (Latora and Marchiori, 2001).

Modules mean to a bunch of nodes joining together in closely integrated groups between which there are only sparser connections in a network (Newman, 2006). Here, modularity could contribute to identify groups of functionally associated components that possess specific biological functions. In this study, we adopted the parcelation schemes of Dos-160, which divides the whole brain into six sub-networks (e.g., cingulo-opercular network, fronto-parietal network, default network, sensorimotor network, occipital network, and cerebellum network) (Dosenbach et al., 2010). We then performed modularity analysis with spectral optimization in the undirected graphs following this parcelation. After that, we calculated the averaged functional connectivity strength within and between the six modules. Finally, we calculated the area under the curve (AUC) of the network measures, which provided us with a summarized scalar for the topological characterization of the brain networks independent of single threshold selection. The AUC has been confirmed to be sensitive to detecting topological alterations of brain disorders by previous studies (He et al., 2009a; Wang et al., 2009).

In addition, to confirm the result's robustness of the graph theory method, we also performed another parcelation scheme, which parcellates the whole brain into 264 ROIs functionally (Power et al., 2011).

Statistical analysis

Differences in network metrics

To determine whether there existed significant group differences in the network properties, we performed statistical comparisons with a two-sample t-test with the AUC, including λ, γ, σ, E_{glob}, and E_{loc} between the two groups ($p < 0.05$, FDR corrected). In addition, we also compared the AUC of the averaged functional connectivity strength over the sparsity from 0.05 to 0.4 within and between the modules ($p < 0.05$, FDR corrected). We performed all the above comparisons with GRETNA. Age and gender as additional covariates were regressed in all the analyses above. Moreover, the Hedges' g was used to calculate the effect size and quantify the difference in network metrics between the two groups with a relatively small sample size (Hentschke and Stüttgen, 2011). The magnitude of Hedges' g refers to the criteria of Cohen's D: d (0.01–0.19) = very small, d (0.2–0.49) = small, d (0.5–0.79) = medium, d (0.8–1.19) = large, d (1.2–1.99) = very large, and d ($\geq$ = 2) = huge (Sawilowsky, 2009).

Association of network measures and clinical characteristics

To detect whether the patient's clinical characteristics had a mutual influence on brain topological changes, Pearson correlation between the network metrics with significant differences and the epilepsy duration and frequency were calculated. We performed a partial correlation analysis to

remove the influence of age and sex. We used a significance level of $p < 0.05$, uncorrected.

Results

The basic demographical and clinical characteristics of subjects

A total of 51 right-handed subjects were recruited, which include 17 patients with IS and 34 age- and sex-matched healthy control participants. Pearson's Chi-square test showed no significant difference in gender ($\chi^2 = 0.386$, $p = 0.534$) and two sample t-tests showed no significant difference in age ($t = 0.016$, $p = 0.988$) between the two groups. Specific demographic and clinical information of all patients with IS is provided in **Table 1**.

Changes in brain functional network topological metrics

Over the sparsity range from 0.05 to 0.4 (step = 0.02), both the IS group and the control group exhibited high-efficiency small-world topology. In the premise of common small-world architecture, it appeared significant differences in the small-world parameters and network efficiency between the two groups. Compared with the controls, the IS group showed significantly decreased AUC of λ ($t = -4.268$, $p = 0.000$), γ ($t = -5.269$, $p = 0.000$), and σ ($t = -4.564$, $p = 0.000$) after FDR correction. The results are shown in **Figures 1A–C**. Regarding network efficiency, the AUC comparisons revealed a significantly increased E_{glob} ($t = 4.009$, $p = 0.000$) and significantly decreased E_{loc} ($t = -5.993$, $p = 0.000$) after FDR correction in the functional networks of patients with IS. The results of the network metrics are shown in **Figures 2A,B**. The λ and Eglob showed large effect sizes between the two groups (λ: Hedges' $g = -1.185$, 95% CI = −1.8125 to -0.558; Eglob: Hedges' $g = 1.117$, 95% CI = 0.495–1.740). The γ, σ, and Eloc exhibited very large effect sizes between the IS and control groups (γ: Hedges' $g = -1.435$, 95% CI = −2.082 to -0.788; σ: Hedges' $g = -1.270$, 95% CI = −1.903 to -0.636; Eloc: Hedges' $g = -1.610$, 95% CI = −2.272 to -0.946).

According to the modular architecture of the Dos-160 template, we found a significant reduction of the averaged functional connectivity strength within DMN (very large effect size), fronto-parietal network (large effect size), and significant enhancement of the averaged functional connectivity strength between occipital network and cingulo-opercular network (large effect size) after FDR correction. In addition, we found that the intra-modular connection decreased (medium effect size), such as the cingulo-opercular network and occipital network. On the contrary, the inter-modular connection mostly increased (medium effect size), such as DMN and fronto-parietal network, DMN and cingulo-opercular network, sensorimotor network, and occipital network without correction. The details of the results of the modules are shown in **Table 2** and **Figure 3**.

The results using 264 ROIs showed a similar trend with significantly decreased AUC of the λ, γ, σ (**Supplementary Figure 1**), Eloc, and significantly increased E_{glob} (**Supplementary Figure 2**) after FDR correction. We also found a significant decline of the averaged functional connectivity strength within DMN, fronto-parietal task control network, and significant ascension of the averaged functional connectivity strength between DMN and module 3 (salience, cingulo-opercular, etc.) after FDR correction, which is consistent with the results above. The details including the p-values and effect sizes are shown in **Supplementary Table 1**.

Association of network properties and clinical variables

We analyzed the correlations between clinical characteristics (such as epilepsy duration and frequency) and network properties (altered global topological parameters and edge number of modular connections) in patients with IS. Of note, the epilepsy frequency of one IS patient is missing. Partial correlation analysis showed that intra-modular connectivity within DMN was significantly negatively correlated with epilepsy frequency after controlling confounding variables ($r = -0.667$, $p = 0.009$; **Figure 4A**). The inter-modular connectivity between the cingulo-opercular and occipital network also showed a significant correlation with epilepsy frequency ($r = 0.665$, $p = 0.01$; **Figure 4B**). However, no remarkable correlation was found between the global topological metrics and clinical variables.

According to the results of 264 ROIs, we also found a significant negatively correlation between the connectivity within DMN and epilepsy frequency ($r = -0.746$, $p = 0.002$; **Supplementary Figure 3**).

Discussion

This is the first study to investigate the topological organization of functional networks in patients with IS with graph theoretical approaches according to brain functional MRI. In this study, we analyzed the alterations of small-world topology and modularity of the resting-state functional network in patients with IS and detected the correlation between the altered metrics and clinical properties. The results can be summarized as follows: (1) patients with IS showed a significant decrease in the small-worldness index and significant changes in their global and local network efficiency compared

TABLE 1 Characteristics of the IS patients.

Patient	Sex	Age (month)	Onset time (month)	Type	Pathogeny	Seizure frequency (time/day)	Antiepileptic drugs
1	F	23	4	No lesion	No	3–4	LEV
2	M	83	24	No lesion	No	10–20	VPA TPM
3	M	8	0.5	Lesion	Temporal lobe cortex dysplasia	1–2	LEV VPA
4	M	18	6	Lesion	Cerebromalacia of right hemisphere	3–15	TPM
5	M	20	13	Lesion	Cerebromalacia of left hemisphere and right temporal lobe	10–20	VPA OXC
6	M	82	24	No lesion	Bilateral gray matter heterotopia	1–2[a]	LEV TPM
7	M	80	6	Lesion	Cerebromalacia of left hemisphere	3–4	CBZ VPA
8	F	8	4	Lesion	Left hemisphere cleft deformity	2–3	CBZ
9	M	12	1	No lesion	No	5–10	VPA LEV
10	M	14		No lesion	Ventricular expansion		Ketogenic diet
11	F	13	5	No lesion	Bilateral parietal-occipital cortex dysplasia	7–10	TPM LEV
12	M	71	3	No lesion	Signal of right anterior cingulate cortex abnormal	1–2	TPM LEV
13	M	42	9	Lesion	Signal of right mesial temporal lobe abnormal	1–2	LEV OXC
14	M	5	5	No lesion	Bilateral pachygyria deformity	1[b]	TPM OXC
15	M	7	7	Lesion	Right temporal lobe lesion	1–3[c]	LEV
16	F	5	4	No lesion	No	4–5	LEV TPM
17	F	25	12	Lesion	Atrophy of the left hemisphere	10[a]	TPM OXC

[a]Time/year; [b]time/month; [c]time/week.
LEV, levetiracetam; VPA, valproic acid; TPM, topiramate; OXC, oxcarbazepine; CBZ, carbamazepine.

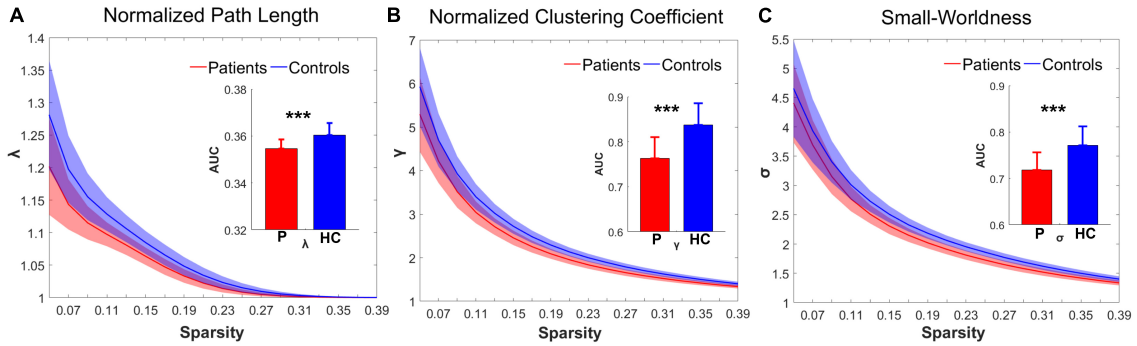

FIGURE 1
Group differences in the small-world topological metrics between the IS and control groups. In the range of sparsity (0.05–0.4), the topologies of **(A)** λ, **(B)** γ, and **(C)** σ in both groups exhibited small-world property. Bar charts plot the significant differences of the AUC of λ, γ, and σ between the IS children and controls ($p < 0.05$, FDR corrected). ***Significant difference between the two groups. P, patient group; HC, healthy control group.

with the normal controls; (2) significantly disrupted intra-module integration within DMN and fronto-parietal network and enhanced inter-module averaged functional connectivity strength between occipital network and cingulo-opercular network. (3) The altered connectivity strength within DMN was negatively correlated with the frequency of seizures, and the inter-modular connectivity between the occipital network and the cingulo-opercular network was positively correlated with the frequency of seizures in patients with IS. Taken together, our study provides strong evidence for the disrupting of topological organization in the functional network in IS based on two parcelation schemes. These findings may greatly deepen our understanding of the topological mechanism underlying the spontaneous brain intrinsic activity in IS.

Changes in small-world topology in patients with infantile spasms

According to the mathematical verdict, a network exists in small-world when it meets the following two conditions: $\gamma > 1$ and $\lambda \approx 1$. Previous studies involving complex brain networks

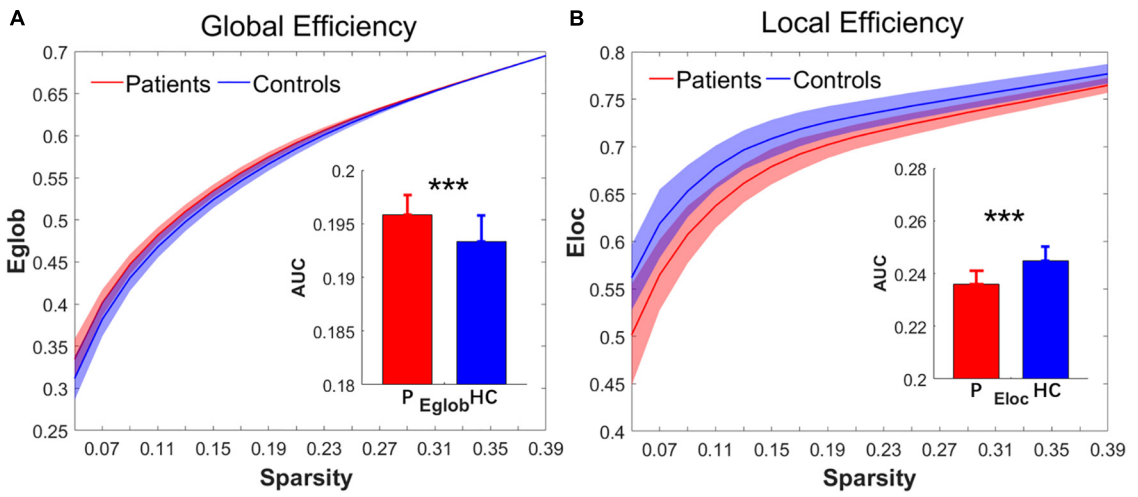

FIGURE 2
Group differences in the network efficiency of **(A)** E_{glob} and **(B)** Eloc between the IS and control groups in the range of sparsity (0.05–0.4). Bar charts plot the significant differences of the AUC of E_{glob} and E_{loc} between the IS children and controls ($p < 0.05$, FDR corrected). ***Significant difference between the two groups. P, patient group; HC, healthy control group.

TABLE 2 The altered edge numbers of connection within or between modules.

Modules	*p*	Correction	Effect size (Hedges' *g*)	Edge numbers of connection
Intra-modular connections				
DMN	0.000	FDR (0.004)	−1.207[a]	↓
Fronto-parietal network	0.001	FDR (0.013)	−1.026[b]	↓
Cingulo-opercular network	0.016	Uncorrected	−0.753[c]	↓
Occipital network	0.012	Uncorrected	−0.780[c]	↓
Inter-modular connections				
DMN and fronto-parietal network	0.047	Uncorrected	0.611[c]	↑
DMN and cingulo-opercular network	0.021	Uncorrected	0.675[c]	↑
Occipital and cingulo-opercular network	0.004	FDR (0.027)	0.894[b]	↑
Sensorimotor and occipital network	0.019	Uncorrected	0.730[c]	↑

[a]Very large; [b]large; [c]medium effect sizes.

also confirmed the existence of small-world topology in both healthy and diseased states (Bullmore and Sporns, 2012; Sporns, 2013; Wen et al., 2017; Li et al., 2018; Chen et al., 2019). In our study, both the IS and the control group also exhibited robust small-world properties. Small-world properties mean that the human brain showed an optimal architecture and the brain network has high efficiency in information transmission (Wang et al., 2010). Our recent work on children with generalized epilepsy has also proven the small-world property of the brain's functional and structural network (Li et al., 2020a,b).

Despite the common small-world topology, patients with IS showed decreased λ, γ, σ, E_{loc}, and increased E_{glob}. The short λ and high E_{glob} express a great ability to integrate global functional information dissemination in the larger and sparser network (Estrada and Hatano, 2008; Rubinov and Sporns, 2010). The IS-related changes in λ and E_{glob} could contribute to increased long-distance functional connections, which may enhance whole brain propagation of information flow. A previous study about small world neuronal network considered that phase synchronization as a function of the locality of network connections changes from local coherence to global coherence dependent on the distance between two neurons (Percha et al., 2005). This may contribute to our comprehension. The high γ and E_{loc} exhibit the ability for specialized processing to occur within densely interconnected groups of brain areas. In the present study, the IS-related decreases in γ and E_{loc} indicate a relatively sparse interconnection between local brain regions and decreased capacity to pass information within the neighbors, suggesting a possible decline in the separation function of brain cognitive processing. A study in epileptic patients with different handle methods also

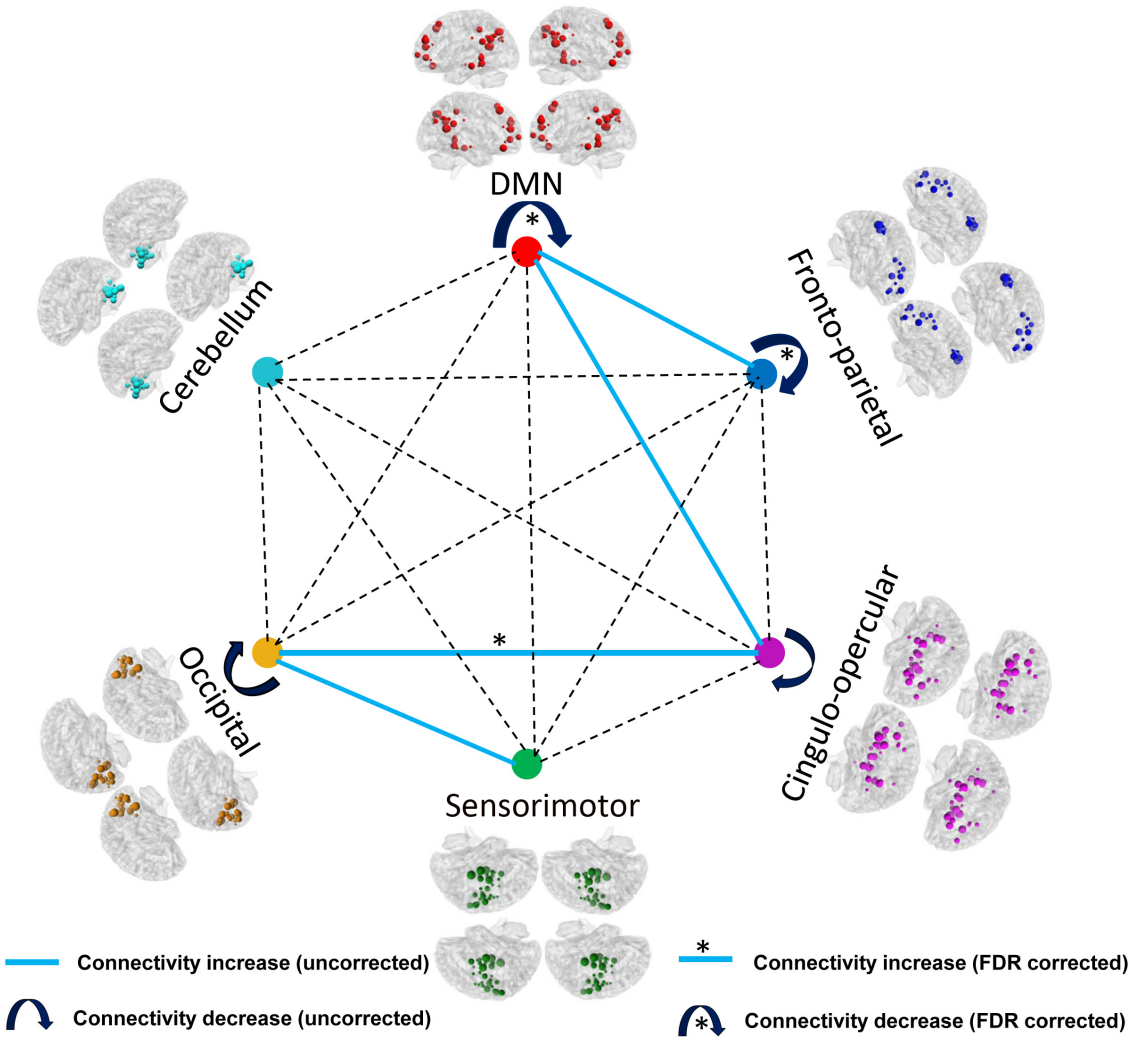

FIGURE 3
Comparison results of the AUC of the averaged functional connectivity strength within and between the modules ($p < 0.05$, FDR corrected).
*The connectivity can withstand the FDR correction.

exhibited the same alterations in network efficiency (Song et al., 2015). One recent research in epilepsy also found a significant decrease in E_{loc} and an increase in E_{glob} in children with generalized tonic-clonic seizures (Li et al., 2020a). The human brain functional network may through increasing the global efficiency compensate for the decreased efficiency of local regions in patients with IS. The lower σ reflects the disrupted proportion of integration and differentiation in the brain network in patients with IS.

To sum up, the current results show that the topological architecture of the global brain functional networks were disrupted in IS characterized by the reduced capacity of information dissemination between local regions and higher whole brain propagation of information flow. The current results may reflect the imbalance between functional segregation and integration in the brain networks of patients with IS and a tendency toward randomization to some extent.

Changes in modularity in patients with infantile spasms

Modular structure as an important organizational principle of complex biological networks has been widely studied in many other networks recently (Girvan and Newman, 2002; Guimera et al., 2005). Nowadays, increasing studies employ this property of modularity to study human brain networks and the results support the existence of the modular architecture in brain functional networks (Newman, 2006; He et al., 2009b; Meunier et al., 2010; Gallen and D'Esposito, 2019). Compared to global topological properties,

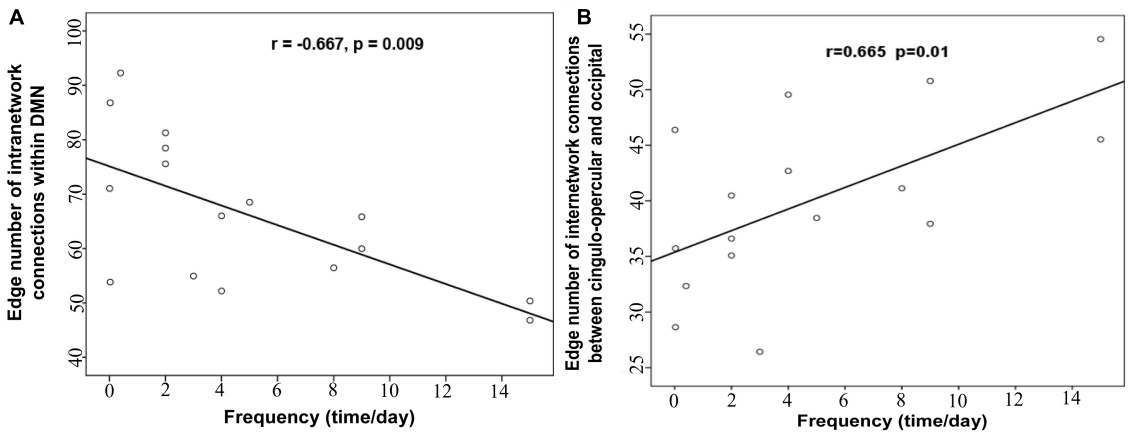

FIGURE 4
The correlation **(A)** between the intra-modular connections within DMN and the epilepsy frequency, **(B)** between the inter-modular connections and the epilepsy frequency.

the detection and characterization of modular architecture could contribute to materialize the groups of functionally and/or anatomically associated components, which are related with specific biological functions, and detect the alterations within and between them (Wang et al., 2010). In this study, we applied the modular parcelation schemes of Dos-160 to reduce the disturbance on account of fewer cases to detect the changes in local topological architecture within and between the six modules.

According to the results, there are significant differences in functional connectivity at the intermediate modular level between the healthy controls and the patients with IS. The number of connections within DMN and the fronto-parietal network was significantly reduced. In addition, the connections within the cingulo-opercular network and occipital network also decreased in spite of being non-significant. However, the functional connectivity strength between DMN and fronto-parietal network, DMN and cingulo-opercular network showed an increasing trend. The functional connectivity strength between the cingulo-opercular network and the occipital also showed a significant increase. DMN is considered to be related to a diverse series of functions including episodic memory, self-referential mental processing, and supervising the external environment (Buckner et al., 2008). In the brains in children with epilepsy, the abnormal internal activities in DMN may underlie poor brain development or regression. In the present study, the decreased connectivity strength in DMN may reflect disrupted neuronal activity within the DMN regions. This result is consistent with our previous study, which showed significantly reduced functional connectivity and lower low-frequency fluctuation in DMN regions in patients with IS (Wang et al., 2017). Other types of epilepsy with mental disorders also showed decreased integration within DMN even during resting interictal durations without interictal epileptiform discharges (Gonen et al., 2020; Parsons et al., 2020; Yang et al., 2021). Our previous studies in children with generalized tonic-clonic seizures also found significant decrease in betweenness centrality and functional connectivity of the DMN regions (Li et al., 2020a,b). The functional damage of DMN in these previous studies and our present results can explain the neuroimaging expression for the damage of cognitive function and the reduction in functional integrations of the DMN in children with epilepsy. In addition, our results also showed a significant negative correlation between the functional connectivity strength and epileptic frequency. This result further indicates that the epileptiform discharges in patients with IS may lead to and aggravate the disruption of neuronal activity in DMN regions, which triggers the reduction in blood oxygenation level-dependent on the increase of epileptic frequency (Shmuel et al., 2006). In this study, the decreased connections were mainly located within DMN and fronto-parietal network, while increased connections were mainly located between DMN and fronto-parietal network or cingulo-opercular network. The increased connections may represent a compensatory mechanism for the disrupted neuronal activity within DMN or the fronto-parietal network to transmit functional information. Enhanced inter-modular connections and decreased intra-modular connections indicated that the architecture of the brain networks was reconfigured in children with IS. Thus, our modular analysis results provide further evidence for the functional disruption of the whole-brain system in patients with IS.

The subcortical network, cingulo-opercular network, also showed increased functional connectivity strength with cortical network DMN and occipital network in children with IS. In addition, the functional connectivity strength between the

cingulo-opercular network and the occipital network was significantly correlated with epileptic frequency. This result indicates that the clinical seizure in patients with IS may contribute to the information transmission between cortical regions and subcortical nuclei. A previous study about the neuronal network with electroencephalogram considered that slow wave activity within the hypsarrhythmia in patients with IS was correlated with blood oxygenation level-dependent signal in brainstem, cortex, and subcortical structures (Siniatchkin et al., 2007). Another study with source analysis in West syndrome also supports the theory that hypsarrhythmia results from ascending brainstem pathways that project widely to subcortical nuclei and cerebral cortex (Japaridze et al., 2013). This theory contributes to our understanding of the underlying increased functional connectivity strength between cortical regions and subcortical nuclei. While the decreased functional connectivity strength within the cortex in our study might be compensated by increased connectivity between cortical regions and subcortical nuclei. Further study about the alterations in cerebral cortex structures would be performed.

Limitations

Several limitations need to be further addressed. First, some participants were sedated with 10% chloral hydrate during the neuroimaging scanning, which may affect the analysis results of the network topological metrics. We thus compared the two groups in which all the subjects without sedation were excluded. Even though we discovered similar global topological changes (**Supplementary Figure 4**), further comparison between the subjects with and without sedation in a large sample size will strengthen our conclusion. Second, the fMRI data length of 130 volumes is relatively short, which might affect the results to some extent. Longer scan time or scanning twice or more times at short time may strengthen the credibility of our results. Third, a larger sample size is needed to contribute to the stability of the results. In addition, combining multimodal neuroimaging data may help to clarify the pathological mechanism and uncover structure-function relationships in patients with IS.

Conclusion

In the current study, we employed graph theoretical analysis to detect the reorganization of brain functional topological architecture at the whole-brain level and the functional network level. The results demonstrate that the global properties and the modular structure were disrupted in patients with IS compared with healthy controls. The decreased γ and E_{loc} reflect the disrupted capacity of information transmission at the global level. At the same time, the decrease of functional connectivity strength within DMN, fronto-parietal network, cingulo-opercular network, and occipital network also support the alterations of global properties. In addition, the increased functional connectivity between modules also showed the same tendency with increased E_{glob}. Our findings suggest that the topological organization is disrupted in patients with IS. These properties may serve as indicators for us to understand the pathogenesis in patients with IS.

Data availability statement

The raw data supporting the conclusions of this article will be made available by the authors, without undue reservation.

Ethics statement

The studies involving human participants were reviewed and approved by the Ethics Committee of Shenzhen Children's Hospital. Written informed consent to participate in this study was provided by the participants' legal guardian/next of kin.

Author contributions

YW: software, writing—original draft preparation and reviewing and editing. YL: methodology, funding acquisition, and data curation. LY: writing—reviewing and editing. WH: conceptualization and supervision. All authors contributed to the article and approved the submitted version.

Funding

This study was supported by the National Natural Science Foundation of China (Nos. 81601483 and 31972915) as well as by the Medical Science and Technology Research Foundation of Guangdong Province (A2021076). This work was also supported by the Administration of Traditional Chinese Medicine of Guangdong Province (20221099), the Sanming Project of Medicine in Shenzhen (SZSM201612019), the Guangdong Basic and Applied Basic Research Foundation (2020B1515120001), the Guang Zhou Science and Technology Project (202201011812), and the Science and Technology Project of Guangdong Province (2015B010125005).

Acknowledgments

We would like to thank all the participants who collocated in this study for their kind cooperation.

Conflict of interest

The authors declare that the research was conducted in the absence of any commercial or financial relationships that could be construed as a potential conflict of interest.

Publisher's note

All claims expressed in this article are solely those of the authors and do not necessarily represent those of their affiliated organizations, or those of the publisher, the editors and the reviewers. Any product that may be evaluated in this article, or claim that may be made by its manufacturer, is not guaranteed or endorsed by the publisher.

Supplementary material

The Supplementary Material for this article can be found online at: https://www.frontiersin.org/articles/10.3389/fnins.2022.952940/full#supplementary-material

References

Achard, S., and Bullmore, E. (2007). Efficiency and cost of economical brain functional networks. *PLoS Comput. Biol.* 3:e17. doi: 10.1371/journal.pcbi.0030017

Ashburner, J., and Friston, K. J. (1999). Nonlinear spatial normalization using basis functions. *Hum. Brain Mapp.* 7, 254–266. doi: 10.1002/(SICI)1097-0193(1999)7:4<254::AID-HBM4>3.0.CO;2-G

Barch, D. M. (2013). Brain network interactions in health and disease. *Trends Cogn. Sci.* 17, 603–605. doi: 10.1016/j.tics.2013.09.004

Bassett, D. S., and Bullmore, E. (2006). Small-world brain networks. *Neuroscientist* 12, 512–523. doi: 10.1177/1073858406293182

Bernhardt, B., Hong, S.-J., Bernasconi, A., and Bernasconi, N. (2013). Imaging structural and functional brain networks in temporal lobe epilepsy. *Front. Hum. Neurosci.* 7:624. doi: 10.3389/fnhum.2013.00624

Birn, R. M. (2012). The role of physiological noise in resting-state functional connectivity. *Neuroimage* 62, 864–870. doi: 10.1016/j.neuroimage.2012.01.016

Buckner, R. L., Andrews-Hanna, J. R., and Schacter, D. L. (2008). The brain's default network: Anatomy, function, and relevance to disease. *Ann. N. Y. Acad. Sci.* 1124, 1–38. doi: 10.1196/annals.1440.011

Bullmore, E. (2012). The future of functional MRI in clinical medicine. *Neuroimage* 62, 1267–1271. doi: 10.1016/j.neuroimage.2012.01.026

Bullmore, E., and Sporns, O. (2009). Complex brain networks: Graph theoretical analysis of structural and functional systems. *Nat. Rev. Neurosci.* 10, 186–198. doi: 10.1038/nrn2575

Bullmore, E. T., and Sporns, O. (2012). The economy of brain network organization. *Nat. Rev. Neurosci.* 13, 336–349. doi: 10.1038/nrn3214

Chen, Y., Huang, X., Wu, M., Li, K., Hu, X., Jiang, P., et al. (2019). Disrupted brain functional networks in drug-naïve children with attention deficit hyperactivity disorder assessed using graph theory analysis. *Hum. Brain Mapp.* 40, 4877–4887. doi: 10.1002/hbm.24743

D'Alonzo, R., Rigante, D., Mencaroni, E., and Esposito, S. (2018). West syndrome: A review and guide for paediatricians. *Clin. Drug Investig.* 38, 113–124. doi: 10.1007/s40261-017-0595-z

Dosenbach, N. U., Nardos, B., Cohen, A. L., Fair, D. A., Power, J. D., Church, J. A., et al. (2010). Prediction of individual brain maturity using fMRI. *Science* 329, 1358–1361. doi: 10.1126/science.1194144

Estrada, E., and Hatano, N. (2008). Communicability in complex networks. *Phys. Rev. E* 77:036111. doi: 10.1103/PhysRevE.77.036111

Fosi, T., Chu, C., Chong, W. K., Clark, C., Scott, R. C., Boyd, S., et al. (2015). Quantitative magnetic resonance imaging evidence for altered structural remodeling of the temporal lobe in West syndrome. *Epilepsia* 56, 608–616. doi: 10.1111/epi.12907

Fox, M. D., and Raichle, M. E. (2007). Spontaneous fluctuations in brain activity observed with functional magnetic resonance imaging. *Nat. Rev. Neurosci.* 8, 700–711. doi: 10.1038/nrn2201

Gallen, C. L., and D'Esposito, M. (2019). Brain modularity: A biomarker of intervention-related plasticity. *Trends Cogn. Sci.* 23, 293–304. doi: 10.1016/j.tics.2019.01.014

Girvan, M., and Newman, M. E. (2002). Community structure in social and biological networks. *Proc. Natl. Acad. Sci. U.S.A.* 99, 7821–7826. doi: 10.1073/pnas.122653799

Gonen, O. M., Kwan, P., O'Brien, T. J., Lui, E., and Desmond, P. M. (2020). Resting-state functional MRI of the default mode network in epilepsy. *Epilepsy Behav.* 111:107308. doi: 10.1016/j.yebeh.2020.107308

Goodman, A. M., and Szaflarski, J. P. (2021). Recent advances in neuroimaging of epilepsy. *Neurotherapeutics* 18, 811–826. doi: 10.1007/s13311-021-01049-y

Guimera, R., Mossa, S., Turtschi, A., and Amaral, L. N. (2005). The worldwide air transportation network: Anomalous centrality, community structure, and cities' global roles. *Proc. Natl. Acad. Sci. U.S.A.* 102, 7794–7799. doi: 10.1073/pnas.0407994102

Hadley, J. A., Kraguljac, N. V., White, D. M., Ver Hoef, L., Tabora, J., and Lahti, A. C. (2016). Change in brain network topology as a function of treatment response in schizophrenia: A longitudinal resting-state fMRI study using graph theory. *NPJ Schizophr.* 2:16014. doi: 10.1038/npjschz.2016.14

Harini, C., Sharda, S., Bergin, A. M., Poduri, A., Yuskaitis, C. J., Peters, J. M., et al. (2018). Detailed magnetic resonance imaging (MRI) analysis in infantile spasms. *J. Child Neurol.* 33, 405–412. doi: 10.1177/0883073818760424

He, Y., Dagher, A., Chen, Z., Charil, A., Zijdenbos, A., Worsley, K., et al. (2009a). Impaired small-world efficiency in structural cortical networks in multiple sclerosis associated with white matter lesion load. *Brain* 132, 3366–3379. doi: 10.1093/brain/awp089

He, Y., Wang, J., Wang, L., Chen, Z. J., Yan, C., Yang, H., et al. (2009b). Uncovering intrinsic modular organization of spontaneous brain activity in humans. *PLoS One* 4:e5226. doi: 10.1371/journal.pone.0005226

He, Y., and Evans, A. (2010). Graph theoretical modeling of brain connectivity. *Curr. Opin. Neurol.* 23, 341–350. doi: 10.1097/WCO.0b013e32833aa567

Hentschke, H., and Stüttgen, M. C. (2011). Computation of measures of effect size for neuroscience data sets. *Eur. J. Neurosci.* 34, 1887–1894. doi: 10.1111/j.1460-9568.2011.07902.x

Japaridze, N., Muthuraman, M., Moeller, F., Boor, R., Anwar, A. R., Deuschl, G., et al. (2013). Neuronal networks in West syndrome as revealed by source analysis and renormalized partial directed coherence. *Brain Topogr.* 26, 157–170. doi: 10.1007/s10548-012-0245-y

Khatri, U., and Kwon, G.-R. (2022). Alzheimer's disease diagnosis and biomarker analysis using resting-state functional MRI functional brain network with multi-measures features and hippocampal subfield and amygdala volume of structural MRI. *Front. Aging Neurosci.* 14:818871. doi: 10.3389/fnagi.2022.818871

Kim, W. H., Adluru, N., Chung, M. K., Okonkwo, O. C., Johnson, S. C., Bendlin, B. B., et al. (2015). Multi-resolution statistical analysis of brain connectivity graphs in preclinical Alzheimer's disease. *Neuroimage* 118, 103–117. doi: 10.1016/j.neuroimage.2015.05.050

Latora, V., and Marchiori, M. (2001). Efficient behavior of small-world networks. *Phys. Rev. Lett.* 87:198701. doi: 10.1103/PhysRevLett.87.198701

Li, G., Nie, J., Wang, L., Shi, F., Gilmore, J. H., Lin, W., et al. (2014). Measuring the dynamic longitudinal cortex development in infants by reconstruction of temporally consistent cortical surfaces. *Neuroimage* 90, 266–279. doi: 10.1016/j.neuroimage.2013.12.038

Li, R., Wang, H., Wang, L., Zhang, L., Zou, T., Wang, X., et al. (2021). Shared and distinct global signal topography disturbances in subcortical and cortical networks in human epilepsy. *Hum. Brain Mapp.* 42, 412–426. doi: 10.1002/hbm.25231

Li, Y., Chen, Q., and Huang, W. (2020a). Disrupted topological properties of functional networks in epileptic children with generalized tonic-clonic seizures. *Brain Behav.* 10:e01890. doi: 10.1002/brb3.1890

Li, Y., Wang, Y., Wang, Y., Wang, H., Li, D., Chen, Q., et al. (2020b). Impaired topological properties of gray matter structural covariance network in epilepsy children with generalized tonic-clonic seizures: A graph theoretical analysis. *Front. Neurol.* 11:253. doi: 10.3389/fneur.2020.00253

Li, Y., Yu, Z., Wu, P., and Chen, J. (2021). The disrupted topological properties of structural networks showed recovery in ischemic stroke patients: A longitudinal design study. *BMC Neurosci.* 22:47. doi: 10.1186/s12868-021-00652-1

Li, Z., Chen, R., Guan, M., Wang, E., Qian, T., Zhao, C., et al. (2018). Disrupted brain network topology in chronic insomnia disorder: A resting-state fMRI study. *Neuroimage Clin.* 18, 178–185. doi: 10.1016/j.nicl.2018.01.012

Liao, W., Zhang, Z., Pan, Z., Mantini, D., Ding, J., Duan, X., et al. (2010). Altered functional connectivity and small-world in mesial temporal lobe epilepsy. *PLoS One* 5:e8525. doi: 10.1371/journal.pone.0008525

Maslov, S., and Sneppen, K. (2002). Specificity and stability in topology of protein networks. *Science* 296, 910–913. doi: 10.1126/science.1065103

Meunier, D., Lambiotte, R., and Bullmore, E. T. (2010). Modular and hierarchically modular organization of brain networks. *Front. Neurosci.* 4:200. doi: 10.3389/fnins.2010.00200

Murphy, K., and Fox, M. D. (2017). Towards a consensus regarding global signal regression for resting state functional connectivity MRI. *Neuroimage* 154, 169–173. doi: 10.1016/j.neuroimage.2016.11.052

Newman, M. E. (2006). Modularity and community structure in networks. *Proc. Natl. Acad. Sci. U.S.A.* 103, 8577–8582. doi: 10.1073/pnas.0601602103

Paldino, M. J., Zhang, W., Chu, Z. D., and Golriz, F. (2017). Metrics of brain network architecture capture the impact of disease in children with epilepsy. *Neuroimage Clin.* 13, 201–208. doi: 10.1016/j.nicl.2016.12.005

Park, K., Lee, B., Shin, K., Ha, S., Park, J., Kim, T., et al. (2018). Progressive topological disorganization of brain network in focal epilepsy. *Acta Neurol. Scand.* 137, 425–431. doi: 10.1111/ane.12899

Parsons, N., Bowden, S. C., Vogrin, S., and D'Souza, W. J. (2020). Default mode network dysfunction in idiopathic generalised epilepsy. *Epilepsy Res.* 159:106254. doi: 10.1016/j.eplepsyres.2019.106254

Pavone, P., Striano, P., Falsaperla, R., Pavone, L., and Ruggieri, M. (2014). Infantile spasms syndrome, West syndrome and related phenotypes: What we know in 2013. *Brain Dev.* 36, 739–751. doi: 10.1016/j.braindev.2013.10.008

Percha, B., Dzakpasu, R., Żochowski, M., and Parent, J. (2005). Transition from local to global phase synchrony in small world neural network and its possible implications for epilepsy. *Phys. Rev. E* 72:031909. doi: 10.1103/PhysRevE.72.031909

Power, J. D., Barnes, K. A., Snyder, A. Z., Schlaggar, B. L., and Petersen, S. E. (2012). Spurious but systematic correlations in functional connectivity MRI networks arise from subject motion. *Neuroimage* 59, 2142–2154. doi: 10.1016/j.neuroimage.2011.10.018

Power, J. D., Cohen, A. L., Nelson, S. M., Wig, G. S., Barnes, K. A., Church, J. A., et al. (2011). Functional network organization of the human brain. *Neuron* 72, 665–678. doi: 10.1016/j.neuron.2011.09.006

Power, J. D., Mitra, A., Laumann, T. O., Snyder, A. Z., Schlaggar, B. L., and Petersen, S. E. (2014). Methods to detect, characterize, and remove motion artifact in resting state fMRI. *Neuroimage* 84, 320–341. doi: 10.1016/j.neuroimage.2013.08.048

Rubinov, M., and Sporns, O. (2010). Complex network measures of brain connectivity: Uses and interpretations. *Neuroimage* 52, 1059–1069. doi: 10.1016/j.neuroimage.2009.10.003

Sawilowsky, S. S. (2009). New effect size rules of thumb. *J. Mod. Appl. Stat. Methods* 8:26. doi: 10.22237/jmasm/1257035100

Sheng, W., Cui, Q., Jiang, K., Chen, Y., Tang, Q., Wang, C., et al. (2022). Individual variation in brain network topology is linked to course of illness in major depressive disorder. *Cereb. Cortex.* 00, 1–10. doi: 10.1093/cercor/bhac015

Shmuel, A., Augath, M., Oeltermann, A., and Logothetis, N. K. (2006). Negative functional MRI response correlates with decreases in neuronal activity in monkey visual area V1. *Nat. Neurosci.* 9, 569–577. doi: 10.1038/nn1675

Siniatchkin, M., Van Baalen, A., Jacobs, J., Moeller, F., Moehring, J., Boor, R., et al. (2007). Different neuronal networks are associated with spikes and slow activity in hypsarrhythmia. *Epilepsia* 48, 2312–2321. doi: 10.1111/j.1528-1167.2007.01195.x

Song, J., Nair, V. A., Gaggl, W., and Prabhakaran, V. (2015). Disrupted brain functional organization in epilepsy revealed by graph theory analysis. *Brain Connect.* 5, 276–283. doi: 10.1089/brain.2014.0308

Sporns, O. (2013). The human connectome: Origins and challenges. *Neuroimage* 80, 53–61. doi: 10.1016/j.neuroimage.2013.03.023

Sporns, O., and Zwi, J. D. (2004). The small world of the cerebral cortex. *Neuroinformatics* 2, 145–162. doi: 10.1385/NI:2:2:145

Tan, Z., Li, Y., Zang, D., Zhang, H., Zhao, C., Jiang, H., et al. (2016). Altered regional homogeneity in epileptic patients with infantile spasm: A resting-state fMRI study. *J. X Ray Sci. Technol.* 24, 285–295. doi: 10.3233/XST-160559

Vaessen, M., Braakman, H., Heerink, J., Jansen, J., Debeij-van Hall, M., Hofman, P., et al. (2013). Abnormal modular organization of functional networks in cognitively impaired children with frontal lobe epilepsy. *Cereb. Cortex* 23, 1997–2006. doi: 10.1093/cercor/bhs186

Vaessen, M. J., Jansen, J. F., Braakman, H. M., Hofman, P. A., De Louw, A., Aldenkamp, A. P., et al. (2014). Functional and structural network impairment in childhood frontal lobe epilepsy. *PLoS One* 9:e90068. doi: 10.1371/journal.pone.0090068

Wang, J., Wang, L., Zang, Y., Yang, H., Tang, H., Gong, Q., et al. (2009). Parcellation-dependent small-world brain functional networks: A resting-state fMRI study. *Hum. Brain Mapp.* 30, 1511–1523. doi: 10.1002/hbm.20623

Wang, J., Wang, X., Xia, M., Liao, X., Evans, A., and He, Y. (2015). GRETNA: A graph theoretical network analysis toolbox for imaging connectomics. *Front. Hum. Neurosci.* 9:386. doi: 10.3389/fnhum.2015.00386

Wang, J., Zuo, X., and He, Y. (2010). Graph-based network analysis of resting-state functional MRI. *Front. Syst. Neurosci.* 4:16. doi: 10.3389/fnsys.2010.00016

Wang, Y., Li, Y., Wang, H., Chen, Y., and Huang, W. (2017). Altered default mode network on resting-state fMRI in children with infantile spasms. *Front. Neurol.* 8:209. doi: 10.3389/fneur.2017.00209

Watts, D. J., and Strogatz, S. H. (1998). Collective dynamics of 'small-world' networks. *Nature* 393, 440–442. doi: 10.1038/30918

Wen, H., Liu, Y., Rekik, I., Wang, S., Zhang, J., Zhang, Y., et al. (2017). Disrupted topological organization of structural networks revealed by probabilistic diffusion tractography in Tourette syndrome children. *Hum. Brain Mapp.* 38, 3988–4008. doi: 10.1002/hbm.23643

Xu, C.-P., Zhang, S.-W., Fang, T., Manxiu, M., Chen, Q., Huafu, C., et al. (2013). Altered functional connectivity within and between brain modules in absence epilepsy: A resting-state functional magnetic resonance imaging study. *BioMed Res. Int.* 2013:734893. doi: 10.1155/2013/734893

Yan, C.-G., Cheung, B., Kelly, C., Colcombe, S., Craddock, R. C., Di Martino, A., et al. (2013). A comprehensive assessment of regional variation in the impact of head micromovements on functional connectomics. *Neuroimage* 76, 183–201. doi: 10.1016/j.neuroimage.2013.03.004

Yang, S., Zhang, Z., Chen, H., Meng, Y., Li, J., Li, Z., et al. (2021). Temporal variability profiling of the default mode across epilepsy subtypes. *Epilepsia* 62, 61–73. doi: 10.1111/epi.16759

frontiers | Frontiers in Neuroscience

TYPE Original Research
PUBLISHED 12 October 2022
DOI 10.3389/fnins.2022.944768

OPEN ACCESS

EDITED BY
Chitresh Bhushan,
GE Global Research, United States

REVIEWED BY
Jinping Xu,
Shenzhen Institutes of Advanced Technology (CAS), China
Jia-Jie Mo,
Beijing Tiantan Hospital, Capital Medical University, China

*CORRESPONDENCE
Yong Zhang
zzuzhangyong2013@163.com
Shaoqiang Han
ShaoqiangHan@163.com
Jingliang Cheng
fccchengjl@zzu.edu.cn

†These authors have contributed equally to this work

SPECIALTY SECTION
This article was submitted to Brain Imaging Methods, a section of the journal Frontiers in Neuroscience

RECEIVED 15 May 2022
ACCEPTED 20 September 2022
PUBLISHED 12 October 2022

CITATION
Gao X, Zhang M, Yang Z, Niu X, Chen J, Zhou B, Wang W, Wei Y, Cheng J, Han S and Zhang Y (2022) Explore the effects of overweight and smoking on spontaneous brain activity: Independent and reverse. *Front. Neurosci.* 16:944768. doi: 10.3389/fnins.2022.944768

Explore the effects of overweight and smoking on spontaneous brain activity: Independent and reverse

Xinyu Gao[1,2,3,4,5,6,7†], Mengzhe Zhang[1,2,3,4,5,6,7†], Zhengui Yang[1,2,3,4,5,6,7], Xiaoyu Niu[1,2,3,4,5,6,7], Jingli Chen[1,2,3,4,5,6,7], Bingqian Zhou[1,2,3,4,5,6,7], Weijian Wang[1,2,3,4,5,6,7], Yarui Wei[1,2,3,4,5,6,7], Jingliang Cheng[1,2,3,4,5,6,7*], Shaoqiang Han[1,2,3,4,5,6,7*] and Yong Zhang[1,2,3,4,5,6,7*]

[1]Department of Magnetic Resonance Imaging, The First Affiliated Hospital of Zhengzhou University, Zhengzhou, China, [2]Key Laboratory for Functional Magnetic Resonance Imaging and Molecular Imaging of Henan Province, Zhengzhou, China, [3]Engineering Technology Research Center for Detection and Application of Brain Function of Henan Province, Zhengzhou, China, [4]Engineering Research Center of Medical Imaging Intelligent Diagnosis and Treatment of Henan Province, Zhengzhou, China, [5]Key Laboratory of Magnetic Resonance and Brain Function of Henan Province, Zhengzhou, China, [6]Key Laboratory of Brain Function and Cognitive Magnetic Resonance Imaging of Zhengzhou, Zhengzhou, China, [7]Key Laboratory of Imaging Intelligence Research Medicine of Henan Province, Zhengzhou, China

Accumulating evidence suggested that overweight and smoking often co-exist. However, current neuroimaging researches have almost always studied smoking or overweight status separately. Here we sought to investigate the neurobiological mechanisms of this comorbid association, by detecting spontaneous brain activity changes associated with smoking and weight status separately and collectively. We used 2 × 2 factorial design and included the following four groups: overweight/normal-weight smokers (n = 34/n = 30) and overweight/normal-weight non-smokers (n = 22/n = 24). The spontaneous brain activity among the four groups was comparable using an amplitude of low-frequency fluctuation (ALFF) method based on resting-state fMRI (rs-fMRI). Furthermore, correlation analyses between brain activity changes, smoking severity and BMI values were performed. A main effect of smoking was discovered in the default mode network (DMN) and visual network related brain regions. Moreover, overweight people had high ALFF value in the brain regions associated with reward and executive control. More importantly, smoking and overweight both affected brain activity of the middle temporal gyrus (MTG), but the effect was opposite. And the brain activity of MTG was negatively correlated with smoking years, pack year and BMI value. These results suggest that smoking and overweight not only affect spontaneous brain activity alone, but also paradoxically affect spontaneous brain activity in the MTG. This suggests that we need to control

for weight as a variable when studying spontaneous brain activity in smokers. Besides, this interaction may provide a neurological explanation for the comorbidity of overweight and smoking and a target for the treatment of comorbid populations.

KEYWORDS

amplitude of low-frequency fluctuation, nicotine addiction, smoke, overweight, body mass index

Introduction

The combination of cigarette smoking and overweight in individuals can synergistically increase risk of mortality (Freedman et al., 2006). Smoking and overweight are major causes for many serious diseases worldwide (Danaei et al., 2005), and in the United States overweight was the second leading cause of preventable, premature death after smoking (Mokdad et al., 2004). And about 30 percent of obese people smoke, compared with 15 percent of the general population in the United States (Hales et al., 2018; Creamer et al., 2019). Many people believe that quitting smoking will lead to weight gain, that's why a lot of people don't want to abandon. Part of the crowd even chooses to relapse because of weight gain (Audrain-McGovern and Benowitz, 2011). Interventions targeting smoking and overweight independently have modest success at best (Spring et al., 2009; Aubin et al., 2012), therefore, understanding the relationship between these two conditions is more conducive to targeted treatment and curb their profound negative impact.

Many studies have been done on the relationship between smoking and weight, with mixed and even contradictory results. For example, epidemiological investigation found that current smokers tend to be leaner than never or former smokers (Plurphanswat and Rodu, 2014). And past investigations have found that when smokers stop smoking, they gain weight and are even fatter than before they started (Audrain-McGovern and Benowitz, 2011). However, a research (Kim et al., 2012) showed that smokers had a higher rate of central adiposity even if smokers are leaner than non-smokers. In addition, Chiolero et al. (2007) found that the more cigarettes a smoker smokes per day, the higher his body mass index (BMI). Mechanically, nicotine is a sympathomimetic agent that can increase adipose tissue thermogenesis by increasing lipolysis and the subsequent recycling of fatty acids into triglycerides (Hellerstein et al., 1994; Andersson and Arner, 2001). In a word, nicotine increases energy consumption via action on peripheral tissue and through regulation of brain metabolism. Smoking increases 24 h energy expenditure by ∼10% (Hofstetter et al., 1986).

Moreover, some studies (Thorgeirsson et al., 2013; Taylor et al., 2019; Wills and Hopfer, 2019; Ely et al., 2021) have indicated that there is a relationship between smoking and weight, with advances in neuroimaging. Structurally, long-term smokers showed a gray matter (GM) volume decrease in the bilateral prefrontal cortex and left insular and GM volume increase in the right lingual cortex and left occipital cortex (Yang et al., 2020). The frontal temporal cortex (including bilateral middle temporal gyrus (MTG), left insula, left precuneus, bilateral orbitofrontal cortex, and so on) was thinner in people with a high BMI (Opel et al., 2021). Functionally, an index called amplitude of low-frequency fluctuation (ALFF) reflects the spontaneous activity of neurons in the resting state by measuring the intensity of the spontaneous fluctuation area (Rubin et al., 2018; Deng et al., 2022). Particularly, previous studies demonstrated that static ALFF changes were mainly concentrated in the right inferior frontal gyrus, left middle frontal gyrus, bilateral precuneus in smokers (Liu et al., 2018; Wen et al., 2021). Also, a weight-related functional MRI study discovered that overweight people showed decreased ALFF in the right superior temporal gyrus and increased ALFF in left inferior temporal gyrus (ITG), hippocampus/parahippocampal gyrus, fusiform gyrus/amygdala and bilateral caudate (Ren et al., 2020; Zhang et al., 2020). Smokers are not a small percentage of overweight people. In conclusion, above evidence suggests that there is an overlap of brain regions that change when people smoke or are overweight are studied separately. However, despite epidemiological and some animal studies (Thorgeirsson et al., 2013; Besson et al., 2019; Wills and Hopfer, 2019), no neuroimaging studies have explored whether there is a brain interaction between smokers and overweight people by using the ALFF method.

To cover these gaps, we divided our subjects into four groups (overweight smokers/non-smokers and normal weight smokers/non-smokers) based on ALFF method. According to previous studies, we hypothesized that the interaction between smoking and weight would alter spontaneous brain activity in certain brain regions (whether in the same direction or in the opposite direction cannot be determined), and that analysis would support that overweight is an influencing factor for the brain function of smoking people. Furthermore, we also assessed the effects of smoking and being overweight on spontaneous brain activity.

Materials and methods

Participants

Sixty-four smokers and forty-six non-smokers were recruited and divided into four groups, including: (i) overweight smokers (n = 34); (ii) normal-weight smokers (n = 30); (iii) overweight non-smokers (n = 22), and (iv) normal-weight non-smokers (n = 24) in this study.

All subjects were right-handed males. The nicotine dependence severity was measured by Fagerström Test for Nicotine Dependence (FTND, for current effects) (Heatherton et al., 1991) and pack-year (for chronic effects, be defined as smoking years × number of cigarettes smoked per day/20). Smokers were included as follows: (1) smoking at least 1 daily for > 2 years; (2) met the DSM-IV criteria for nicotine dependence (Wu et al., 2015; Sadeghi-Ardekani et al., 2018). Sex- and age-matched non-smokers (N = 46) who did not currently smoke and had no history of consumption of cigarettes or any nicotine products (Liu et al., 2018) take part in this study. BMI is calculated by height (m) divided by weight squared (kg). Normal-weight participants were defined as those with a BMI less than 25.0, and overweight participants had a BMI of more than 25.0 and less than 30.0 (Ely et al., 2021).

Exclusion criteria for all groups are as follows: (1) any physical or neuropsychiatric disease; (2) urine test and self-report indicating other substance or drug abuse (except nicotine); (3) contraindications to magnetic resonance imaging.

This study was reviewed and approved by the Ethics Committee of the First Affiliated Hospital of Zhengzhou University. All examinations were conducted under the guidance of the 1975 Declaration of Helsinki (Shephard, 1976). All patients were recruited via the Internet or through advertising at the First Affiliated Hospital of Zhengzhou University. Written informed consent was obtained from all subjects.

Imaging acquisition measures

All images were acquired on a 3.0T MRI scanner (Siemens Skyra) at the First Affiliated Hospital of Zhengzhou University. Smokers were required to smoke a cigarette 20 min prior to scanning to avoid nicotine withdrawal-related imaging after-effects. All participants were offered a snack before scanning. The participants remained stationary during the scan. All participants were requested to keep their eyes closed and relax their minds without falling asleep. Foam padding and earplugs were used to reduce subjects' head movements and scanner noises. At the end of scanning, participants were also asked if they had fallen asleep during scanning. BOLD resting-state fMRI (rs-fMRI) images were collected using an echo-planar imaging sequence (repetition time = 2,000 ms, echo time = 30 ms, flip angle = 80°). 36 transverse slices (field of view = 240 × 240 mm^2, matrix = 64 × 64, slice thickness = 4 mm, 180 volumes) that aligned along the AC-PC line were acquired with a total scan time of 360 s.

Imaging analysis procedure

The rs-fMRI data were preprocessed using the Toolkit (DPARSF, V4.3, advanced edition)[1] in MATLAB. The first 5 volumes were excluded then slice-timing and realignment. Subjects with a maximum head motion > 2.5 mm or > 2.5° head rotation were excluded. No subjects were excluded in this step. The functional images were spatially normalized and re-sampled to 3 × 3 × 3 mm^3. Next, 24 motion parameters, global signals, cerebrospinal fluid signals and white matter signals were regressed using multiple linear regression analysis. Frame wise displacement (FD) was calculated for each time point (Power et al., 2012; Han et al., 2020), and mean FD > 0.5 mm was excluded. Functional images were spatially smoothed with a 6 mm full width at half maximum Gaussian kernel and then detrended.

ALFF was calculated in REST (rs-fMRI Data Analysis Toolkit). Fast Fourier Transform (FFT) is used to transform the time series after Scrubbing (parameter: taper percentage = 0, FFT length = shortest), and then the power spectrum is obtained. Since the power of a given frequency is proportional to the square of the amplitude of this frequency component in the time domain of the original time series, the square root of the power spectrum is calculated at the given frequency range and the root mean square of 0.01∼0.08 Hz is obtained at each voxel, which is called ALFF. For standardization purposes, the ALFF of each voxel is divided by the global mean ALFF value.

Statistic analysis

Demographic and clinical characteristics were evaluated among four groups. Two-sample t-tests or the Mann-Whitney U-test were used for the demographic characteristics (age and education level) and clinical scores (smoking years, pack year, and FTND score). Differences were considered significant at $P < 0.05$.

Using the full factorial model in SPM12, we conducted two-way analysis of variance (ANOVA) to analyze the two factors—smoking (smokers and non-smokers) and weight status (overweight and normal-weight)—of whole-brain ALFF maps (Yang et al., 2019). Education, age, and the mean FD were entered as covariates. The results were set at a threshold of $P < 0.05$ (voxel threshold $P < 0.005$ and cluster extent threshold $P < 0.05$, GRF corrected).

1 www.restfmri.net

Each identified cluster where ALFF was found to be significant for the effect of both smoking and BMI was set as the region of interest (ROI). The ALFF value was extracted from the ROI, and then *post hoc* comparisons were performed using a two-sample *t*-test for interaction effect analyses ($P < 0.0125$, Bonferroni correction).

Correlation analyses

To examine the association of ALFF change with smoking severity and BMI status, we performed Spearman's correlation analyses between brain regions (altered in interaction effect analyses) and clinical data (smoking years, pack-year, FTND score, and BMI value).

Result

Demographics and clinical characteristics

Demographic and clinical characteristics were shown in Table 1. Smokers did not differ from non-smokers in age, education years and mean FD (two sample *t*-test, $t = -0.027$, $P = 0.979$; $t = 0.449$, $P = 0.654$; Mann-Whitney *U*-test, $Z = -1.714$, $P = 0.086$, respectively). Smokers and non-smokers who are overweight did not differ from normal weight people in age, education years and mean FD (details in Table 1). Smokers with high body weight did not differ from normal-weight controls who smoked in FTND ($t = 0.297$, $P = 0.767$), smoking years ($t = 1.871$, $P = 0.066$), and pack-years ($t = 1.919$, $P = 0.060$).

The main effects

The main effect of smoking was found in the left ITG, left SFG, middle frontal gyrus, right calcarine sulcus, right precuneus, and the right MTG. Compared with non-smokers, smokers group indicated increasing ALFF value in all brain regions mentioned above (Figure 1A and Table 2). The main effect of weight was found in the midbrain, left insula, bilateral inferior frontal gyrus, left SFG, and right precuneus (Figure 1B and Table 2), with overweight groups exhibiting elevated brain spontaneous fluctuations than normal-weight groups.

Interaction effects

The interaction effect between smoking and weight was showed in the MTG (Figure 2A). *Post hoc* analysis showed normal-weight smokers had increased ALFF value in the MTG compared with normal-weight non-smokers ($t = 3.554$, $P = 0.001$). However, the mean ALFF values of the MTG were more similar between overweight smokers and normal-weight non-smokers (see details in Figure 2B).

Correlation analysis

Spearman's correlation analysis found that the value of ALFF in the MTG was negatively correlated with smoking years, pack year, and BMI value ($r = -0.283$, $P = 0.023$; $r = -0.276$, $P = 0.027$; $r = -0.338$, $P = 0.007$, respectively) in smokers (Figure 3).

Discussion

The current study used a 2 × 2 factorial design for smoking and weight status. We identified the spontaneous brain activity among four groups of subjects using ALFF method. Compared to non-smokers, smokers displayed raised brain activity in the left ITG, left SFG, middle frontal gyrus, right calcarine sulcus, right precuneus, right middle occipital gyrus, and right MTG no matter how much their weight. Moreover, overweight people had high ALFF value in the midbrain, left insula, bilateral inferior frontal gyrus, left SFG and right precuneus. More importantly, however, we found that smoking and body weight affected the spontaneous brain activity in the left MTG due to the interaction effect, which provides a possible explanation for their comorbidity.

The smoking main effect showing changed spontaneous fluctuations in the left ITG, left SFG, middle frontal gyrus, right calcarine sulcus, right precuneus, right middle occipital gyrus, and the right MTG, which was consistent with previous studies. Right calcarine sulcus, right middle occipital gyrus, and right MTG are involved in the formation of the visual cortex. Gallivan et al. (2011) found that a smoker's attention is biased toward smoking cues, which potentially due to early processing changes in the visual system and reward-related areas. Changes in these brain regions in smokers may lead them to be more likely to associate smoking behavior with smoking cues in the environment when faced with temptation (such as watching other people smoking or pictures of cigarettes) (Gallivan et al., 2011). Left superior frontal gyrus (SFG), left ITG, and right precuneus are parts of the DMN. SFG is anatomically connected with the cingulate cortex (mostly the anterior cingulate and the middle cingulate, involved in cognitive control) through the cingulum and that it is functionally correlated with the default mode network (DMN) (Li et al., 2013). Abnormalities in the DMN can be observed in people with different substance use disorders (Zhang and Volkow, 2019). In short, failed inhibition of DMN activity during tasks in substance addiction was associated with increased drug-cue reactivity and impaired

TABLE 1 Demographic and clinical characteristics.

Demographics	Smokers (n = 64)		Non-smokers (n = 46)		Comparison		
	OW-SM (n = 34)	NW-SM (n = 30)	OW-NSM (n = 22)	NW-NSM (n = 24)	SM vs. NSM	OW vs. NW	ANOVA
Sex (M/F)	34/0	30/0	22/0	24/0	–	–	–
Race	Mongoloid	Mongoloid	Mongoloid	Mongoloid	–	–	–
Age (years)	35.03 ± 6.37	33.03 ± 7.08	36.68 ± 7.36	28.50 ± 4.80	t = −0.027, P = 0.979	t = 1.969, P = 0.052	F = 2.170, P = 0.096
Education (years)	15.35 ± 0.98	14.97 ± 1.77	14.77 ± 2.77	16.67 ± 2.14	Z = −1.714, P = 0.086	Z = −1.326, P = 0.185	F = 2.027, P = 0.115
Mean FD	0.10 ± 0.08	0.11 ± 0.10	0.09 ± 0.06	0.09 ± 0.04	t = 0.449, P = 0.654	t = 0.487, P = 0.628	F = 2.063, P = 0.110
FTND	4.77 ± 1.78	4.63 ± 1.75	–	–	–	t = 0.297, P = 0.767	–
Pack-year	19.26 ± 10.04	13.95 ± 12.09	–	–	–	t = 1.919, P = 0.060	–
Smoking year	16.00 ± 5.43	13.07 ± 7.09	–	–	–	t = 1.871, P = 0.066	–
Weight (kg)	82.06 ± 8.39	68.99 ± 5.65	78.82 ± 7.64	66.5 ± 6.21	t = 1.070, P = 0.287	t = 10.737, P = 0.000	–
BMI	26.84 ± 2.07	21.88 ± 1.56	26.60 ± 1.98	22.11 ± 1.31	t = 0.443, P = 0.659	t = 14.059, P = 0.000	–

SM, smokers; NSM, non-smokers; OW, overweight; NW, normal weight; FTND, Fagerström Test for Nicotine Dependence; BMI, body mass index; M, males; F, females.

10.3389/fnins.2022.944768

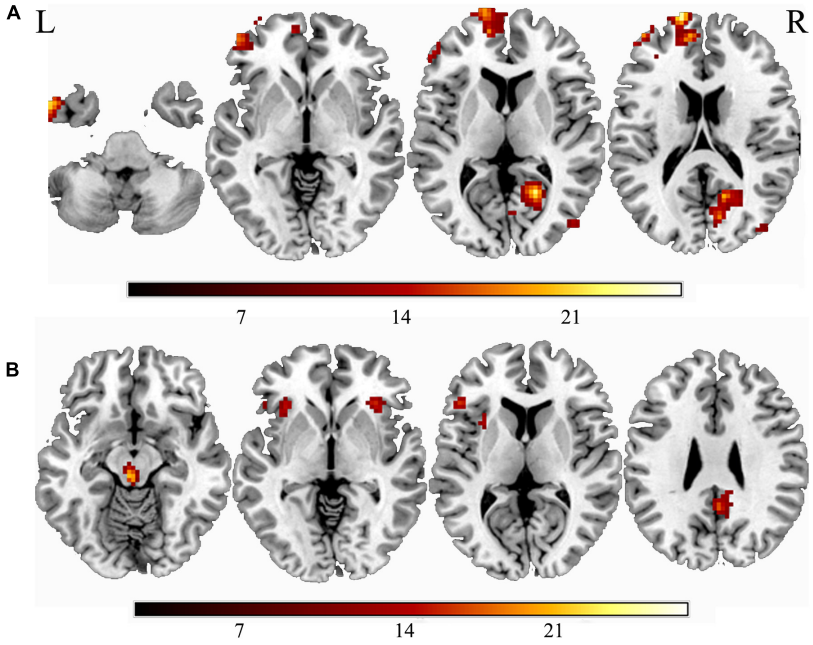

FIGURE 1
The main effect of smoking or weight. **(A)** The main effect of smoking; **(B)** the main effect of overweight. "L" means the side is to the left and "R" means the side is to the right.

cognitive control (Garavan et al., 2000; Bednarski et al., 2011; Vollstädt-Klein et al., 2011). The cognitive impairment of addicts may be partly due to their impaired ability to relax emotional involvement in cognitive control processes and to shift attention from self-generated thoughts to external stimuli, mediated by interruptions in pre-DMN and post-DMN activity, respectively (Zhang and Volkow, 2019). These brain changes suggest when smokers faced with a temptation, have a bias of attention and are more likely to elicit the urge to smoke.

The main effect of overweight was found in the midbrain, insula, bilateral inferior frontal gyrus and right precuneus. Midbrain, a brain region composed largely of DA (60–65%), γ-amino butyric acid (GABA; ∼30–35%) and glutamatergic neurons (2–3%), is the core components of reward circuitry (Cooper et al., 2017). The feeding behavior is partly regulated by the mesolimbic dopamine system (Berridge and Robinson, 1998), and the neurotransmitter dopamine plays a crucial role in the regulation of food reward within this system. If the body lacks dopamine receptors, it becomes insensitive to excitement. For example, overweight people, who lack dopamine receptors, tend to receive food stimuli more slowly than normal people, so they need more food to satisfy their pleasure. The NAc represents the central to desire and is an important anatomical component of reward circuitry, receiving extensive projections of DA neurons from the ventral tegmental area (VTA) of the midbrain (Ikemoto and Wise, 2004). Activation of these midbrain DA neurons is associated with the motivating, rewarding and motivational saliency properties of natural stimuli such as food and drug abuse (Richardson and Gratton, 1996; Ikemoto and Wise, 2004; Hardman et al., 2012). Moreover, the neural mechanisms of food reward are thought to be similar to

TABLE 2 Significant group differences in amplitude of low-frequency fluctuation.

Brain region	MNI coordinates (X, Y, Z)	Cluster size	Peak *F*-value
Interaction effect			
MTG_L	−63, −33, −12	33	21.780
Main effect of smoking			
ITG_L	−51, 6, −45	58	23.153
SFG_LMFG_L	−15, 69, 18	514	26.116
Calcarine_R/precuneus	21, −60, 12	319	27.643
MOG_R/MTG_R	45, −78, 12	56	15.621
Main effect of overweight			
Midbrain/brainstem_L	−3, −27, −9	44	22.185
Insula_L	−36, 18, 0	77	17.674
IFG_R	36, 24, 0	47	15.202
IFG_L	−45, 27, 6	34	15.276
SFG_L	−21, 48, 18	35	17.099
Precuneus_R	3, −51, 30	189	28.661

MTG, middle temporal gyrus; ITG, inferior temporal gyrus; SFG, superior frontal gyrus; MFG, middle frontal gyrus; MOG, middle occipital gyrus; IFG, inferior frontal gyrus; MSFG, medial superior frontal gyrus; L, left; R, right.

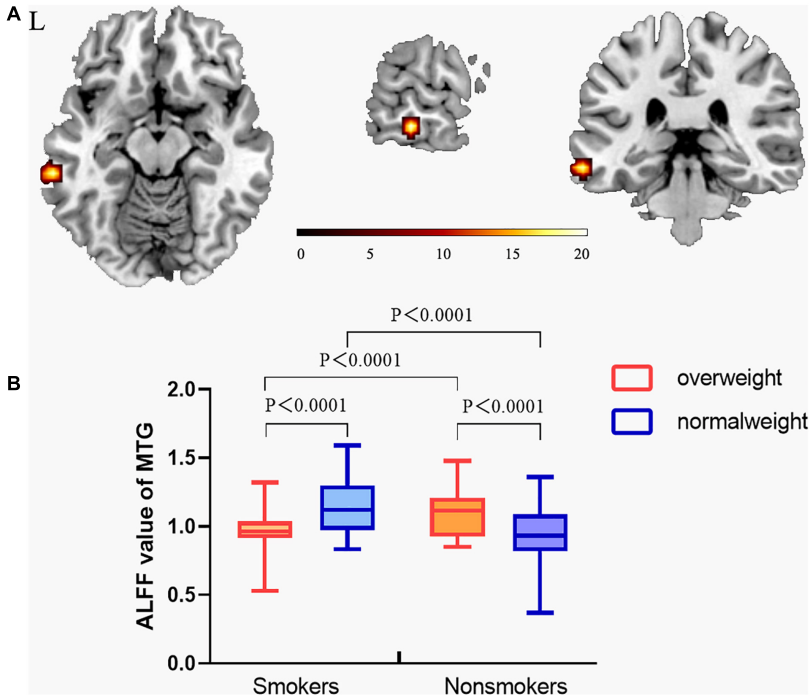

FIGURE 2
The interaction effect between smoking and overweight. **(A)** A significant interaction effect shown by ALFF in the MTG using two-way ANOVA. The statistical significance level was set at voxel threshold $P < 0.005$ and cluster extent threshold $P < 0.05$, GRF corrected. **(B)** *Post hoc* analysis of the MTG among the four groups. From this figure, normal-weight smokers had increased ALFF value in middle temporal gyrus compared with normal-weight non-smokers. However, the ALFF value of the middle temporal gyrus of overweight smokers was still higher than that of normal-weight non-smokers, but the difference decreased. This suggests that the ALFF value of the middle temporal gyrus of overweight smokers is closer to that of normal-weight non-smokers, compared to that of normal-weight smokers. (The vertical bar indicates the maximum and minimum across subjects. The bars in the box represent the mean ALFF for each group.) "L" means the side is to the left.

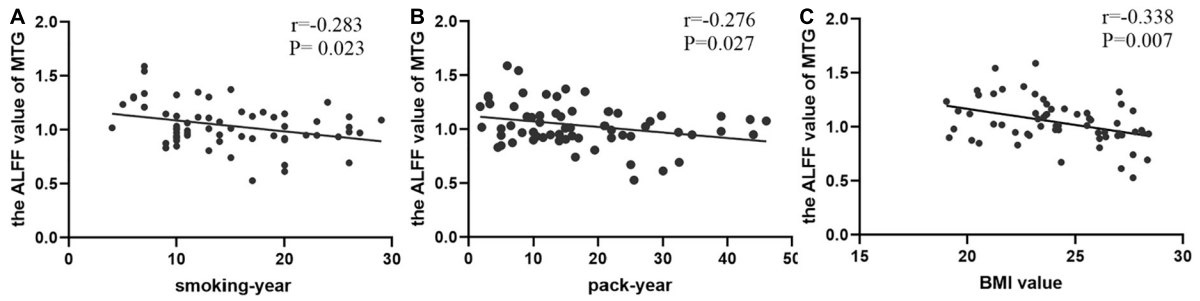

FIGURE 3
The correlations between the value of ALFF in the middle temporal gyrus (MTG) and clinical data. **(A)** In smokers, smoking-year was negatively correlated with the value of MTG (Spearman's correlation, $r = -0.283$, $p = 0.023$); **(B)** pack-year was negatively correlated with the value of MTG (Spearman's correlation, $r = -0.276$, $p = 0.027$); **(C)** BMI value was negatively correlated with the value of MTG (Spearman's correlation, $r = -0.338$, $p = 0.007$).

drug rewards. The insula was also modulated by dopaminergic activity to involve in motivation, rewards, and cognitive control (Chikama et al., 1997), which can enhance reward drive and weaken cognitive control. Therefore, altered insula activity may result in lower self-control ability and increased distractibility (Gao et al., 2021), this causes people to increase their eating behavior and gain weight. In addition, increased ALFF value in bilateral inferior frontal gyrus and right precuneus in our study, these brain regions are parts of a network involved in executive control function (ability to inhibit behavioral responses in the face of distractions) (Hardee et al., 2020). Prior studies have linked changes in this functional network, interpreted as less efficient processing, to risk for substance use problems (such as food) (Heitzeg et al., 2015).

In our research, the interaction effect of smoking and overweight status was observed in the MTG. Previous studies have found changes in MTG brain activity in both smokers (Xue et al., 2020) and overweight people (Hardee et al., 2020). MTG has a variety of functions including emotion, memory, and cognition (Rizzolatti et al., 1996; Giraud et al., 2004; Hesling et al., 2005; Sato et al., 2012), whose impairments have been reported to be associated with various brain disorders, such as major depression disorders (Cheng et al., 2019) and obsessive-compulsive disorder (Fan et al., 2017). Based on anatomical and functional connectivity, Xu et al. (2015, 2019) found bilateral anterior MTG (aMTG) mainly connected with left precuneus and SFG (two key nodes of the DMN). Fingerprint analysis further confirmed this, indicating a high functional connection between aMTG and DMN. Furthermore, during external-oriented tasks, drug-cues and food-cues elicited MTG activity in substance use disorder people, which perhaps is related with shifting attention from self-related thoughts to external stimuli (Andrews-Hanna et al., 2014; Tomasi et al., 2015). This suggests that when smokers see smoking cues, their desire to smoke trumps their inner desire not to smoke. Above failed inhibition of MTG and DMN activity during tasks in substance addiction was associated with increased drug-cue reactivity and impaired cognitive control (Bednarski et al., 2011; Zhang and Volkow, 2019). In addition, it has been reported that activity in the left posterior MTG increases as the number of suggestive movements associated with the object being observed increases (Schubotz et al., 2014). Recently, it has been found that posterior MTG is related to the proper objects grasping ability (Amoruso et al., 2018). All evidence suggested that the posterior MTG might play an important role in action observation and integrating the motoric details of the action. Overall, our findings show the MTG plays an integrated role in motor observation, external information response and cognitive control, these functions in the MTG provide a possible neurological explanation for the altered MTG in both overweight and smokers, and may be one of the possible reasons for their frequent comorbidities.

Additionally, *Post hoc* analysis of the MTG showed that normal-weight smokers have increased ALFF value with regard to normal-weight non-smokers, which is consistent with previous research (Gearhardt et al., 2014). However, the ALFF value of the MTG of overweight smokers is closer to that of normal-weight non-smokers, compared to that of normal-weight smokers. In a word, smoking activates spontaneous brain fluctuations in the MTG, and overweight mitigated these changes in smoking populations, this suggests that smoking and being overweight have opposite effects on the activity of the MTG. In all smokers, the value of ALFF in the MTG was negatively correlated with smoking years, pack year and BMI value ($r = -0.283$, $P = 0.023$; $r = -0.276$, $P = 0.027$; $r = -0.338$, $P = 0.007$, respectively).

There are several limitations to consider when designing our study. Firstly, all subjects were males, which is because (1) the smoking rate of males is much higher than that of females, the issue of male smoking needs to be focused on (Nakagawa et al., 2022); (2) It has been reported that gender has an effect on the brain function of smokers (Zhang et al., 2017), therefore, in order to control the influencing factors, only males were included in our study. Secondly, the overweight volunteers and smokers we included lacked a few clinical data (e.g., abdominal circumference and serum cholesterol level in overweight people; exhaled carbon monoxide levels in smokers), so we couldn't conduct correlation analysis between the different brain regions with these data. Thirdly, this study included daily smokers with low cigarette count. Because even if a smoker may smoke one cigarette a day, he meets the criteria for nicotine addiction, so we count him as a smoker (Wen et al., 2021). At the same time, studies have found that daily smokers may have higher mortality rates (Inoue-Choi et al., 2019) and lower awareness of clinical prevention services (Vander Weg et al., 2012) than non-daily smokers, so we feel it is important to highlight the concept of daily smoking. Fourthly, this study excluded obese population by limiting BMI to 30. Studies have shown that overweight differs substantially from obesity. A study of the effect of BMI on intra-network rest-state connectivity in smokers showed heavier smoking was related to greater rsFC in the salience network among lean and obese groups but reduced rsFC in the overweight group (Ely et al., 2021). At the same time, BMI had a significant secondary effect on DMN connectivity. In addition, Luo et al. (2018) showed that the voxel-mirrored homotopic connectivity (VMHC) in the calcarine gyrus and post-central gyrus was different in obese and overweight individuals. In a word, focusing on overweight is a separate issue and should be treated as such. Finally, this study was cross-sectional and the sample size of this study is relatively small, so more data can be collected for analysis in future studies, making the statistical effect higher and the conclusion more reliable.

Conclusion

In this study, we found that both smoking and body weight affect spontaneous brain activity, and a novel antagonistic interaction effect of smoking and overweight in the MTG of smokers who are overweight. This suggests that we need to control for weight as a variable when studying spontaneous brain activity in smoking. In addition, the interaction between smoking and overweight on the MTG may provide a neurological explanation for the comorbidities between overweight and smoking and a target for treatment of the comorbidities.

Data availability statement

The raw data supporting the conclusions of this article will be made available by the authors, without undue reservation.

Ethics statement

The studies involving human participants were reviewed and approved by the Ethics Committee of the First Affiliated Hospital of Zhengzhou University. The patients/participants provided their written informed consent to participate in this study.

Author contributions

XG: data curation, formal analysis, methodology, visualization, and writing—original draft. MZ: data curation, formal analysis, methodology, and writing—original draft. ZY and SH: methodology and writing—review and editing. XN and JCn: methodology. BZ and YW: writing—review and editing. WW: resources. YZ: conceptualization, funding acquisition, methodology, resources, supervision, and writing—review and editing. JCg: conceptualization, funding acquisition, resources, supervision, and writing—review and editing. All authors contributed to the article and approved the submitted version.

Funding

This work was supported by the National Natural Science Foundation of China (81601467 and 81871327) and the Medical Science and Technology Research Project of Henan Province (201701011).

Acknowledgments

We thank all participants for investing their time and effort in this study. Also, we thank everybody that helped with recruitment of participants.

Conflict of interest

The authors declare that the research was conducted in the absence of any commercial or financial relationships that could be construed as a potential conflict of interest.

Publisher's note

All claims expressed in this article are solely those of the authors and do not necessarily represent those of their affiliated organizations, or those of the publisher, the editors and the reviewers. Any product that may be evaluated in this article, or claim that may be made by its manufacturer, is not guaranteed or endorsed by the publisher.

References

Amoruso, L., Finisguerra, A., and Urgesi, C. (2018). Contextualizing action observation in the predictive brain: Causal contributions of prefrontal and middle temporal areas. *Neuroimage* 177, 68–78. doi: 10.1016/j.neuroimage.2018.05.020

Andersson, K., and Arner, P. (2001). Systemic nicotine stimulates human adipose tissue lipolysis through local cholinergic and catecholaminergic receptors. *Int. J. Obesity Related Metab. Disord.* 25, 1225–1232. doi: 10.1038/sj.ijo.0801654

Andrews-Hanna, J. R., Smallwood, J., and Spreng, R. N. (2014). The default network and self-generated thought: Component processes, dynamic control, and clinical relevance. *Ann. N Y. Acad. Sci.* 1316, 29–52. doi: 10.1111/nyas.12360

Aubin, H. J., Farley, A., Lycett, D., Lahmek, P., and Aveyard, P. (2012). Weight gain in smokers after quitting cigarettes: Meta-analysis. *BMJ* 345:e4439.

Audrain-McGovern, J., and Benowitz, N. L. (2011). Cigarette smoking, nicotine, and body weight. *Clin. Pharmacol. Ther.* 90, 164–168.

Bednarski, S. R., Zhang, S., Hong, K. I., Sinha, R., Rounsaville, B. J., and Li, C. S. (2011). Deficits in default mode network activity preceding error in cocaine dependent individuals. *Drug Alcohol Depend.* 119, e51–e57. doi: 10.1016/j.drugalcdep.2011.05.026

Berridge, K. C., and Robinson, T. E. (1998). What is the role of dopamine in reward: Hedonic impact, reward learning, or incentive salience? *Brain Res. Brain Res. Rev.* 28, 309–369.

Besson, M., Forget, B., Correia, C., Blanco, R., and Maskos, U. (2019). Profound alteration in reward processing due to a human polymorphism in CHRNA5: A role in alcohol dependence and feeding behavior. *Neuropsychopharmacology* 44, 1906–1916. doi: 10.1038/s41386-019-0462-0

Cheng, C., Dong, D., Jiang, Y., Ming, Q., Zhong, X., Sun, X., et al. (2019). State-related alterations of spontaneous neural activity in current and remitted depression revealed by resting-state fMRI. *Front. Psychol.* 10:245. doi: 10.3389/fpsyg.2019.00245

Chikama, M., McFarland, N. R., Amaral, D. G., and Haber, S. N. (1997). Insular cortical projections to functional regions of the striatum correlate with cortical cytoarchitectonic organization in the primate. *J Neurosci.* 17, 9686–9705. doi: 10.1523/JNEUROSCI.17-24-09686.1997

Chiolero, A., Jacot-Sadowski, I., Faeh, D., Paccaud, F., and Cornuz, J. (2007). Association of cigarettes smoked daily with obesity in a general adult population. *Obesity* 15, 1311–1318. doi: 10.1038/oby.2007.153

Cooper, S., Robison, A. J., and Mazei-Robison, M. S. (2017). Reward circuitry in addiction. *Neurotherapeutics* 14, 687–697.

Creamer, M. R., Wang, T. W., Babb, S., Cullen, K. A., Day, H., Willis, G., et al. (2019). Tobacco product use and cessation indicators among adults - United States, 2018. *MMWR Morb. Mortal. Week. Rep.* 68, 1013–1019.

Danaei, G., Vander Hoorn, S., Lopez, A. D., Murray, C. J., and Ezzati, M. (2005). Causes of cancer in the world: Comparative risk assessment of nine behavioural and environmental risk factors. *Lancet* 366, 1784–1793.

Deng, S., Franklin, C. G., O'Boyle, M., Zhang, W., Heyl, B. L., Jerabek, P. A., et al. (2022). Hemodynamic and metabolic correspondence of resting-state voxel-based physiological metrics in healthy adults. *Neuroimage* 250:118923. doi: 10.1016/j.neuroimage.2022.118923

Ely, A. V., Jagannathan, K., Spilka, N., Keyser, H., Rao, H., Franklin, T. R., et al. (2021). Exploration of the influence of body mass index on intra-network resting-state connectivity in chronic cigarette smokers. *Drug Alcohol Depend.* 227:108911. doi: 10.1016/j.drugalcdep.2021.108911

Fan, J., Zhong, M., Gan, J., Liu, W., Niu, C., Liao, H., et al. (2017). Spontaneous neural activity in the right superior temporal gyrus and left middle temporal gyrus

is associated with insight level in obsessive-compulsive disorder. *J. Affect. Disord.* 207, 203–211.

Freedman, D. M., Sigurdson, A. J., Rajaraman, P., Doody, M. M., Linet, M. S., and Ron, E. (2006). The mortality risk of smoking and obesity combined. *Am. J. Prevent. Med.* 31, 355–362.

Gallivan, J. P., McLean, D. A., Valyear, K. F., Pettypiece, C. E., and Culham, J. C. (2011). Decoding action intentions from preparatory brain activity in human parieto-frontal networks. *J. Neurosci.* 31, 9599–9610. doi: 10.1523/JNEUROSCI.0080-11.2011

Gao, X., Zhang, M., Yang, Z., Wen, M., Huang, H., Zheng, R., et al. (2021). Structural and functional brain abnormalities in internet gaming disorder and attention-deficit/hyperactivity disorder: A comparative meta-analysis. *Front. Psychiatr.* 12:679437. doi: 10.3389/fpsyt.2021.679437

Garavan, H., Pankiewicz, J., Bloom, A., Cho, J. K., Sperry, L., Ross, T. J., et al. (2000). Cue-induced cocaine craving: Neuroanatomical specificity for drug users and drug stimuli. *Am. J. Psychiatry* 157, 1789–1798. doi: 10.1176/appi.ajp.157.11.1789

Gearhardt, A. N., Yokum, S., Stice, E., Harris, J. L., and Brownell, K. D. (2014). Relation of obesity to neural activation in response to food commercials. *Soc. Cogn. Affect. Neurosci.* 9, 932–938.

Giraud, A. L., Kell, C., Thierfelder, C., Sterzer, P., Russ, M. O., Preibisch, C., et al. (2004). Contributions of sensory input, auditory search and verbal comprehension to cortical activity during speech processing. *Cereb. Cortex* 14, 247–255. doi: 10.1093/cercor/bhg124

Hales, C. M., Fryar, C. D., Carroll, M. D., Freedman, D. S., Aoki, Y., and Ogden, C. L. (2018). Differences in obesity prevalence by demographic characteristics and urbanization level among adults in the United States, 2013-2016. *JAMA* 319, 2419–2429. doi: 10.1001/jama.2018.7270

Han, S., Cui, Q., Wang, X., Li, L., Li, D., He, Z., et al. (2020). Resting state functional network switching rate is differently altered in bipolar disorder and major depressive disorder. *Hum. Brain Mapp.* 41, 3295–3304. doi: 10.1002/hbm.25017

Hardee, J. E., Phaneuf, C., Cope, L., Zucker, R., Gearhardt, A., and Heitzeg, M. (2020). Neural correlates of inhibitory control in youth with symptoms of food addiction. *Appetite* 148:104578. doi: 10.1016/j.appet.2019.104578

Hardman, C. A., Herbert, V. M., Brunstrom, J. M., Munafò, M. R., and Rogers, P. J. (2012). Dopamine and food reward: Effects of acute tyrosine/phenylalanine depletion on appetite. *Physiol. Behav.* 105, 1202–1207. doi: 10.1016/j.physbeh.2011.12.022

Heatherton, T. F., Kozlowski, L. T., Frecker, R. C., and Fagerström, K. O. (1991). The fagerström test for nicotine dependence: A revision of the fagerström tolerance questionnaire. *Br. J. Add.* 86, 1119–1127.

Heitzeg, M. M., Cope, L. M., Martz, M. E., and Hardee, J. E. (2015). Neuroimaging risk markers for substance abuse: Recent findings on inhibitory control and reward system functioning. *Curr. Add. Rep.* 2, 91–103.

Hellerstein, M. K., Benowitz, N. L., Neese, R. A., Schwartz, J. M., Hoh, R., Jacob, P. III., et al. (1994). Effects of cigarette smoking and its cessation on lipid metabolism and energy expenditure in heavy smokers. *J. Clin. Invest.* 93, 265–272.

Hesling, I., Clément, S., Bordessoules, M., and Allard, M. (2005). Cerebral mechanisms of prosodic integration: Evidence from connected speech. *Neuroimage* 24, 937–947.

Hofstetter, A., Schutz, Y., Jéquier, E., and Wahren, J. (1986). Increased 24-hour energy expenditure in cigarette smokers. *N Eng. J. Med.* 314, 79–82.

Ikemoto, S., and Wise, R. A. (2004). Mapping of chemical trigger zones for reward. *Neuropharmacology* 47, 190–201. doi: 10.1016/j.neuropharm.2004.07.012

Inoue-Choi, M., McNeel, T. S., Hartge, P., Caporaso, N. E., Graubard, B. I., and Freedman, N. D. (2019). Non-daily cigarette smokers: Mortality risks in the U.S. *Am. J. Prevent. Med.* 56, 27–37.

Kim, J. H., Shim, K. W., Yoon, Y. S., Lee, S. Y., Kim, S. S., and Oh, S. W. (2012). Cigarette smoking increases abdominal and visceral obesity but not overall fatness: An observational study. *PLoS One* 7:e45815. doi: 10.1371/journal.pone.0045815

Li, W., Qin, W., Liu, H., Fan, L., Wang, J., Jiang, T., et al. (2013). Subregions of the human superior frontal gyrus and their connections. *Neuroimage* 78, 46–58.

Liu, H., Luo, Q., Du, W., Li, X., Zhang, Z., Yu, R., et al. (2018). Cigarette smoking and schizophrenia independently and reversibly altered intrinsic brain activity. *Brain Imaging Behav.* 12, 1457–1465. doi: 10.1007/s11682-017-9806-8

Luo, X., Li, K., Jia, Y. L., Zeng, Q., Jiaerken, Y., Qiu, T., et al. (2018). Abnormal of inter-hemispheric functional connectivity in elderly subjects with overweight/obesity. *Obesity Res. Clin. Practice* 12, 555–561. doi: 10.1016/j.orcp.2018.01.003

Mokdad, A. H., Marks, J. S., Stroup, D. F., and Gerberding, J. L. (2004). Actual causes of death in the United States, 2000. *JAMA* 291, 1238–1245.

Nakagawa, S., Takahashi, Y., Nakayama, T., Muro, S., Mishima, M., Sekine, A., et al. (2022). Gender differences in smoking initiation and cessation associated with the intergenerational transfer of smoking across three generations: The nagahama study. *Int. J. Environ. Res. Public Health* 19:1511. doi: 10.3390/ijerph19031511

Opel, N., Thalamuthu, A., Milaneschi, Y., Grotegerd, D., Flint, C., Leenings, R., et al. (2021). Brain structural abnormalities in obesity: Relation to age, genetic risk, and common psychiatric disorders : Evidence through univariate and multivariate mega-analysis including 6420 participants from the ENIGMA MDD working group. *Mol. Psychiatry* 26, 4839–4852. doi: 10.1038/s41380-020-0774-9

Plurphanswat, N., and Rodu, B. (2014). The association of smoking and demographic characteristics on body mass index and obesity among adults in the U.S., 1999-2012. *BMC Obesity* 1:18. doi: 10.1186/s40608-014-0018-0

Power, J. D., Barnes, K. A., Snyder, A. Z., Schlaggar, B. L., and Petersen, S. E. (2012). Spurious but systematic correlations in functional connectivity MRI networks arise from subject motion. *Neuroimage* 59, 2142–2154. doi: 10.1016/j.neuroimage.2011.10.018

Ren, Y., Xu, M., von Deneen, K. M., He, Y., Li, G., Zheng, Y., et al. (2020). Acute and long-term effects of electroacupuncture alter frontal and insular cortex activity and functional connectivity during resting state. *Psychiatr. Res. Neuroimag.* 298:111047. doi: 10.1016/j.pscychresns.2020.111047

Richardson, N. R., and Gratton, A. (1996). Behavior-relevant changes in nucleus accumbens dopamine transmission elicited by food reinforcement: An electrochemical study in rat. *J. Neurosci.* 16, 8160–8169. doi: 10.1523/JNEUROSCI.16-24-08160.1996

Rizzolatti, G., Fadiga, L., Matelli, M., Bettinardi, V., Paulesu, E., Perani, D., et al. (1996). Localization of grasp representations in humans by PET: 1. Observation versus execution. *Exp. Brain Res.* 111, 246–252. doi: 10.1007/BF00227301

Rubin, L. H., Li, S., Yao, L., Keedy, S. K., Reilly, J. L., Hill, S. K., et al. (2018). Peripheral oxytocin and vasopressin modulates regional brain activity differently in men and women with schizophrenia. *Schizophr. Res.* 202, 173–179. doi: 10.1016/j.schres.2018.07.003

Sadeghi-Ardekani, K., Haghighi, M., and Zarrin, R. (2018). Effects of omega-3 fatty acid supplementation on cigarette craving and oxidative stress index in heavy-smoker males: A double-blind, randomized, placebo-controlled clinical trial. *J. Psychopharmacol.* 32, 995–1002. doi: 10.1177/0269881118788806

Sato, W., Toichi, M., Uono, S., and Kochiyama, T. (2012). Impaired social brain network for processing dynamic facial expressions in autism spectrum disorders. *BMC Neurosci.* 13:99. doi: 10.1186/1471-2202-13-99

Schubotz, R. I., Wurm, M. F., Wittmann, M. K., and von Cramon, D. Y. (2014). Objects tell us what action we can expect: Dissociating brain areas for retrieval and exploitation of action knowledge during action observation in fMRI. *Front. Psychol.* 5:636. doi: 10.3389/fpsyg.2014.00636

Shephard, D. A. (1976). The 1975 declaration of Helsinki and consent. *Can. Med. Assoc. J.* 115, 1191–1192.

Spring, B., Howe, D., Berendsen, M., McFadden, H. G., Hitchcock, K., Rademaker, A. W., et al. (2009). Behavioral intervention to promote smoking cessation and prevent weight gain: A systematic review and meta-analysis. *Addiction* 104, 1472–1486.

Taylor, A. E., Richmond, R. C., Palviainen, T., Loukola, A., Wootton, R. E., Kaprio, J., et al. (2019). The effect of body mass index on smoking behaviour and nicotine metabolism: A Mendelian randomization study. *Hum. Mol. Genet.* 28, 1322–1330. doi: 10.1093/hmg/ddy434

Thorgeirsson, T. E., Gudbjartsson, D. F., Sulem, P., Besenbacher, S., Styrkarsdottir, U., Thorleifsson, G., et al. (2013). A common biological basis of obesity and nicotine addiction. *Trans. Psychiatr.* 3:e308. doi: 10.1038/tp.2013.81

Tomasi, D., Wang, G. J., Wang, R., Caparelli, E. C., Logan, J., and Volkow, N. D. (2015). Overlapping patterns of brain activation to food and cocaine cues in cocaine abusers: Association to striatal D2/D3 receptors. *Hum. Brain Mapp.* 36, 120–136. doi: 10.1002/hbm.22617

Vander Weg, M. W., Howren, M. B., and Cai, X. (2012). Use of routine clinical preventive services among daily smokers, non-daily smokers, former smokers, and never-smokers. *Nicotine Tob. Res.* 14, 123–130. doi: 10.1093/ntr/ntr141

Vollstädt-Klein, S., Loeber, S., Kirsch, M., Bach, P., Richter, A., Bühler, M., et al. (2011). Effects of cue-exposure treatment on neural cue reactivity in alcohol dependence: A randomized trial. *Biol. Psychiatr.* 69, 1060–1066.

Wen, M., Yang, Z., Wei, Y., Huang, H., Zheng, R., Wang, W., et al. (2021). More than just statics: Temporal dynamic changes of intrinsic brain activity in cigarette smoking. *Add. Biol.* 26:e13050. doi: 10.1111/adb.13050

Wills, A. G., and Hopfer, C. (2019). Phenotypic and genetic relationship between BMI and cigarette smoking in a sample of UK adults. *Addict. Behav.* 89, 98–103. doi: 10.1016/j.addbeh.2018.09.025

Wu, G., Yang, S., Zhu, L., and Lin, F. (2015). Altered spontaneous brain activity in heavy smokers revealed by regional homogeneity. *Psychopharmacology* 232, 2481–2489. doi: 10.1007/s00213-015-3881-6

Xu, J., Lyu, H., Li, T., Xu, Z., Fu, X., Jia, F., et al. (2019). Delineating functional segregations of the human middle temporal gyrus with resting-state functional connectivity and coactivation patterns. *Hum. Brain Mapp.* 40, 5159–5171. doi: 10.1002/hbm.24763

Xu, J., Wang, J., Fan, L., Li, H., Zhang, W., Hu, Q., et al. (2015). Tractography-based parcellation of the human middle temporal gyrus. *Sci. Rep.* 5:18883.

Xue, T., Dong, F., Huang, R., Tao, Z., Tang, J., Cheng, Y., et al. (2020). Dynamic neuroimaging biomarkers of smoking in young smokers. *Front. Psychiatr.* 11:663. doi: 10.3389/fpsyt.2020.00663

Yang, S., Meng, Y., Li, J., Fan, Y. S., Du, L., Chen, H., et al. (2019). Temporal dynamic changes of intrinsic brain activity in schizophrenia with cigarette smoking. *Schizophr. Res.* 210, 66–72. doi: 10.1016/j.schres.2019.06.012

Yang, Z., Zhang, Y., Cheng, J., and Zheng, R. (2020). Meta-analysis of brain gray matter changes in chronic smokers. *Eur. J. Radiol.* 132:109300.

Zhang, P., Wu, G. W., Yu, F. X., Liu, Y., Li, M. Y., Wang, Z., et al. (2020). Abnormal regional neural activity and reorganized neural network in obesity: Evidence from resting-state fMRI. *Obesity* 28, 1283–1291. doi: 10.1002/oby.22839

Zhang, R., and Volkow, N. D. (2019). Brain default-mode network dysfunction in addiction. *Neuroimage* 200, 313–331.

Zhang, S., Hu, S., Fucito, L. M., Luo, X., Mazure, C. M., Zaborszky, L., et al. (2017). Resting-state functional connectivity of the basal nucleus of meynert in cigarette smokers: Dependence level and gender differences. *Nicotine Tob. Res.* 19, 452–459. doi: 10.1093/ntr/ntw209

frontiers | Frontiers in Neuroscience

TYPE Original Research
PUBLISHED 24 November 2022
DOI 10.3389/fnins.2022.1030230

OPEN ACCESS

EDITED BY
Chitresh Bhushan,
GE Global Research, United States

REVIEWED BY
Zi-Fang Zhao,
Peking University Third Hospital, China
Nastaren Abad,
General Electric, United States

*CORRESPONDENCE
Yongmei Li
lymzhang70@aliyun.com
Chun Zeng
zengchun19840305@163.com

†These authors have contributed equally to this work and share first authorship

‡These authors have contributed equally to this work and share last authorship

SPECIALTY SECTION
This article was submitted to Brain Imaging Methods, a section of the journal Frontiers in Neuroscience

RECEIVED 28 August 2022
ACCEPTED 08 November 2022
PUBLISHED 24 November 2022

CITATION
Liu H, Xiang Y, Liu J, Feng J, Du S, Luo T, Li Y and Zeng C (2022) Diffusion kurtosis imaging and diffusion tensor imaging parameters applied to white matter and gray matter of patients with anti-N-methyl-D-aspartate receptor encephalitis.
Front. Neurosci. 16:1030230.
doi: 10.3389/fnins.2022.1030230

Diffusion kurtosis imaging and diffusion tensor imaging parameters applied to white matter and gray matter of patients with anti-N-methyl-D-aspartate receptor encephalitis

Hanjing Liu[1†], Yayun Xiang[1†], Junhang Liu[1], Jinzhou Feng[2], Silin Du[1], Tianyou Luo[1], Yongmei Li[1*‡] and Chun Zeng[1*‡]

[1]Department of Radiology, The First Affiliated Hospital of Chongqing Medical University, Chongqing, China, [2]Department of Neurology, The First Affiliated Hospital of Chongqing Medical University, Chongqing, China

Objectives: To compare parameters of diffusion tensor imaging (DTI) and diffusion kurtosis imaging (DKI) to evaluate which can better describe the microstructural changes of anti-N-methyl-D-aspartate receptor (NMDAR) encephalitis patients and to characterize the non-Gaussian diffusion patterns of the whole brain and their correlation with neuropsychological impairments in these patients.

Materials and methods: DTI and DKI parameters were measured in 57 patients with anti-NMDAR encephalitis and 42 healthy controls. Voxel-based analysis was used to evaluate group differences between white matter and gray matter separately. The modified Rankin Scale (mRS) was used to evaluate the severity of the neurofunctional recovery of patients, the Montreal Cognitive Assessment (MoCA) was used to assess global cognitive performance, and the Hamilton Depression Scale (HAMD) and fatigue severity scale (FSS) were used to evaluate depressive and fatigue states.

Results: Patients with anti-NMDAR encephalitis showed significantly decreased radial kurtosis (RK) in the right extranucleus in white matter ($P < 0.001$) and notably decreased kurtosis fractional anisotropy (KFA) in the right precuneus, the right superior parietal gyrus (SPG), the left precuneus, left middle occipital gyrus, and left superior occipital gyrus in gray matter ($P < 0.001$). Gray matter regions with decreased KFA overlapped with those with decreased RK in the left middle temporal gyrus, superior temporal gyrus (STG), supramarginal gyrus (SMG), postcentral gyrus (POCG), inferior parietal but supramarginal gyrus, angular gyrus (IPL) and angular gyrus (ANG) ($P < 0.001$). The KFA and RK in the left ANG, IPL and POCG correlated positively with MoCA scores. KFA and RK in the left ANG, IPL, POCG and SMG

correlated negatively with mRS scores. KFA in the left precuneus and right SPG as well as RK in the left STG correlated negatively with mRS scores. No significant correlation between KFA and RK in the abnormal brain regions and HAMD and FSS scores was found.

Conclusion: The microstructural changes in gray matter were much more extensive than those in white matter in patients with anti-NMDAR encephalitis. The brain damage reflected by DKI parameters, which have higher sensitivity than parameters of DTI, correlated with cognitive impairment and the severity of the neurofunctional recovery.

KEYWORDS

anti-N-methyl-D-aspartate receptor encephalitis, microstructural changes, white matter, gray matter, diffusion kurtosis imaging, diffusion tensor imaging

Introduction

Anti-N-methyl-D-aspartate receptor (NMDAR) encephalitis is the most common type of autoimmune encephalitis, with an incidence of 0.85 per million in children, while no data is available in adults (Guan et al., 2016). However, a previous study has shown that the global incidence of this disease has increased significantly, surpassing that of viral encephalitis in young people (Gable et al., 2012). Its clinical manifestations are complex and varied, often with abnormal mental behaviors, seizures, dysphasia, memory loss, involuntary movement, and autonomic dysfunction (Dalmau et al., 2019). Approximately 25% of patients may have severe disability or even die, with a mortality rate of 10%, whereas approximately 75% of patients experience sequelae, such as cognitive impairment (McKeon et al., 2018; Zhong et al., 2022). These consequences might have serious effects on patient prognosis.

Despite the severity and rapid progression of the clinical presentation, nearly half of the patients exhibited normal or non-specific manifestations on conventional magnetic resonance imaging (MRI) (Zhang et al., 2018). However, previous studies have confirmed that patients with anti-NMDAR encephalitis have alterations in the integrity and microstructural arrangement of brain white matter tissues, which can be detected by diffusion MRI techniques. Among these critical studies, previous reports have reached different conclusions by applying diffusion tensor imaging (DTI). One study reported that patients with anti-NMDAR encephalitis had extensive white matter changes (Finke et al., 2013), while another discovered that anti-NMDAR encephalitis patients had superficial white matter damage predominantly in the frontal and temporal lobes (Phillips et al., 2018). Consequently, in order to reach an objective conclusion, more sophisticated techniques must be used to investigate the plausible changes in white matter microstructure and associated pathophysiological pathways in patients with anti-NMDAR encephalitis.

Based on the assumption that the diffusion of water molecules obeys a Gaussian distribution, DTI is the most widely used technique to assess white matter changes. However, due to the presence of cell membranes, neurons, and other organelles in tissues, the diffusion of water molecules obeys a non-Gaussian distribution (Shi et al., 2021); hence, the parameters of DTI, including mean diffusivity (MD), axial diffusivity (AD), radial diffusivity (RD) and fractional anisotropy (FA), cannot describe water diffusion accurately. Diffusion kurtosis imaging (DKI) is regarded as a complementary technique for DTI, which can not only probe white matter changes accurately but can also assess the microstructural alternations in the gray matter which by the aggregation of many neuron cells and dendrites (Jensen et al., 2005).Studies have shown that the parameters of DKI, including mean kurtosis (MK), axial kurtosis (AK), radial kurtosis (RK) and kurtosis fractional anisotropy (KFA) is more suitable for assessing microstructural changes of white matter and gray matter regions with complex fiber arrangements (Qiao et al., 2020; Thaler et al., 2021).

In addition, voxel-based analysis (VBA) and region of interest (ROI)-wise analysis were applied in this study. VBA, a popular technique for assessing whole-brain DTI and/or DKI measurements, is an image postprocessing analysis method based on the evaluation of voxels. This method can avoid previous assumptions and automatically analyze the differences in various diffusion parameters in the whole brain including gray matter (Yuan et al., 2016; Yang et al., 2021; Wang et al., 2022). In this study, an ROI-wise VBA algorithm was used to detect brain regions with different diffusion parameters, and the diffusion parameters of corresponding brain regions were extracted and correlated with various clinical scales. This method is conducive to describing a comprehensive overview of anti-NMDAR patients' brain microstructural damage. To our

knowledge, the application of both DTI and DKI parameters to explore microstructure alternations in the whole brain, including white matter, gray matter and deep gray matter structures, in patients with anti-NMDAR encephalitis is rarely been reported.

Therefore, in this study, we aimed to characterize the non-Gaussian diffusion patterns of the whole brain in patients with anti-NMDAR encephalitis using DKI. The DKI parameters including MK, AK, RK and KFA and DKI-derived DTI parameters including MD, AD, RD and FA were used to detect brain microstructural changes. We compared the two methods to evaluate which method can better describe the microstructural changes of anti-NMDAR encephalitis patients. Our hypothesis was that DKI parameters might be more helpful in detecting brain microstructural changes in patients with anti-NMDAR encephalitis after the acute stage than DTI parameters, and these changes were related to patients' neuropsychological impairments.

Materials and methods

Participants

Fifty-seven patients with anti-NMDAR encephalitis after the acute stage were recruited from the First Affiliated Hospital of Chongqing Medical University, and 42 age-, sex- and education level matched healthy controls (HCs) were recruited from the community. All the participants were enrolled between October 2015 and April 2022. All patients met the diagnostic criteria for anti-NMDAR encephalitis recommended by Lancet Neuro in 2016 (Graus et al., 2016) which included (1) acute onset of one or more of the following eight major clinical manifestations: psychosis, memory impairment, speech impairment, seizures, movement disorder, disturbance of consciousness, autonomic dysfunction, and central hypoventilation; (2) positive immunoglobulin G (IgG) NMDAR antibodies in the serum and/or cerebrospinal fluid (CSF); and (3) reasonable exclusion of other disorders. Exclusion criteria for all patients included: (1) being in the acute stage; (2) having a history of other non-anti-NMDAR encephalitis psychoneurosis, craniocerebral trauma and surgery; (3) having MRI contraindications; and (4) having images with artifacts or poor quality. HCs were defined as those without a history of neurological or psychiatric disorders or any other organic disease related to the central nervous system. All participants were right-handed.

Two experienced neurologists independently assessed patients' disease severity and neuropsychological performances at the time of the study based on a comprehensive set of scales. The modified Rankin Scale (mRS) was used to evaluate the severity of the neurofunctional recovery of patients. The Montreal Cognitive Assessment (MoCA) was used to assess the global cognitive performance of all participants. The Hamilton Depression Scale (HAMD) was used to evaluate the depressive state of participants. The fatigue severity scale (FSS) was used to evaluate fatigue and the impact of fatigue on daily life.

Magnetic resonance imaging data acquisitions

All MR images were acquired on a 3.0T MR scanner (Magnetom Skyra, Siemens Healthcare GmbH, Erlangen, Germany) with a 32-channel head coil. DKI images with 3 b-values (b = 0, 1000 and 2000 s/mm^2) along 30 diffusion directions were acquired by using a single-shot, spin-echo echo planar imaging (EPI) sequence. Other MR scanning parameters included: slices = 50, voxel = 2 × 2 × 2 mm^3, field of view (FOV) = 250 mm^2, repetition time (TR) = 4500 ms, echo time (TE) = 94 ms, acquisition time (TA) = 5:25 min, integrated parallel acquisition techniques (iPAT) acceleration factor = 4 (GRAPPA), and partial-Fourier = 6/8. A magnetization prepared rapid gradient-echo (MPRAGE) sequence was used to acquire anatomical T1-weighted images (T_1WI). The parameters included: voxel = 1 × 1 × 1 mm^3, FOV = 256 mm^2, TR = 2300 ms, TE = 2.26 ms, slices = 192, inversion time = 900 ms, and flip angle = 8 deg.

Data processing and voxel-based analysis

First, we checked the basic parameters of the images, including resolution, dimension information and so on, then we visually inspected the images to assess the quality of the images and removed the images with obvious head movements and artifacts. Second, all DICOM images were converted into Neuroimaging Informatics Technology Initiative (NIfTI) format using the MRIcron tool named dcm2nii[1] (SedDB, RRID, SCR_002403). Third, converted data were then loaded into the "Eddy-current" toolbox of the Functional Magnetic Resonance Imaging of the Brain software library (FSL)[2] (SedDB, RRID, SCR_00283) to perform motion and eddy currents distortion correction (Andersson et al., 2003). Forth, the kurtosis and diffusion tensors were estimated using a constrained linear least square (CLLS) algorithm model in Diffusional Kurtosis Estimator[3] (Tabesh et al., 2011). DKI tensor fitting was performed with constrained linear weighted fitting and DTI tensor fitting was performed with linear weighted fitting to obtain the DKI- and DTI-based parametric maps, respectively.

1 http://www.mricro.com/
2 http://www.fmrib.ox.ac.uk/fsl/
3 http://www.nitrc.org/projects/dke/

Fifth, all the parametric maps were then normalized to the standard Montreal Neurological Institute (MNI) space. To normalize all the b0 images into the T2W template of the statistical parametric mapping (SPM)[4] (SedDB, RRID, SCR_007110), we applied a non-linear registration tool in SPM8 with a resolution of $2 \times 2 \times 2$ mm^3. Then, a full width at half maximum (FWHM) kernel of $6 \times 6 \times 6$ mm^3 was used to make these images averaged and smoothed to generate a new b0 template (Good et al., 2001). For each parametric map, voxel-wise *t*-test were conducted using the white matter, gray matter and deep gray matter masks with sex, age and education adjusted in SPM8. The MNI T1 template was segmented in FSL to generate the white matter and gray matter masks.

Statistical analyses

Demographic information and clinical assessment were compared between anti-NMDAR patients and HCs using the chi-square test and Mann-Whitney *U* test. Data that followed a normal distribution are represented as the mean ± standard deviation, and data that did not follow a normal distribution are represented as the median and interquartile range. A two-sample *t*-test in SPM8 with age, sex and education as nuisance variables was performed to compare differences between groups in white matter, gray matter and deep gray matter, statistical results were presented using the xjView toolbox. The significance level was set at a cluster level of uncorrected $P < 0.001$. Cluster size > 30 contiguous voxels was considered statistically significant. To account for multiple comparisons across the whole brain, false discovery rate (FDR) correction was performed and $P < 0.05$ were considered to show a significant difference. The diffusion parameters of brain regions that showed significant differences in VBA were extracted. Then, Spearman correlational analysis was performed to explore the relationship between the diffusion parameters and clinical scales, including MoCA, HAMD, and FSS scales; Kendall correlation analysis was performed to explore the relationship between the diffusion parameters and mRS scores. The statistical analysis was performed with SPSS software version 23.0. The criterion for statistical significance was set at *P* value < 0.05.

Results

Demographic information and clinical scale scores

The demographics information and clinical scales of the participants are shown in **Table 1**. Fifty-seven anti-NMDAR patients (27 males, 30 females) and 42 HCs (16 males, 26 females) were included in the study. There was no statistically significant difference in age ($P = 0.673$), sex ($P = 0.415$) or education level ($P = 0.139$) between patients with anti-NMDAR encephalitis and HCs. The patients underwent clinical scale evaluation and MRI scanning 15.44 ± 9.08 months after clinical onset. Two patients were moderately disabled (mRS = 3), six patients fully recovered (mRS = 0), and 48 patients still had mild symptoms but were able to accomplish their daily routine (mRS = 1–2). Compared to HCs, the MoCA scores were significantly decreased ($P < 0.001$), while HAMD ($P < 0.001$) and FSS ($P < 0.001$) scores were increased significantly in patients with anti-NMDAR encephalitis.

TABLE 1 Demographics information and clinical scales of the participants.

	Patients ($n = 57$)	HCs ($n = 42$)	*P*-value
Age (years)	31 (23,46)	30 (25,46.5)	0.673*
Sex, male/female	27/30	16/26	0.415#
Education (years)	12 (9,12.5)	12 (9,18)	0.139*
mRS	1(1,2)	N/A	N/A
MoCA	23 (20,25)	28 (26,29)	$P < 0.001$*
HAMD	10 (6,16)	3 (1,7)	$P < 0.001$*
FSS	21 (13, 31)	13.33 ± 4.83	$P < 0.001$*

HCs, healthy controls; mRS, modified Rankin Scale; N/A, not applicable; MoCA, Montreal Cognitive Assessment; HAMD, Hamilton Depression Scale; FSS, Fatigue Severity Scale. The data that follow a normal distribution were represented by mean ± standard deviation, and data that do not follow a normal distribution were represented as median and interquartile range.
* Mann-Whitney *U* test.
# Chi-square test.

Group differences in white matter, gray matter and deep gray matter

Compared with HCs, RK in the right extranuclear which located in white matter significantly decreased in patients with anti-NMDAR encephalitis ($P < 0.001$). Compared with HCs, patients with anti-NMDAR encephalitis displayed significant decrease in KFA in the right precuneus, the right superior parietal gyrus (SPG), the left precuneus, left middle occipital gyrus (MOG) and left superior occipital gyrus (SOG) ($P < 0.001$). Gray matter regions with significant KFA reduction overlapped with those with significant RK reduction in the left middle temporal gyrus (MTG), superior temporal gyrus (STG), supramarginal gyrus (SMG), postcentral gyrus (POCG), inferior parietal but supramarginal gyrus and angular gyrus (IPL) and angular gyrus (ANG) ($P < 0.001$). In the deep gray matter regions, there were no brain regions with diffusion parameters that were significantly different from those of HCs. In addition, compared with HCs, DKI-derived DTI parameters, including FA, MD, AD, RD, and DKI parameters MK and AK were not markedly changed in the

4 http://www.fil.ion.ucl.ac.uk/spm/

brain regions of patients with anti-NMDAR encephalitis. The brain regions of anti-NMDAR encephalitis patients showing significant microstructural changes are shown in Figure 1 and Table 2. These results were obtained by setting the significance level at a cluster level of uncorrected $P < 0.001$, and all results were not significantly different after FDR correction at the statistical significance level set at $P \leq 0.05$.

Correlations between diffusion parameters and clinical scale scores

In the correlation analyses, KFA and RK in the left ANG ($r = 0.277$, $P = 0.037$; $r = 0.323$, $P = 0.014$), IPL ($r = 0.287$, $P = 0.031$; $r = 0.365$, $P = 0.005$) and POCG ($r = 0.270$, $P = 0.042$; $r = 0.280$, $P = 0.035$) correlated positively with MoCA scores. KFA and RK in the left ANG ($r = -0.272$, $P = 0.009$; $r = -0.213$, $P = 0.042$), IPL ($r = -0.326$, $P = 0.002$; $r = -0.337$, $P = 0.001$), POCG ($r = -0.326$, $P = 0.002$; $r = -0.336$, $P = 0.001$) and SMG ($r = -0.283$, $P = 0.007$; $r = -0.313$, $P = 0.003$) correlated negatively with mRS scores. In addition, KFA in the left precuneus ($r = -0.213$, $P = 0.042$) and right SPG ($r = -0.265$, $P = 0.012$) as well as RK in the left STG ($r = -0.242$, $P = 0.021$) correlated negatively with mRS scores. No correlation was found between KFA and RK in the abnormal brain regions and HAMD and FSS scores ($P > 0.05$). Correlations between clinical scale scores and KFA and RK values in abnormal brain regions in patients with anti-NMDAR encephalitis are shown in Figure 2 and Table 3.

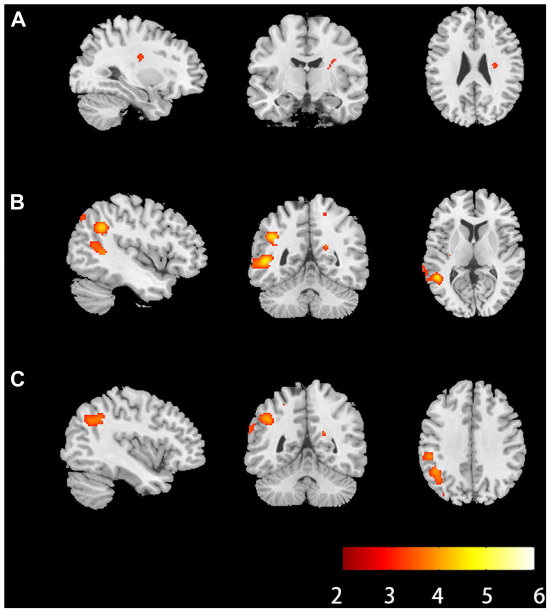

FIGURE 1
Brain regions of anti-NMDAR encephalitis patients showed significant microstructural changes. **(A)** Brain regions where radial kurtosis (RK) values changed in the white matter ($P < 0.001$, uncorrected, cluster size = 30). **(B)** Brain regions where kurtosis fractional anisotropy values changed in the gray matter ($P < 0.001$, uncorrected, cluster size = 30). **(C)** Brain regions where RK values changed in the gray matter ($P < 0.001$, uncorrected, cluster size = 30). The hot color represents the lower diffusion parameters values in the patients' group. L, left; R, right; anti-NMDAR, anti-N-methyl-D-aspartate receptor.

Discussion

To the best of our knowledge, this is the first study to investigate the microstructure changes in the whole brain, including white matter, gray matter and deep gray matter in patients with anti-NMDAR encephalitis after the acute stage by applying the DKI method. Our study found that, compared to HCs, patients with anti-NMDAR encephalitis had a distinct pattern of microstructural abnormalities characterized by widespread gray matter damage other than white matter damage, and was correlated with cognitive impairment and the severity of neurofunctional recovery.

Comparison of diffusion kurtosis imaging and diffusion tensor imaging parameters

In the present study, we found that extensive microstructural changes in patients with anti-NMDAR encephalitis could be quantitatively assessed by DKI parameters. Our results showed that only two kurtosis parameters, RK and KFA changed in patients compared with HCs. Kurtosis values are a series of indices used to describe the complexity of organizational structure. The higher the kurtosis values are, the more restricted and complex the environment is (Das et al., 2017). RK mainly describes the degree to which water molecules are confined in the radial direction and is sensitive to myelin sheath changes (Liang et al., 2021). KFA is an anisotropy parameter measured on the fourth-order tensor based on DKI, similar to FA. FA reflects the difference in the dispersion coefficient in the three axis directions of the ellipsoid and the organizational structure's directivity, which is positively correlated with the directivity. However, KFA provides more information about anisotropic diffusion dynamics than FA as it is affected by many factors, such as intermolecular distance, cerebrospinal fluid flow, fiber structural integrity, and fiber structural compactness. When KFA is close to zero, the diffusion is close to isotropic. The larger the FKA value is, the closer the organizational structure is (Jensen et al., 2005). It is important to note that changes in diffusion parameters refer to structures such as fiber arrangement and myelin density that can impact the complexity of the environment. In this study, we found that both RK and KFA were decreased in

TABLE 2 Brain regions of anti-NMDAR encephalitis patients showed significant microstructural changes.

Mask	Index	Side	Brian region	Peak MNI coordinates			Peak intensity	Cluster size
				X	Y	Z		
WM	RK	R	Extranuclear	24	−14	16	3.8277	69
GM	KFA	L	MTG; STG	−50	−48	6	4.7968	651
		L	SMG	−66	−28	30	3.7275	92
		R	Precuneus	19	−53	21	3.7829	35
		L	ANG; IPL; precuneus; MOG; SOG	−42	50	34	4.4133	570
		L	POCG	−52	−14	44	3.4781	46
		R	SPG	16	−54	60	3.4684	69
	RK	L	STG; MTG	−70	−40	8	3.8475	160
		L	POCG	−62	−6	16	3.5157	47
		L	IPL; SMG	−52	−32	38	4.055	195
		L	IPL; ANG	−44	50	38	4.0567	346

Anti-NMDAR, anti-N-methyl-D-aspartate receptor; RK, radial fractional; KFA, kurtosis fractional anisotropy; WM, white matter; GM, gray matter; MTG, middle temporal gyrus; STG, superior temporal gyrus; SMG, supramarginal gyrus; ANG, angular gyrus; IPL, inferior parietal but supramarginal and angular gyrus; MOG, middle occipital gyrus; SOG, superior occipital gyrus; POCG, postcentral gyrus; SPG, superior parietal gyrus.

the corresponding brain regions, thus we speculated that the fiber structure arrangement and myelin sheath density of anti-NMDAR encephalitis patients were sparser than those of HCs. However, no abnormalities were detected in brain microstructural changes by DKI-derived DTI parameters when a $P < 0.001$ was set. Therefore, we speculated that DKI parameters were more sensitive than DTI parameters in detecting brain microstructural changes of anti-NMDAR encephalitis patients at the same P value threshold. Other studies also supported this speculation. A comparative study in bipolar disorder showed that DKI parameters could detect wider regions and have higher fidelity than DTI parameters at the same P value threshold (Yang et al., 2021). DKI parameters also showed more WM microstructural alternations in patients with poststroke cognitive impairment than DTI parameters revealed (He et al., 2022). Consistent with previous findings, the DKI method greatly exceeded the DTI method for the detection of gray-white matter structures in anti-NMDAR encephalitis patients. This could be attributed to the fact that the DKI algorithm can detect more water molecules that obey a non-Gaussian distribution of diffusion.

White matter microstructural changes

Our results showed that only the right extranuclear with reduced RK in the white matter regions was found in patients compared with HCs. However, another retrospective study found that patients with anti-NMDAR encephalitis had widespread microstructural alternations with FA decreased in the right MTG, right precuneus, and left middle cerebellar peduncle, and MD increased in the left frontal lobe and MTG (Liang et al., 2020). This might be because the study enrolled patients with a shorter time from clinical onset to MRI scanning (3.1 ± 2.1months) than we did (15.44 ± 9.08months). In addition, the study only included 15 patients and we included a much larger sample with 57 patients. In addition, a case was reported in which a 24-year-old woman with multifocal subcortical white matter lesions in the acute stage showed complete resolution after two months of appropriate immunotherapy (Wang et al., 2015). Therefore, we speculated that the white matter damage in patients with anti-NMDAR encephalitis was not permanent but could be gradually repaired over time. A previous study also indicated that the disease was reversible, immune-mediated neuronal dysfunction rather than irreversible degeneration (Hughes et al., 2010; Dalmau et al., 2011). Although some previous studies using the DTI method reported extensive white matter alterations in anti-NMDAR encephalitis, this appears to conflict with our findings of only RK and KFA changes. However, some of these studies focused on the superficial white matter areas rather than the whole-brain including white-gray matter and deep gray matter areas of recovered and partially recovered patients (Phillips et al., 2018), while others used Tract-Based Spatial Statistic (TBSS) analysis methods that were inconsistent with ours (Finke et al., 2013; Yang et al., 2022). Recently, Wang et al. applied multimodal brain network analysis to show that changes in structural networks were mainly in fiber number and fiber length, and very few significant changes in FA in anti-NMDAR encephalitis (Wang et al., 2021), which is consistent with our findings. While in our research, we didn't found changes of DTI parameters in white matter. Thus, we speculated that TBSS analysis might be more sensitive than voxel-based analysis in detecting a wide range of white

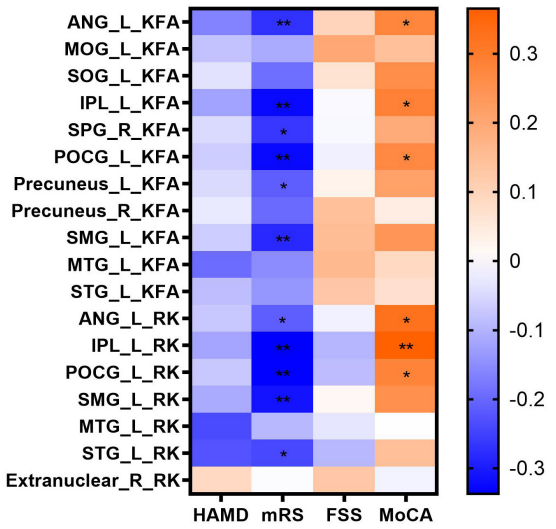

FIGURE 2
Correlations between clinical scale scores and KFA and RK values in abnormal brain regions in patients with anti-NMDAR encephalitis. Statistical differences are $^{*}P < 0.05$, $^{**}P < 0.01$. Anti-NMDAR, anti-N-methyl-D-aspartate receptor; HAMD, Hamilton Depression Scale; mRS, Modified Rankin Scale; FSS, Fatigue Severity Scale; MoCA, Montreal Cognitive Assessment; KFA, kurtosis fractional anisotropy; RK, radial kurtosis; ANG_L, left angular gyrus; MOG_L, left middle occipital gyrus; SOG_L, left superior occipital gyrus; IPL_L, left inferior parietal but supramarginal and angular gyrus; SPG_R, right superior parietal gyrus; POCG_L, left postcentral gyrus; Precuneus_ L, left precuneus; Precuneus_ R, right precuneus; SMG_L, left supramarginal gyrus; MTG_L, left middle temporal gyrus; STG_L, left superior temporal gyrus.

matter microstructural changes of anti-NMDAR encephalitis. As widespread gray matter damage was observed in this study, we speculated that the recovery rate of abnormal white matter microstructure was faster than that of gray matter, or the severity of white matter damage was lower than that of gray matter damage.

Gray matter microstructural changes and their relationship with cognitive performance

In this study, we found that KFA and RK decreased in the left ANG, IPL and POCG and these changes were correlated with MoCA scores, suggesting that these brain regions play an important role in cognitive impairment in patients with anti-NMDAR encephalitis. Cognitive function is a complex brain activity based on local information processing and effective integration among different brain regions. Therefore, pathological processes can contribute to cognitive dysfunction by directly participating in and disrupting activity in gray matter regions associated with cognitive function (Rocca et al., 2015). The associations between these regions and cognitive damage have been widely reported in previous studies.

The ANG is closely related to a variety of cognitive processes, including spatial cognition, language, number processing, memory retrieval, and attention. From a neuroanatomical perspective, it occupies a central position and acts as a hub of multiple nodes within the default network. It receives input from the sensory cortex and integrates different forms of sensory information (Bonner et al., 2013; Seghier, 2013). ANG injury has been confirmed to produce a variety of cognitive impairments such as aphasia, agraphia and poor arithmetic skills (Price et al., 2018; Sakurai et al., 2021; Liu et al., 2022). These findings supported the function of the ANG in integrating multiple inputs of external information and that changes in the microstructure of the ANG are associated with cognitive impairment.

The IPL is responsible for receiving and integrating information from different modes of physical movement, hearing and vision (Binder et al., 2009). Previous studies have shown that IPL plays an important role in auditory working memory and episodic memory (Mottaghy et al., 2002; Sestieri et al., 2013). In addition, higher pattern similarity in bilateral IPL was found to be associated with better learning performance during the early learning phase (Qu et al., 2021). Recently, a multiparameter study found that neurovascular coupling in the ANG and IPL was decreased and was associated with cognitive deficits (Guo et al., 2022).

The POCG is mainly responsible for integrating the information of various somatosensory stimuli to help individual correctly realize the correct recognition of objects. Some studies have shown that it is involved in cognitive activities. Reduced functional connectivity between the dentate nucleus and the POCG is associated with cognitive impairment in patients with schizophrenia (Xie et al., 2021). A study of patients undergoing cognitive behavioral therapy for mild depression found that increased functional connectivity between the left POCG and the parahippocampal gyrus may be associated with enhanced memory recognition (Du et al., 2016). Previously, a resting state functional MRI found that functional connectivity in the POCG was increased in patients with anti-NMDAR encephalitis after the acute stage. These changes were considered compensation after an injury, or these changes might be caused by the glial cell proliferation at the injury site during recovery (Cai et al., 2020), which contradicts our conclusion that the microstructures of anti-NMDAR encephalitis patients are sparser than those of HCs. Compared with functional sequences, DKI is more able to reflect structural changes, and more patients were included in this study; it is considered that the results in this study may be somewhat more accurate, but the exact changes warrant further pathological study.

TABLE 3 Correlations between clinical scale scores and KFA and RK values in abnormal brain regions in patients with anti-NMDAR encephalitis.

		HAMD		mRS		FSS		MoCA	
		r	*P*	r	*P*	r	*P*	r	*P*
KFA	ANG_L	−0.164	0.222	−0.272**	0.009	0.097	0.475	0.277*	0.037
	MOG_L	−0.081	0.549	−0.113	0.280	0.198	0.140	0.144	0.286
	SOG_L	−0.039	0.773	−0.192	0.067	0.064	0.638	0.258	0.053
	IPL_L	−0.123	0.361	−0.326**	0.002	−0.008	0.953	0.287*	0.031
	SPG_R	−0.049	0.720	−0.265*	0.012	−0.010	0.943	0.193	0.151
	POCG_L	−0.067	0.620	−0.326**	0.002	−0.021	0.879	0.270*	0.042
	Precuneus_L	−0.050	0.711	−0.213*	0.042	0.027	0.843	0.214	0.111
	Precuneus_R	−0.028	0.835	−0.198	0.058	0.144	0.287	0.040	0.767
	SMG_L	−0.067	0.621	−0.283**	0.007	0.150	0.267	0.240	0.072
	MTG_L	−0.195	0.146	−0.152	0.147	0.162	0.230	0.087	0.520
	STG_L	−0.086	0.526	−0.140	0.180	0.127	0.347	0.069	0.608
RK	ANG_L	− 0.074	0.587	−0.213*	0.042	−0.019	0.886	0.323*	0.014
	IPL_L	−0.120	0.374	−0.337**	0.001	−0.099	0.465	0.365**	0.005
	POCG_L	−0.074	0.583	−0.336**	0.001	−0.089	0.512	0.280*	0.035
	SMG_L	−0.113	0.401	−0.313**	0.003	0.014	0.915	0.253	0.058
	MTG_L	−0.240	0.072	−0.094	0.370	−0.034	0.804	−0.002	0.988
	STG_L	−0.227	0.089	−0.242*	0.021	−0.094	0.489	0.146	0.279
	Extranuclear_R	0.087	0.519	−0.004	0.969	0.127	0.347	−0.016	0.907

Anti-NMDAR, anti-N-methyl-D-aspartate receptor; HAMD, Hamilton Depression Scale; mRS, modified Rankin Scale; FSS, Fatigue Severity Scale; MoCA, Montreal Cognitive Assessment; KFA, kurtosis fractional anisotropy; RK, radial kurtosis; ANG_L, left angular gyrus; MOG_L, left middle occipital gyrus; SOG_L, left superior occipital gyrus; IPL_L, left inferior parietal but supramarginal and angular gyrus; SPG_R, right superior parietal gyrus; POCG_L, left postcentral gyrus; Precuneus_ L, left precuneus; Precuneus_ R, right precuneus; SMG_L, left supramarginal gyrus; MTG_L, left middle temporal gyrus; STG_L, left superior temporal gyrus.
Statistical differences are *$P < 0.05$, **$P < 0.01$.

Gray matter microstructural changes and their relationship with disease severity

The mRS scale was used to evaluate the severity of the neurofunctional recovery of patients, which is a comprehensive assessment of neurological functional recovery (Sagnier et al., 2020). This study found that the RK value of the left STG decreased and was associated with mRS scores but not MoCA scores, which may be related to the microstructural damage caused by the high incidence of temporal lobe epilepsy in patients with anti-NMDAR encephalitis (Song et al., 2016; Prager et al., 2019). This finding can also explain the decreased neurovascular coupling of the left STG (Guo et al., 2022). In conclusion, we speculated that the impaired microstructure of the left STG led to its reduced function and low metabolism. This study also found that the left precuneus, left SMG, and right SPG had microstructural changes and were associated with mRS scores. A previous study showed decreased cerebellar blood flow in the precuneus in patients with anti-NMDAR encephalitis (Miao et al., 2020), while this study found that KFA decreased in the left precuneus. Thus, we hypothesized that structural damage to nerve fibers and other structures of precuneus led to a decrease in metabolism. The SMG participates in action planning, and its impairment can lead to mobility impairments (Króliczak et al., 2016). Therefore, reducing RK and KFA in the SMG may be associated with impaired motor function in patients with anti-NMDAR encephalitis.

Gray matter microstructural changes and the relationship with depression and fatigue

This study did not find any correlation among KFA and RK in the abnormal brain regions, HAMD scores and FSS scores, which means that microstructural damage may not be associated with increased depression or fatigue. Another resting-state functional MRI study also did not find correlations between abnormal functional connectivity and depression (Cai et al., 2020). However, we did not find other studies demonstrating a correlation between fatigue and structural or functional abnormalities in patients with anti-NMDAR encephalitis. It is clear that many patients are chronically depressed or prone to fatigue after the acute stage, but no correlation has been found in functional or structural sequences. It is possible that these changes are more subtle

and will require more sensitive techniques to detect them in the future.

Laterality of patients' microstructural changes

It is interesting that the brain regions with microstructural changes are primarily located in the left hemisphere. Thus, we speculated that the effects of anti-NMDAR encephalitis on the brain are asymmetrical. This might be because NMDARs are unevenly distributed on both sides of the brain (Ferreira et al., 2020). For a right-handed person, the left hemisphere is their dominant hemisphere, responsible for language production and comprehension, motor processing, and logical interpretation (Rentería, 2012). As all of our patients are right-handed, the impact of anti-NMDAR encephalitis on these functions mentioned above is significant. Studies have already found that changes in lateralization of the cortex are a prominent marker of several neurological disorders, such as schizophrenia, Alzheimer's disease, and depression (Sheng et al., 2013; Liu et al., 2018; Yang et al., 2022), and may also be a well-known marker of anti-NMDAR encephalitis.

Limitations

There were several limitations to this study. First, to detect larger activated areas of gray matter and white matter, we used a Gaussian kernel of $6 \times 6 \times 6$ mm FWHW. However, applying a larger kernel has the disadvantage of reducing its ability to detect smaller regions. In our study, the diffusion parameters in deep gray matter regions were not significantly different patients and HCs. This result might be due to the large smoothing kernel applied to the deep gray matter regions resulting in detectability reduced. To date, little attention has been specifically paid to the deep gray matter in patients with anti-NMDAR encephalitis. Applying a smaller Gaussian kernel and combining other techniques to further explore the changes of deep gray matter in patients with anti-NMDAR encephalitis are needed in the future. Second, cognitive function can be divided into different cognitive domains, with different pathological substrates that contribute to the disease. In this study, we only used MoCA scores to assess the overall cognitive function of the subjects, a more refined cognitive scale are needed in the future. Third, the mRS scale was used to comprehensively evaluate the severity of the neurofunctional recovery of patients. This study speculated that, in addition to cognitive function impairment, patients with anti-NMDAR encephalitis still had impaired motor and sensory functions after the acute stage. Future adoption of specialized scales for assessing motor dysfunction, such as the Motor Assessment Scale, will be considered. Nevertheless, this study did not use the scale, especially for motor and sensory function evaluation. Finally, patients with anti-NMDAR encephalitis included in this study had different disease durations. They are in different stages after acute phase, which may have resulted in different degrees of damage and microstructures repair.

Conclusion

In conclusion, by means of the DKI method, our study demonstrated that the microstructural changes in gray matter were much more extensive than those in white matter in patients with anti-NMDAR encephalitis after the acute stage. The brain damage reflected by DKI parameters, which have higher sensitivity than DTI parameters, was correlated with the cognitive impairment and severity of the neurofunctional recovery, which may help to assess the severity and progression of this disease.

Data availability statement

The original contributions presented in this study are included in the article/supplementary material, further inquiries can be directed to the corresponding authors.

Ethics statement

The studies involving human participants were reviewed and approved by the Institutional Review Board of The First Affiliated Hospital of Chongqing Medical University, Chongqing, China. The patients/participants provided their written informed consent to participate in this study.

Author contributions

JF and JL offered the study design. SD and JL collected all the data. YX and SD offered the data processing support. HL and YX contributed to writing the first draft of the manuscript. CZ, TL, and YL provided the guidance and critical reviews. All authors contributed to the article and approved the submitted version.

Funding

This study was supported by the Medicine Scientific Key Research Project of Chongqing Municipal Health and Family Planning Commission of China (No. 2016ZDXM002), the Chongqing Basic Research and Frontier Exploration Project of Chongqing Science and Technology Commission (No. cstc2018jcyjAX0584), the Medical Scientific Youth Project of Chongqing Municipal Health and Family Planning Commission of China (No. 2018QNXM004), and the Key Project of Technological Innovation and Application Development

of Chongqing Science and Technology Bureau (CSTC2021 jscx-gksb-N0008).

Conflict of interest

The authors declare that the research was conducted in the absence of any commercial or financial relationships that could be construed as a potential conflict of interest.

Publisher's note

All claims expressed in this article are solely those of the authors and do not necessarily represent those of their affiliated organizations, or those of the publisher, the editors and the reviewers. Any product that may be evaluated in this article, or claim that may be made by its manufacturer, is not guaranteed or endorsed by the publisher.

References

Andersson, J. L., Skare, S., and Ashburner, J. (2003). How to correct susceptibility distortions in spin-echo echo-planar images: Application to diffusion tensor imaging. *Neuroimage* 20, 870–888. doi: 10.1016/S1053-8119(03)00336-7

Binder, J. R., Desai, R. H., Graves, W. W., and Conant, L. L. (2009). Where is the semantic system? A critical review and meta-analysis of 120 functional neuroimaging studies. *Cereb. Cortex* 19, 2767–2796. doi: 10.1093/cercor/bhp055

Bonner, M. F., Peelle, J. E., Cook, P. A., and Grossman, M. (2013). Heteromodal conceptual processing in the angular gyrus. *Neuroimage* 71, 175–186. doi: 10.1016/j.neuroimage.2013.01.006

Cai, L., Liang, Y., Huang, H., Zhou, X., and Zheng, J. (2020). Cerebral functional activity and connectivity changes in anti-N-methyl-D-aspartate receptor encephalitis: A resting-state fMRI study. *Neuroimage Clin.* 25:102189. doi: 10.1016/j.nicl.2020.102189

Dalmau, J., Armangué, T., Planagumà, J., Radosevic, M., Mannara, F., Leypoldt, F., et al. (2019). An update on anti-NMDA receptor encephalitis for neurologists and psychiatrists: Mechanisms and models. *Lancet Neurol.* 18, 1045–1057. doi: 10.1016/s1474-4422(19)30244-3

Dalmau, J., Lancaster, E., Martinez-Hernandez, E., Rosenfeld, M. R., and Balice-Gordon, R. (2011). Clinical experience and laboratory investigations in patients with anti-NMDAR encephalitis. *Lancet Neurol.* 10, 63–74. doi: 10.1016/s1474-4422(10)70253-2

Das, S. K., Wang, J. L., Bing, L., Bhetuwal, A., and Yang, H. F. (2017). Regional values of diffusional kurtosis estimates in the healthy brain during normal aging. *Clin. Neuroradiol.* 27, 283–298. doi: 10.1007/s00062-015-0490-z

Du, X., Mao, Y., Ran, Q., Zhang, Q., Luo, Q., and Qiu, J. (2016). Short-term group cognitive behavior therapy contributes to recovery from mild depression: Evidence from functional and structural MRI. *Psychiatry Res. Neuroimaging* 251, 53–59. doi: 10.1016/j.pscychresns.2016.04.010

Ferreira, J. S., Dupuis, J. P., Kellermayer, B., Bénac, N., Manso, C., Bouchet, D., et al. (2020). Distance-dependent regulation of NMDAR nanoscale organization along hippocampal neuron dendrites. *Proc. Natl. Acad. Sci. U.S.A.* 117, 24526–24533. doi: 10.1073/pnas.1922477117

Finke, C., Kopp, U. A., Scheel, M., Pech, L. M., Soemmer, C., Schlichting, J., et al. (2013). Functional and structural brain changes in anti-N-methyl-D-aspartate receptor encephalitis. *Ann. Neurol.* 74, 284–296. doi: 10.1002/ana.23932

Gable, M. S., Sheriff, H., Dalmau, J., Tilley, D. H., and Glaser, C. A. (2012). The frequency of autoimmune N-methyl-D-aspartate receptor encephalitis surpasses that of individual viral etiologies in young individuals enrolled in the California Encephalitis Project. *Clin. Infect. Dis.* 54, 899–904. doi: 10.1093/cid/cir1038

Good, C. D., Johnsrude, I. S., Ashburner, J., Henson, R. N., Friston, K. J., and Frackowiak, R. S. (2001). A voxel-based morphometric study of ageing in 465 normal adult human brains. *Neuroimage* 14, 21–36. doi: 10.1006/nimg.2001.0786

Graus, F., Titulaer, M. J., Balu, R., Benseler, S., Bien, C. G., Cellucci, T., et al. (2016). A clinical approach to diagnosis of autoimmune encephalitis. *Lancet Neurol.* 15, 391–404. doi: 10.1016/s1474-4422(15)00401-9

Guan, H. Z., Ren, H. T., and Cui, L. Y. (2016). Autoimmune encephalitis: An expanding frontier of neuroimmunology. *Chin. Med. J.* 129, 1122–1127. doi: 10.4103/0366-6999.180514

Guo, Y., Lv, X., Wei, Q., Wu, Y., Chen, Y., Ji, Y., et al. (2022). Impaired neurovascular coupling and cognitive deficits in anti-N-methyl-D-aspartate receptor encephalitis. *Brain Imaging Behav.* 16, 1065–1076. doi: 10.1007/s11682-021-00588-4

He, C., Gong, M., Li, G., Shen, Y., Han, L., Han, B., et al. (2022). Evaluation of white matter microstructural alterations in patients with post-stroke cognitive impairment at the sub-acute stage. *Neuropsychiatr. Dis. Treat.* 18, 563–573. doi: 10.2147/ndt.S343906

Hughes, E. G., Peng, X., Gleichman, A. J., Lai, M., Zhou, L., Tsou, R., et al. (2010). Cellular and synaptic mechanisms of anti-NMDA receptor encephalitis. *J. Neurosci.* 30, 5866–5875. doi: 10.1523/jneurosci.0167-10.2010

Jensen, J. H., Helpern, J. A., Ramani, A., Lu, H., and Kaczynski, K. (2005). Diffusional kurtosis imaging: The quantification of non-gaussian water diffusion by means of magnetic resonance imaging. *Magn. Reson. Med.* 53, 1432–1440. doi: 10.1002/mrm.20508

Króliczak, G., Piper, B. J., and Frey, S. H. (2016). Specialization of the left supramarginal gyrus for hand-independent praxis representation is not related to hand dominance. *Neuropsychologia* 93, 501–512. doi: 10.1016/j.neuropsychologia.2016.03.023

Liang, W., Fan, Z., Cui, S., Shen, X., and Wang, L. (2021). The association between white matter microstructure alterations detected by diffusional kurtosis imaging in neural circuit and post-stroke depression. *Neurol. Res.* 43, 535–542. doi: 10.1080/01616412.2021.1888033

Liang, Y., Cai, L., Zhou, X., Huang, H., and Zheng, J. (2020). Voxel-based analysis and multivariate pattern analysis of diffusion tensor imaging study in anti-NMDA receptor encephalitis. *Neuroradiology* 62, 231–239. doi: 10.1007/s00234-019-02321-x

Liu, H., Zhang, L., Xi, Q., Zhao, X., Wang, F., Wang, X., et al. (2018). Changes in brain lateralization in patients with mild cognitive impairment and Alzheimer's disease: A resting-state functional magnetic resonance study from Alzheimer's disease neuroimaging initiative. *Front. Neurol.* 9:3. doi: 10.3389/fneur.2018.00003

Liu, Q. Q., Li, W. B., Song, Y. W., Zhao, Z. B., Yan, Y. N., Yang, Y. H., et al. (2022). Correlation between focal lesion sites and language deficits in the acute phase of post-stroke aphasia. *Folia Neuropathol.* 60, 60–68. doi: 10.5114/fn.2022.114343

McKeon, G. L., Robinson, G. A., Ryan, A. E., Blum, S., Gillis, D., Finke, C., et al. (2018). Cognitive outcomes following anti-N-methyl-D-aspartate receptor encephalitis: A systematic review. *J. Clin. Exp. Neuropsychol.* 40, 234–252. doi: 10.1080/13803395.2017.1329408

Miao, A., Liu, Q., Li, Z., Liu, W., Wang, L., Ge, J., et al. (2020). Altered cerebral blood flow in patients with anti-NMDAR encephalitis. *J. Neurol.* 267, 1760–1773. doi: 10.1007/s00415-020-09747-x

Mottaghy, F. M., Döring, T., Müller-Gärtner, H. W., Töpper, R., and Krause, B. J. (2002). Bilateral parieto-frontal network for verbal working memory: An interference approach using repetitive transcranial magnetic stimulation (rTMS). *Eur. J. Neurosci.* 16, 1627–1632. doi: 10.1046/j.1460-9568.2002.02209.x

Phillips, O. R., Joshi, S. H., Narr, K. L., Shattuck, D. W., Singh, M., Di Paola, M., et al. (2018). Superficial white matter damage in anti-NMDA receptor encephalitis. *J. Neurol. Neurosurg. Psychiatry* 89, 518–525. doi: 10.1136/jnnp-2017-316822

Prager, O., Kamintsky, L., Hasam-Henderson, L. A., Schoknecht, K., Wuntke, V., Papageorgiou, I., et al. (2019). Seizure-induced microvascular injury is associated with impaired neurovascular coupling and blood-brain barrier dysfunction. *Epilepsia* 60, 322–336. doi: 10.1111/epi.14631

Price, G. R., Yeo, D. J., Wilkey, E. D., and Cutting, L. E. (2018). Prospective relations between resting-state connectivity of parietal subdivisions and arithmetic competence. *Dev. Cogn. Neurosci.* 30, 280–290. doi: 10.1016/j.dcn.2017.02.006

Qiao, P. G., Cheng, X., Li, G. J., Song, P., Han, C., and Yang, Z. H. (2020). MR diffusional kurtosis imaging-based assessment of brain microstructural changes in

patients with Moyamoya disease before and after revascularization. *AJNR Am. J. Neuroradiol.* 41, 246–254. doi: 10.3174/ajnr.A6392

Qu, J., Hu, L., Liu, X., Dong, J., Yang, R., and Mei, L. (2021). The contributions of the left hippocampus and bilateral inferior parietal lobule to form-meaning associative learning. *Psychophysiology* 58:e13834. doi: 10.1111/psyp.13834

Rentería, M. E. (2012). Cerebral asymmetry: A quantitative, multifactorial, and plastic brain phenotype. *Twin Res. Hum. Genet.* 15, 401–413. doi: 10.1017/thg.2012.13

Rocca, M. A., Amato, M. P., De Stefano, N., Enzinger, C., Geurts, J. J., Penner, I. K., et al. (2015). Clinical and imaging assessment of cognitive dysfunction in multiple sclerosis. *Lancet Neurol.* 14, 302–317. doi: 10.1016/s1474-4422(14)70250-9

Sagnier, S., Catheline, G., Dilharreguy, B., Linck, P. A., Coupé, P., Munsch, F., et al. (2020). Normal-appearing white matter integrity is a predictor of outcome after ischemic stroke. *Stroke* 51, 449–456. doi: 10.1161/strokeaha.119.026886

Sakurai, T., Hirano, S., Abe, M., Uji, Y., Shimizu, K., Suzuki, M., et al. (2021). Dysfunction of the left angular gyrus may be associated with writing errors in ALS. *Amyotroph. Lateral Scler. Frontotemporal Degener.* 22, 267–275. doi: 10.1080/21678421.2020.1861021

Seghier, M. L. (2013). The angular gyrus: Multiple functions and multiple subdivisions. *Neuroscientist* 19, 43–61. doi: 10.1177/1073858412440596

Sestieri, C., Capotosto, P., Tosoni, A., Luca Romani, G., and Corbetta, M. (2013). Interference with episodic memory retrieval following transcranial stimulation of the inferior but not the superior parietal lobule. *Neuropsychologia* 51, 900–906. doi: 10.1016/j.neuropsychologia.2013.01.023

Sheng, J., Zhu, Y., Lu, Z., Liu, N., Huang, N., Zhang, Z., et al. (2013). Altered volume and lateralization of language-related regions in first-episode schizophrenia. *Schizophr. Res.* 148, 168–174. doi: 10.1016/j.schres.2013.05.021

Shi, D., Pan, Z., Li, X., Guo, H., and Zheng, Q. (2021). Diffusion coefficient orientation distribution function for diffusion magnetic resonance imaging. *J. Neurosci. Methods* 348:108986. doi: 10.1016/j.jneumeth.2020.108986

Song, Y., Torres, R. A., Garcia, S., Frometa, Y., Bae, J., Deshmukh, A., et al. (2016). Dysfunction of neurovascular/metabolic coupling in chronic focal epilepsy. *IEEE Trans. Biomed. Eng.* 63, 97–110. doi: 10.1109/tbme.2015.2461496

Tabesh, A., Jensen, J. H., Ardekani, B. A., and Helpern, J. A. (2011). Estimation of tensors and tensor-derived measures in diffusional kurtosis imaging. *Magn. Reson. Med.* 65, 823–836. doi: 10.1002/mrm.22655

Thaler, C., Kyselyova, A. A., Faizy, T. D., Nawka, M. T., Jespersen, S., Hansen, B., et al. (2021). Heterogeneity of multiple sclerosis lesions in fast diffusional kurtosis imaging. *PLoS One* 16:e0245844. doi: 10.1371/journal.pone.0245844

Wang, J., Duan, Y., Zhang, T., Huang, J., Ren, Z., Ye, J., et al. (2021). Aberrant multimodal brain networks in patients with anti-NMDA receptor encephalitis. *CNS Neurosci. Ther.* 27, 652–663. doi: 10.1111/cns.13632

Wang, M. L., Wei, X. E., Yu, M. M., and Li, W. B. (2022). Cognitive impairment in mild traumatic brain injury: A diffusion kurtosis imaging and volumetric study. *Acta Radiol.* 63, 504–512. doi: 10.1177/0284185121998317

Wang, R. J., Chen, B. D., and Qi, D. (2015). Anti-N-methyl-D-aspartate receptor encephalitis concomitant with multifocal subcortical white matter lesions on magnetic resonance imaging: A case report and review of the literature. *BMC Neurol.* 15:107. doi: 10.1186/s12883-015-0366-5

Xie, Y. J., Xi, Y. B., Cui, L. B., Guan, M. Z., Li, C., Wang, Z. H., et al. (2021). Functional connectivity of cerebellar dentate nucleus and cognitive impairments in patients with drug-naive and first-episode schizophrenia. *Psychiatry Res.* 300:113937. doi: 10.1016/j.psychres.2021.113937

Yang, H. G., Liu, W. V., Wen, Z., Hu, L. H., Fan, G. G., and Zha, Y. F. (2022). Altered voxel-level whole-brain functional connectivity in multiple system atrophy patients with depression symptoms. *BMC Psychiatry* 22:279. doi: 10.1186/s12888-022-03893-4

Yang, J., Jiang, X., Wei, S., Deng, X., Zhu, Y., Chang, M., et al. (2021). White matter tracts in bipolar disorder patients: A comparative study based on diffusion kurtosis and tensor imaging. *J. Affect. Disord.* 292, 45–55. doi: 10.1016/j.jad.2021.05.030

Yuan, L., Sun, M., Chen, Y., Long, M., Zhao, X., Yin, J., et al. (2016). Non-Gaussian diffusion alterations on diffusion kurtosis imaging in patients with early Alzheimer's disease. *Neurosci. Lett.* 616, 11–18. doi: 10.1016/j.neulet.2016.01.021

Zhang, T., Duan, Y., Ye, J., Xu, W., Shu, N., Wang, C., et al. (2018). Brain MRI characteristics of patients with anti-N-methyl-D-aspartate receptor encephalitis and their associations with 2-year clinical outcome. *AJNR Am. J. Neuroradiol.* 39, 824–829. doi: 10.3174/ajnr.A5593

Zhong, R., Chen, Q., Zhang, X., Zhang, H., and Lin, W. (2022). Risk factors for mortality in anti-NMDAR, anti-LGI1, and anti-GABABR encephalitis. *Front. Immunol.* 13:845365. doi: 10.3389/fimmu.2022.845365

frontiers | Frontiers in Neuroscience

TYPE Original Research
PUBLISHED 24 November 2022
DOI 10.3389/fnins.2022.1035308

OPEN ACCESS

EDITED BY
Anand Joshi,
University of Southern California,
United States

REVIEWED BY
Qi Wan,
The First Affiliated Hospital of Guangzhou Medical University, China
Tian Tieqiao,
Doctor Peset University Hospital, Spain

*CORRESPONDENCE
Yong Li
aliyong@126.com

†These authors have contributed equally to this work

SPECIALTY SECTION
This article was submitted to Brain Imaging Methods, a section of the journal Frontiers in Neuroscience

RECEIVED 02 September 2022
ACCEPTED 31 October 2022
PUBLISHED 24 November 2022

CITATION
Zhong M, Zeng H, Wang D, Li J, Duan X and Li Y (2022) Structure and activity alteration in adult highland residents' cerebrum: Voxel-based morphometry and amplitude of low-frequency fluctuation study. *Front. Neurosci.* 16:1035308. doi: 10.3389/fnins.2022.1035308

Structure and activity alteration in adult highland residents' cerebrum: Voxel-based morphometry and amplitude of low-frequency fluctuation study

Minzhi Zhong[1†], Huaqu Zeng[2†], Dongye Wang[3], Jiesheng Li[4], Xuguang Duan[5] and Yong Li[3*]

[1]Department of Radiology, Guangzhou Red Cross Hospital, Guangzhou, China, [2]Department of Radiotherapy Center, Gaozhou People's Hospital, Guangdong, China, [3]Department of Radiology, Sun Yat-sen Memorial Hospital, Guangzhou, China, [4]Department of Radiology, Sanshui People's Hospital, Foshan, China, [5]Department of Radiology, Nyingchi People's Hospital of Tibet Autonomous Region, Nyingchi, China

Introduction: People living in highland areas may have factors that allow them to adapt to chronic hypoxia, but these physiological mechanisms remain unclear. This study aimed to investigate the brain mechanism in a cohort of adult residents of Tibet, a well-known plateau section in China, by observing differences in brain structure and function in non-plateau populations.

Methods: The study included 27 Tibetan and 27 non-plateau region residents who were matched in age, sex, and education. All participants underwent high-resolution three-dimensional T1 weighted imaging (3D-T1WI) and resting-state functional magnetic resonance imaging (rs-fMRI) scans on a 1.5 Tesla MR. Gray matter volumes and regional spontaneous neuronal activity (SNA) were calculated and compared between the two groups.

Results: When comparing gray matter in people living in high altitudes to those living in the flatlands, the results showed positive activation of gray matter in local brain regions ($p < 0.05$, false discovery rate (FDR) corrected), in the right postcentral [automated atomic labeling (aal)], left postcentral (aal), and right lingual (aal) regions. Comparing the people of high altitude vs. flat land in the brain function study ($p < 0.05$, FDR corrected), positive activation was found in the right superior motor area (aal) and left superior frontal (aal), and negative activation was found in the right precuneus (aal).

Conclusion: In high-altitude individuals, larger regional gray matter volumes and higher SNA may represent a compensatory mechanism to adapt to chronic hypoxia.

KEYWORDS

high altitude, structure, function, cerebrum, fMRI

Introduction

Hypoxia is a common phenomenon and is characterized by a decrease in oxygen content in cells or tissues relative to normal levels (Zhang et al., 2022). The brain is highly sensitive to changes in oxygen content because the central nervous system is highly oxidized (Otero-Losada et al., 2019; Burtscher et al., 2021; Li et al., 2021). The effects of hypoxia on the nervous system are related to the severity of systemic hypoxia and the differential expression patterns of neurogenesis factors at maturity (Johnston, 1995; Schneider et al., 2012; Chen and Gaber, 2021).

Acute hypoxia usually presents obvious neurological symptoms, which are of concern to us, whereas the effects of chronic hypoxia on the body do not appear immediately and are often overlooked. Some studies have pointed out that elderly people living for a long time in a low-oxygen environment have a higher incidence of Alzheimer's disease than in a plain area, which suggests that environmental factors have an important impact on the onset of cognitive impairment (Ma et al., 2014). The hypoxia symptoms, such as anxiety, depression, and cognitive impairment, have been reported mainly in the migrant population, but less so in the locals living on the plateau (Tibetans). Mammals have evolved physiological mechanisms to cope with hypoxia, including increased ventilation, cardiac output, vascular growth, and the number of circulating red blood cells (McClelland and Scott, 2019; Lee et al., 2020; Biller et al., 2021). Compared with people living in plain areas, Tibetans exposed to changes in the acute oxygen environment have an obvious cerebral hemodynamic regulation mode (Wu and Kayser, 2006; Xing et al., 2019). Hypoxia activates a variety of epigenetic mechanisms in the fetal brain, increasing the vulnerability of the offspring to neurodevelopmental disorders (Li et al., 2006; Butt et al., 2021). Acute and chronic hypoxia elicits many responses at the cellular level, with an overall decline in oxygen consumption with age. The adjustment of the adaptive mechanisms that arise in the brain is unclear. The anti-oxidative stress theory proposed by scholars to protect the cognitive function of people at high altitudes remains uncertain, and the extent to which chronic hypoxia affects the body is unclear.

Voxel-based morphometry (VBM) is a hypothesis-free, whole-brain, voxel-by-voxel analytical method that attempts to compare imaging data between populations (Melonakos et al., 2011). It is a technology used to analyze brain structures (Richardson et al., 2011; Herrera and González-Candia, 2021). It was used to generate 3D high-resolution T1 images that were used for segmentation to obtain gray matter, white matter, and cerebrospinal fluid images to analyze brain microstructure (Bashir et al., 2019). The amplitude of low-frequency fluctuation (ALFF) is used for resting-state functional magnetic resonance imaging (fMRI) performed by the Data Processing and Analysis of Brain Imaging (DPABI) software to detect blood flow changes associated with neural activity in different tasks by detecting local blood-oxygen level signals (Vanasse et al., 2018).

By gaining an in-depth understanding of the mechanisms of various hypoxia patterns, we hoped to reduce the impact on the human body and find the beneficial aspects of hypoxia in humans. In our study, 54 healthy adults were enrolled and underwent magnetic resonance imaging (MRI) for structural and functional studies. The aim of this study was to investigate the effects of chronic hypoxia on the brains of healthy individuals to understand the mechanism of the brain's response to hypoxia.

Materials and methods

Participants and procedures

There were 27 participants (11 men) in the high-altitude group (HA) enrolled in the study, aged 35–45 years (mean: 38.65 ± 5.4). The average schooling year of HA was 12.04 ± 0.6 years. The control group (CG) consisted of 27 (13 men) medical staff who had been in Tibet for <2 weeks, aged 28–45 years (mean: 41.77 ± 6.4) years, with an average schooling year of 12.52 ± 3.0 years. All participants were informed of the purpose and procedures of the study, and informed consent was obtained from all participants.

The HA had lived at an altitude of over 2,800 m for more than 30 years. The CG had lived in the flatlands of Tibet for less than 2 weeks. The inclusion criteria were as follows: (1) right hand; (2) no respiratory symptoms and cardiopulmonary diseases, history of diabetes, and hypertension; (3) no abnormal brain structure found on routine series MRI; (4) no history of neurological disease or cognitive decline; (5) Mini-Mental State Examination (MMSE) score >28; and (6) test for oxyhemoglobin saturation (SpO_2) and hemoglobin (Hb).

MRI data equipment

All subjects underwent brain MRI scans using a GE Medical Systems 1.5T-scanner (GE, Signa, USA) at the Department of Diagnostic Imaging in Linzhi People's Hospital of Tibet with an 8-channel head coil in 2018. When routine protocols used to scan the brain had no organ disease, high-resolution T1-weighted images (BRAVO) with good contrast between gray and white matter were collected. The following image parameters were included: TR = 12.5 ms, TE = 5.2 ms, flip angle = 5°, slice thickness =1 mm, TI = 1100 ms, 130 slices, matrix =1 × 1 × 1 mm^3, field of view =240 × 240 mm. The gradient echo-planar imaging (EPI) sequence was blood oxygen level-dependent (BOLD) for resting-state functional MRI as follows: TR = 3,000 ms, TE = 40 ms, flip angle = 90°, 33 slices, slice

thickness = 3 mm, resolution =64 × 46 × 5 mm^3, time-point 128, the field of view= 240 × 240 mm.

Image processing

All data processing was performed on the Matlab version R2013a platform (nl.mathworks.com/products/matlab/) (Yan et al., 2016; Chen et al., 2022).

Brain volume (BRAVO) imaging was subjected to voxel-based morphometry (VBM) analysis and was performed using Statistical Parametric Mapping (SPM8, The Wellcome Center for Human Neuroimaging, London, UK; http://www.fil.ion.ucl.ac.uk/spm) running under MATLAB software (The Mathworks, Inc., Natick, MA, USA). All 3D-T1 images were corrected for rough bias, affine registered to a template image in the Montreal Neurology Institute (MNI) space, and then segmented into white matter (WM), gray matter (GM), and cerebrospinal fluid (CSF) maps. The segmented images were spatially normalized by high-dimensional diffeomorphic anatomical registration using the DARTEL algorithm. Finally, all normalized images of regional gray matter volume were smoothed with an 8-mm full-width at half maximum (FWHM) Gaussian kernel to improve the signal-to-noise ratio.

BOLD imaging was performed using DPABI (http://rfmri.org/dpabi). First, the first 10 s were removed to allow the magnetization to reach a steady state. The following main steps were included: (1) slice timing to head motion correction; (2) realignment; (3) normalization to the MNI coordinate space with 3 Ã−3 Ã−3 mm^3; (4) linear detrending; (5) band-pass filtering (0.01–0.08 Hz); and (6) nuisance signals, which regressed out the signal including white matter and cerebrospinal fluid. Subsequently, spatial smoothing with a 6-mm FWHM isotropic Gaussian kernel was performed to reduce the noise.

Neuropsychiatric test

The Mini-Mental State Examination (MMSE) score includes orientation, memory, attention, calculation, recall ability, and language ability. The total possible score was 30 points. A score of <27 points indicated cognitive dysfunction.

Statistical analysis

All demographic and clinical data were analyzed using IBM SPSS Statistics 25. A two-sample *t*-test was used to compare age, education, pulse oximetry [SpO_2 (%)], MMSE score, and hemoglobin level. To determine the differences between HA and CG, two-sample *t*-tests were performed on gray matter and function images: voxel-level, $p < 0.05$; cluster size >200; voxel number = 5,000; and false discovery rate (FDR) correction. Spearman's correlation analysis was conducted to observe the relationship between the clinical hemoglobin level and activation in the VBM and ALFF values. The statistical significance level was set at $p < 0.05$.

TABLE 1 Demographic, clinical data of the HA and CG.

	HA	CG	*p*-value
Age (years)	38.65 ± 5.4	41.77 ± 6.4	0.079
Gender (male, female)	11, 40.7%, 16, 59.2%	13, 48.1%, 14, 51.9%	–
Education (years)	12.04 ± 0.6	12.52 ± 3.0	0.554
Hb (mg)	169 ± 14.6	135 ± 16.8	<0.000
SpO_2 (%)	93 ± 2.5	98.0 ± 0.92	<0.000
MMSE score	29.22 ± 0.6	29.65 ± 0.6	0.067

All data were recorded as mean ± standard deviation (SD).

Results

Demographic and clinical characteristics

The clinical and demographic characteristics of the participants are presented in Table 1, which are included in the analysis. The MMSE test scores of all participants were >29. Of the total participants, 25 men (92.6%) graduated from high school or above. There was no significant difference in age, education, and MMSE scores between the HA and CG. The SpO_2 value was 93 ± 2.5% and the Hb value was 169 ± 14.6 mg in HA; the SpO_2 value was 98.0 ± 0.92% and the Hb value was 135 ± 16.8 mg in CG (Figure 1). The values of Hb and SpO_2 (%) were significantly different between the HA group and CG ($p < 0.05$) (Table 1).

VBM between HA and CG

The VBM analysis revealed a significantly increased volume of gray matter in HA compared to CG in the bilateral somatosensory cortex (Brodmann 3, left, t = 4.88; right, t = 4.26, FDR corrected, cluster size number >200, $p < 0.05$) and the vision cortex (Brodmann 18, t = 4.26, FDR corrected, cluster size number >200, $p < 0.05$; Figure 2, Table 2). This showed a uncorrelation between changes in gray structure and Hb.

ALFF between HA and CG

When the functional area with HA was compared to CG, there was positive activity in the Brodmann 6 and Brodmann 8 regions of the brain in the upper motor cortex, in the Brodmann 18 region (Figure 3, Table 3).

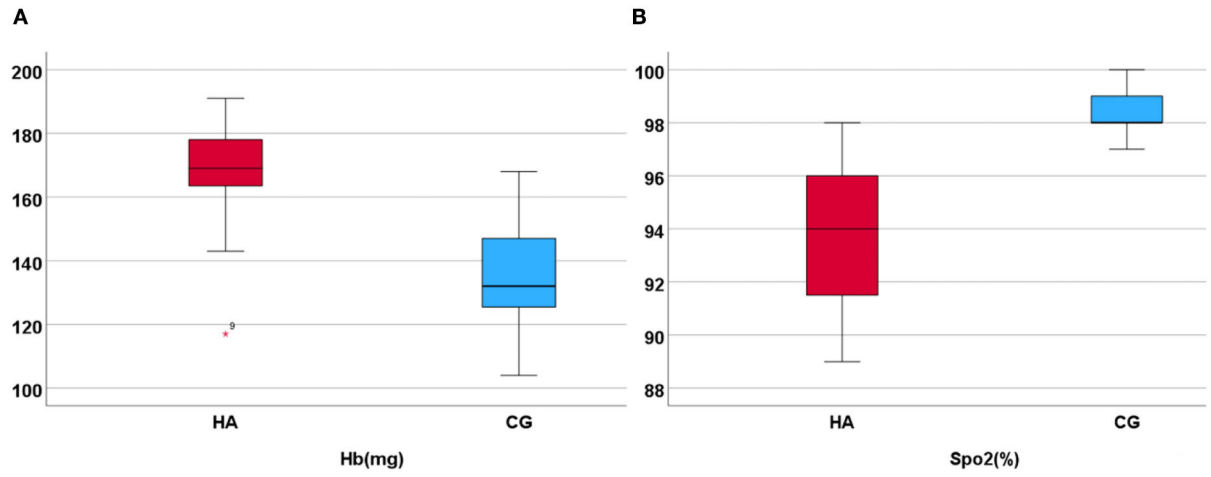

FIGURE 1
Hb and SpO_2 in HA and CG show that the Hb is higher in HA than in CG, but the SpO_2 (%) is lower. **(A)** Display the hemoglobin higher in high altitude group. **(B)** Display the SpO_2 higher in control group.

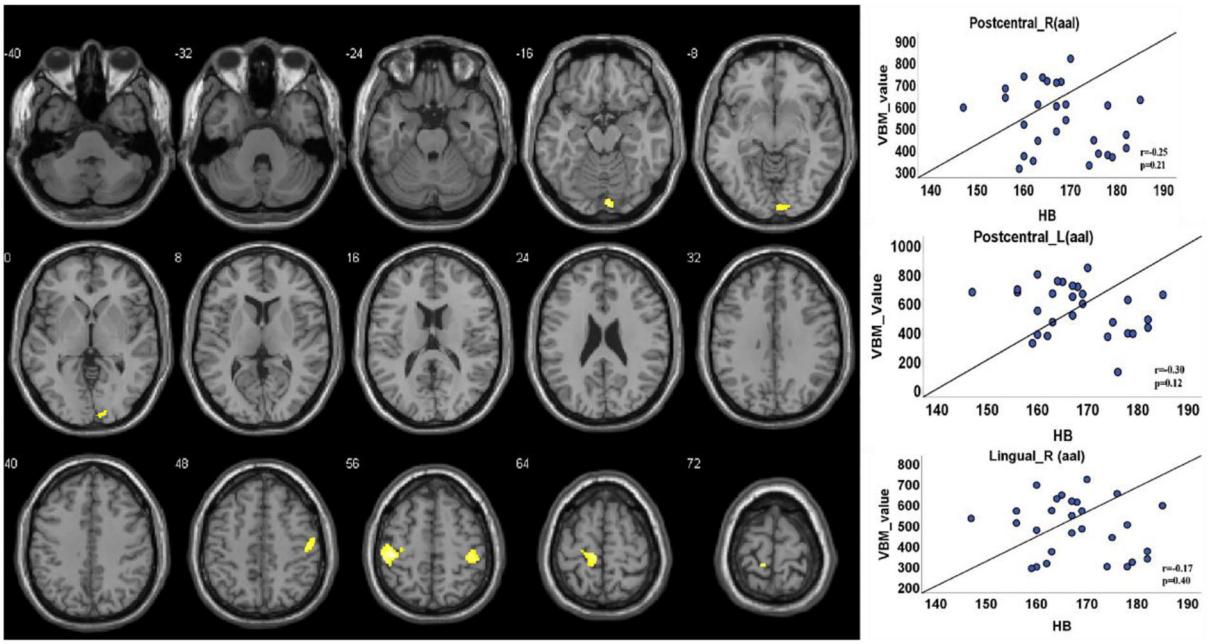

FIGURE 2
Gray matter structure cluster area differs from HA to CG and uncorrelates with Hb. The volume is significantly higher with the people of HA than CG. The color yellow represents the brain regions that positively activate gray matter. Correlations with Hb: Right lingual ($r = 0.17$, $p = 0.40$); right postcentral ($r = 0.25$, $p = 0.21$); left postcentral ($r = 0.30$, $p = 0.12$).

Discussion

Tibetans are known to have high hemoglobin levels, a hallmark feature of adaptation to high-altitude exposure (Chen et al., 2022). Previous studies have suggested that Hb concentration is closely related to the severity of leukoaraiosis and is an independent factor with a positive correlation (Long and Xiuli, 2012; Tang et al., 2012). However, plateau and plain residents have completely different adaptations to hypoxia (Yonglan, 2021). In this study, we found that gray matter volume decreased in parts of the cerebral cortex in HA, which were the bilateral postcentral cortex and the right lingual cortex. The results showed that compared with the CG group, the right superior motor area and left superior frontal cortex ALFF

TABLE 2 VBM analysis of significant GM cluster in HA vs. CG.

Brain region	BA	Cluster size (mm^3)	*t*	MNI		
				X	*Y*	*Z*
Left postcentral (aal)	3	466	4.88	−45.5	−34	57
Right postcentral (aal)	3	409	4.26	39	−28	57
Right lingual (aal)	18	403	4.32	21.6	−90.3	−13.5

t: peak value; MNI: coordinates established for MRI images of the normal human brain. The coordinates x, y, and z refer to the anatomical location.

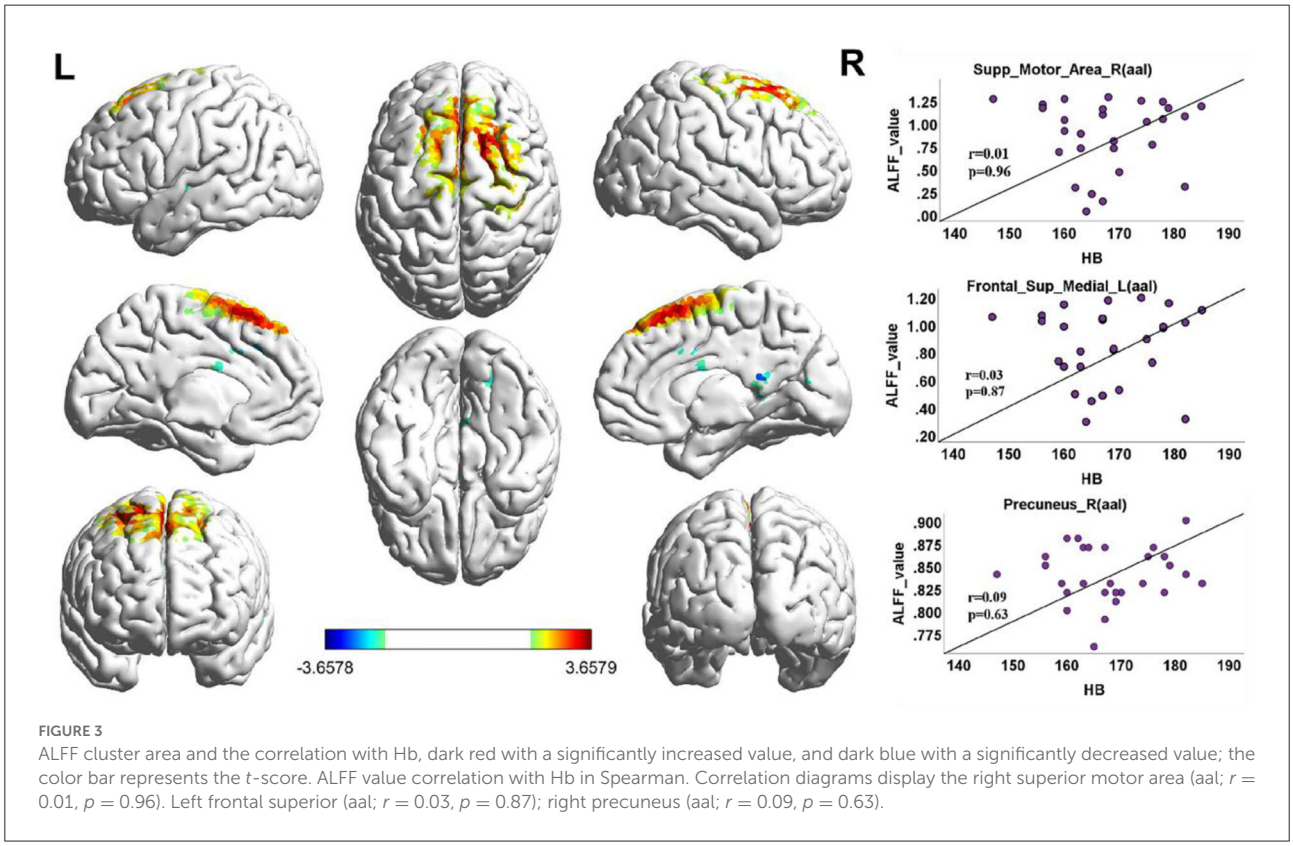

FIGURE 3
ALFF cluster area and the correlation with Hb, dark red with a significantly increased value, and dark blue with a significantly decreased value; the color bar represents the *t*-score. ALFF value correlation with Hb in Spearman. Correlation diagrams display the right superior motor area (aal; $r = 0.01$, $p = 0.96$). Left frontal superior (aal; $r = 0.03$, $p = 0.87$); right precuneus (aal; $r = 0.09$, $p = 0.63$).

TABLE 3 Between-group differences in the function area.

Brain region	BA	Cluster size	*t*	MNI		
				X	*Y*	*Z*
Right superior motor area (aal)	6	140	3.50	16	14	57
Left superior frontal cortex (aal)	8	153	3.60	−9	55	52
Right precuneus (aal)	18	52	−4.08	12	−51	18

R, right; L, left; BA, Brodmann area; MNI, coordinates established for MRI images of the normal human brain; AlphaSim correction, cluster size number > 200; $p_{value} > 0.01$.

increased in the HA group, and the right precuneus decreased. These results uncorrelated with low Hb levels.

The lingual gyrus is the occipital visual cortex that processes visual information. It is at the core of visual analysis and plays an important role in visuospatial perception. Somatosensory systems have commonalities with auditory and visual cortical functional units and conduction pathways, and mutual compensatory functions exist among the three (Zhang et al., 2018). Each retinal point responds to a portion of its visual cortex; hypoxia is an important factor and is related to

the longer time that hypoxia factors act on the body (Guoen and Rili, 2021; Haoyu and Qing, 2021; Zhang, 2021). In our results, both gray matter and ALFF were activated in the right lingual gyrus of the HA, suggesting that the structure and function have changed in the visual area of the brain. Yin et al. (2017) believed that ALFF decreased in the right lingual gyrus of normal adults 2 years after the migration to high altitudes, compared with that before migration. Experts point out that long-term living in high-altitude environments can cause retinal diseases due to chronic hypoxia, high ultraviolet radiation, strong wind and sand stimulation, and vitamin deficiency, such as macular degeneration and optic nerve damage that impair visual function (El Chehab et al., 2012; Runjia et al., 2013; Jing et al., 2019). This can explain the gray matter and functional changes in the occipital lingual gyrus in the high-altitude population in our study.

Postcentral is the first motion sensory area, which mainly collects sensory input from the limbs, reflecting that the sensitivity of that population was affected. It is related to tactile (pain, temperature, touch, pressure, and position) information of the entire body. The functional region of the occipital lobe is closely associated with the postcentral region; it is involved in attention and visuospatial perception, and there are a variety of nerve conduction pathways. In our study, there was a large decrease in gray matter in the lingual gyrus, consistent with previous studies (Li and Li, 2020). This helps us understand the mechanism of visual impairment in people at high altitudes. Meanwhile, the cluster of the postcentral gyrus was also obviously activated, perhaps because of various tactile changes in the body to adapt to the extreme high-altitude environment or occipital interaction with the regulation of postcentral gyrus function.

Functional studies have implicated the superior frontal cortex, including the supplementary motor area (SMA) and pre-supplementary motor area (preSMA), in movement and cognitive control (Caixia et al., 2014). Brodmann 8 is involved in controlling saccadic movement (Zhang et al., 2012). It plays an important role in receiving visual information from space and organizing eye motor commands toward it, which is related to the function of the retina (Watanabe, 2017). In high-altitude migrants, bilateral visual cortex mirror functional connectivity was significantly increased, which was positively correlated with hemoglobin concentration (Lanzilotto et al., 2013). The superior motor area in Brodmann type 6 is the premotor cortex. The supplementary motor area is involved in the planning and execution of intentional movements. Our studies were conducted on Brodmann 6 using ALFF processing, suggesting that exercise capacity is affected in high-altitude people. Chen et al. (2016) found that hypoxia reduces exercise capacity, which is related to the quantity of Hb and the affinity of Hb-O_2. Jay et al. (2022) suggested that the motility of people at high altitudes is inversely correlated with the concentration of Hb. The higher the Hb value, the lower the motility. Some studies suggest that people from high-altitude areas migrate to low-altitude areas, and their athletic ability is better than that of residents living in low-altitude areas, which is related to the genetic variation of Tibetans in high-altitude areas (Tatum et al., 2015). Although the correlation between motility and Hb values was not analyzed in this study, the changes in cortical function associated with exercise in structural and functional studies were consistent with those of previous studies. The neural connection between them needs to be further evaluated.

In recent years, the precuneus has received considerable attention in the study of neural functions. It is believed that this cortex plays a central role in a wide range of highly integrated tasks, including visuospatial imaging, episodic memory retrieval, and self-processing. Brodmann 18 is the visual cortex, which, when impaired, causes several visual disorders, including visual field defects, metamorphopsia, and different kinds of visual agnosia (Chuanming et al., 2006; Bianba et al., 2014; Kawachi, 2017). Functional analysis of our study revealed that the right precuneus was negatively activated in ALFF, suggesting that the high-altitude population has weakened visual functions in this aspect, which is consistent with the structural analysis results.

Conclusion

This study showed consistent changes in the structure and activity of the sensorimotor regions. The eyes and visual control areas have the same time-frequency, showing that the high-altitude population differs from the plain population in terms of athletic ability and vision in the physiological state. These differences may be related to changes in brain function caused by living conditions and the environment. There were no obvious clinical manifestations of cognition in our study, which may be affected by the volunteers being young at a high living and education level.

The next study will evaluate the white matter fibers of this group of people to perform functional connectivity (FC) analysis to understand the coordination between white matter pathways and functional areas. A limitation of this study might be the small number of participants. Second, all cases were tested at high altitudes; although we performed a simple mental quantification test, we could not rule out that mild hypoxia may cause short-term asymptomatic damage to the brain of the control group.

Data availability statement

The raw data supporting the conclusions of this article will be made available by the authors, without undue reservation.

Ethics statement

Ethical review and approval was not required for the study on human participants in accordance with the local legislation

and institutional requirements. The patients/participants provided their written informed consent to participate in this study.

Author contributions

MZ completed the study design, data collection, and article writing. XD completed the data collection work, MR image quality analysis, and chart making. HZ completed the statistical analysis. DW and JL mainly completed MR image quality analysis. YL participated in the revision of the manuscript. All authors contributed to the article and approved the submitted version.

Funding

This work was supported by Traditional Chinese Medicine Research Project of Guangdong Traditional Chinese Medicine Bureau No. 20232132 and Nyingchi Science and Technology Bureau No. 2018KJYZ016.

Conflict of interest

The authors declare that the research was conducted in the absence of any commercial or financial relationships that could be construed as a potential conflict of interest.

Publisher's note

References

Bashir, S., Baradi, R., and Al-Ghamdi, F. (2019). Gender and hemispheric differences in epilepsy diagnosed by voxel-based morphometry (VBM) method: a pilot cortical thickness study. *Acta Inform. Med.* 27, 171–176. doi: 10.5455/aim.2019.27.171-176

Bianba, Andersen, L. B., Stigum, H., Ouzhuluobu, and Bjertness, E. (2014). Children's exercise capacity at high altitude in Tibet. *Chin. J. Appl. Physiol.* 06, 481–488.

Biller, A., Badde, S., Heckel, A., Guericke, P., Bendszus, M., Nagel, A. M., et al. (2021). Exposure to 16h of normobaric hypoxia induces ionic edema in the healthy brain. *Nat. Commun.* 12, 5987. doi: 10.1038/s41467-021-26116-y

Burtscher, J., Mallet, R. T., Burtscher, M., and Millet, G. P. (2021). Hypoxia and brain aging: neurodegeneration or neuroprotection? *Ageing Res. Rev.* 68, 101343. doi: 10.1016/j.arr.2021.101343

Butt, U. J., Steixner-Kumar, A. A., Depp, C., Sun, T., Hassouna, I., Wüstefeld, L., et al. (2021). Hippocampal neurons respond to brain activity with functional hypoxia. *Mol. Psychiatry* 26, 1790–1807. doi: 10.1038/s41380-020-00988-w

Caixia, L., Haihua, B., Weixia, L., et al. (2014). VBM-MRI study of gray matter changes in chronic altitude patients. *Magn. Reson. Imaging* 5, 211–215. doi: 10.3969/j.issn.1674-8034.2014.03.012

Chen, J., Li, J., Han, Q., Lin, J., Yang, T., Chen, Z., et al. (2016). Long-term acclimatization to high-altitude hypoxia modifies interhemispheric functional and structural connectivity in the adult brain. *Brain Behav.* 6, e00512. doi: 10.1002/brb3.512

Chen, M., Li, Y., Chen, J., Gao, L., Sun, J., Gu, Z., et al. (2022). Structural and functional brain alterations in patients with idiopathic rapid eye movement sleep behavior disorder. *J. Neuroradiol.* 49, 66–72. doi: 10.1016/j.neurad.2020.04.007

Chen, Y., and Gaber, T. (2021). Hypoxia/HIF modulates immune responses. *Biomedicines* 9, 260. doi: 10.3390/biomedicines9030260

Chuanming, L., Jiang, W., Qiongwu, Y., et al. (2006). Functional magnetic resonance study on Brodmann areas 17, 18 and 19 of the patients with anisometropic amblyopia. *J. Third Mil. Med. Uni.* 28, 987–989. doi: 10.3321/j.issn:1000-5404.2006.09.038

El Chehab, H., Blein, J. P., Herry, J. P., Chave, N., Ract-Madoux, G., Agard, E., et al. (2012). Ocular phototoxicity and altitude among mountain guide. *World Latest Med. Inf. Dig.* 35, 809–815. doi: 10.1016/j.jfo.2012.06.012

Guoen, J., and Rili, G. (2021). High altitude hypoxia and brain tissue structure and function damage. *Chin. J. Hight Alt. Med. Biol.* 03, 185–189. doi: 10.13452/j.cnki.jqmc.2021.03.008

Haoyu, L., and Qing, H. (2021). Effects of hypoxia at high altitude on retinal neovascularization. *Chin. J. Plateau Med. Biol.* 42, 200–204. doi: 10.13452/j.cnki.jqmc.2021.03.011

Herrera, E. A., and González-Candia, A. (2021). Gestational hypoxia and blood-brain barrier permeability:early origins of cerebrovascular dysfunction induced by epigenetic mechanisms. *Front. Physiol.* 12, 717550. doi: 10.3389/fphys.2021.717550

Jay, F., Storz, Naim, M., and Bautista. (2022). Altitude acclimatization, hemoglobin-oxygen affinity, and circulatory oxygen transport in hypoxia. *Mol. Aspects Med.* 84, 101052. doi: 10.1016/j.mam.2021.101052

Jing, L., Zhang, Q. L., Fang, J. W., et al. (2019). Risk factors and characteristics of age-related macular degeneration in high altitude area. *Chin. J. Mod. Drug Appl.* 13, 19–20. doi: 10.14164/j.cnki.cn11-5581/r.2019.04.010

Johnston, M. V. (1995). Neurotransmitters and vulnerability of the devel oping brain. *Brain* 17, 301–306. doi: 10.1016/0387-7604(95)00079-Q

Kawachi, J. (2017). Brodmann areas 17, 18, and 19 in the human brain: an overview. *Brain Nerve* 69, 397–410. doi: 10.11477/mf.1416200756

Lanzilotto, M., Perciavalle, V., and Lucchetti, C. (2013). Auditory and visual systems organization in Brodmann Area 8 for gaze-shift control: where we do not see, we can hear. *Front. Behav. Neurosci.* 7, 198. doi: 10.3389/fnbeh.2013.00198

Lee, P., Chandel, N. S., and Simon, M. C. (2020). Cellular adaptation to hypoxia through hypoxia inducible factors and beyond. *Nat. Rev. Mol. Cell Biol.* 21, 268–283. doi: 10.1038/s41580-020-0227-y

Li, G., Liu, J., Guan, Y., and Ji, X. (2021). The role of hypoxia in stem cell regulation of the central nervous system: from embryonic development to adult proliferation. *CNS Neurosci. Ther.* 27, 1446–1457. doi: 10.1111/cns.13754

Li, S. Z., Zheng, B. H., Wang, H. B., et al. (2006). Characteristics of severe acute altitude sickness among Tibetan residents living on the hight altitude. *Chin. J. Tuberc. Respir. Med.* 12, 835–836. doi: 10.3760/j:issn:1001-0939.2006.12.012

Li, Y., and Li, P. (2020). Analysis of 515 cases of ophthalmic diseases in highland immigrants. *China Pract. Med.* 15, 54–56. doi: 10.14163/j.cnki.11-5547/r.2020.29.019

Long, M., and Xiuli, Z. (2012). Study on thes correlation between leukoaraiosis and hemoglobin in high altitude area. *Hight Alt. Med. J.* 2, 21–22. doi: 10.3969/j.issn.1007-3809.2012.02.005

Ma, Q., Xiong, F., and Zhang, L. (2014). Gestational hypoxia and epigenetic programming of brain development disorders. *Drug Discov. Today* 19, 1883–1896. doi: 10.1016/j.drudis.2014.09.010

McClelland, G. B., and Scott, G. R. (2019). Evolved mechanisms of aerobic performance and hypoxia resistance in high-altitude natives. *Annu. Rev. Physiol.* 81, 561–583. doi: 10.1146/annurev-physiol-021317-121527

Melonakos, E. D., Shenton, M. E., Rathi, Y., Terry, D. P., Bouix, S., Kubicki, M., et al. (2011). Voxel-based morphometry (VBM) studies in schizophrenia-can white matter changes be reliably detected with VBM? *Psychiatry Res.* 193, 65–70. doi: 10.1016/j.pscychresns.2011.01.009

Otero-Losada, M., Wandosell, F. G., Garcia-Segura, L. M., and Capani, F. (2019). Editorial: neuroprotection in brain hypoxia. *Front. Neurosci.* 13, 212. doi: 10.3389/fnins.2019.00212

Richardson, C., Hogan, A. M., Bucks, R. S., Baya, A., Virues-Ortega, J., Holloway, J. W., et al. (2011). Neurophysiological evidence for cognitive and brain functional adaptation in adolescents living at high altitude Clinical. *Neurophysiology* 122, 1726–1734. doi: 10.1016/j.clinph.2011.02.001

Runjia, L., Dan, H., Peng, Z., et al. (2013). Effects of hypoxia on expression of angiogenin-1 and angiogenin-2 in human retinal pigment epithelial cells. *Recent Adv. Ophthalmol.* 33, 435–438. doi: 10.13389/j.cnki.rao.2013.05.010

Schneider, C., Krischke, G., Rascher, W., Gassmann, M., and Trollmann, R. (2012). Systemic hypoxia differentially affects neurogenesis during early mouse brain maturation. *Brain* 34, 261–273. doi: 10.1016/j.braindev.2011.07.006

Tang, D. J., Ye, Y. X., Su, J., et al. (2012). Analysis of clinical characteristics and gene mutation of patients with polycythemia in hight altitude Tibetans. *Chin. J. Hematol.* 11, 960–962. doi: 10.3760/cma.j.issn.0253-2727.2012.11.017

Tatum, S., Simonson, Peter, D., and Wagner. (2015). Oxygen transport adaptations to exercise in native highland populations. *Exp. Physiol.* 100, 1231–1232. doi: 10.1113/EP085073

Vanasse, T. J., Fox, P. M., Barron, D. S., Robertson, M., Eickhoff, S. B., Lancaster, J. L., et al. (2018). BrainMap VBM: an environment for structural meta-analysis. *Hum. Brain Mapp.* 39, 3308–3325. doi: 10.1002/hbm.24078

Watanabe, M. (2017). Brodmann AREAS 8 AND 9 including the frontal eye field. *Brain Nerve* 69, 347—354. doi: 10.11477/mf.1416200751

Wu, T., and Kayser, B. (2006). High altitude adaptation in Tibetans. *High Alt. Med. Biol.* 7, 193–208. doi: 10.1089/ham.2006.7.193

Xing, C.-Y., Serrador, J. M., Knox, A., Ren, L. H., Zhao, P., Wang, H., et al. (2019). Cerebral blood flow, oxygen delivery, and pulsatility responses to oxygen inhalation at high altitude: highlanders vs. lowlanders. *Front. Physiol.* 10, 61. doi: 10.3389/fphys.2019.00061

Yan, C. G., Wang, X. D., Zuo, X. N., and Zang, Y. F. (2016). DPABI: data processing and analysis for (resting-state) brain imaging. *Neuroinformatics* 14, 339–351. doi: 10.1007/s12021-016-9299-4

Yin, H., Bao, H. H., W, F. F., et al. (2017). Adaptive changes in the brain of low-altitude normal adults after 2 years of migration to high-altitude areas. *Shandong Med.* 57, 92–94. doi: 10.3969/j.issn.1002-266X.2017.38.030

Yonglan, H. (2021). Comparison of cognitive function and white matter lesions among Tibetan and Han middle-aged and elderly people in middle and high altitude areas. *Qinghai Univ.* 2. doi: 10.27740/d.cnki.gqhdx.2021.000335

Zhang, C. L., Tan, Y. M., He, L. C., et al. (2018). fMRI study of functional connectivity of the posterior central gyrus before and after decompression in patients with cervical spondylotic myelopathy. *J. Clin. Radiol.* 37, 1246–1251. doi: 10.13929/j.1003-3289.201804134

Zhang, G., Zhou, Y., Cao, Z., and Zhu, L. (2022). Preliminary intermittent hypoxia training alleviates the damage of sustained normobaric hypoxia on human hematological indexes and cerebral white matter. *High Alt. Med. Biol.* 4, 0166. doi: 10.1089/ham.2021.0166

Zhang, S., Ide, J. S., and Li, C.-s. R. (2012). Resting-state functional connectivity of the medial superior frontal cortex. *Cereb. Cortex* 22, 99–111. doi: 10.1093/cercor/bhr088

Zhang, W. (2021). Focus on central visual impairment. *Chin. J. Ophthalmol.* 57, 321–325. doi: 10.3760/cma.j.cn112142-20210201-00062

frontiers | Frontiers in Neuroscience

TYPE Original Research
PUBLISHED 09 January 2023
DOI 10.3389/fnins.2022.985213

OPEN ACCESS

EDITED BY
Chitresh Bhushan,
GE Global Research, United States

REVIEWED BY
Yuyang Luo,
Massachusetts Eye and Ear Infirmary and Harvard Medical School, United States
Roger Jacob Mullins,
National Institutes of Health (NIH), United States
Jolanta Dorszewska,
Poznań University of Medical Sciences, Poland

*CORRESPONDENCE
Huasong Wang
✉ whss1104@163.com
Hongjun Li
✉ lihongjun00113@ccmu.edu.cn

†These authors have contributed equally to this work

SPECIALTY SECTION
This article was submitted to Brain Imaging Methods, a section of the journal Frontiers in Neuroscience

RECEIVED 03 July 2022
ACCEPTED 12 December 2022
PUBLISHED 09 January 2023

CITATION
Wang W, Liu D, Wang Y, Li R, Liu J, Liu M, Wang H and Li H (2023) Frequency-dependent functional alterations in people living with HIV with early stage of HIV-associated neurocognitive disorder. *Front. Neurosci.* 16:985213. doi: 10.3389/fnins.2022.985213

Frequency-dependent functional alterations in people living with HIV with early stage of HIV-associated neurocognitive disorder

Wei Wang[1†], Dan Liu[2†], Yuanyuan Wang[3], Ruili Li[4], Jiaojiao Liu[1], Mingming Liu[5], Huasong Wang[6*] and Hongjun Li[1*]

[1]Department of Radiology, Beijing Youan Hospital, Capital Medical University, Beijing, China, [2]Department of Radiology, Renji Hospital, Shanghai Jiao Tong University School of Medicine, Shanghai, China, [3]Department of Radiology, Beijing Second Hospital, Beijing, China, [4]Department of Radiology, Xuanwu Hospital, Capital Medical University, Beijing, China, [5]Physical Examination Center, Cangzhou Central Hospital, Cangzhou, Hebei, China, [6]Department of Neurosurgery, Zhuhai People's Hospital, Zhuhai, Guangdong, China

Background: HIV enters the brain soon after seroconversion and causes HIV-associated neurocognitive disorder (HAND). However, the pathogenesis of this insidious impairment at an early stage remains unclear.

Objectives: To explore functional integration and segregation changes at the early stages of HAND, voxel-level indices of regional homogeneity (ReHo), the amplitude of low-frequency fluctuations (ALFF), and voxel-mirrored homotopic connectivity (VMHC) under two different frequency bands (slow-5: 0.01–0.027 Hz; slow-4: 0.027–0.073 Hz) were analyzed.

Methods: Ninety-eight people living with HIV (PLWH) and 44 seronegative controls underwent resting-state functional magnetic resonance imaging. Furthermore, all PLWHs underwent neuropsychological and daily functioning tests. The main effect of the group and the interaction between the group and frequency band were investigated. Finally, the relationship between the altered indices and the cognitive domains was explored.

Results: A significant group-by-frequency interaction was demonstrated in the right thalamus for ReHo; for VMHC, the interaction was observed in the bilateral precuneus and paracentral gyrus. The *post hoc* Bonferroni test indicated that the alteration of ReHo and VMHC could only be detected in slow-5. PLWH showed significantly reduced ALFF in both the frequency bands in the right occipital gyrus and right calcarine. Moreover, some altered functional integration and segregation indices are related to impaired cognitive function.

Conclusion: People living with HIV displayed aberrant functional integration and segregation at the early stages of HAND, which is linked to cognitive function. The frequency band of slow-5 might be more sensitive for detecting insidious damage at an early stage.

KEYWORDS

HIV-associated neurocognitive disorder, functional MRI, voxel-mirrored homotopic connectivity, people living with HIV, amplitude of low-frequency fluctuation, regional homogeneity

1. Introduction

With advances in combination antiretroviral therapy (cART), the life expectancy of people living with HIV (PLWH) has approached that of the general population (van Sighem et al., 2010). Despite sustained viral suppression, the latent reservoir of the virus cannot be eradicated (Rojas-Celis et al., 2019; Wallet et al., 2019), and the risk of HIV-associated neurocognitive disorder (HAND) increased accordingly with increased cognitive impairment in multiple domains (Eggers et al., 2017; Winston and Spudich, 2020).

According to the Frascati criteria, HAND is divided into three categories: asymptomatic neurocognitive impairment (ANI), symptomatic mild neurocognitive impairment (MND), and HIV-associated dementia (HAD). For the diagnosis of MND and HAD, self-reported or knowledgeable others observed that everyday functioning decline is required, while in ANI, everyday functioning does not interfere (Antinori et al., 2007). In the cART era, the most severe form of HAND, that is HAD, has reduced dramatically, but milder forms are prevalent, especially ANI (Wang et al., 2020). As PLWH age, their cognitive impairment exacerbates and interferes with their daily life, including drug compliance (Woods et al., 2017; Gouse et al., 2021). Therefore, early detection and interference are important. While the commonly used Frascati criteria provide a uniform approach to the diagnosis of HAND, it requires neuropsychological tests in at least five cognitive domains from a qualified third party. The time-consuming nature and complexity of the assessment make these criteria difficult to implement widely in clinical practice. Moreover, differences in cognitive reserve may render neuropsychological tests insufficiently sensitive to detect early cognitive impairment.

In recent years, there has been increased interest in functional imaging in neuroHIV, especially resting-state functional magnetic resonance imaging (rs-fMRI), which maps the spontaneous neural activity at the macroscopic scale. Diverse analysis and processing methods allow us to study functional integration and segregation from different perspectives (Lv et al., 2018). The amplitude of low-frequency fluctuation (ALFF), regional homogeneity (ReHo), and voxel-mirrored homotopic connectivity (VMHC) are whole-brain, voxel-wise analytic approaches that can be used to explore the intensity of spontaneous activity of each voxel, the synchronicity of a particular voxel compared to its surrounding voxels, and the synchronicity of two mirrored voxels, respectively (Zang et al., 2004; Yang et al., 2007; Zuo et al., 2010b). Studies have shown that PLWH display abnormal ALFF and ReHo in the frontal lobe, the occipital lobe, the primary sensorimotor area, and the temporal lobe (Bak et al., 2018; Yadav et al., 2018; Li et al., 2019). These studies were not focused on PLWH at the early stages of HAND. Moreover, all studies were conducted within a traditional frequency band, while ignoring sub-frequency bands within this typically adopted band may have different properties and physiological implications (Zuo et al., 2010a; Chang et al., 2019; Yang et al., 2021; Zhang et al., 2021). Slow-4 and slow-5 oscillations were mainly detected within gray matter and were related to functional connectivity, while slow-3 and slow-2 oscillations were mainly restricted within white matter and were related to respiratory and cardiac signals (De Luca et al., 2006; Zuo et al., 2010a). Zuo et al. (2010a) showed that slow-4 was more robust in the basal ganglia, the thalamus, and the precuneus, while slow-5 was more robust in the medial prefrontal cortex. Subsequent frequency-specific studies demonstrated that functional alterations in Parkinson's disease were more prominent in slow-4 (Liao et al., 2021), while in Alzheimer's disease, slow-5 can be more sensitive (Han et al., 2011). However, more studies suggested the two frequency bands offer complementary information (Wu et al., 2020; Yang et al., 2021).

We used slow-5 and slow-4 in our study to explore functional segregation (ALFF) and integration (ReHo and VMHC) in different frequency bands in PLWH with early cognitive impairment. The combined use of these three indices in different frequency bands may potentially reveal the specific brain regions affected in PLWH at the early stage of HAND. We also investigated the relationship between altered indices and

neurocognitive functions, which may provide new insights into the pathogenesis of HAND.

2. Materials and methods

2.1. Subjects

The study was conducted in accordance with the Declaration of Helsinki, and the protocol was approved by the Ethics Committee of Beijing You'an Hospital. Signed informed consent was obtained from all patients before any study-specific procedure was performed. Ninety-eight HIV-seropositive individuals from the You'an Hospital's STD/AIDS Clinic and 44 seronegative controls from communities were recruited. For seronegative controls, we recruited age-matched participants using flyers. The inclusion criteria are as follows: 1. Confirmed HIV infection by PLWH treatment qualified institutions; 2. For PLWH, no self-reported or knowledgeable informant-reported acquired everyday functioning impairment for primary screening to exclude those with MND or HAD; 3. Volunteered to participate in the study and signed a written informed consent; 4. Right-handed. The exclusion criteria are as follows: anxiety and depression disorder, obsessive–compulsive disorder, history of head trauma or coma, or history of drug or alcohol abuse.

2.2. Neuropsychological assessment

In this study, detailed neuropsychological examinations were conducted in six cognitive domains using the validated Chinese version of the psychological tests normed for age, years of education, and residence scale (Shi et al., 2015). The neuropsychological suite contains nine subtests, including, 1. Speed of information processing [trail-making test part A (TMT A)]; 2. Memory, including learning and recall [Hopkins Verbal Learning Test-Revised (HVLT-R) and Brief Visuospatial Memory Test-Revised (BVMT-R)]; 3. Abstraction and executive function [Wisconsin Card Sorting Test 64-card version (WCST-64)]; 4. Attention and working memory [continuous performance test-identical pairs (CPT-IP), Wechsler Memory Scale-III (WMS-III), and Paced Auditory Serial Addition Test (PASAT)]; 5. Fine motor skills (Grooved Pegboard Test); 6. Verbal and language (animal-naming tests). The original scores measured in the nine subtests were converted into T-scores in six cognitive domains according to the norm. The activities of the daily living scale were also applied to further confirm whether there was a functional decline in PLWH. Only PLWH received a neurocognitive assessment. Due to incomplete information, the neuropsychological assessment results of four men and three women were not included.

2.3. Magnetic resonance imaging data acquisition

All images were collected using a 3.0 T magnetic resonance scanner (Siemens Trio Tim B17 software, Erlangen, Germany) equipped with a 32-channel head coil. During the rs-fMRI imaging data acquisition, subjects were instructed to remain awake and relaxed with closed eyes. T1-weighted structural images were collected using a magnetization-prepared rapid gradient-echo sequence (MRP-RAGE), with a repetition time (TR) = 1,900 ms, echo time (TE) = 2.52 ms, inversion time (TI) = 900 ms, acquisition matrix = 256 × 246, the field of view (FOV) = 250 × 250 mm, flip angle = 9°, and voxel size = 1 mm × 1 mm × 1 mm. Functional images were acquired using a gradient-echo single-shot echo-planar imaging (EPI) sequence, with TR = 2,000 ms, TE = 30 ms, acquisition matrix = 64 × 64, voxel size = 3.5 × 3.5 × 3.5 mm, and flip angle = 90°. A total of 240-time points (35 slices) were collected within 8 min.

The rs-fMRI data were processed using Data Processing & Analysis for Brain Imaging (DPABI) V5.1 (Yan et al., 2016), which is based on Statistical Parametric Mapping.[1] The preprocessing procedures were as follows: (1) The first 10 time points were removed to minimize the influence of magnetic field instability during the initial scanning. (2) The scanning times of all slices were aligned to the reference slice, using the time of the middle layer as a reference. (3) Head movements were corrected using the realign procedure, and the T1-weighted image was co-registered with the mean of all realigned images. Subjects with an average head movement of >0.2 mm were excluded. (4) The co-registered T1-weighted image was normalized to the Montreal Neurological Institute (MNI) space using the Diffeomorphic Anatomical Registration Through Exponentiated Lie (DARTEL) procedure. The parameters generated in DARTEL registration and normalization were applied to each functional image. (5) The Friston 24-parameter model was used to regress the head motion effects (Friston et al., 1996; Yan et al., 2013). The mean framewise displacement (FD), which was calculated using Jenkinson's relative root mean square algorithm (Jenkinson et al., 2002), was included in the group analysis as a covariate to further minimize the effect of head motion. A linear detrend was used to reduce high-frequency noise and low-frequency drift. White matter and cerebrospinal fluid signals were also regressed to reduce respiratory and cardiac effects. (6) Temporal bandpass filtering was performed in the slow-5 (0.01–0.027 Hz) and slow-4 bands (0.027–0.073 Hz).

The values of ALFF, ReHo, and VMHC were calculated using DPABI. A fast Fourier transformation was used

1 http://www.fil.ion.ucl.ac.uk/spm

to convert the time series to the frequency domain for each voxel, and the square root was calculated at each frequency of the power spectrum. ALFF is the average square root of a given voxel. The ReHo was computed using Kendall's concordance coefficient, which measures the similarity between the time series of a given voxel and its 26 neighboring voxels. The VMHC was calculated as the Pearson correlation coefficient between each pair of mirrored interhemispheric voxel time series. The values of ALFF, ReHo, and VMHC at each voxel were normalized using z-score transformation to improve the reliability and normality across subjects.

In our study, nine seronegative controls and seven PLWHs were excluded because of excessive head movement (mean FD > 0.2 mm). Subsequently, we created a group mask that included all voxels present in at least 90% of participants to ensure that the coverage of these voxels is the same across participants.

2.4. Statistical analysis

The general information of the two groups, including age, sex, and years of education, was compared using the two-sample *t*-test (age and years of education) and Fisher's exact test (sex composition ratio).

Two-way ANOVA was conducted using statistical parametric mapping 12 (see text footnote 1) with the groups (seronegative controls and PLWH) as between-subject factor and different frequency bands as within-subject factors. Age, sex, and head motion were added as covariates. Cluster-level family-wise error (FWE) correction was set at $P < 0.05$. Clusters that survived multiple corrections were extracted as regions of interest (ROIs) for further *post hoc* analysis. The Bonferroni test was used to compare the differences between the two groups at different frequency bands.

Partial correlation analysis was carried out among ALFF, VMHC, ReHo, and each cognitive domain (age and head movement as covariable). *P*-value < 0.05 (not corrected for multiple comparisons) was considered statistically significant.

3. Results

3.1. Demographic information and clinical variables

There were no statistically significant differences in the age and sex composition ratio between PLWH and seronegative controls ($P = 0.077$ and 0.254, respectively). For PLWH, the viral load, CD4/CD8 ratio, and CD4 + T cell counts were estimated. Among the 98 PLWHs, 66 subjects were tested for plasma viral load within 2 weeks, with 53 subjects showing plasma viral load below the detection limit, 93 subjects were tested for CD4/CD8 ratio, and 98 subjects were tested for CD4 + T cell count. Demographic and clinical information are shown in Table 1.

3.2. Neurocognitive performance in PLWH

Of the 98 PLWHs, 91 completed neurocognitive tests and activities of daily living scales, and all of them demonstrated intact daily function. For neurocognitive performance, 37 subjects had at least two cognitive domains with at least one standard deviation below the norm and were classified as ANI, 31 had no cognitive deficits in any of the six domains, and 23 had one cognitive domain with at least one standard deviation below the norm. Neurocognitive performance in PLWH is listed in Table 2.

3.3. Main effect of group and group-by-frequency interaction of three indices

The main effect of the group can only be detected in the ALFF, with differences located in the right superior/middle/inferior occipital gyrus and right calcarine (extending to the right lingual gyrus and right precuneus; BA18, BA19) ($F = 25.2$, $\eta^2 = 0.168$). Group-by-frequency interactions were detected in ReHo and VMHC. For ReHo, the interaction was found in the right thalamus and right globus pallidus (extending to the right caudate nucleus) ($F = 24.8$, $\eta^2 = 0.138$); for VMHC, the interaction was observed in the bilateral precuneus and bilateral paracentral gyrus ($F = 18.6$, $\eta^2 = 0.131$).

The subsequent Bonferroni test further supported that the differences in ALFF were independent of frequency bands, with PLWH showing decreased ALFF in the right superior/middle/inferior occipital gyrus and right calcarine (extending to the right lingual gyrus and right precuneus)

TABLE 1 Demographics and clinical information.

Variable	Controls (*n* = 44)	PLWH (*n* = 98)	*P*-value
Age (mean ± SD)	33.7 ± 6.0	31.6 ± 6.9	0.077a
Male, *n* (%)	40 (91.3%)	94 (98.2%)	0.254b
Education years (mean ± SD)	/	13.5 ± 3.1	/
CD4 + T (mean ± SD)	/	476.6 ± 222.0	/
CD4/CD8 (mean ± SD)	/	0.6 ± 0.4	/
TND, *n* (%)	/	53 (80.3%)	/

TND, virus not detectable. Statistical tests including (a) *t*-test; (b) Fisher's exact test.

TABLE 2 Applied neurocognitive test battery and neurocognitive performance in PLWH.

Test	Cognitive domain	T scores
Trail-making test part A	Speed of information processing	48.4 ± 7.2
Hopkins verbal learning test-revised Brief visuospatial memory test-revised	Memory (learning and recall)	46.8 ± 6.5
Wisconsin card sorting test 64-card version	Abstraction/executive	58.4 ± 9.1
Continuous performance test-identical pairs Wechsler memory scale-III Paced auditory serial addition test	Attention/working memory	44.8 ± 7.2
Grooved Pegboard Test	Fine motor skills	48.4 ± 7.7
Animal naming test	Verbal and language	48.7 ± 7.0

($P < 0.001$). The difference in the ReHo of clusters located in the right thalamus/globus pallidus can only be detected in slow-5 with PLWH, showing increased synchronization with nearby voxels ($P = 0.046$). For VMHC, differences could only be detected in slow-5 in the spatially homotopic clusters located in the bilateral precuneus/paracentral gyrus, with PLWH showing decreased synchronization of these mirrored voxels ($P < 0.001$) (see **Figure 1** and **Table 3**).

3.4. Relationship among ALFF, ReHo, and VMHC indices at different frequency bands and cognition

Partial correlation analysis revealed a significant correlation between the altered indices (except VMHC) and cognition. Specifically, the ALFF of the right occipital gyrus/calcarine in both frequency bands was positively correlated with the speed of information processing (slow-5: $r = 0.278$, $P = 0.013$; slow-4: $r = 0.286$, $P = 0.010$) and abstract/executive function (slow-5: $r = 0.238$, $P = 0.033$; slow-4: $r = 0.274$, $P = 0.014$). The ReHo of the right thalamus/globus pallidus in slow-5 was positively correlated with fine motor skills ($r = 0.263$, $P = 0.018$) (see **Figure 2**).

4. Discussion

In this study, we used three voxel-level fMRI indices (ALFF, ReHo, and VMHC) in two sub-frequency bands (slow-5 and slow-4) to explore functional brain integration and segregation characteristics in neuro-asymptomatic PLWH. Our results indicated that PLWH displayed aberrant functional segregation and integration, including decreased strength of low-frequency oscillations in the right occipital gyrus, increased synchronization of nearby voxels (right thalamus/globus pallidus), and decreased synchronization of mirrored voxels (bilateral precuneus and paracentral gyrus). Applying sub-frequency analysis might be able to detect functional alterations related to the early stages of HAND, and the sub-frequency of slow-5 might be more sensitive in detecting altered intrinsic brain activity than slow-4 in PLWH. Decreased low-frequency fluctuations in the right occipital lobe and increased regional synchronization in the thalamus are associated with impaired cognitive function.

The cortical cortex involved in PLWH detected in our study is mainly the posterior brain cortex, with decreased spontaneous neural activity in the right occipital lobe (mostly in the visual cortex) and reduced neural synchronization of mirrored voxels in the bilateral precuneus/paracentral gyrus. In addition, decreased spontaneous neural activity in the occipital lobe is related to a reduced speed of information processing and abstract/executive skills.

A large body of research supports occipital damage in PLWH (Ances et al., 2009; Wang et al., 2011; Narvid et al., 2018; Wiesman et al., 2018). Wang et al. (2011) indicated abnormal functional connectivity of the external occipital cortex (LOC) network and reduced coactivation of the left inferior parietal cortex in the LOC network 1 year after HIV infection. Ances et al. (2009) found that the primary visual cortex was less activated, and the resting cerebral blood flow in the visual cortex was reduced in PLWH (Narvid et al., 2018). A magnetoencephalography study also revealed aberrant spontaneous and neural oscillatory activity within the visual cortices during a visuospatial processing task (Wiesman et al., 2018). Experimental studies in animals have demonstrated that the occipital cortex is among the most Tat permeable regions (Banks et al., 2005), and this viral protein-induced senescence may contribute to the development of HAND (Marino et al., 2020). In a PET study, higher translocator protein (TSPO), a marker of microglial activation, was detected in the occipital and parietal cortex (Rubin et al., 2018), suggesting pronounced neuroinflammation in this brain region. A similar result was demonstrated by a magnetic resonance spectroscopy study showing cellular inflammation in the occipital cortex and the basal ganglia (Sailasuta et al., 2012). We conjecture that the occipital lobe is likely to be involved in PLWH with prominent inflammation, severe blood–brain barrier disruption, and viral protein accumulation, inducing neurodegeneration, which can be detected by functional imaging. The more prominent the reduction in low-frequency fluctuations, the more pronounced the neuronal damage, resulting in more severe cognitive impairment.

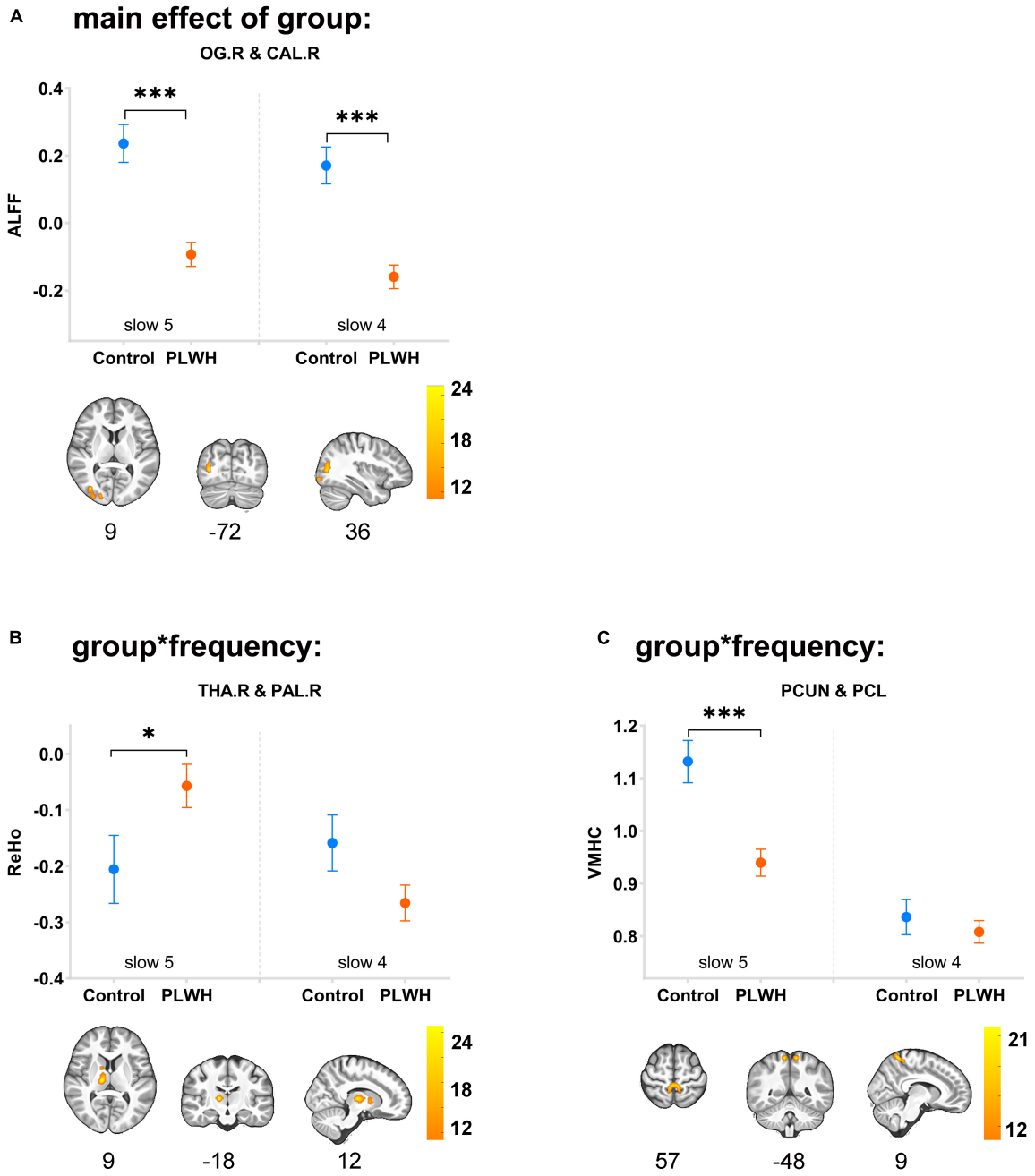

FIGURE 1
Main effects of group and group-by-frequency interaction in PLWH are compared with seronegative controls. The main effect of group was detected in ALFF **(A)**, with differences located in the OG.R and CAL.R; group-by-frequency interactions were detected in the THA.R and PAL.R for ReHo **(B)** and bilateral PCUN and PCL for VMHC **(C)**. Brain regions showing the main effect of group or group-by-frequency interaction were colored by F-statistic (red/yellow). The upper row graph displayed the differences (mean ± SEM) between groups in slow-5 (plotted on the left side of the separatrix line) and slow-4 (plotted on the right side). ***$P < 0.001$; *$P < 0.05$. Corrected for multiple comparisons ($P < 0.001$, corrected at cluster level with FWE $P < 0.05$). OG.R, right superior/middle/inferior occipital gyrus; CAL.R, right calcarine; THA.R, right thalamus; PAL.R, right globus pallidus; PCUN, precuneus; PCL, paracentral lobe; control, seronegative controls; PLWH, people living with HIV.

The precuneus is the core area of the default mode network. It shows the highest metabolic rate at rest, has rich anatomical and functional connections with a wide range of brain regions, and participates in multiple complex cognitive functions, such as visuospatial imagination, episodic memory retrieval, and self-task processing (Cavanna and Trimble, 2006). Damage to this brain region was supported by Hall et al. with a task-based functional MRI showing hypoactivation in the precuneus

TABLE 3 Main effect of group and group * frequency interaction in PLWH compared with seronegative controls.

Effect	Indices	Structure	L/R	Volumes (mm^3)	Coordinates			F value
					X	Y	Z	
Main effect (group)	ALFF	Superior/middle/inferior occipital gyrus, calcarine (BA18, BA19)	R	3,915	36	−72	9	25.2
Interaction (group * frequency)	ReHo	Thalamus/globus pallidus	R	1,674	12	−18	9	24.8
	VMHC	Precuneus/paracentral lobe (BA5)	L/R	2,241	9	−48	60	18.6

BA, Brodmann area.

Coordinates (X, Y, and Z) refer to the peak MNI coordinates of brain regions with peak intensity. Corrected for multiple comparisons ($P < 0.001$, corrected at cluster level with FWE $P < 0.05$).

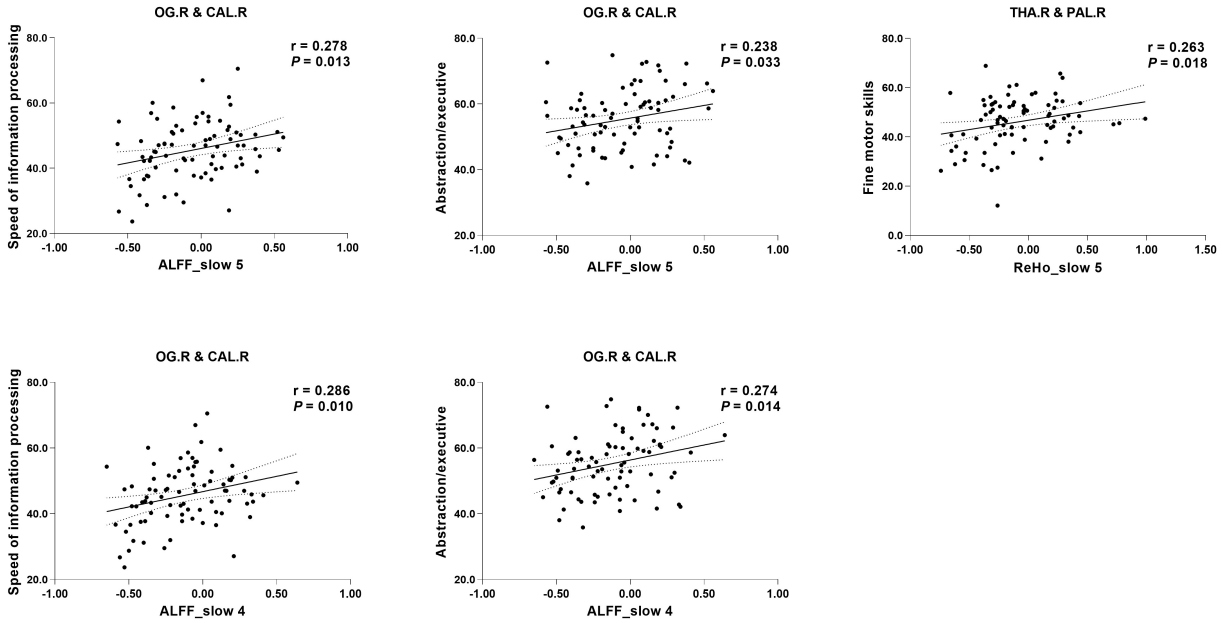

FIGURE 2

Correlation between specific cognitive domains and imaging indices. The areas between two dotted curves indicate the 95% confidence interval. THA.R, right thalamus; PAL.R, right globus pallidus; PCUN, precuneus; PCL, paracentral lobe.

during ambiguous decision-making in PLWH (Hall et al., 2021). In a magnetic resonance spectroscopy study, glutamate reduction in the precuneus of PLWH was reported, and this reduction was associated with information processing speed (Mohamed et al., 2018). In our study, homotopic functional connectivity abnormalities in the bilateral precuneus were detected; however, the reduction was not linked to any of the six assessed domains. One possible reason is the differences in brain reserve and cognitive reserve among PLWHs, which are influenced by neurobiological capacity, genetically determined innate differences, and lifetime exposures (e.g., education, intelligence, and physical activity) (Stern et al., 2019; Zijlmans et al., 2022).

The subcortical nucleus is also involved in PLWH, with increased neural coherence in the right thalamus/globus pallidus. Previous studies have reported thalamic volume loss, even in PLWH with sustained cART (Chiang et al., 2007; Janssen et al., 2015; Wade et al., 2015). Quantitative measurements of [18F] fluorodeoxyglucose (FDG) uptake in PLWH demonstrated that the thalamus showed the most significant hypometabolism (Hammoud et al., 2018). Notably, the subcortical nuclei involved in our study are important components of the cortical-basal ganglia-thalamocortical circuit (Taylor and Taylor, 2000; Chiang et al., 2007). Abnormal quality and quantity of neurotransmitters (decreased dopamine concentration, accumulation of glutamate concentration, and dysfunction of the gamma-aminobutyric acid system) in this circuit were verified by autopsy, cerebrospinal fluid, and animal experiments (Kumar et al., 2009, 2011; Gorska and Eugenin, 2020). In our study, neural synchronization of the right thalamus/globus pallidus was increased in PLWH and

positively correlated with fine motor skills. We speculated that the increased coherence in these nuclei might be evidence of brain reorganization in PLWH to maintain cognitive function.

Blood-oxygen-level-dependent (BOLD) signals in slow-4 and slow-5 are considered distinct entities, although the origin and physiological significance of the different sub-frequencies remain unclear. It has been speculated that different frequency bands correlate with different physiological processes (Yang et al., 2020; Liu et al., 2022) and show different properties at the regional, interregional, and network levels (Xue et al., 2014). In our study, group differences were mainly detected in slow-5, indicating that slow-5 might be more sensitive in detecting functional alterations in PLWH, similar to the findings in Alzheimer's disease (Yang et al., 2020). If only one frequency is analyzed, slow-5 might be a better choice. Previous studies supported that ReHo in slow-4 is enhanced in the ventrolateral thalamus and caudate compared with slow-5 (Xue et al., 2014), and low-frequency fluctuations in slow-4 are more robust in the basal ganglia and the thalamus (Zuo et al., 2010a). However, these studies were conducted in a healthy population; thus, the results may not be generalizable to PLWH. In conclusion, we speculate that the neural activity patterns of some impaired brain regions in PLWH are frequency-specific, and adopting a sub-frequency analysis is helpful in identifying altered functional integration and segregation, which may be related to neurocognition at the early stage of HAND.

Our study had some limitations. First, the neurocognitive function was not observed in seronegative controls. It was reported that 15–22% of seronegative controls score below the threshold of HAND (Cysique et al., 2011). Neurocognitive function in seronegative controls would allow a more objective analysis and conclusion. Second, some risk or causative factors (such as cardiovascular disease, smoking, alcohol abuse, antiviral drug neurotoxicity, and co-infection) were not considered. Third, this was a cross-sectional study, and brain function data before infection or follow-up data were unavailable. Future studies should consider using sub-frequency bands and longitudinal studies to assess cognitive function and brain functional alterations.

5. Conclusion

People living with HIV displayed aberrant functional integration and segregation at the early stage of HAND, with altered low-frequency fluctuations in the occipital lobe, enhanced neural synchronization in the right thalamus, and reduced synchronization of mirrored voxels in the precuneus. Most of these alterations are frequency-dependent and are linked to cognitive function. Our study indicates that sub-frequency analysis may show some features that are related to the early stages of HAND and slow-5 might be more sensitive to detect the insidious damage in PLWH. More rigorous study is needed to confirm our findings.

Data availability statement

The original contributions presented in this study are included in this article/supplementary material, further inquiries can be directed to the corresponding authors.

Ethics statement

This study was conducted in accordance with the Declaration of Helsinki, and the protocol was approved by the Ethics Committee of Beijing Youan Hospital. The patients/participants provided their written informed consent to participate in this study.

Author contributions

HL, WW, and DL contributed to the conception and design of the study. WW, YW, RL, JL, and ML recruited the participants and organized the database. DL and WW performed parts of the statistical analysis. WW, DL, and HW contributed to the writing the manuscript. All authors contributed to the manuscript revision and read and approved the submitted version.

Funding

This research was supported by the National Science Foundation of China (Grant nos. 61936013 and 82271963) and the Beijing Natural Science Foundation (7212051).

Acknowledgments

We are grateful to the participants who volunteered for our study and our team in Beijing Youan Hospital for recruiting and collecting these data.

Conflict of interest

The authors declare that the research was conducted in the absence of any commercial or financial relationships that could be construed as a potential conflict of interest.

Publisher's note

References

Ances, B. M., Sisti, D., Vaida, F., Liang, C. L., Leontiev, O., Perthen, J. E., et al. (2009). Resting cerebral blood flow: a potential biomarker of the effects of HIV in the brain. *Neurology* 73, 702–708. doi: 10.1212/WNL.0b013e3181b59a97

Antinori, A., Arendt, G., Becker, J. T., Brew, B. J., Byrd, D. A., Cherner, M., et al. (2007). Updated research nosology for HIV-associated neurocognitive disorders. *Neurology* 69, 1789–1799. doi: 10.1212/01.WNL.0000287431.88658.8b

Bak, Y., Jun, S., Choi, J. Y., Lee, Y., Lee, S. K., Han, S., et al. (2018). Altered intrinsic local activity and cognitive dysfunction in HIV patients: a resting-state fMRI study. *PLoS One* 13:e0207146. doi: 10.1371/journal.pone.0207146

Banks, W. A., Robinson, S. M., and Nath, A. (2005). Permeability of the blood-brain barrier to HIV-1 Tat. *Exp. Neurol.* 193, 218–227. doi: 10.1016/j.expneurol.2004.11.019

Cavanna, A. E., and Trimble, M. R. (2006). The precuneus: a review of its functional anatomy and behavioural correlates. *Brain* 129, 564–583. doi: 10.1093/brain/awl004

Chang, M., Edmiston, E. K., Womer, F. Y., Zhou, Q., Wei, S., Jiang, X., et al. (2019). Spontaneous low-frequency fluctuations in the neural system for emotional perception in major psychiatric disorders: amplitude similarities and differences across frequency bands. *J. Psychiatry Neurosci.* 44, 132–141. doi: 10.1503/jpn.170226

Chiang, M. C., Dutton, R. A., Hayashi, K. M., Lopez, O. L., Aizenstein, H. J., Toga, A. W., et al. (2007). 3D pattern of brain atrophy in HIV/AIDS visualized using tensor-based morphometry. *Neuroimage* 34, 44–60. doi: 10.1016/j.neuroimage.2006.08.030

Cysique, L. A., Franklin, D. Jr., Abramson, I., Ellis, R. J., Letendre, S., Collier, A., et al. (2011). Normative data and validation of a regression based summary score for assessing meaningful neuropsychological change. *J. Clin. Exp. Neuropsychol.* 33, 505–522. doi: 10.1080/13803395.2010.535504

De Luca, M., Beckmann, C. F., De Stefano, N., Matthews, P. M., and Smith, S. M. (2006). fMRI resting state networks define distinct modes of long-distance interactions in the human brain. *Neuroimage* 29, 1359–1367. doi: 10.1016/j.neuroimage.2005.08.035

Eggers, C., Arendt, G., Hahn, K., Husstedt, I. W., Maschke, M., Neuen-Jacob, E., et al. (2017). HIV-1-associated neurocognitive disorder: epidemiology, pathogenesis, diagnosis, and treatment. *J. Neurol.* 264, 1715–1727. doi: 10.1007/s00415-017-8503-2

Friston, K. J., Williams, S., Howard, R., Frackowiak, R. S., and Turner, R. (1996). Movement-related effects in fMRI time-series. *Magn. Reson. Med.* 35, 346–355. doi: 10.1002/mrm.1910350312

Gorska, A. M., and Eugenin, E. A. (2020). The glutamate system as a crucial regulator of CNS toxicity and survival of HIV reservoirs. *Front. Cell Infect. Microbiol.* 10:261. doi: 10.3389/fcimb.2020.00261

Gouse, H., Masson, C. J., Henry, M., Thomas, K. G. F., Robbins, R. N., Kew, G., et al. (2021). The impact of HIV-associated neurocognitive impairment on driving performance in commercial truck drivers. *AIDS Behav.* 25, 689–698. doi: 10.1007/s10461-020-03033-7

Hall, S. A., Towe, S. L., Nadeem, M. T., Hobkirk, A. L., Hartley, B. W., Li, R., et al. (2021). Hypoactivation in the precuneus and posterior cingulate cortex during ambiguous decision making in individuals with HIV. *J. Neurovirol.* 27, 463–475. doi: 10.1007/s13365-021-00981-1

Hammoud, D. A., Sinharay, S., Steinbach, S., Wakim, P. G., Geannopoulos, K., Traino, K., et al. (2018). Global and regional brain hypometabolism on FDG-PET in treated HIV-infected individuals. *Neurology* 91, e1591–e1601. doi: 10.1212/wnl.0000000000006398

Han, Y., Wang, J., Zhao, Z., Min, B., Lu, J., Li, K., et al. (2011). Frequency-dependent changes in the amplitude of low-frequency fluctuations in amnestic mild cognitive impairment: a resting-state fMRI study. *Neuroimage* 55, 287–295. doi: 10.1016/j.neuroimage.2010.11.059

Janssen, M. A., Meulenbroek, O., Steens, S. C., Góraj, B., Bosch, M., Koopmans, P. P., et al. (2015). Cognitive functioning, wellbeing and brain correlates in HIV-1 infected patients on long-term combination antiretroviral therapy. *Aids* 29, 2139–2148. doi: 10.1097/qad.0000000000000824

Jenkinson, M., Bannister, P., Brady, M., and Smith, S. (2002). Improved optimization for the robust and accurate linear registration and motion correction of brain images. *Neuroimage* 17, 825–841. doi: 10.1016/s1053-8119(02)91132-8

Kumar, A. M., Fernandez, J. B., Singer, E. J., Commins, D., Waldrop-Valverde, D., Ownby, R. L., et al. (2009). Human immunodeficiency virus type 1 in the central nervous system leads to decreased dopamine in different regions of postmortem human brains. *J. Neurovirol.* 15, 257–274. doi: 10.1080/13550280902973952

Kumar, A. M., Ownby, R. L., Waldrop-Valverde, D., Fernandez, B., and Kumar, M. (2011). Human immunodeficiency virus infection in the CNS and decreased dopamine availability: relationship with neuropsychological performance. *J. Neurovirol.* 17, 26–40. doi: 10.1007/s13365-010-0003-4

Li, R., Wang, W., Wang, Y., Peters, S., Zhang, X., and Li, H. (2019). Effects of early HIV infection and combination antiretroviral therapy on intrinsic brain activity: a cross-sectional resting-state fMRI study. *Neuropsychiatr. Dis. Treat.* 15, 883–894. doi: 10.2147/ndt.S195562

Liao, H., Yi, J., Cai, S., Shen, Q., Liu, Q., Zhang, L., et al. (2021). Changes in degree centrality of network nodes in different frequency bands in parkinson's disease with depression and without depression. *Front. Neurosci.* 15:638554. doi: 10.3389/fnins.2021.638554

Liu, S., Zhang, C., Meng, C., Wang, R., Jiang, P., Cai, H., et al. (2022). Frequency-dependent genetic modulation of neuronal oscillations: a combined transcriptome and resting-state functional MRI study. *Cereb Cortex* 32, 5132–5144. doi: 10.1093/cercor/bhac003

Lv, H., Wang, Z., Tong, E., Williams, L. M., Zaharchuk, G., Zeineh, M., et al. (2018). Resting-state functional MRI: everything that nonexperts have always wanted to know. *AJNR Am. J. Neuroradiol.* 39, 1390–1399. doi: 10.3174/ajnr.A5527

Marino, J., Maubert, M. E., Mele, A. R., Spector, C., Wigdahl, B., and Nonnemacher, M. R. (2020). Functional impact of HIV-1 tat on cells of the CNS and its role in HAND. *Cell Mol. Life Sci.* 77, 5079–5099. doi: 10.1007/s00018-020-03561-4

Mohamed, M., Barker, P. B., Skolasky, R. L., and Sacktor, N. (2018). 7T brain MRS in HIV infection: correlation with cognitive impairment and performance on neuropsychological tests. *AJNR Am. J. Neuroradiol.* 39, 704–712. doi: 10.3174/ajnr.A5547

Narvid, J., McCoy, D., Dupont, S. M., Callen, A., Tosun, D., Hellmuth, J., et al. (2018). Abnormal cerebral perfusion profile in older adults with HIV-associated neurocognitive disorder: discriminative power of arterial spin-labeling. *AJNR Am. J. Neuroradiol.* 39, 2211–2217. doi: 10.3174/ajnr.A5902

Rojas-Celis, V., Valiente-Echeverría, F., Soto-Rifo, R., and Toro-Ascuy, D. (2019). New challenges of HIV-1 infection: how HIV-1 attacks and resides in the central nervous system. *Cells* 8:1245. doi: 10.3390/cells8101245

Rubin, L. H., Sacktor, N., Creighton, J., Du, Y., Endres, C. J., Pomper, M. G., et al. (2018). Microglial activation is inversely associated with cognition in individuals living with HIV on effective antiretroviral therapy. *Aids* 32, 1661–1667. doi: 10.1097/qad.0000000000001858

Sailasuta, N., Ross, W., Ananworanich, J., Chalermchai, T., DeGruttola, V., Lerdlum, S., et al. (2012). Change in brain magnetic resonance spectroscopy after treatment during acute HIV infection. *PLoS One* 7:e49272. doi: 10.1371/journal.pone.0049272

Shi, C., Kang, L., Yao, S., Ma, Y., Li, T., Liang, Y., et al. (2015). The MATRICS consensus cognitive battery (MCCB): co-norming and standardization in China. *Schizophr. Res.* 169, 109–115. doi: 10.1016/j.schres.2015.09.003

Stern, Y., Barnes, C. A., Grady, C., Jones, R. N., and Raz, N. (2019). Brain reserve, cognitive reserve, compensation, and maintenance: operationalization, validity, and mechanisms of cognitive resilience. *Neurobiol. Aging* 83, 124–129. doi: 10.1016/j.neurobiolaging.2019.03.022

Taylor, J. G., and Taylor, N. R. (2000). Analysis of recurrent cortico-basal ganglia-thalamic loops for working memory. *Biol. Cybern.* 82, 415–432. doi: 10.1007/s004220050595

van Sighem, A. I., Gras, L. A., Reiss, P., Brinkman, K., and de Wolf, F. (2010). Life expectancy of recently diagnosed asymptomatic HIV-infected patients approaches that of uninfected individuals. *Aids* 24, 1527–1535. doi: 10.1097/QAD.0b013e32833a3946

Wade, B. S., Valcour, V. G., Wendelken-Riegelhaupt, L., Esmaeili-Firidouni, P., Joshi, S. H., Gutman, B. A., et al. (2015). Mapping abnormal subcortical brain morphometry in an elderly HIV+ cohort. *Neuro. Clin.* 9, 564–573. doi: 10.1016/j.nicl.2015.10.006

Wallet, C., De Rovere, M., Van Assche, J., Daouad, F., De Wit, S., Gautier, V., et al. (2019). Microglial cells: the main HIV-1 reservoir in the brain. *Front. Cell Infect. Microbiol.* 9:362. doi: 10.3389/fcimb.2019.00362

Wang, X., Foryt, P., Ochs, R., Chung, J. H., Wu, Y., Parrish, T., et al. (2011). Abnormalities in resting-state functional connectivity in early human immunodeficiency virus infection. *Brain Connect* 1, 207–217. doi: 10.1089/brain.2011.0016

Wang, Y., Liu, M., Lu, Q., Farrell, M., Lappin, J. M., Shi, J., et al. (2020). Global prevalence and burden of HIV-associated neurocognitive disorder: a meta-analysis. *Neurology* 95, e2610–e2621. doi: 10.1212/wnl.0000000000010752

Wiesman, A. I., O'Neill, J., Mills, M. S., Robertson, K. R., Fox, H. S., Swindells, S., et al. (2018). Aberrant occipital dynamics differentiate HIV-infected patients with and without cognitive impairment. *Brain* 141, 1678–1690. doi: 10.1093/brain/awy097

Winston, A., and Spudich, S. (2020). Cognitive disorders in people living with HIV. *Lancet* 7, e504–e513. doi: 10.1016/S2352-3018(20)30107-7

Woods, S. P., Iudicello, J. E., Morgan, E. E., Verduzco, M., Smith, T. V., and Cushman, C. (2017). Household everyday functioning in the internet age: online shopping and banking skills are affected in hiv-associated neurocognitive disorders. *J. Int. Neuropsychol. Soc.* 23, 605–615. doi: 10.1017/s1355617717000431

Wu, Z., Luo, Q., Wu, H., Wu, Z., Zheng, Y., Yang, Y., et al. (2020). Amplitude of low-frequency oscillations in major depressive disorder with childhood trauma. *Front. Psychiatry* 11:596337. doi: 10.3389/fpsyt.2020.596337

Xue, S. W., Li, D., Weng, X. C., Northoff, G., and Li, D. W. (2014). Different neural manifestations of two slow frequency bands in resting functional magnetic resonance imaging: a systemic survey at regional, interregional, and network levels. *Brain Connect* 4, 242–255. doi: 10.1089/brain.2013.0182

Yadav, S. K., Gupta, R. K., Hashem, S., Bhat, A. A., Garg, R. K., Venkatesh, V., et al. (2018). Changes in resting-state functional brain activity are associated with waning cognitive functions in HIV-infected children. *Neuro. Clin.* 20, 1204–1210. doi: 10.1016/j.nicl.2018.10.028

Yan, C. G., Cheung, B., Kelly, C., Colcombe, S., Craddock, R. C., Di Martino, A., et al. (2013). A comprehensive assessment of regional variation in the impact of head micromovements on functional connectomics. *Neuroimage* 76, 183–201. doi: 10.1016/j.neuroimage.2013.03.004

Yan, C. G., Wang, X. D., Zuo, X. N., and Zang, Y. F. (2016). DPABI: data processing & analysis for (resting-state) brain imaging. *Neuroinformatics* 14, 339–351. doi: 10.1007/s12021-016-9299-4

Yang, H., Long, X. Y., Yang, Y., Yan, H., Zhu, C. Z., Zhou, X. P., et al. (2007). Amplitude of low frequency fluctuation within visual areas revealed by resting-state functional MRI. *Neuroimage* 36, 144–152. doi: 10.1016/j.neuroimage.2007.01.054

Yang, L., Yan, Y., Li, Y., Hu, X., Lu, J., Chan, P., et al. (2020). Frequency-dependent changes in fractional amplitude of low-frequency oscillations in Alzheimer's disease: a resting-state fMRI study. *Brain Imag. Behav.* 14, 2187–2201. doi: 10.1007/s11682-019-00169-6

Yang, Y., Cui, Q., Pang, Y., Chen, Y., Tang, Q., Guo, X., et al. (2021). Frequency-specific alteration of functional connectivity density in bipolar disorder depression. *Prog. Neuropsychopharmacol. Biol. Psychiatry* 104:110026. doi: 10.1016/j.pnpbp.2020.110026

Zang, Y., Jiang, T., Lu, Y., He, Y., and Tian, L. (2004). Regional homogeneity approach to fMRI data analysis. *Neuroimage* 22, 394–400. doi: 10.1016/j.neuroimage.2003.12.030

Zhang, S., Li, H., Xu, Q., Wang, C., Li, X., Sun, J., et al. (2021). Regional homogeneity alterations in multi-frequency bands in tension-type headache: a resting-state fMRI study. *J. Head. Pain* 22:129. doi: 10.1186/s10194-021-01341-4

Zijlmans, J. L., Lamballais, S., Vernooij, M. W., Ikram, M. A., and Luik, A. I. (2022). Sociodemographic, lifestyle, physical, and psychosocial determinants of cognitive reserve. *J. Alzheimers Dis.* 85, 701–713. doi: 10.3233/jad-215122

Zuo, X. N., Di Martino, A., Kelly, C., Shehzad, Z. E., Gee, D. G., Klein, D. F., et al. (2010a). The oscillating brain: complex and reliable. *Neuroimage* 49, 1432–1445. doi: 10.1016/j.neuroimage.2009.09.037

Zuo, X. N., Kelly, C., Di Martino, A., Mennes, M., Margulies, D. S., Bangaru, S., et al. (2010b). Growing together and growing apart: regional and sex differences in the lifespan developmental trajectories of functional homotopy. *J. Neurosci.* 30, 15034–15043. doi: 10.1523/jneurosci.2612-10.2010

frontiers | Frontiers in Neuroscience

TYPE Original Research
PUBLISHED 26 January 2023
DOI 10.3389/fnins.2023.1025745

OPEN ACCESS

EDITED BY
Chitresh Bhushan,
GE Global Research, United States

REVIEWED BY
Yijie Lai,
Shanghai Jiao Tong University, China
Markus Zedler,
Hannover Medical School, Germany

*CORRESPONDENCE
Naoki Kodama
✉ kodama@nuhw.ac.jp

SPECIALTY SECTION
This article was submitted to Brain Imaging Methods, a section of the journal Frontiers in Neuroscience

RECEIVED 23 August 2022
ACCEPTED 11 January 2023
PUBLISHED 26 January 2023

CITATION
Sakurai N, Nagasaka K, Takahashi S, Kasai S, Onishi H and Kodama N (2023) Brain function effects of autonomous sensory meridian response (ASMR) video viewing. *Front. Neurosci.* 17:1025745. doi: 10.3389/fnins.2023.1025745

Brain function effects of autonomous sensory meridian response (ASMR) video viewing

Noriko Sakurai[1], Kazuaki Nagasaka[2], Shingo Takahashi[3], Satoshi Kasai[1], Hideaki Onishi[2] and Naoki Kodama[1]*

[1]Department of Radiological Technology, Niigata University of Health and Welfare, Niigata, Japan, [2]Department of Physical Therapy, Niigata University of Health and Welfare, Niigata, Japan, [3]Department of Healthcare Informatics, Takasaki University of Health and Welfare, Gunma, Japan

Background: Autonomous sensory meridian response (ASMR) is the sensation of tingling from audiovisual stimuli that leads to positive emotions. ASMR is used among young people to relax, induce sleep, reduce stress, and alleviate anxiety. However, even without experiencing tingling, ASMR is used by many young people to seek relaxation. Auditory stimulation in ASMR is thought to play the most important role among its triggers, and previous studies have used a mixture of auditory and visual stimulation and auditory stimulation. This is the first study to approach the differences between the effects of direct audiovisual and auditory stimulation from the perspective of brain function using functional magnetic resonance imaging (fMRI) and to clarify the effects of ASMR, which attracts many young people.

Methods: The subjects were 30 healthy subjects over 19 years old or older who had not experienced tingling. Brain function was imaged by fMRI while watching ASMR videos or listening to the sound files only. We administered a questionnaire based on a Likert scale to determine if the participants felt a "relaxed mood" and "tingling mood" during the task.

Results: Significant activation was found in the visual cortex for audiovisual stimulation and in the visual and auditory cortex for auditory stimulation. In addition, activation of characteristic sites was observed. The specific sites of activation for audiovisual stimulation were the middle frontal gyrus and the left nucleus accumbens, while the specific sites of activation for auditory stimulation were the bilateral insular cortices. The questionnaire showed no significant differences in either "relaxed mood" or "tingling mood" in response to auditory and visual stimulation or auditory stimulation alone.

Conclusion: The results of this study showed that there was a clear difference between auditory and audiovisual stimulation in terms of the areas of activation in the brain, but the questionnaire did not reveal any difference in the subjects' mood. Audiovisual stimulation showed activation of the middle frontal gyrus and the nucleus accumbens, whereas auditory stimulation showed activation of the insular cortex. This difference in brain activation sites suggests a difference in mental health effects between auditory and audiovisual stimulation. However, future research on comparisons between those who experience tingling and those who do not, as well as investigations of physiological indices, and examination of the relationship with activated areas in the brain may show that ASMR is useful for mental health.

KEYWORDS

ASMR, audiovisual stimulation, auditory stimulation, nucleus accumbens, fMRI

1. Introduction

Autonomous sensory meridian response (ASMR) is a tingling somatosensory phenomenon that begins in the scalp and extends to the back of the neck, arms, and legs (Barratt and Davis, 2015). Many videos that elicit ASMR, which are becoming increasingly popular among young people, have been posted on YouTube and other social media sites so that people can experience the sensation (Barratt and Davis, 2015; Barratt et al., 2017). This somatic somatosensory is reported to be more likely to be experienced by open-minded individuals based on personality trait analysis (Fredborg et al., 2017). It is believed that to experience tingling, one would wear headphones and choose a quiet, calm place, which is a very limited time and place. However, feeling relaxed and positive even when no tingling occurred, suggesting possible relief of chronic pain and coping with anxiety (Barratt and Davis, 2015; Morales et al., 2021). ASMR is used by many young people to seek relaxation, even if they do not experience tingling. The videos are created by emulating a wide variety of real-life experiences, such as tapping sounds, crisp sounds, nature sounds, soft whispers, and role-playing actions. Triggers of ASMR have been grouped into five categories (Watching, Touching, Repetitive Sounds, Simulations, and Mouth Sounds). However, some triggers do not fall into any of these categories, as ASMR is a highly personal and wide-ranging event (Fredborg et al., 2017).

The effects of ASMR have both a relaxing and calming aspect and an exciting and stimulating aspect. Lochte et al. (2018) evaluated people viewing ASMR videos with functional magnetic resonance imaging (fMRI) and reported brain activity during tingling. The results indicate that it is involved in the reward system, social behavior, and empathy, suggesting that the ASMR videos activate brain regions previously observed during experiences like social bonding and musical frisson. In terms of physiological responses, some individuals experienced increased skin conductance responses (a measure of autonomic nervous system arousal) and decreased heart rate (Poerio et al., 2018) when viewing ASMR videos. Valtakari et al. (2019) found that tingling causes pupil dilation, a physiological reaction toward ASMR stimulation that is similar to the increase in the skin conductance response. In electroencephalography (EEG), an increase in alpha waves in the frontal lobes of experienced ASMR subjects and a decrease in non-experienced subjects suggest the possibility of opposite effects among users (Engelbregt et al., 2022).

As for its relaxing and calming aspect, there are many reports that ASMR affects stress reduction, sleep, and relaxation. ASMR has been proposed as a way to improve sleep quality (Lee et al., 2019; Vardhan et al., 2020). This sleep induction is limited to auditory stimulation and uses natural sounds as triggers that are not likely to induce tingling. EEG measurements of the transition to sleep with combined auditory stimulation of binaural beats suggest that this combined stimulation may help in the transition to sleep (Lee et al., 2019). Cash et al. (2018) reported a placebo effect of ASMR, suggesting that a possible stress reduction effect can be induced by a somatosensory response with a 5-min audio file. ASMR is an efficient way to relax people's minds and allows for easy home-based stress and pain management. Paszkiel et al. (2020) investigated the effects of four types of sound stimuli on stress levels based on four parameters (EEG, blood pressure, pulse, and questionnaire) and reported that both relaxing music and ASMR induce relaxation at a faster rate and have an effect on stress level reduction. We also used fMRI to elucidate the relaxing effects of ASMR on brain function. To compare with classical music, we focused our experiment on the ASMR sound file alone. In both cases, activation of the thalamus and other areas involved in sleep was observed. In particular, activation of the medial prefrontal cortex was observed in ASMR, suggesting that it is involved in the induction of relaxation (Sakurai et al., 2021).

Thus, Previous studies have reported on the effects of ASMR on relaxation, but they have reported only video or only sound evaluations. As a motivation for using ASMR, Barratt and Davis (2015) reported that ASMR helped 98% of participants to relax, 82% to sleep, 70% to cope with stress, and 80% to have a positive effect on mood. In a survey study, ASMR videos showed potential to improve mood and alleviate symptoms of insomnia and depression (Smejka and Wiggs, 2022). Poerio et al. (2018) also associated ASMR experiences with increased positive mood and relaxation. These reports of research on motivations for use are also about ASMR as a whole and do not clearly distinguish between audiovisual and auditory stimulation. Auditory stimulation of ASMR plays the most important role among the triggers, and auditory stimulation is reported to be more triggering than visual stimulation (Barratt et al., 2017). In our previous study, we compared the relaxation effects of ASMR sound alone with classical music as a control (Sakurai et al., 2021). Based on this further, the present study examined the brain activity of ASMR with images, in addition to the sound alone. However, there are no reports directly examining the comparative However, there are no reports directly examining the comparative effects of audiovisual and auditory stimulation. Furthermore, since ASMR is used by many young people to seek relaxation even if they have not experienced tingling, we decided to target those who have never experienced tingling. Therefore, the effectiveness of ASMR, which many young people are seeking, can be verified. To the best of the authors' knowledge, this is the first study to clarify the effect of ASMR in attracting many young people based on the difference in brain function mechanisms between audiovisual and auditory stimuli of ASMR using fMRI.

2. Materials and methods

2.1. Participants

Thirty healthy subjects (15 males and 15 females, mean age 20.8 ± 0.5 years) aged 19 years and older, who had viewed ASMR videos but had never experienced tingling. They also had no history of psychiatric disorders, and were not taking any medications. In order to avoid the effects of habituation, the subjects were not allowed to watch ASMR at all for 1 week prior to the start of the experiment. Tingling was defined in this study as a creeping somatic sensation that originates in the scalp and extends from the back of the neck to the back or limbs. This study was approved by the Research Ethics Committee of Niigata University of Health and Welfare (approval No. 18218-190722). We provided informed consent to all subjects and obtained written consent. We also interviewed the subjects to ensure the safety of MRI imaging.

2.2. Stimuli task

The subjects were asked to select their preferred ASMR as the stimulus task. Five ASMRs of repetitive, crisp, and refreshing sounds

(are scratching, eating cucumber, typing, pouring soda water, and rain sound) were selected from among the 10 used in our previous study. We excluded those that emphasized activity in the visual cortex, such as touching, because ASMR also can also be induced by a sound file alone.

Participants listened to all five types at least 1 week before the experiment and selected the one ASMR type that was most to their preference. We prepared a video of the selected ASMR and a sound file alone from that video. Editing was done using the video editing software Power Director 18 (Cyber Link Corporation) to create compressed audio data in MP4, and the volume was set at 98 dB for all participants. While listening to the sound file alone, the participant viewed a fixed white cross on a black screen.

The resting task prior to the stimulus task was listening to white noise. White noise was used because it is a random signal with equal power at any frequency within a given bandwidth that does not stimulate emotional involvement (Cardona et al., 2020). The same fixed crosses were displayed on the screen during the resting task.

2.3. Block design

A block design was used to alternate between the resting task and the stimulus task for 30 s each, for a total of 6 min. White noise and fixed crosses were included during the resting task to separate the stimulation time from the baseline blood oxygenation signal from the fMRI. The block design is shown in **Figure 1**.

2.4. Apparatus

Imaging was performed using a 3-tesla MRI system (Vantage Galan, Canon Medical Systems, Tochigi, Japan) with a 16-channel head coil. The participant laid down in the MRI machine and watched the block design. The images were displayed on the MR-theater (Canon, Inc.) and could be viewed while lying down. The sound source was an MRI headphone system (Star Products, Inc., iMage), which has high sound insulation and blocks out scanning sounds.

2.5. MRI Acquisition

High-resolution MRI images were captured separately to obtain detailed anatomical information before fMRI imaging. The structural image for this purpose was a high-resolution T1-weighted magnetization-prepared rapid-gradient-echo (MP-RAGE) sequence. The settings were: repetition time (TR) = 5.8 ms, echo time (TE) = 2.7 ms, inversion time (TI) = 900 ms, flip angle (FA) = 9°, number of matrix (matrix) = 256 × 256, field of view (FOV) = 23 × 23 cm, slice thickness = 1.2 mm. Echo-planar imaging (EPI) sequences were used to capture fMRI images. The imaging conditions for the fMRI images were as follows: TR = 2,000 ms, TE = 25 ms, FA = 85°, matrix = 64 × 64, FOV = 24 × 24 cm, and slice thickness = 3 mm so that the entire brain could be covered.

2.6. fMRI data analyses

The fMRI data were preprocessed and analyzed using Statistical Parametric Mapping 12 (Wellcome Trust Center for Neuroimaging) running on Matlab (Mathworks Inc.). After correcting for time differences with slice timing correction, displacement due to motion was corrected with realignment. In addition, coregisters were used to compare structural and fMRI images. The coregister corrected for displacement between structural and functional images and normalized the data by aligning each participant's brain with the Montreal Neurological Institute's standard brain coordinate system template. Normalized images were smoothed using an 8 mm Gaussian kernel. After preprocessing, changes in brain activity associated with audiovisual and auditory stimulation of ASMR were identified by block design using the general liner model (GLM). A head movement parameter was added to remove the effect

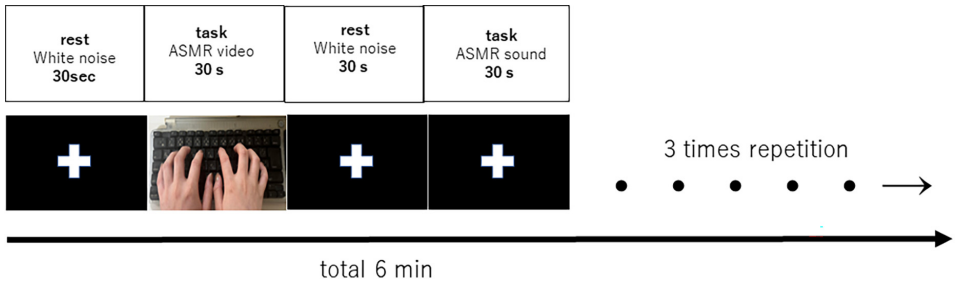

FIGURE 1
Block design of 6 min with 30 s rest and 30 s task (auditory and visual stimulation, auditory stimulation), repeated three times. Each subject listened or viewed the tasks in random order.

TABLE 1 Questionnaire results for the two moods ("relaxed mood" and "tingling mood").

Likert scale point		1	2	3	4	5	
Relaxed mood	Audiovisual stimulations	0 (0.00%)	1 (3.33%)	4 (13.33%)	18 (60.00%)	7 (23.33%)	$p = 1.000$
	Auditory stimulations	0 (0.00%)	1 (3.33%)	4 (13.33%)	18 (60.00%)	7 (23.33%)	
Tingling mood	Audiovisual stimulations	7 (23.33%)	4 (13.33%)	3 (10.00%)	14 (46.67%)	2 (6.67%)	$p = 0.895$
	Auditory stimulations	6 (20.00%)	4 (13.33%)	5 (16.67%)	12 (40.00%)	3 (10.00%)	

of movement. Contrast images were produced at the first level (single subject) with the following contrasts: (1) ASMR audiovisual stimulation = 1, rest = 0, (2) ASMR auditory stimulation = 1, rest = 0, (3) ASMR audiovisual stimulation = 1, ASMR auditory stimulation = −1, and (4) ASMR audiovisual stimulation = −1, ASMR auditory stimulation = 1, respectively. The contrasts in (3) were used to identify brain regions that showed significantly increased activity with audiovisual stimulation compared to the auditory stimulation condition. The contrasts in (4) were used to identify brain regions that showed significantly increased activity with auditory stimulation compared to the audiovisual stimulation condition. In the next group analysis (second level), a one-sample *t*-test was performed using the above four contrasts. The initial threshold for voxel level was set at uncorrected $p < 0.001$. Clusters were considered significant if they were below $p = 0.05$ corrected for family wise errors. Audiovisual and auditory stimulation of ASMR were analyzed separately; audiovisual stimulation minus auditory stimulation and auditory stimulation minus audiovisual stimulation was subtracted from audiovisual stimulation.

2.7. Questionnaire

We administered a mood questionnaire to all subjects after fMRI imaging. We investigated two different mood intensities for each ASMR for audiovisual and auditory stimulation. The two moods were "relaxed mood" and "tingling mood," using a Likert-type scale from 1 to 5: (1) totally disagree, (2) disagree, (3) neither agree nor disagree, (4) agree, (5) agree very much. The subjects were told that "relaxed mood" refers to a state of calm and peacefulness. Statistical analysis was conducted using SPSS (IBM SPSS Statistics Base) 26.0 with the Mann–Whitney U test. The significance level was set at 5%.

3. Results

The questionnaire results showed no significant difference between audiovisual and auditory stimulation of ASMR in terms of "relaxed mood" and "tingling mood." The results are shown in Table 1.

Audiovisual stimulation of ASMR showed activation of the visual cortex, the left and right middle frontal gyrus, and the nucleus accumbens. Auditory stimulation showed activation of the auditory and visual cortices and the left and right insular cortices. Table 2 shows the coordinates of the areas that were significantly activated during the stimulation task. Figure 2 shows a glass-brain image of the activation of the whole brain during the stimulation task.

Figure 3 shows an image of the activation of the nucleus accumbens, which is a characteristic feature of the ASMR audiovisual stimulation task.

TABLE 2 Significantly activated areas and *T*-values of stimulation task performance.

Hemisphere		Locations	Cluster *p*-value (FWE)	Cluster size (voxels)	*T*-value	Z-score	X {mm}	Y {mm}	Z {mm}
Audiovisual stimulations	Right	Calcarine cortex	<0.001	26,869	13.49	7.53	12	−92	0
	Left	Middle frontal gyrus	<0.001	1,024	7.32	5.47	−26	−4	48
	Right	Middle frontal gyrus	<0.001	960	6.62	5.13	32	4	66
	Left	Accumbens area	0.009	419	6.05	4.83	−14	4	−20
Auditory stimulations	Left	Insula	<0.001	2,536	11.82	7.09	−46	−22	4
	Right	Insula	<0.001	2,648	11.68	7.05	50	−14	4
	Right	Occipital pole	0.001	593	5.43	4.48	24	−90	16
	Left	Lingual gyrus	0.005	459	4.81	4.09	−14	−74	−18

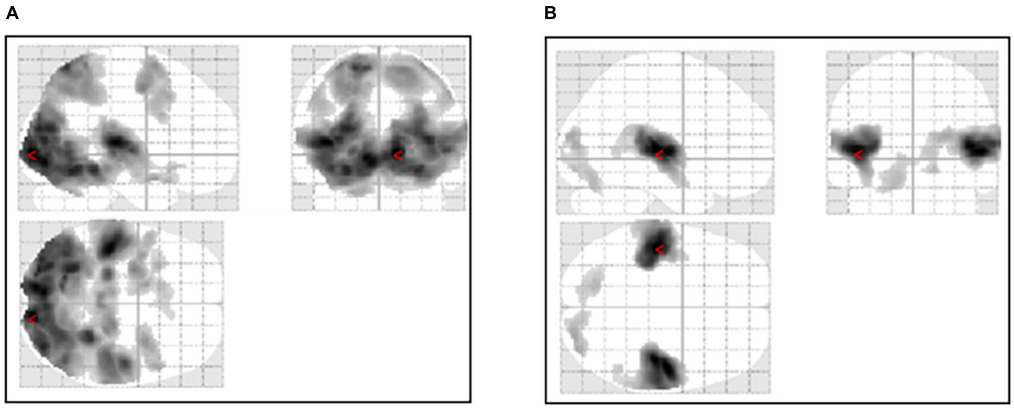

FIGURE 2
Activation of the whole brain during the stimulation task. **(A)** Activation during the ASMR audiovisual stimulation task. **(B)** Activation during the ASMR auditory stimulation task.

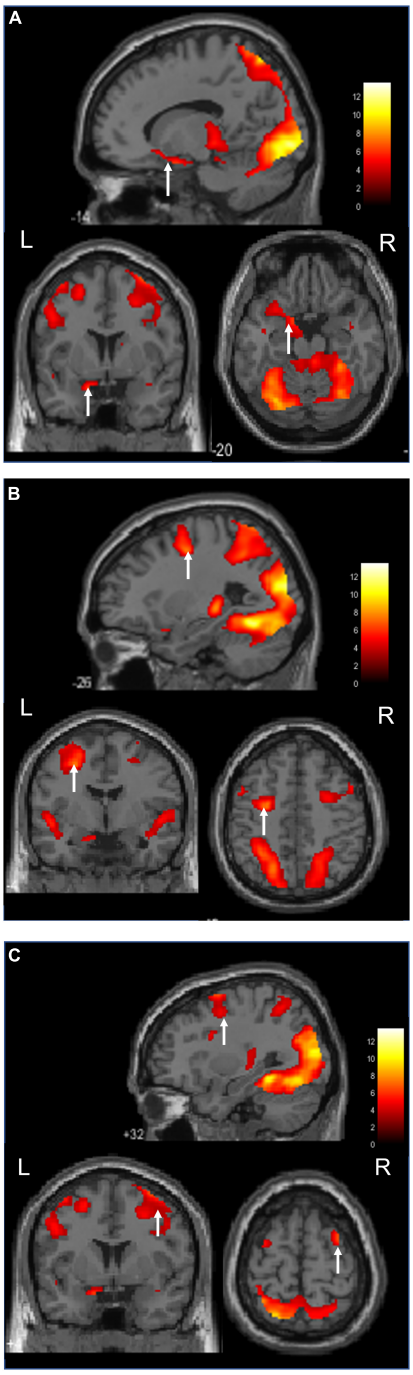

FIGURE 3
Activation during the ASMR audiovisual stimulation task (Sagittal, coronal, and axial images.). **(A)** Activation of the left nucleus accumbens is confirmed. **(B)** Activation of the left middle frontal gyrus is confirmed. **(C)** Activation of the right middle frontal gyrus is confirmed.

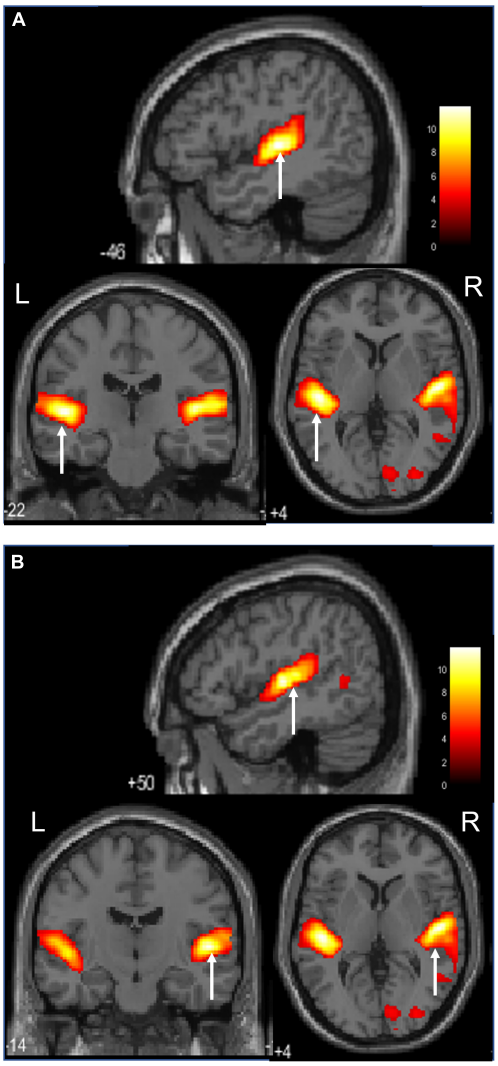

FIGURE 4
Activation during the ASMR audiovisual stimulation task (Sagittal, coronal, and axial images.).**(A)** Activation of the left insula cortices is confirmed. **(B)** Activation of the right insula cortices is confirmed.

Figure 4 shows images of the activation of the left and right insular cortices, which characteristic the ASMR auditory stimulation task.

The regions with significantly increased activity during audiovisual stimulation compared to auditory stimulation were the left lingual gyrus, left postcentral gyrus, left and right middle frontal gyrus, and left lateral nucleus accumbens. The regions of significantly increased activity during auditory stimulation compared to the audiovisual stimulation condition were the left middle occipital gyrus, right precuneus, right angular gyrus, and left lateral ventricle. Their *T*-values and coordinates are shown in Table 3.

4. Discussion

This is the first fMRI-based brain function study focusing on the effects of ASMR video viewing compared with listening to sound file alone. The participants showed no difference in mood when they watched the ASMR video or listened to the sound file alone, but they revealed a difference in the brain function.

The audiovisual ASMR task stimulated the visual cortex, whereas the auditory task stimulated the auditory and visual cortices. As for the difference between visual and auditory stimulation, according to Norretranders, human sensory organs receive over 11.1 (Mbit/s) of external information, of which 10 (Mbit/s) is visual and 0.1 (Mbit/s) is auditory. The amount of information input to the brain per second for visual stimulation is said to be 100 times greater than

TABLE 3 *T*-values and coordinates of the sites of significantly increased activity by audiovisual stimulation and auditory stimulation.

	Hemisphere	Locations	Cluster *p*-value (FWE)	Cluster size (voxels)	*T*-value	Z-score	X {mm}	Y {mm}	Z {mm}
Audiovisual stimulations > Auditory stimulations	Left	Lingual gyrus	<0.001	21,737	13.67	7.57	−10	−82	−10
	Left	postcentral gyrus	0.007	419	8.62	6.02	−54	−22	38
	Left	Middle frontal gyrus	<0.001	756	7.06	5.34	−24	−6	48
	Right	Middle frontal gyrus	0.015	351	5.57	4.55	28	0	68
	Left	Accumbens area	0.007	426	4.99	4.2	−14	6	−20
	Left	Middle frontal gyrus	0.007	420	4.65	3.99	−52	8	38
	Right	Middle frontal gyrus	0.067	226	4.62	3.97	36	10	26
Audiovisual stimulations < Auditory stimulations	Left	Middle occipital gyrus	0.001	675	9.10	6.21	−46	−68	32
	Right	Precuneus	<0.001	2,059	8.61	6.02	22	−44	22
	Right	Angular gyrus	<0.001	767	7.77	5.67	46	−64	42
	Left	Lateral ventricle	0.021	325	5.24	4.36	−22	−28	30

that for auditory stimulation (Norretranders, 1998). It is thought that the greater amount of information from the visual stimuli during audiovisual stimulation focuses attention on movement. In the auditory task, the visual cortex was also activated because the participants were watching the presentation of the fixed cross, but it is thought that their attention was focused more on the sound. However, since the fixed crosses were identical during the resting time and the audio, we believe that they may not have been separated from the resting time. In the future, the experimental design for auditory stimulation needs to be improved and additional experiments should be conducted in the absence of a fixed cross during auditory stimulation. In addition to the visual and auditory cortices, activation was also observed in more characteristic areas. Audiovisual stimulation showed activation in the middle frontal gyrus and left temporal nucleus, which is not seen in other areas, and auditory stimulation showed activation in the bilateral insular cortex. Lochte et al. (2018) reported brain function during tingling while viewing ASMR videos; subjects experiencing ASMR showed significant activation in the nucleus accumbens, dorsal anterior cingulate cortex, insular cortex, and inferior frontal gyrus, and these are regions associated with both reward and emotional arousal. Although the block design differed from the present study, the results were similar, if not tingling.

Audiovisual stimulation of the middle frontal gyrus and nucleus accumbens plays an important role in the mesolimbic dopamine pathway, which operates as a reward mechanism. Dopaminergic input from the ventral tegmental area connects to the limbic system, including the nucleus accumbens, and to other structures, such as the prefrontal cortex and amygdala. The nucleus accumbens is an important brain region for reward, gratification, and emotion and is largely responsible for the release of dopamine (Pereira et al., 2011). It is also involved in improving pain, depression, and anxiety symptoms (Du et al., 2017; Harris and Peng, 2020).

The middle frontal gyrus involvement was bilateral, while the nucleus accumbens was left-sided. Du et al. (2017) reported that the strength of connectivity between the left dorsolateral prefrontal cortex and the left nucleus accumbens was negatively correlated with improvement in depressive and anxiety symptoms. The activation of the left middle frontal gyrus and left nucleus accumbens in the present results suggests a sufficient involvement in depression and anxiety. From the results of differential ASMR audiovisual and auditory stimulation, the left and right middle frontal gyrus and left temporal nucleus were identified as the regions significantly activated by audiovisual stimulation. The involvement of the mesolimbic dopamine circuitry seems certain. Smejka and Wiggs (2022) also reported that ASMR movies might improve mood and alleviate symptoms of insomnia and depression. These reports are also considered encouraging from the viewpoint of brain function. In addition, subtraction of audiovisual and auditory stimuli in ASMR revealed that audiovisual stimulation significantly activated the left and right middle frontal gyrus and left lateral nucleus. The involvement of mesolimbic dopamine pathways seems certain.

The left and right insular cortices activated by auditory stimulation are adjacent to the primary auditory cortex, which is essential for human cognitive behavior and is involved in sensorimotor activity, pain, empathy, and high levels of attention and decision making (Uddin et al., 2017). In particular, the posterior insula is closely associated with the auditory cortex and is involved in the network for receiving and processing auditory information. The anterior insula is also involved in processing autonomic information

and in perceiving the emotional states of others and feeling those emotions yourself (Zhang et al., 2019). Thus, the insular cortex is involved in integrating internal and external information and is present to form a global perception of how the self feels (Craig, 2009). The left insula is involved in parasympathetic control, while the right insula is involved in sympathetic control (Nagai et al., 2010). The left insula is activated by pleasant emotions, such as pleasant music, while the right insula is activated by unpleasant emotions, such as various types of pain. Right insular activation has been reported in misophonia, which is an aversion or hatred to a specific sound (Schröder et al., 2019). There is an inhibitory relationship between the left and right insula that maintains sympathetic balance. Autonomic balance is said to be a physiological response to stress (Dearing et al., 2022), which indicates that the autonomic nervous system is balanced and responds to stress. Subtraction of audiovisual stimuli in ASMR also showed no significant activation of the insular cortex in the left and right insula.

We attempted to clarify the differences in mood by means of a questionnaire, but no differences were found. The 30-s ASMR video viewing may not have improved Tingling or mood due to the short duration of video viewing. Future improvements are needed, such as lengthening the video viewing time. However, the present study showed that there is a clear difference between auditory stimulation and audiovisual stimulation in terms of brain activation sites. The subjects of this study were those who had no experience with tingling, which we believe is supportive of the fact that many young people use the device for relaxation purposes regardless of tingling. However, it cannot be said that the non-experienced tinglers were accurate in their evaluation of tingling and comfort. Considering the effect on the activated areas in the brain, the mood questionnaire was also administered immediately after the MRI imaging, but it was a retrospective self-report, so further study and improvement could be needed. In the next step, we believe that the subjects also need to be compared between those who experienced tingling and those who did not. In the future, it will be necessary to evaluate stress, anxiety, and pain using physiological indices and rating scales. This could clarify the effects of ASMR on anxiety, stress, and pain by showing the relationship between physiological indices and rating scales and brain activation sites, and may indicate that ASMR is useful for mental health.

The present study has several other limitations. We believe that physiological indices and rating scales for stress, anxiety, and pain could also be investigated to clarify differences in mood improvement and physiological responses. In this study, there was no control group, such as non-ASMR. Comparison of relaxing videos may be useful to further elucidate the unique nature of ASMR. In the future, a three-way comparison between non-ASMR, sound-only ASMR, and moving image ASMR should be conducted simultaneously. In addition, it will be necessary in the future to analyze and examine whether there is a functional relationship between the characteristic activation sites at the network level. Also, the number of ASMR types was quite limited to 5. Preference for ASMR is largely a matter of personal choice, and a wider selection might have yielded different characteristics and results. We would like to consider further increasing the number of participants. The age range was also limited to young people, and the results may differ if a wider range of age groups is targeted. Further experiments targeting older adults are needed.

5. Conclusion

The results of this study showed that there was a clear difference between auditory and audiovisual stimulation in terms of the areas of activation in the brain, but the questionnaire did not reveal any difference in the subjects' mood. Audiovisual stimulation showed activation of the middle frontal gyrus and the nucleus accumbens, whereas auditory stimulation showed activation of the insular cortex. The difference in brain activation sites suggests a difference in the effects of auditory and audiovisual stimulation. However, in the future, it will be necessary to investigate the relationship between the brain activation sites by comparing the effects of ASMR on those who have experienced tingling and those who have not, and by investigating physiological indices. This will clarify the effects of ASMR on depression, anxiety, stress, and pain, and may indicate that ASMR is useful for mental health.

Data availability statement

The original contributions presented in this study are included in this article/supplementary material, further inquiries can be directed to the corresponding author.

Ethics statement

The studies involving human participants were reviewed and approved by the Research Ethics Committee of Niigata University of Health and Welfare. The patients/participants provided their written informed consent to participate in this study.

Author contributions

NS and NK conceived the study and designed the experiments. NS, KN, ST, and NK collected MR data and performed statistical analysis. NS and KN performed data interpretation. SK, HO, and NK helped draft the manuscript. All authors approved the final version of the submitted manuscript.

Funding

This study was supported by KAKENHI (No. 20K11059) from the Japan Society for the Promotion of Science.

Acknowledgments

We would like to thank Editage (www.editage.com) for English language editing.

Conflict of interest

The authors declare that the research was conducted in the absence of any commercial or financial relationships that could be construed as a potential conflict of interest.

Publisher's note

References

Barratt, E. L., and Davis, N. J. (2015). Autonomous sensory meridian response (ASMR): A flow-like mental state. *PeerJ* 3:e851. doi: 10.7717/peerj.851

Barratt, E. L., Spence, C., and Davis, N. J. (2017). Sensory determinants of the autonomous sensory meridian response (ASMR): Understanding the triggers. *PeerJ* 5:e3846. doi: 10.7717/peerj.3846

Cardona, G., Rodriguez-Fornells, A., Nye, H., Rif-Ros, X., and Ferreri, L. (2020). The impact of musical pleasure and musical hedonia on verbal episodic memory. *Sci. Rep.* 10:16113. doi: 10.1038/s41598-020-72772-3

Cash, D. K., Heisick, L. L., and Papesh, M. H. (2018). Expectancy effects in the autonomous sensory meridian response. *PeerJ* 6:e5229. doi: 10.7717/peerj.5229

Craig, A. D. (2009). How do you feel – Now? The anterior insula and human awareness. *Nat. Rev. Neurosci.* 10, 59–70. doi: 10.1038/nrn2555

Dearing, C., Handa, R. J., and Myers, B. (2022). Sex differences in autonomic responses to stress: Implications for cardiometabolic physiology. *Am. J. Physiol. Endocrinol. Metab.* 323, E281–E289. doi: 10.1152/ajpendo.00058.2022

Du, L., Liu, H., Du, W., Chao, F., Zhang, L., Wang, K., et al. (2017). Stimulated left DLPFC-nucleus accumbens functional connectivity predicts the antidepression and antianxiety effects of rTMS for depression. *Transl. Psychiatry* 7:3. doi: 10.1038/s41398-017-0005-

Engelbregt, H. J., Brinkman, K., van Geest, C. C. E., Irrmischer, M., and Deijen, J. B. (2022). The effects of autonomous sensory meridian response (ASMR) on mood, attention, heart rate, skin conductance and EEG in healthy young adults. *Exp. Brain Res.* 240, 1727–1742. doi: 10.1007/s00221-022-06377-9

Fredborg, B., Clark, J., and Smith, S. (2017). An examination of personality traits associated with autonomous sensory meridian response (ASMR). *Front Psychol.* 8:247. doi: 10.3389/fpsyg.2017.00247

Harris, H. N., and Peng, Y. B. (2020). Evidence and explanation for the involvement of the nucleus accumbens in pain processing. *Neural Regen. Res.* 15, 597–605. doi: 10.4103/1673-5374.266909

Lee, M., Song, C. B., Shin, G. H., and Lee, S. W. (2019). Possible effect of binaural beat combined with autonomous sensory meridian response for inducing sleep. *Front. Hum. Neurosci.* 13:425. doi: 10.3389/fnhum.2019.00425

Lochte, B. C., Guillory, S. A., Richard, C. A. H., and Kelley, W. M. (2018). An fMRI investigation of the neural correlates underlying the autonomous sensory meridian response (ASMR). *Bioimpacts* 8, 295–304. doi: 10.15171/bi.2018.32

Morales, R., Ramírez-Benavides, D., and Villena-Gonzalez, M. (2021). Autonomous sensory meridian response self-reporters showed higher scores for cognitive reappraisal as an emotion regulation strategy. *PeerJ* 9:e11474. doi: 10.7717/peerj.11474

Nagai, M., Hoshide, S., and Kario, K. (2010). The insular cortex and cardiovascular system: A new insight into the brain-heart axis. *J. Am. Soc. Hypertens.* 4, 174–182. doi: 10.1016/j.jash.2010.05.001

Norretranders, T. (1998). *The user illusion: Cutting consciousness down to size.* New York, NY: Penguin.

Paszkiel, S., Dobrakowski, P., and Łysiak, A. (2020). The impact of different sounds on stress level in the context of EEG, cardiac measures and subjective stress level: A pilot study. *Brain Sci.* 10:728. doi: 10.3390/brainsci10100728

Pereira, C. S., Teixeira, J., Figueiredo, P., Xavier, J., Castro, S. L., and Brattico, E. (2011). Music and emotions in the brain: Familiarity matters. *PLoS One* 6:27241. doi: 10.1371/journal.pone.0027241

Poerio, G. L., Blakey, E., Hostler, T. J., and Veltri, T. (2018). More than a feeling: Autonomous sensory meridian response (ASMR) is characterized by reliable changes in affect and physiology. *PLoS One* 13:e0196645. doi: 10.1371/journal.pone.0196645

Sakurai, N., Ohno, K., Kasai, S., Nagasaka, K., Onishi, H., and Kodama, N. (2021). Induction of relaxation by autonomous sensory meridian response. *Front. Behav. Neurosci.* 15:761621. doi: 10.3389/fnbeh.2021.761621

Schröder, A., van Wingen, G., Eijsker, N., San Giorgi, R., Vulink, N. C., Turbyne, C., et al. (2019). Misophonia is associated with altered brain activity in the auditory cortex and salience network. *Sci. Rep.* 9:7542. doi: 10.1038/s41598-019-44084-8

Smejka, T., and Wiggs, L. (2022). The effects of autonomous sensory meridian response (ASMR) videos on arousal and mood in adults with and without depression and insomnia. *J. Affect. Disord.* 301, 60–67. doi: 10.1016/j.jad.2021.12.015

Uddin, L. Q., Nomi, J. S., Hébert-Seropian, B., Ghaziri, J., and Boucher, O. (2017). Structure and function of the human insula. *J. Clin. Neurophysiol.* 34, 300–306. doi: 10.1097/WNP.0000000000000377

Valtakari, N. V., Hooge, I. T., Benjamins, J. S., and Keizer, A. (2019). An eye-tracking approach to autonomous sensory meridian response (ASMR): The physiology and nature of tingles in relation to the pupil. *PLoS One* 14:e0226692. doi: 10.1371/journal.pone.0226692

Vardhan, V. V., Venkatesh, U., and Yadav, S. (2020). "Signal processing based autonomous sensory meridian response to treat insomnia," in *Proceedings of the international conference on electronics and sustainable communication systems (ICESC)*, (Coimbatore: IEEE).

Zhang, Y., Zhou, W., Wang, S., Zhou, Q., Wang, H., Zhang, B., et al. (2019). The roles of subdivisions of human insula in emotion perception and auditory processing. *Cereb. Cortex.* 29, 517–528. doi: 10.1093/cercor/bhx334

Frontiers in Neuroscience

Provides a holistic understanding of brain function from genes to behavior

Part of the most cited neuroscience journal series which explores the brain - from the new eras of causation and anatomical neurosciences to neuroeconomics and neuroenergetics.

Discover the latest Research Topics

See more →

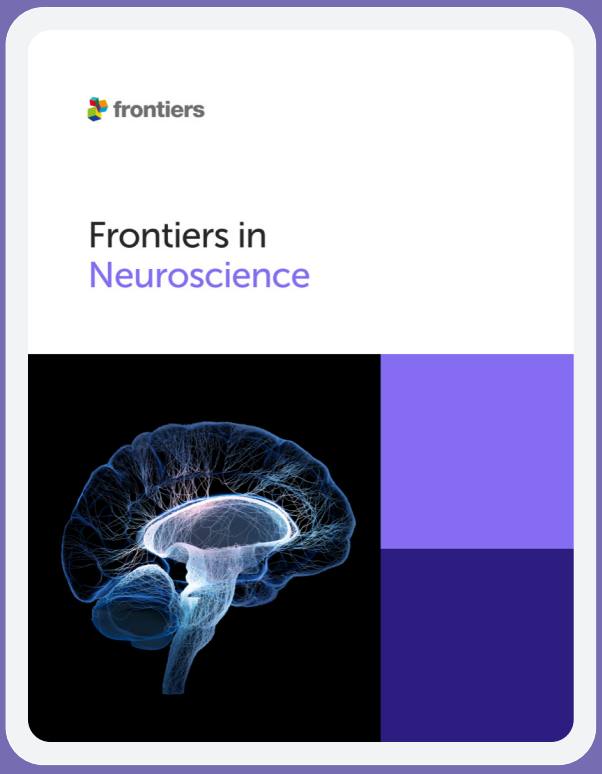

Frontiers

Avenue du Tribunal-Fédéral 34
1005 Lausanne, Switzerland
frontiersin.org

Contact us

+41 (0)21 510 17 00
frontiersin.org/about/contact